Spring 1-1-2013

Centrifuge Modeling of the Thermo-Mechanical Response of Energy Foundations

Joseph Collin Goode III
University of Colorado at Boulder, joseph.goode@colorado.edu

Centrifuge Modeling of the Thermo-Mechanical Response of Energy Foundations

by

Joseph Collin Goode III

A thesis submitted to the
Faculty of the Graduate School of the
University of Colorado in partial fulfillment
Of the requirement for the degree of
Master of Science
Department of Civil, Environmental and Architectural Engineering
2013

This thesis entitled:

Centrifuge Modeling of the Thermo-Mechanical Response of Energy Foundations

written by Joseph Collin Goode III

has been approved by the Department of Civil, Environmental, and Architectural Engineering

_____

Professor John S. McCartney (committee chair)

_____

Professor Dobroslav Znidarcic

Date_____

The final copy of this thesis has been examined by the signatories, and we

Find that both the content and the form meet the acceptable presentation standards

Of scholarly work in the above mentioned discipline.

Goode III, Joseph Collin. (M.S. Civil Engineering, Department of Civil, Environmental, and Architectural Engineering)

Centrifuge Modeling of the Thermo-Mechanical Response of Energy Foundations
Thesis directed by Professor John S. McCartney

ABSTRACT

This thesis presents the results from a series of centrifuge tests performed to understand the profiles of thermo-mechanical axial strain, axial displacement, and axial stress in semi-floating and end-bearing energy foundations installed in dry Nevada sand and Bonny silt layers during different combinations of mechanical loading and foundation heating. In addition to the construction details for the centrifuge scale-model reinforced concrete energy foundations, the results from 1-g thermo-mechanical characterization tests performed on the foundations to evaluate their mechanical and thermal material properties are presented in this thesis.

In general, the centrifuge-scale tests involve application of an axial load to the head of the foundation followed by circulation of a heat exchange fluid through embedded tubing to bring the foundation to a constant temperature. After this point, mechanical loads were applied to the foundation to characterize their thermo-mechanical response. Specifically, loading tests to failure were performed on the semi-floating foundation installed in different soil layers to characterize the impact of temperature on the load-settlement curve, and elastic loading tests were performed on the end-bearing foundation to characterize the impact of temperature on the mobilized side shear distributions. During application of mechanical loads and changes in foundation temperature, the axial strains are measured using embedded strain gages. The soil and foundation temperatures, foundation head movement, and soil surface deformations are also monitored to characterize the thermo-mechanical response of the system.

The tests performed in this study were used to investigate different phenomena relevant to the thermo-mechanical response of energy foundations. First, the role of end-restraint boundary conditions in both sand and silt were investigated by comparing the strain distributions for the end-bearing and semi-floating foundations in each soil type. The tests on sand and silt permit evaluation of the soil-structure interaction in dry and unsaturated soils with different mechanisms of side shear resistance (i.e., primarily frictional and primarily cohesive, respectively). End-bearing foundations were observed to have higher magnitudes of thermal axial stress than semi-floating foundations, with a more uniform distribution in thermal axial strain in the sand. A general conclusion from these tests is that the unsaturated silt led to a more pronounced soil structure interaction effect than the dry sand. For example, temperature did not affect the ultimate capacity of the semi-floating foundation in dry sand, while it had a pronounced effect in unsaturated silt. Two approaches for controlling the foundation head restraint boundary condition were investigated for the end-bearing foundation in sand: load control conditions (free expansion) as well as stiffness control conditions (restrained expansion). As expected, greater expansion was observed in the case of free expansion, and greater thermal axial stresses were observed in the case of restrained expansion. The effects of temperature cycles were also investigated for the semi-floating foundation in Bonny silt, and less upward movement was observed during each cycle of heating, with a slight softening in behavior on each cycle. Overall, the results provide a suite of information which is suitable to define soil-structure interaction parameters under realistic stress states for deep foundations.

ACKNOWLEDGEMENTS

Special thanks are given to the author's advisor John McCartney for the opportunities he has afforded me through my years at the University of Colorado as well as his countless hours of guidance and assistance in all aspects of this thesis. Thanks are given to Min Zhang for all the assistance through testing, especially weekend spins. This project would not have been completed without the help of many geotechnical graduate and undergraduate students who helped with their time and insight: Kyle Murphy, Bryan Black, Wyatt Weiss, Thierry Traore, and Melissa Stewart. Special recognition is given to the members of the thesis committee: Professors Dobroslav Znidarcic and Richard Regueiro. Funding from NSF grant CMMI 0928159 is greatly appreciated.

Table of Contents

List of Figures

CHAPTER 1 Introduction

1.1 Motivation

Although incorporation of heat exchangers into deep foundation elements (energy foundations) reduces the installation costs of ground-source heat exchange systems (Brandl 1998; Ennigkeit and Katzenbach 2001; Brandl 2006), an issue encountered is the potential for foundation movements due to thermal expansion and contraction of the foundation element or surrounding soil. Further, soil-structure interaction may restrain movement of the foundation, leading to generation of thermal axial stresses. This behavior has been documented in several field-scale case histories (Laloui et al. 2006; Bourne-Webb et al. 2009; Amatya et al. 2012; McCartney and Murphy 2012). Although thermo-mechanical soil-structure interaction analyses permit prediction of changes in axial stress or strain during heating and cooling operations (Knellwolf et al. 2011; Plaseied 2011), they require empirical data for calibration of model parameters and verification of predictions. This is especially the case when considering the behavior of energy piles in some soil deposits, such as soft clays or unsaturated soils. This empirical data is often difficult to collect from field-scale case histories due to cost and logistical constraints, and may also be difficult to interpret due to the complex soil stratigraphy and foundation installation effects encountered during real projects. The use of centrifuge modeling facilitates the collection of empirical data in a cost-effective manner using simple soil and foundation properties that can be carefully controlled or characterized.

This study builds upon two previous centrifuge testing programs at the University of Colorado Boulder on the topic of energy foundations. McCartney and Rosenberg (2011) performed isothermal loading tests on semi-floating energy foundations in compacted silt to quantify the impact of temperature on the ultimate capacity of energy foundations. They

observed an increase in stiffness of the load-settlement curve, and an increase in ultimate capacity determined using Davisson's criterion. This change in behavior with temperature was attributed to an increase in side shear resistance due to the differential expansion of the foundation into the soil. Stewart (2012) and Stewart and McCartney (2013) measured the impact of end boundary conditions on the thermal axial strains in energy foundations in compacted silt using embedded strain gages within the scale-model energy foundations. They found that the location of the point of zero thermal displacement and the location of the maximum thermal axial stress shifted downward when the toe of the foundation was resting on a rigid base as compared to relatively flexible soil. Stewart and McCartney (2012) also evaluated the role of cyclic heating and cooling on the strain distribution. A ratcheting effect was observed where the end-bearing foundation heaved upward by a successively lower amount on each heating cycle. This was postulated to be due to thermally induced water flow away from the foundation, as well as potential thermal consolidation of the unsaturated soil surrounding the foundation.

This study seeks to build upon this database of centrifuge modeling results by combining the experimental approaches used in these two studies. Specifically, this study will use two new centrifuge-scale model foundations (end-bearing and semi-floating) with embedded instrumentation to study the impact of different variables on the axial thermo-mechanical response during changes in temperature or mechanical loading. Another goal of this study is to provide results and relevant material properties that can be used for calibration and validation of advanced thermo-hydro-mechanical finite element models.

1.2 Approach

The approach used in this study is to utilize geotechnical centrifuge modeling to evaluate the axial stress-strain and load-settlement response of two energy foundations, one with end-

bearing toe boundary conditions and the other with semi-floating toe boundary conditions. The configuration of the experiment will be changed to investigate the impacts of soil type (cohesive and cohesionless), toe and head end-restraint boundary conditions, and thermal load programs applied to the foundations. Centrifuge modeling permits characterization of the thermo-mechanical behavior of both energy foundations and the surrounding soil in carefully controlled and repeatable conditions. Relevant variables that can be measured include the foundation head displacement, the thermo-mechanical strain profiles, the foundation temperature, the soil temperature, and the soil water content. This information can also be processed to understand the thermo-mechanical stress profiles and thermo-mechanical axial displacement profiles in the energy foundations.

1.3 Objectives

The goal of this study is to provide experimental data on the response of energy foundations that may be difficult or impossible to obtain from full-scale field tests on energy foundations, in carefully controlled conditions that permit isolation of the effects of different variables. To reach the goal of this study, the specific objectives of this study are to:

1. Characterize the thermo-mechanical properties of reinforced concrete used in energy foundations.
2. Understand the role of soil type (cohesive and cohesionless) on the thermo-mechanical behavior of energy foundations.
3. Understand the role of toe end-constraint boundary conditions for different soil types (end-bearing and semi-floating).
4. Understand the role of head end-restraint on the strain profiles and head displacement.

5. Understand the change in side shear resistance interpreted through the load-settlement curve during heating of semi-floating energy foundations to different temperatures.
6. Develop additional data that can be used to understand the mechanisms of changes in head displacement during cyclic heating and cooling.

1.4 Scope of Study

Chapter 2 includes a literature review on the thermo-mechanical response of full-scale energy foundations as well as results from previous centrifuge modeling studies. Further, this chapter presents the basis of centrifuge scale-modeling of energy foundations employed in this study, which is a complex topic as heat flow does not scale in the same manner as other phenomena governed by self-weight. Chapter 3 provides a description of the experimental setup used in this study, along with the different variations employed to investigate different variables. Chapter 4 includes an overview of the relevant material properties of the foundation and soil. This chapter is particularly important, as the 1g characteristics of the foundation have a major impact on the interpretation of the centrifuge results. The procedures used in the different centrifuge tests are presented in Chapter 5. The results from the centrifuge tests are presented in Chapter 6, which includes a table describing the details and inter-relationships between the 14 tests performed as part of this study. The analysis of the impacts of the different variables affecting the thermo-mechanical response of energy foundations is presented in Chapter 7, and the conclusions of this study are presented in Chapter 8.

CHAPTER 2 Background

2.1 Energy Foundations

Energy foundations are defined as drilled shaft foundations with embedded heat exchange elements. The purpose of these foundations is twofold; (1) they provide the necessary structural support for buildings or other civil engineering infrastructure and (2) they provide a means to access the heat stored within the subsurface using a ground-source heat pump (GSHP). Ground-source heat pumps (GSHP) are a well-established technology to move heat to or from the ground through circulation of fluid through closed-loop heat exchanger pipes to provide heating and cooling to a building. The fact that energy foundations are necessary as structural elements for buildings reduces the capital cost required to install the heat exchanger component of a GSHP. Different than conventional GSHP borehole heat exchangers, energy foundations have the advantage of the heat storage capacity of concrete (0.88 J/gK), which is greater than most soils (0.80 J/gK). Because the depth and spacing of energy foundations is governed by structural requirements, they are not expected to be sufficient to provide all of the heating and cooling for buildings, but it is generally accepted that they can provide 10 to 20% of the heating and cooling load.

Although energy foundations provide a useful pathway to the heat stored in the subsurface, the thermo-mechanical behavior of the foundation and surrounding soil, as well as soil-structure interaction, must be characterized and understood for implementation of energy foundations to become commonplace in geotechnical engineering. Heating and cooling operations in energy foundations could lead to thermally-induced movements or stresses induced in the pile, changes in axial capacity, and changes in soil-structure interaction due to changes in

soil behavior with temperature. All of these effects could lead to a change in how a drilled shaft foundation would typically function (Amatya et al. 2012).

2.1.1 Soil-Structure Interaction

As with any element that is heated or cooled an energy foundation expands and contracts. If the foundation is in unconstrained conditions, the thermal axial strains developed during this heating event can be quantified as follows:

$$\varepsilon_{T-Free} = \alpha_c \Delta T \quad \text{(Eq. 2.1)}$$

where α_c represents the coefficient of linear thermal expansion for the concrete foundation and ΔT is the temperature change. Throughout this study, thermal strains are represented as positive in compression, thus heating induces a negative strain. This implies that α_c has a negative value. The coefficient of linear thermal expansion of reinforced concrete in energy foundations typically ranges from -9 to -14.5 με/°C depending on the concrete mix design and aggregate mineralogy (Stewart and McCartney 2012). Although the temperature change may not be constant along the length of an energy foundation, the free expansion strain is an upper bound on the thermal expansion of the material. For an actual energy foundation is in soil, the thermal axial strains are restrained by the surrounding soil and end-restraint boundary conditions, so the thermal axial strains in energy foundations are defined as $\varepsilon_{T-Obstructed}$. $\varepsilon_{T-Obstructed}$ represents the strain that would be measured by a strain gage within an energy foundation during heating or cooling. By definition, $\varepsilon_{T-Obstructed}$ must be less than $\varepsilon_{T\text{-}Free}$, although the total thermo-mechanical axial strain in the foundation may be greater than $\varepsilon_{T\text{-}Free}$ depending on the mechanical loading or the impact of temperature changes on the surrounding soil. The restrained thermal axial strain $\varepsilon_{T\text{-}Restrained}$ is defined as the difference between $\varepsilon_{T\text{-}Free}$ and $\varepsilon_{T-Obstructed}$, as follows:

$$\varepsilon_{T-Restrained} = \varepsilon_{T-Free} - \varepsilon_{T-\text{Obstructed}} \quad \text{(Eq. 2.2)}$$

Measurements of the restrained thermal strain using embedded strain gages in the energy foundation can be used to determine the axial thermal stress in a foundation (Laloui et al. 2006; Bourne-Webb et al. 2009; McCartney and Murphy 2012). The thermal axial stress provides a value that must be accounted for in design of energy foundations, which can be calculated as follows:

$$\sigma_T = \mathrm{E}(\varepsilon_{T-\text{Restrained}}) \quad \text{(Eq. 2.3)}$$

where E is the Young's modulus of the reinforced concrete foundation. Soil-structure interaction as well as the end-constraint boundary conditions plays a major role in the distribution and magnitude of $\varepsilon_{T-\text{Obstructed}}$ and σ_T during heating and cooling.

2.1.2 Field Studies on Thermo-Mechanical Behavior of Energy foundations

Full-scale tests can provide significant insight into evaluation of soil-structure interaction and thermal axial stress and strain. Bourne-Webb et al. (2009), Brandl (2006), and Laloui et al. 2006) provide full scale field trials performed in Europe. These three tests are synthesized by Amatya et al. (2012) in order to expand on the soil-structure interaction mechanisms in energy foundations. Amatya et al. (2012) provides an expanded discussion on the simplified thermo-mechanical explanation of Bourne-Webb et al. (2009). Amatya et al. (2012) defined the thermal axial stress and strains in a similar manner to those presented in Section 2.1.1. The thermal axial stress and strain in the foundation were found to be affected by two main variables. The first is the influence of the side shear resistance at the foundation-soil interface. For the case that the foundation has low end restraint (semi-floating conditions), the largest thermal stress is expected to occur at the midpoint of the foundation, as shown in Figure 2.2.2-1 for the case of strong side shear resistance. Smaller side shear resistance from the soil will result in a smaller thermal stress.

End restraint boundary conditions play a major role in the restriction of thermal expansion and can cause additional compressive loads depending on the combination of end restraints (Amatya et al. 2012; Stewart and McCartney 2013). In the case of a stiff superstructure (head) resistance and a stiff bearing strata at the toe of the foundation, the foundation may not experience extreme variations in axial loads along the shaft due to the fact that it is not able to move within the soil and mobilize side shear resistance.

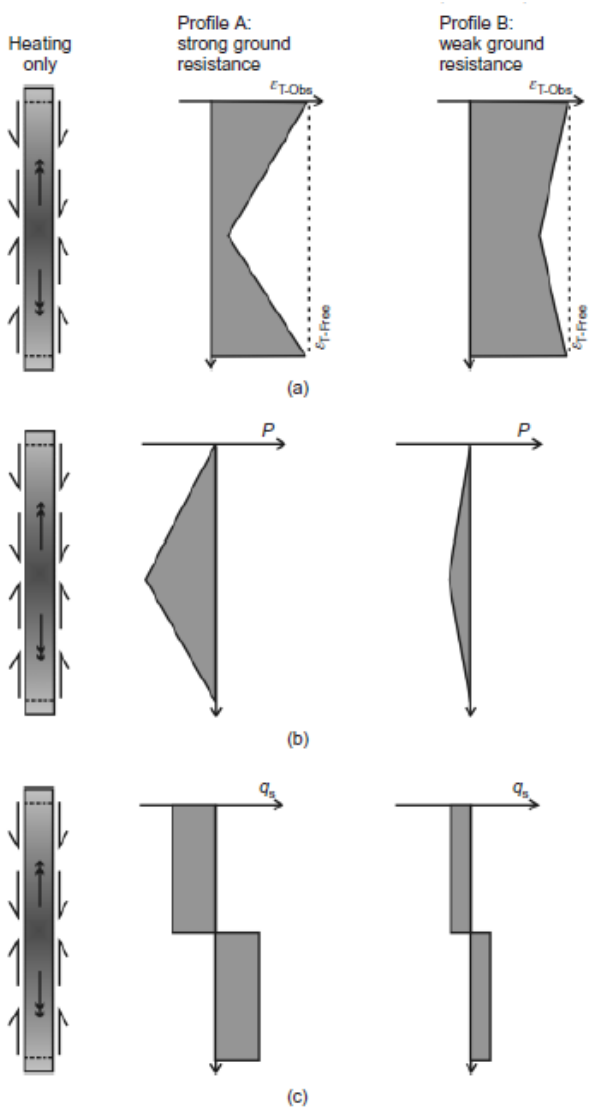

Figure 2.1.2-1 Thermal loading effects of semi-floating energy foundation with no end restraint (Amatya et al. 2012)

For thermal loading, only the energy foundation located in London (Bourne-Webb et al. 2009) showed a triangular distribution in axial load that was consistent with the model in Figure 2.2.2-1. This foundation was installed with the toe in overconsolidated clay, which may have provided a less stiff boundary condition than a foundation socketed into rock. The energy foundation in Lausanne presented by Laloui et al. (2006) experienced a large axial stress near the bottom of the energy foundation. This was hypothesized to be due to the higher end restraint boundary condition. Amatya et al. (2012) developed a hypothetical soil-structure interaction model for the case of an end-bearing foundation, shown in Figure 2.1.2-2.

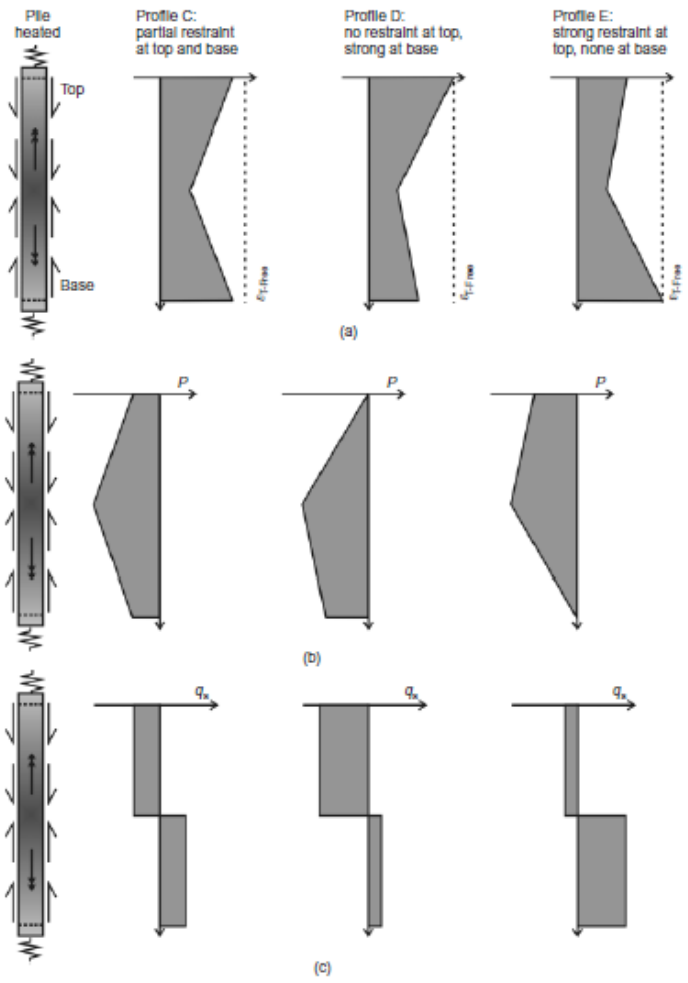

Figure 2.1.2-2 Effects of end restraint and high side shear resistance on the behavior of an end-bearing energy foundation during heating (Amatya et al. 2012)

For the case of a strong end-restraint boundary condition, Amatya et al. (2012) noted the potential for tensile axial stresses in the foundation during cooling, which can be an issue for foundations without a full-length reinforcement cage. The variables investigated by Amatya et al. (2012) will be further investigated in this study by changing the soil type as well as evaluating the difference in response of the end-bearing foundation and the semi-floating foundations.

2.2 Centrifuge Modeling

Centrifuge modeling is a useful approach to measure empirical parameters for soil-structure interaction analyses for energy foundations, as the properties of scale-model foundations and soil layers can be carefully controlled and different configurations can be considered for lower costs than full-scale field testing. An additional benefit of centrifuge modeling is that scale-model energy foundations can be loaded to failure to characterize the effects of temperature on the load-settlement curve. The back-calculated ultimate side shear stress distribution and end bearing are useful parameters for soil-structure interaction analyses. Further, centrifuge tests on scale-model foundations with embedded instrumentation permit measurement of thermal axial stresses and strains in the foundation, which can be used to validate soil-structure interaction analyses or finite element models.

Centrifuge modeling relies on the concept of geometric similitude, which assumes that a full-scale prototype soil layer will have the same stress state as a model-scale soil layer that is N times smaller when spinning in a geotechnical centrifuge at a centripetal acceleration that is N times larger than that of earth's gravity (Ko 1998; Taylor 1995). The centripetal acceleration generates an increased body force field in the scale-model. Geometric similitude can be employed to extrapolate the load-settlement behavior and thermal soil-structure interaction phenomena of scale-model energy foundations to those representative of full-scale prototype

foundations in the real world. After scaling the length of the foundation by a factor of 1:N (model:prototype), strains in the foundation scale by a factor of 1:1, and forces scale by a factor of $1:N^2$ (Ko 1998; Taylor 1995). Other relevant scaling relationships defined using the concept of geometric similitude are presented in Table 2-1.

Table 2-1 Centrifuge Scaling Relationships (Ko 1988)

Quantity	**Prototype**	**Model**
Acceleration	1	N
Length	1	1/N
Force	1	$1/N^2$
Stress	1	1
Strain	1	1
Stiffness	1	1
Displacement	1	1/N
Time (Diffusive flow processes)	1	$1/N^2$
Temperature	1	1

One issue in centrifuge modeling of energy foundations is that the temperature does not depend on the increased body forces in the centrifuge. Spatial measurements of temperature in dry quartz sand surrounding a cylindrical heat source during centrifugation at different g-levels by Krishnaiah and Singh (2004) confirm that centrifugation does not lead to a change in the heat flow process, as shown in Figure 2.3.1-2. However, if the dimensions associated with the spatial distribution of heat flow were scaled from model to prototype scale (assuming the same thermal conductivity in both cases), the time required for heat flow by conduction would be N^2 times faster in the centrifuge model ($1:N^2$). Saviddou (1988) derived the scaling factor for heat flow of $1/N^2$ from the diffusion equation, which only includes scaling of the length. An implication of temperature scaling is that a greater volume of soil surrounding the model-scale foundation will be affected by changes in temperature.

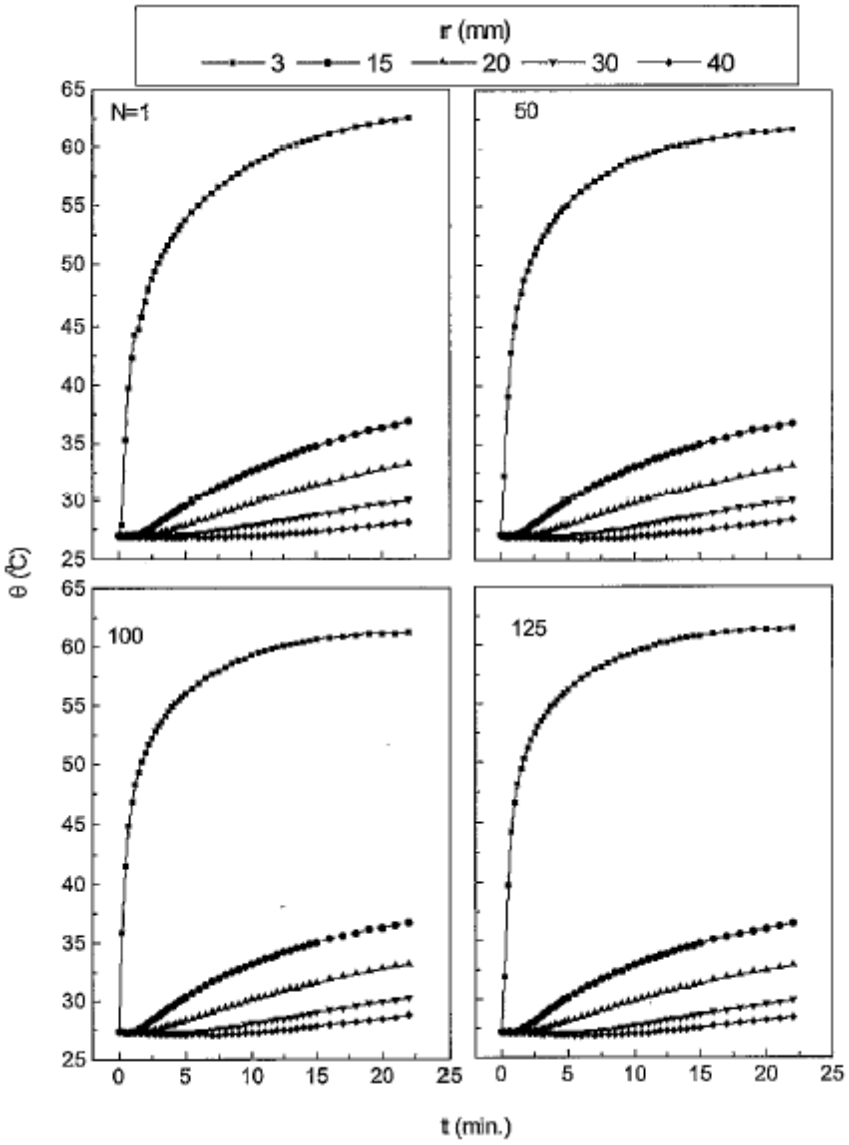

Figure 2.2.1-2 Temperatures measured in water-saturated sand layers at different g-levels (Krishnaiah and Singh 2004)

Results from Krishnaiah and Singh (2004) demonstrating the time scaling of heat flow in the centrifuge are shown in Figure 2.2.1-3. These results indicate that in prototype scale, a larger volume of soil experiences an increase in temperature. Soils change in volume with temperature, so if a greater zone of soil around the foundation is affected then the effects of differential volume change of the foundation and soil may be emphasized.

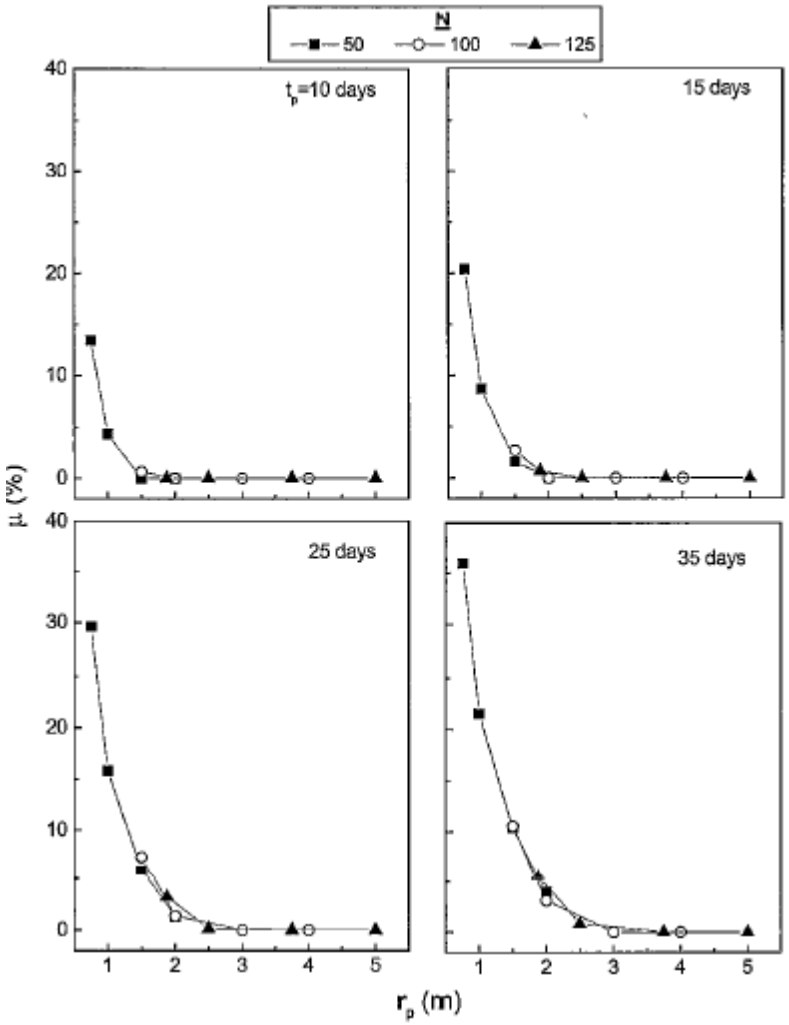

Figure 2.2.1-3 Time scaling of heat flow in the centrifuge

From this perspective, centrifuge modeling of heat flow in energy foundations will provide a worst-case scenario for the impact of temperature on the soil surrounding the energy foundation. One solution to address the scaling issue is to calibrate numerical simulations of the tests using the data from model scale. However, if the results are to be interpreted in terms of prototype-scale dimensions, the conditions of the test depend on the goal of testing. If the goal of testing is to evaluate the impact of temperature on the load-settlement curve of the foundations, it is important to provide sufficient heating time to reach steady-state conditions. On the other hand, if the goal is to evaluate the impact of temperature on the axial strain distribution in the

foundation, tests can be performed until strains stabilize while the foundation temperature is held constant. The time required for strains to stabilize depends on the soil type. The second approach was followed in the study as a strategy to overcome the temperature-time scaling issue, and all dimensions in the analysis section are presented in prototype scale.

CHAPTER 3 Experimental Setup

3.1 Model Foundations

Two scale-model energy foundations were fabricated to study the impact of mechanical loading and heating on the internal strain distribution in energy foundations. The semi-floating foundation has a diameter of 63.5 mm and length of 343 mm, and the end bearing foundation has a diameter of 63.5 mm and length of 533 mm. Throughout this study, the semi-floating foundation (or "short" foundation) is identified with a "S" in test identifications. The end-bearing foundation (or "long" foundation) is identified with an "L" in test identifications. A centrifuge acceleration of 24g was used throughout this study, so the corresponding prototype-scale foundation lengths were 8.2 m and 12.8 m, respectively, with a foundation diameter of 1.5 m. The foundations were both tested in soil layers that have a thickness of 533.4 mm. Although drilled shafts are typically cast-in-place, the model foundations were precast in a cardboard mold to ensure quality construction considering the extensive instrumentation. This approach also allows for characterization of the mechanical and thermal properties of each foundation. The foundation has a larger diameter than that of Stewart (2012) to provide more space around embedded instrumentation. Further, the larger diameter permitted a larger fraction and size of coarse aggregates to be incorporated into the concrete mix design. This led to a Young's modulus of reinforced concrete that was closer to that of drilled shaft foundations in the field than obtained by Stewart (2012).

The reinforcing cage was formed from welded steel hardware cloth that simulates the longitudinal and lateral members of a steel reinforcing cage. The cage has 12.7 mm square openings, with 19 gage wire thickness. The cage diameter is 48.5 mm with 7.5 mm of concrete cover on the sides. The cage has 6.35 mm of concrete cover on the top and bottom in both foundations. A cross-section schematic of the two energy foundations along with location of the

different embedded instrumentation and heat exchange loop is shown in Figure 3.1.1-1. Both foundations have a bolt cast into the concrete at the top to facilitate load transfer from the loading system to the concrete.

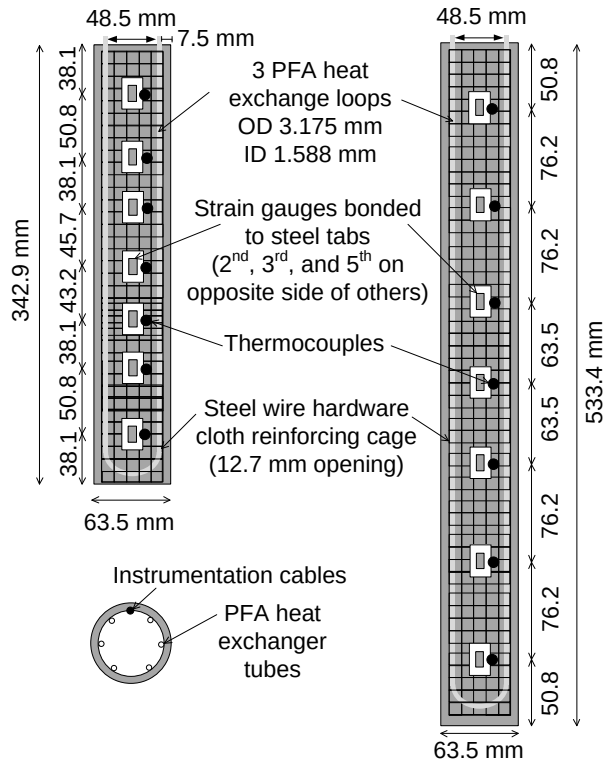

Figure 3.1.1-1 Cross-section schematics of the two scale-model energy foundations used in this study, along with the locations of embedded instrumentation.

Seven strain gages and thermocouples were embedded within each foundation to characterize the strain response and temperature distribution within the foundation. The strain gages were model CEA-13-250UW-350 from Vishay Precision Group, and were bonded using M-Bond AE-15 to 50.8 mm-long, 12.7 mm-wide steel plates having a thickness of 1.78 mm. The plates have two 6.1 mm-diameter holes at top and bottom to provide a secure hold for small wire ties as well as good contact with the concrete. The zinc plating on the steel was sanded off to provide a smooth steel surface. M-Bond AE-15 was used as the bonding agent due to its ability to withstand cyclic temperatures. The bonded gages were cured under pressure for 4 hours at a

constant temperature of 57.2 ^{o}C. A Teflon strip was placed over the gage after the epoxy cured, and the assembly was then covered using a waterproof epoxy (Gagekote #5). Miniature thermocouples (Omega fine wire Type K Model STC TT K 36 3C) were attached to the steel plates next to the strain gages. 14 gages were created in the same batch, 7 for each foundation. Small wires were used within the foundation, and were soldered to shielded wires at the top of the foundation to resist mechanical noise created within the centrifuge. These shielded wires were then led to a short extension of CAT-5 cable to a jack wired appropriately for the data acquisition on the centrifuge. Heating tests were performed on the gage-steel assemblies before installation into the concrete to define the coefficient of thermal expansion of the steel, which was found to be α_{steel} = -13.0 με/°C. The results from these heating tests will be presented in the next section. The finished strain gages were then attached to the inside of the reinforcing cage using thin wire thread. The placement of the gages is shown in Figure 3.1.1-1.

Three heat exchanger loops were affixed to the reinforcement cage. The loops were equally spaced around the circumference of the cage and affixed to the cage with small cable stays. Perfluoroalkoxy (PFA) tubing with a 3.175 mm inside diameter was used for the heat exchange loops, with the bottom loops held tight to the cage in order to avoid loops crossing the bottom of the cage. A cardboard tube with a 63.5 mm inside diameter was used as the form for the concrete. A wood platform was created to provide a stable base and sealed bottom for the cardboard tube. The base of the tube was sealed to the bottom piece of wood with a waterproof bathroom sealant. The cage was centered in the form, and concrete having a 1:2:1.5:1.5 water:cement:sand:coarse aggregate mixture was poured into the form using a miniature tremie pipe. This approach prevented damage of strain gages and ensured that the concrete was reaching the bottom of the form. Concrete placement was performed on a large vibrating table to

guarantee the concrete was flowing to all areas of the form as well as extruding entrapped air. When the concrete had reached the top of the form, a set screw was placed in the middle of the foundation to provide a good centering point for mechanical loading of the foundation. The foundations were cured in a fog room for 14 days, after which 14 more days of curing were permitted after removing the form. Figure 3.1.1-2 (a) and (b) show the semi-floating and end bearing foundation in the fog room prior to form removal. The model energy piles are pictured in Figure 3.1.1-3 (a) and (b).

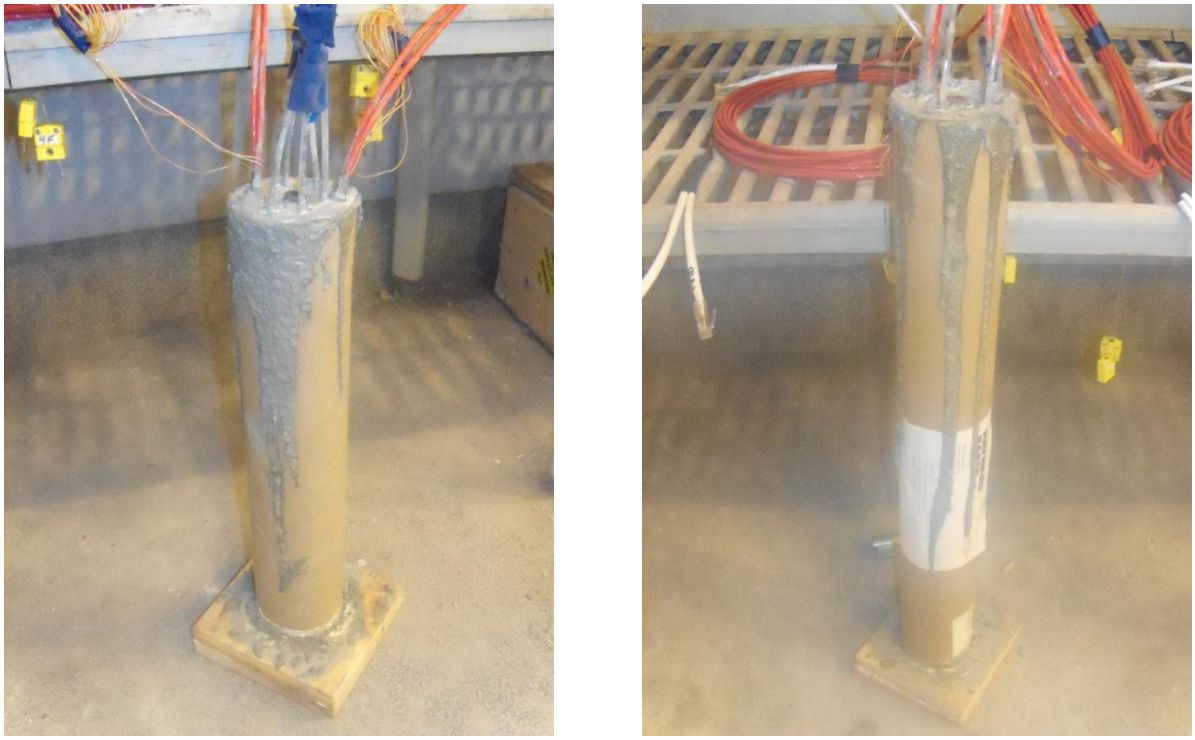

(a) (b)

Figure 3.1.1-2 Curing process in the fog room: (a) Semi-floating foundation; (b) End-bearing foundation.

(a) (b)

Figure 3.1.1-3 Model energy foundations: (a) Semi-floating foundation; (b) End-bearing foundation.

3.2 Centrifuge Facility

The 400 g-ton geotechnical centrifuge facility at the University of Colorado Boulder was utilized throughout this study, pictured in Figure 3.2.1-1. Certain aspects of the centrifuge facility should be noted as they were pertinent in testing. The tests are observed by the project and centrifuge engineer in the control room where various tools are utilized to complete a project. Temperature control was performed through the LabView program control the two servo valves. The load control was performed by adjusting the air pressure regulator added to the control room for this particular study. A cooling system lines the walls of the centrifuge chamber to keep the centrifuge from overheating during spinning. During the longer tests in this study it was required to turn on the cooling system to keep the ambient temperature at a

reasonable level. Video of the spinning arm and the top of the sample is shown in a live feed. This was a helpful feature, as any unexpected behavior or leaks of heat transfer fluid could be detected during spinning. Fortunately, no such events occurred during testing.

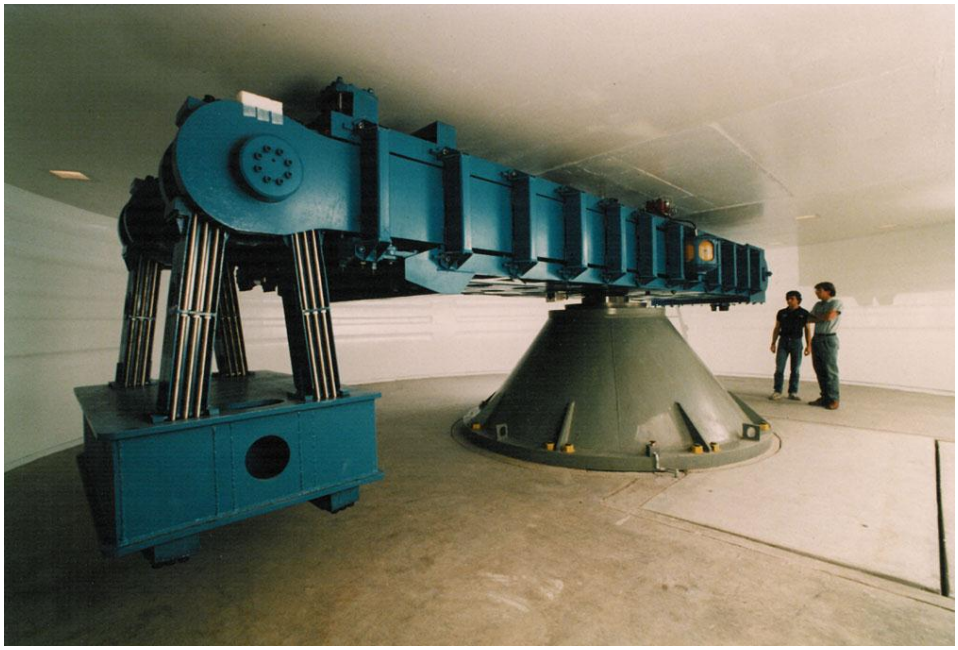

Figure 3.2.1-1 400 g-ton centrifuge at the University of Colorado Boulder.

3.3 Centrifuge Basket Setup

The basket on the end of the centrifuge is a swinging platform with 1.44 m^2 area which can support a 2 ton payload up to a g-level of 200 g. The payload weight for this study was 1.6 tonnes, which was balanced using counterweights on the other side of the arm.

3.4 Testing Frame and Soil Container

The testing frame designed for loading the soil container used in this study is a frame structure from which downward loads could be applied from a Bellofram pneumatic piston attached to the loading frame (which was connected to a platform beneath the soil container to provide a reaction). The pneumatic piston is mounted with counter sunk holes to an aluminum plate which is then mounted to the frame. A hole through the frame allows the loading rod to

pass through the 101.6 mm-thick, hollow beam to a coupler which then is connected to the load cell. Figure 3.4.1-1 shows the loading frame as well as the pneumatic piston mounted for loading purposes.

Figure 3.4.1-1 Loading frame used in the centrifuge.

Schematics of the container used for testing of the two different foundations are shown in Figure 3.4.1-2. This figure shows the dimensions and layout for both the long and semi-floating foundations. The container is an aluminum cylinder with an inside diameter of 0.6 m, wall thickness of 13 mm, and a height of 0.54 m. A 13 mm-thick insulation sheet was wrapped around the container to prevent heat transfer through the sides of the cylinder (no-flow boundary). The un-insulated bottom of the container permits some loss of heat, but this was preferred to have a stiff base for loading.

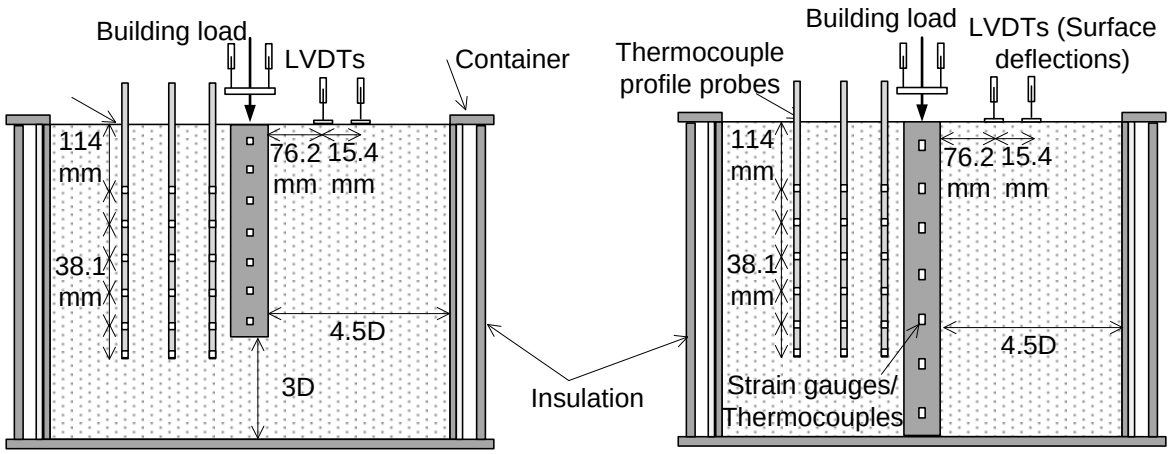

(a) (b)

Figure 3.4.1-2 Test schematics for: (a) Semi-floating foundation tests, (b) End-bearing foundation tests.

Loads were applied to the foundation using the pneumatic Bellofram pneumatic piston. Air was supplied through the slip ring stack via a compressed air line as mentioned in Section 2.2. The compressed air line was led to the control room, to the control regulator with bleeder valve, to the slip-ring stack, and then to the end of the arm where it was attached to the pneumatic piston. A constant loading rate was applied to the head of the foundation by applying the load increments of 34.5 kPa over constant time increments of 25 seconds, corresponding to a loading rate of 1.4 kPa/sec. During loading, the applied loads were measured using the load cell. The piston rod extended through the loading frame to a coupler which was then attached to an 8896 N Futek LSB 350 S Beam Load Cell. A doubly threaded stud was then attached to the load cell and an acorn nut was attached to the bottom of the stud for loading purposes. The LVDT platform was also configured on the stud to measure foundation displacements. Pictures of the loading apparatus are shown in Figures 3.4.1-3(a) and 3.4.1-3(b). A stiffness control setup was also utilized for one test. This required removal of the pneumatic piston and replacing it with threaded rod set in place with spacers about the top brace of the loading frame. Schematic drawings of these setups are presented in Figure 3.4.1-4.

(a) (b)

Figure 3.4.1-3 Loading systems: (a) Load control; (b) Stiffness control.

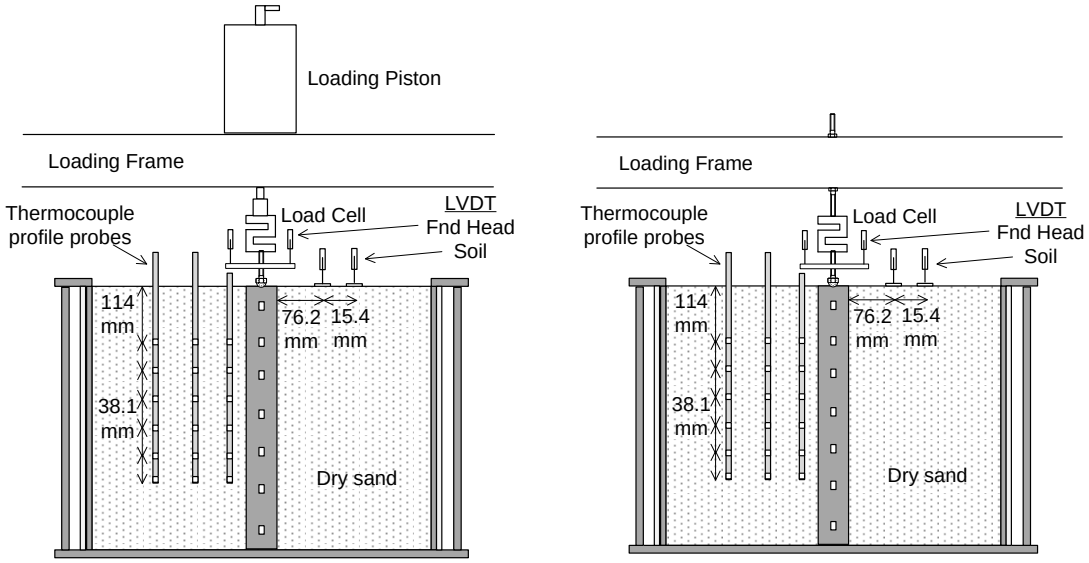

(a) (b)

Figure 3.4.1-4 Testing container schematics for different loading conditions: (a) Load control; (b) Stiffness control.

The locations of instrumentation incorporated into the centrifuge container for the tests involving sand are shown in Figure 3.4.1-5. Linearly variable differential transformers (LVDTs) were used to measure displacements of the foundation head and soil surface. Two LVDTs attached to beams spanning between two support beams were used to monitor movement of the foundation head and deflections of the soil surface. Two LVDTs were positioned over the loading platform to characterize the foundation head displacements. The remaining two LVDTs

were placed on the soil surface to measure the free-field settlement under the centrifuge acceleration. Thermocouple profile probes were inserted into the soil at different radial locations to measure transient changes in soil temperature. The thermocouple profile probes have six thermocouples that are spaced at 50 mm increments from the tip of the probe. The probes were inserted through the support beam for the LVDTs in order to insure that the distances of the probes were equal each time. Pictures of the setups are shown in Figures 3.4.1-6 and 3.4.1-7.

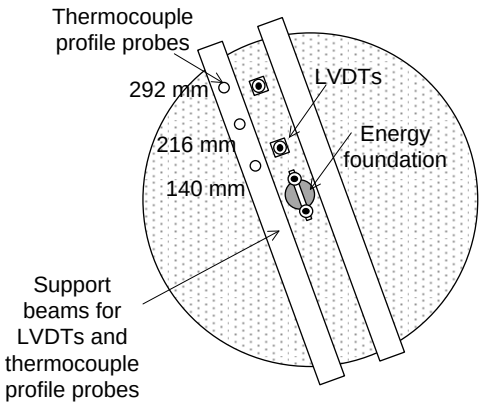

Figure 3.4.1-5 Top view of instrumentation layout in the soil container.

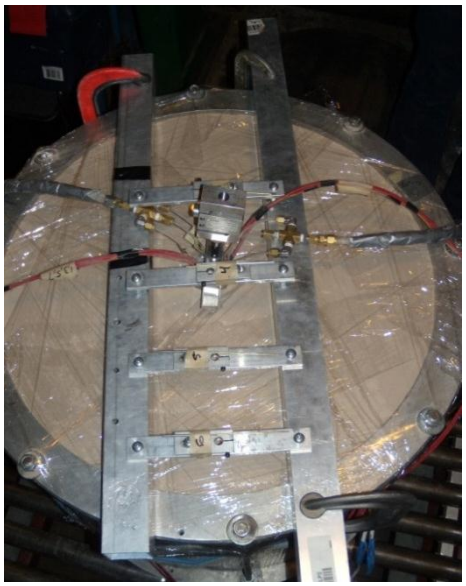

Figure 3.4.1-6 Overhead view of container prior to inserting into load frame.

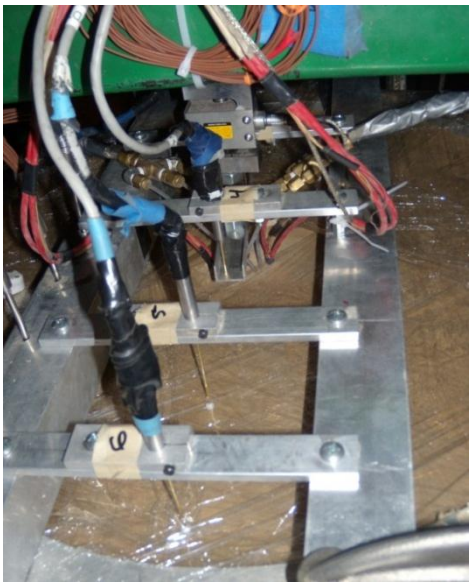

Figure 3.4.1-7 Soil container prior to testing.

The LVDT readings were found to be very sensitive to the ambient temperature of the centrifuge chamber. During spinning the centrifuge chamber warms significantly throughout the test and when the cooling system is started a sharp decrease in temperature is noticed in the ambient temperature, which was observed to lead to a change in behavior of the LVDTs. This could be due to their own thermal effects or to the thermal deflection of the beam. It should be noted that the change in temperature of the centrifuge chamber is independent of the change in temperature of the energy foundation; the change in temperature of the centrifuge chamber occurs due to friction of the air circulating in the chamber. The calibrated LVDT readings were corrected to account for the thermal deflection of the system. The final displacement of the LVDTs was determined as follows:

$$\Delta_{final} = \Delta_{raw} - 0.0246\left(\frac{mm}{^oC}\right) * \Delta T(\,^oC)$$

where the calibrated, raw displacement (Δ_{raw}) is the calibrated displacement in [mm] and ΔT is the change in ambient temperature of the centrifuge chamber. The change in temperature of the centrifuge chamber was defined as the difference in ambient temperature from the start of the test.

For the tests performed on silt, Decagon EC-TM capacitance sensors were used to infer volumetric water content as well as temperatures. Three sensors were placed one inch from the foundation at increasing depths and with two more placed at increasing radial distances at the deepest location. The cables were extended to the wall of the container and compaction was continued was usual. The cables were connected to a Decagon Devices EM50 datalogger, which collected the data from these sensors independent from the rest of the instrumentation, which was monitored using National Instruments LabView software.

Schematics of the four test setups, end-bearing foundation in sand and silt, and semi-floating foundation in sand and silt, are shown in Figure 3.4.1-8. The dielectric sensors can be seen in the silt tests along with the locations of the various pieces of instrumentation. Addition pictures are shown in in Figure 3.4.1-9 and 3.4.1-10, which show how the thermocouple profile probes were inserted into the soil layer through the instrumentation bracket with the LVDT and load cell configuration, respectively.

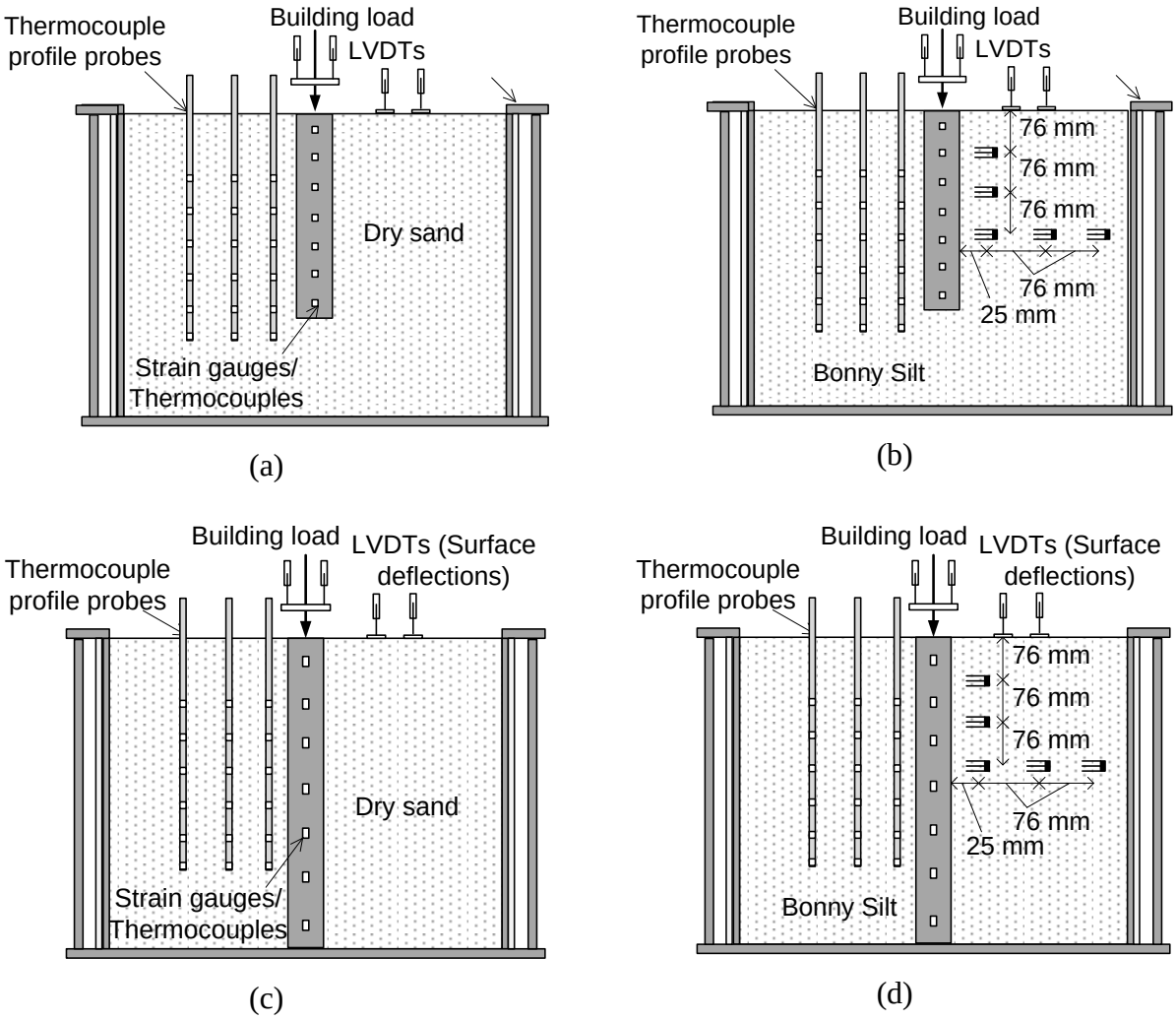

Figure 3.4.1-8 Schematics of test setups: (a) Semi-floating foundation in Nevada sand, (b) Semi-floating foundation in Bonny silt, (c) End-bearing foundation in Nevada sand, (d) End-bearing foundation in Bonny silt

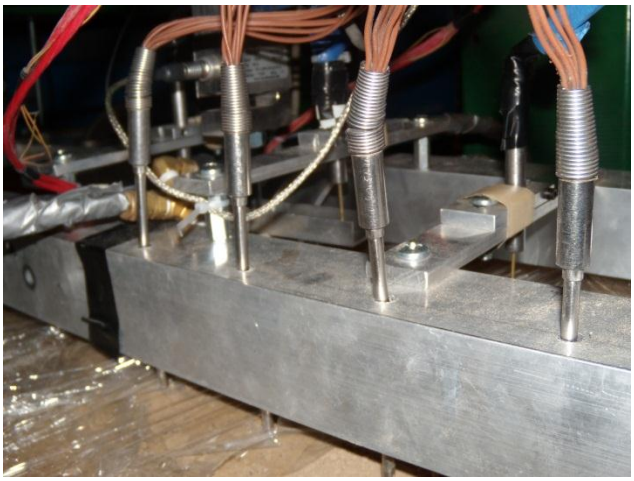

Figure 3.4.1-9 Thermocouple profile probes.

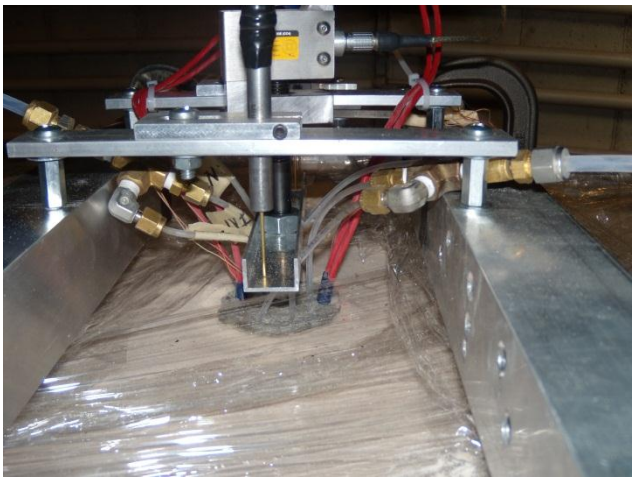

Figure 3.4.1-10 LVDT and load cell.

3.5 Temperature Control System

Temperature control for the system is accomplished through a Julabo F25-ME heat pump with a working temperature range of -28 to 200 °C in series with an in-line centrifugal booster pump. The heat pump contains a 4.5 liter bath with automated temperature control system for heating or cooling. Silicon fluid was used as the heat transfer fluid for all tests in the centrifuge as it maintains a viscosity close to that of water for different temperatures, but is still compatible with the slip ring stack of the centrifuge. The heat pump and centrifugal pump sat outside the centrifuge cellar during spinning and pumped the fluid through a slip-ring stack to the spinning basket. The setup is shown in Figure 3.5.1-1. Two servo-control valves were used to control the amount of pre-heated fluid circulated through the foundation. This approach effectively controlled the flow rate of fluid through the foundation, and thus the amount of heat transferred from the fluid into the energy foundation. The bypass valve was used to recirculate heated fluid back into the heat pump, while the inlet valve was used to meter the fluid flow through the foundation to reach a target temperature. Pipe-plug thermocouples were used to determine the fluid temperatures going in and out of the foundation. Quick connect valves were used to installed on the four inlet and outlets of the valve setup allowing for easy switching between

foundations with no losses in heating fluid. The servo-controlled valve setup, which includes the fluid supply, foundation supply, foundation return, and fluid return connections, is shown in Figure 3.5.1-2. The pipe plug thermocouples can be seen on the foundation supply and return. The centrifuge slip-ring stack along with the connected heat pump is shown in Figure 3.5.1-3.

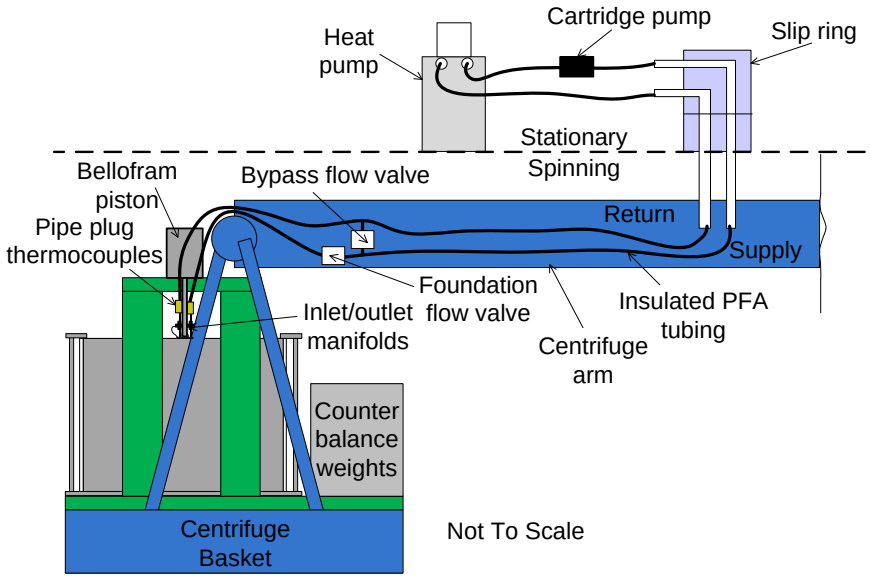

Figure 3.5.1-1 Temperature control system in the geotechnical centrifuge.

Figure 3.5.1-2 Servo-controlled valve setup

Figure 3.5.1-3 Heat pump and slip ring stack

CHAPTER 4 Material Properties

4.1 Energy Foundation Characterization

The thermo-mechanical properties of the scale-model energy foundation were characterized using three separate tests: (1) a test on the strain gages attached to the steel tabs (outside of the reinforced concrete) to characterize the mechanical and thermal response of the strain gages on the steel tabs; (2) a mechanical loading test on the foundation with the embedded strain gages to determine the Young's modulus of the reinforced concrete; and (3) a free expansion heating test on the foundation with the embedded strain gages to determine the coefficient of thermal expansion of the foundation, as well to define correction factors to account for the concrete-steel interaction. The latter two tests on the energy foundations were performed at 1-g in the same loading frame used in the centrifuge.

4.2 Strain Gage Calibration

Prior to placing the strain gages in the foundation cages they were tested to define mechanical and thermal correction factors. The results from the thermal heating tests on the strain gages incorporated into the semi-floating foundation and end-bearing foundation are shown in Figures 4.2.1-2 and 4.2.1-3, respectively. During a given test, a steel tab was first loaded axially by hanging masses from the tab to apply a tensile stress of -11.8 MPa. Next, the steel tab was heated with a heat gun, while temperature and strain were recorded. First, the sign of each strain gage was changed to reflect the geotechnical convention that compressive strains are positive. Equations were then defined to correct the mechanical response of each gage to a Young's modulus of steel of 200 GPa and a coefficient of thermal expansion of -13 με/°C. The mechanical correction value for each gage was defined as follows:

$$\varepsilon_{gage,mech} = \varepsilon_{Raw} \times \chi \quad \text{(Eq. 4.1)}$$

where χ is a mechanical correction factor specific to each gage and ε_{Raw} is the raw reading from the strain gage (after the sign convention change). The mechanical load was applied instantaneously and was maintained throughout the test, so this correction was applied to the entire time series. The thermal correction was then applied to match the thermal strain of each gage to a coefficient of thermal expansion of -13 με/°C, as follows:

$$\varepsilon_{gage,corrected} = \varepsilon_{Raw} \times \chi + \beta \Delta T \quad \text{(Eq. 4.2)}$$

where β represents the additive thermal correction factor, and ΔT is the change in temperature of the gage. The results in Figures 4.2.1-2 and 4.2.1-3 show the raw readings (after application of the sign change) and the readings after application of the mechanical and thermal correction factors, along with the change in temperature. It is clear that the strain gages show unexpected behavior in the raw strain values, with compressive (contraction) strains instead of tensile (expansion) strains observed during heating. This unexpected behavior was attributed to the complex interaction between the strain gages, the steel tab, and the epoxy. However, application of the correction factor with Eq. 4.2 was found to result in the expected behavior with expansion strains during application of the tensile mechanical load followed by further expansion strains during heating. A summary of the values of χ and β for each gage is presented in Table 4.1 for the semi-floating foundation and Table 4.2 for the end-bearing foundation.

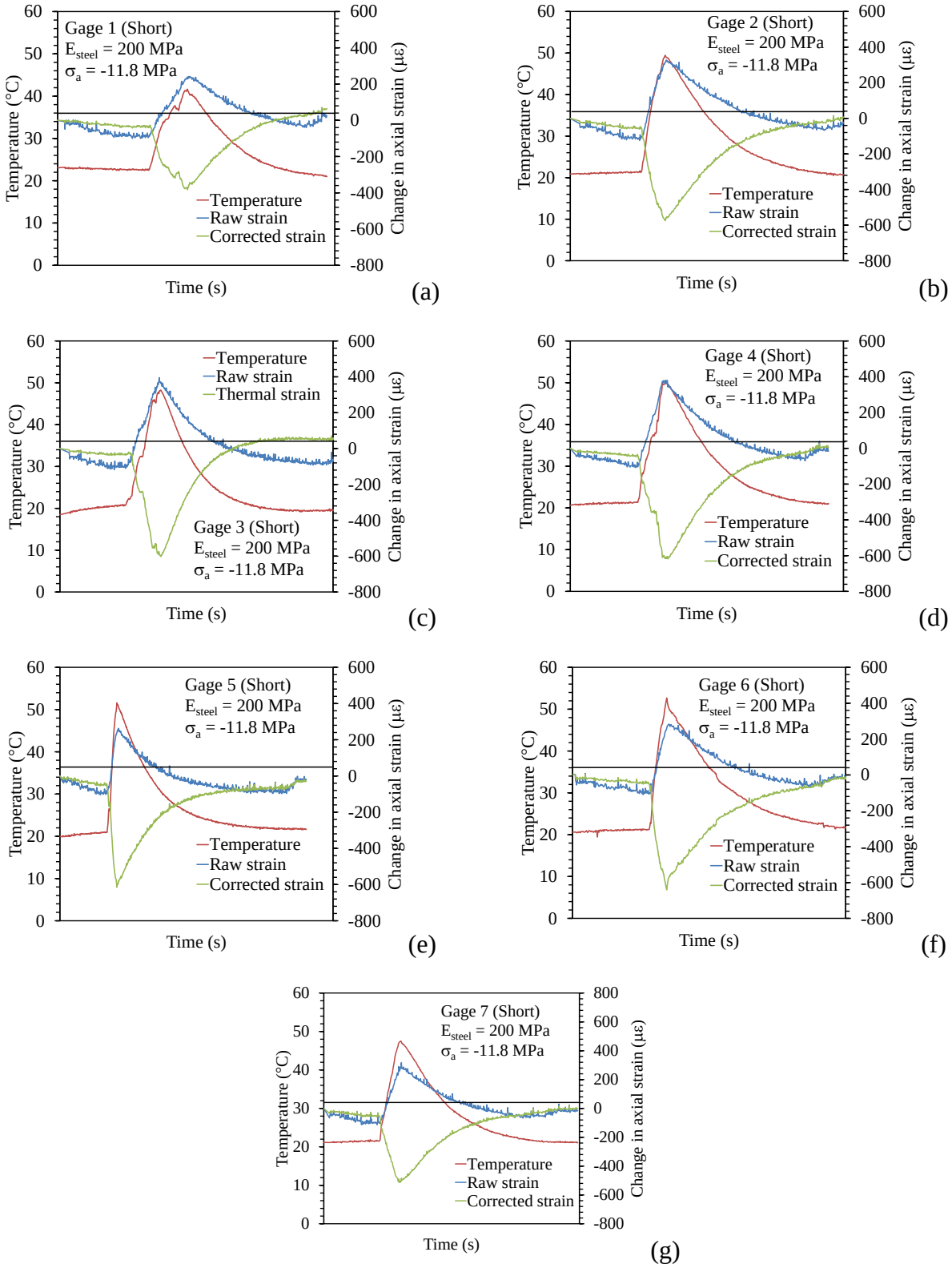

Figure 4.2.1-1 Strain gage calibration results for the gages incorporated in the semi-floating foundation: (a) Gage 1, (b) Gage 2 (c) Gage 3 (d) Gage 4 (e) Gage 5 (f) Gage 6 (g) Gage 7.

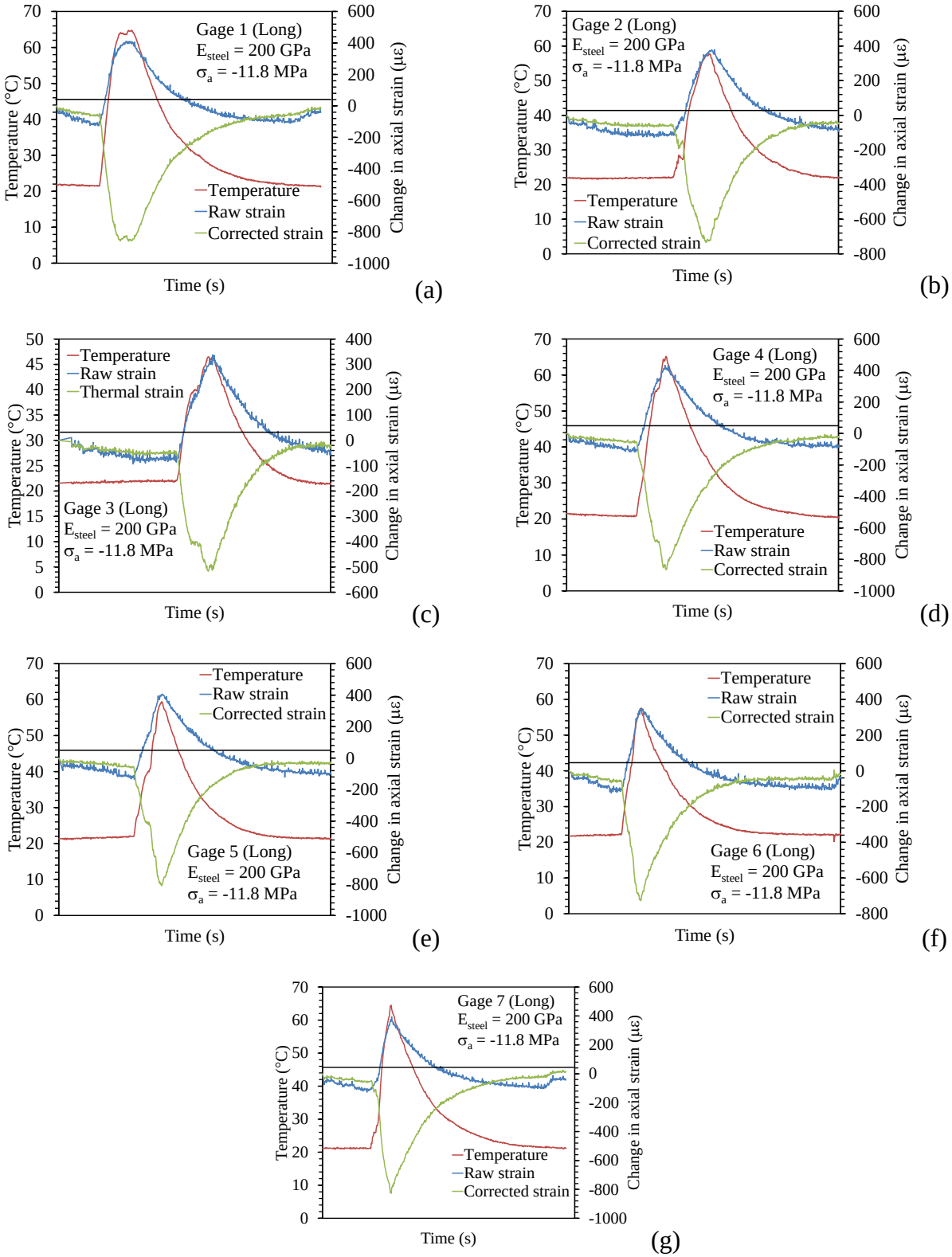

Figure 4.2.1-2 Strain gage calibration results for the gages incorporated in the end-bearing foundation: (a) Gage 1, (b) Gage 2 (c) Gage 3 (d) Gage 4 (e) Gage 5 (f) Gage 6 (g) Gage 7

Table 4-1 Semi-floating foundation summary table of strain gage correction factors

Short Foundation		
Gage	χ	β
1S	0.338	-25.0
2S	0.492	-26.0
3S	0.328	-27.8
4S	0.428	-27.1
5S	0.523	-24.1
6S	0.465	-24.2
7S	0.523	-25.2

Table 4-2 End-bearing foundation summary table of strain gage correction factors

Long Foundation		
Gage	χ	β
1L	0.518	-24.2
2L	0.532	-25.5
3L	0.528	-26.6
4L	0.514	-24.1
5L	0.477	-26.2
6L	0.537	-25.6
7L	0.492	-23.5

4.3 Mechanical Characterization of the Energy Foundations

Mechanical testing involved placing the foundation in the load frame with no surrounding soil. The foundation was then loaded axially in increments of 138 kPa up to 350 kPa. A linearly variable differential transformer (LVDT) was used to measure the deflection of the foundation, and the axial strains were measured using the embedded strain gages. Five mechanical tests were performed on each foundation to determine how each particular foundation and gage responded to mechanical loading. These tests were also useful to determine the average Young's modulus for the reinforced concrete. All seven strain gages were calibrated individually using the factors defined in the previous section. A typical example of the loading time history is shown in Figure

4.2.1-1. The end-bearing foundation in the loading frame prior to mechanical tests is shown in Figure 4.2.1-2. The LVDT setup has not yet been assembled in this photo.

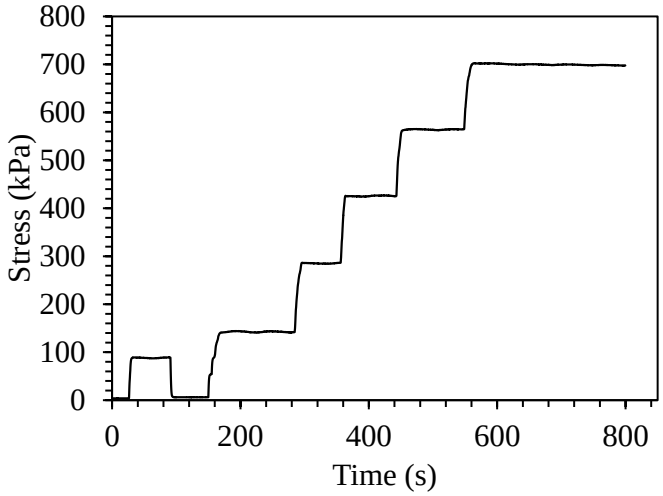

Figure 4.3.1-1 Typical time series of axial stress applied to the short and end-bearing foundations during the mechanical loading test.

Figure 4.3.1-2 End-bearing foundation prior to thermal and mechanical testing.

4.3.2 Semi-Floating Foundation Mechanical Loading Test Results

The mechanical results for the semi-floating foundation provided information about how each individual strain gage responded to uniaxial loading. During mechanical loading of the foundation, it was assumed that each gage should provide the same axial strain (in the absence of bending). This was the case for five of the gages as shown in Figure 4.2.2-1, although two strain gages did not respond logically to mechanical loading for unknown reasons, perhaps because of problems in bonding the gage to the steel plate. These two gages, located at 88.9 and 254 mm from the top of the foundation, were not included in the analyses in the rest of this study as they do not respond to mechanical or thermal loading. Nonetheless, the 5 remaining functional strain gages provided consistent values for the 5 mechanical tests. A profile of mechanical axial strain for varying axial stresses from one mechanical loading test is shown in Figure 4.2.2-1. The average Young's modulus obtained from these results is 33 GPa. The strain gages may have not provided consistent results with height along the foundation due to uneven loading or slight bending.

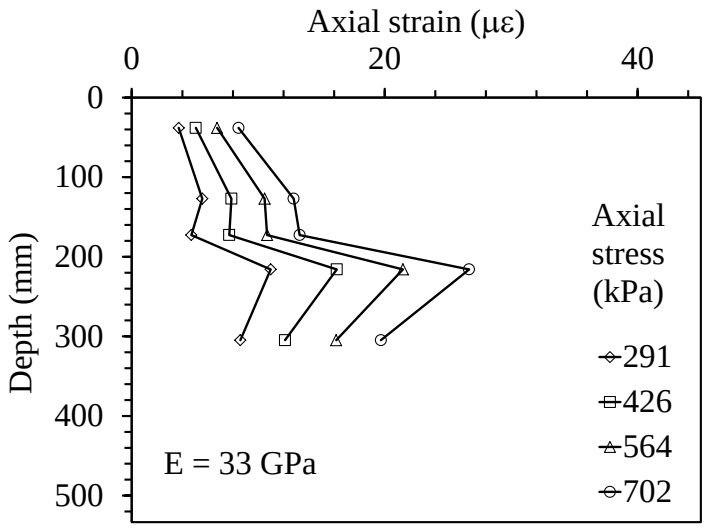

Figure 4.3.2-1 Strain profile in the semi-floating foundation during a mechanical loading test.

4.3.3 End-Bearing Foundation Mechanical Loading Test Results

Similar to the mechanical loading test on the semi-floating foundation, the mechanical loading test on the end-bearing foundation also provided consistent results corresponding to a Young's modulus of 33 GPa. The strain profile with depth for the end-bearing foundation during mechanical loading is shown in Figure 4.2.3-1. The slight variations observed in the measurements from the gages on either side of the foundation may indicate that slight bending was superimposed upon the axial compressive loading.

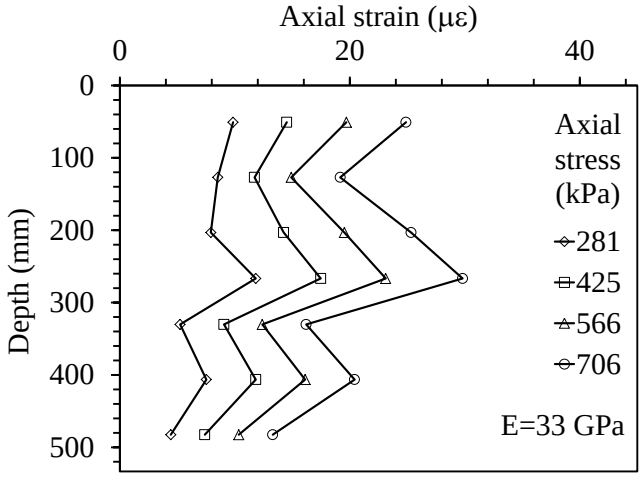

Figure 4.3.3-1 Strain profile in the end-bearing foundation during mechanical loading.

4.4 Characterization of the Thermal Response of the Energy Foundations

A free-expansion heating test was performed on each of the energy foundations under a nominal axial stress of 5 kPa in load-controlled conditions with no surrounding soil. The foundations were heated by circulating silicon fluid having a temperature of 55 °C through the heat exchange tubing. The axial strains were measured using the embedded strain gages as well as using the displacements from two LVDTs mounted on the foundation head. The correction factors from the strain gage calibration first applied to the measured strains (after application of the change in sign convention). It was observed that the gages did not provide a consistent

response as expected even though the change in temperature of each gage was similar. This was attributed to differences in concrete-steel interaction, slight differences in gage orientation, and the impact of the curing process. Accordingly, a new correction factor was incorporated to account for the differences in behavior. Specifically, an additional additive correction factor is incorporated to account for the concrete-steel interaction, as follows:

$$\varepsilon_{T-Corrected} = \varepsilon_{gage,corrected} + (\psi \Delta T) \quad \text{(Eq. 4.3)}$$

where ψ is the concrete steel factor and all other factors are discussed in Section 4.2, and ΔT is the change in temperature at the specific gage location. This equation is design to correct the strain gages so that they match the slope of the theoretical free expansion strain (which was determined from the foundation head displacements measured using the LVDT). The values of the correction factor ψ for the different gages ranged from -1.5 to 16 με/°C, .

4.4.1 Results of the Free Expansion Test on the Semi-Floating Foundation

The results from the free expansion test on the semi-floating foundation are shown in Figures 4.4.1-1 and 4.4.1-2. The time series of the inlet and outlet fluid temperatures, along with the average foundation temperature, is shown in Figure 4.4.1-1. These results can be used to estimate the thermal conductivity of the reinforced concrete (Stewart 2012). The LVDT head displacements shown in Figure 4.4.1-2 indicate that the reinforced concrete has a coefficient of thermal expansion (α_c) of -15 με/C^o. The free expansion strain is also shown in this figure, indicating that the semi-floating foundation expands slightly nonlinearly during heating. The test was repeated several times, and consistent coefficients of thermal expansion were obtained. The response from each strain gage provided consistent results from test to test when subjected to thermal loading, and the results will be summarized at the end of this chapter. The data for the steel-concrete correction factor (ψ) is presented below in Table 4-3.

Table 4-3 Semi-floating foundation steel-concrete correction factors

Short Foundation	
Gage	ψ
1S	10
2S	16
3S	9.7
4S	4.0
5S	3.3
6S	8.0
7S	4.8

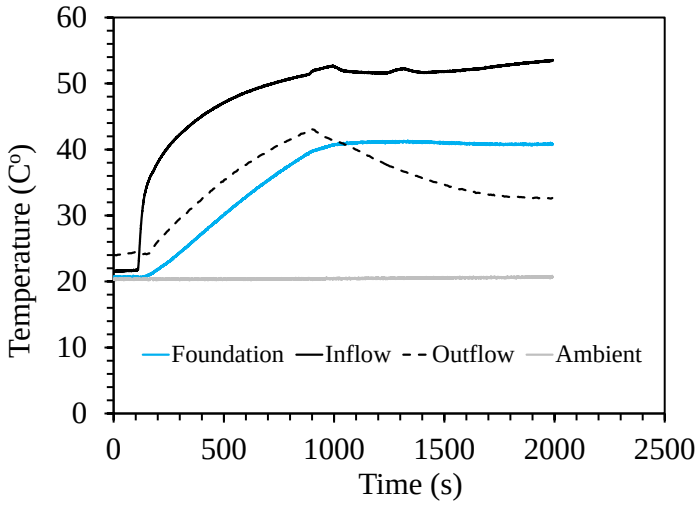

Figure 4.4.1-1 Temperatures during the free expansion test on the semi-floating foundation.

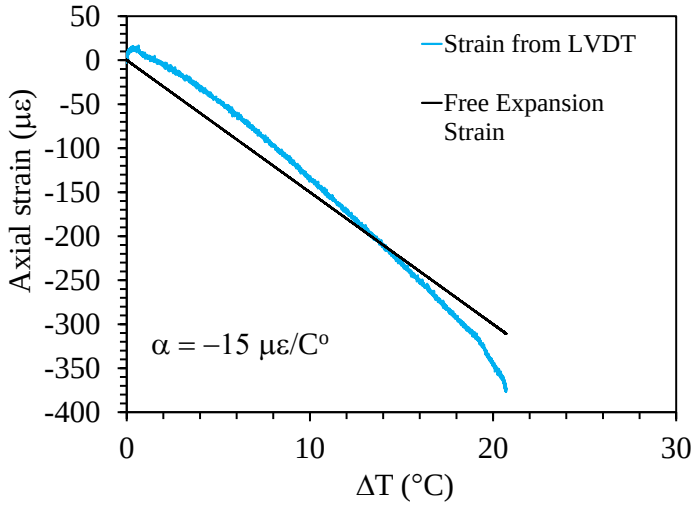

Figure 4.4.1-2 Semi-floating foundation strain defined from LVDT displacements along with the theoretical free expansion strains.

4.4.2 Results of Free Expansion Test on the End-Bearing Foundation

The results from the free expansion test on the end-bearing foundation are shown in Figures 4.4.2-1 and 4.4.2-2. The time series of the inlet and outlet fluid temperatures, along with the average foundation temperature, is shown in Figure 4.4.2-1. These results can be used to estimate the thermal conductivity of the reinforced concrete (Stewart 2012). The LVDT head displacements shown in Figure 4.4.2-2 indicate that the reinforced concrete has a coefficient of thermal expansion (α_c) of -15 $\mu\varepsilon/C^o$. The free expansion strain is also shown in this figure, indicating that the end-bearing foundation expands slightly nonlinearly during heating. Multiple tests were performed and repeatable results were obtained. The response from each strain gage provided consistent results from test to test when subjected to thermal loading, and the results will be summarized at the end of this chapter. The data for the steel-concrete correction factor (ψ) is presented below in Table 4-4.

Table 4-4 End-bearing foundation steel-concrete correction factors

Long Foundation	
Gage	ψ
1L	1.0
2L	1.5
3L	2.5
4L	-1.5
5L	13
6L	11
7L	1.0

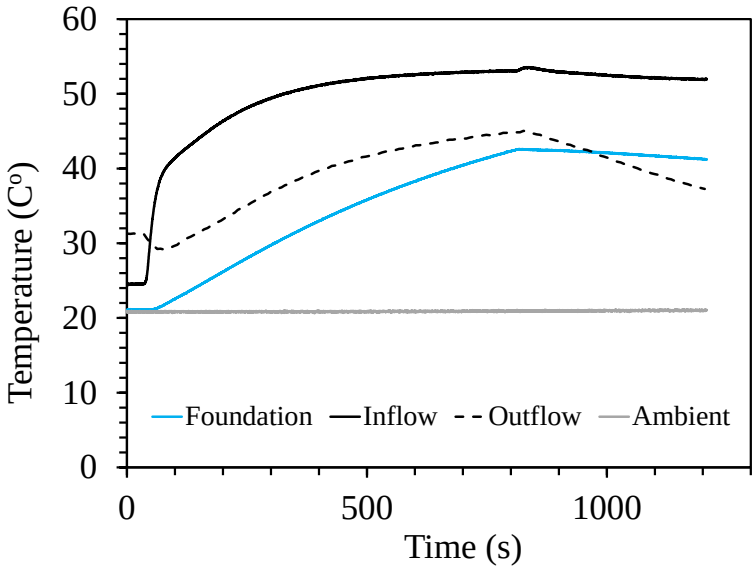

Figure 4.4.2-1 Temperatures for free expansion test on the end-bearing foundation.

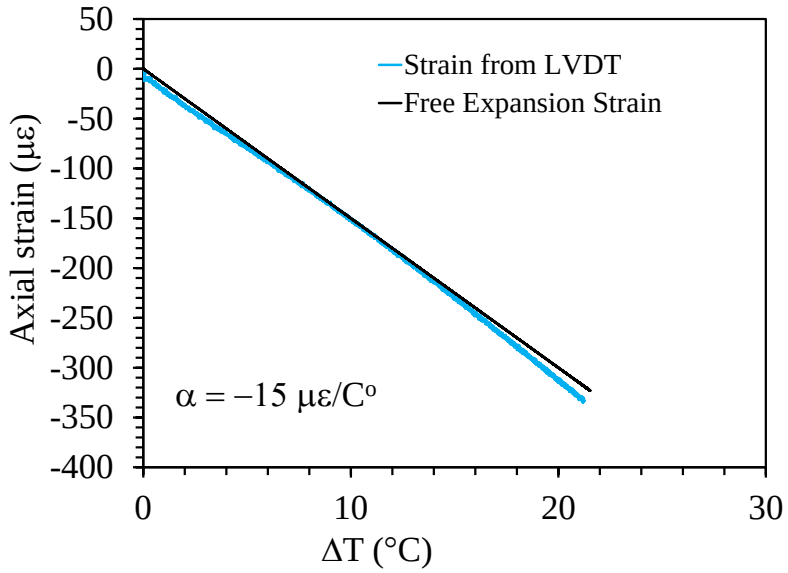

Figure 4.4.2-2 End-bearing foundation strains defined from the LVDT displacements along with the theoretical free expansion strains.

4.5 Thermal Conductivity of Concrete

In order to determine the thermal conductivity of the concrete used in the energy foundations, a 76 mm-diameter by 152 mm-tall cylinder was poured for supplemental testing. A small hole was created in the center of the foundation using a disposable wooden needle, which was covered with vacuum grease for ease of removal. After removal of the disposable wooden

needle, Arctic Silver thermal paste was inserted into the hole to provide intimate contact between the thermal needle and the concrete. The thermal conductivity was found to be 1.978 W/(mK). Figure 4.4.1-1 shows the thermal conductivity test being performed on the concrete cylinder.

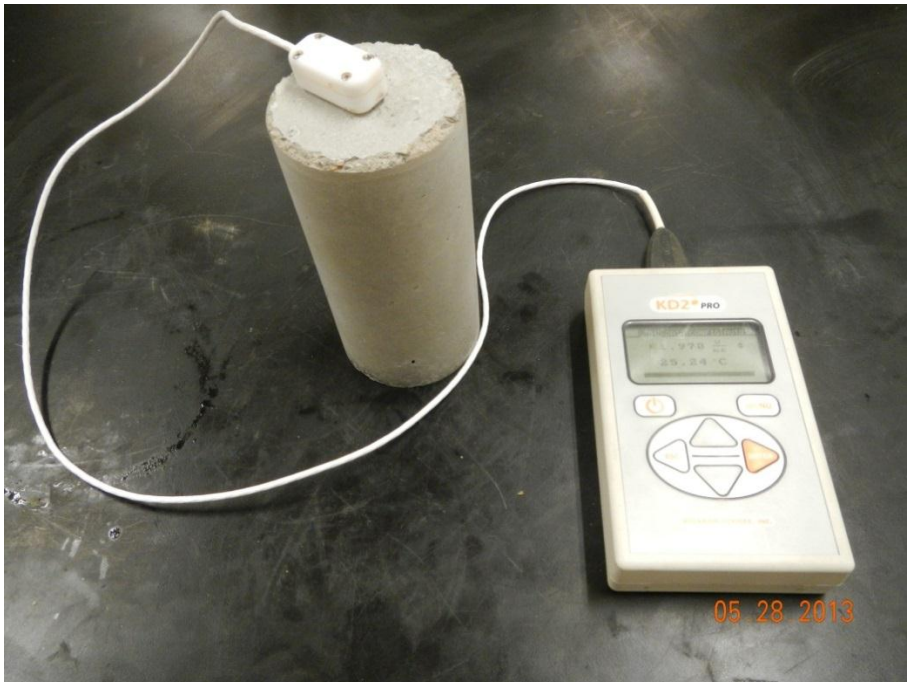

Figure 4.5.1-1 Thermal conductivity test of concrete.

4.6 Summary of Energy Foundation Properties

The mechanical and thermal foundation properties were determined for both model foundations through the foundation characterization process explained above. The material properties for both foundations are summarized in Tables 4-3 and 4-4.

Table 4-5 Summary of Energy Foundation Properties

	Semi-floating foundation	**End-bearing foundation**
Young's Modulus (E)	33 GPa	33 GPa
Coefficient of Thermal Expansion (α)	-15 $\mu\varepsilon/C^o$	-15 $\mu\varepsilon/C^o$
Thermal Conductivity	1.978 W/(mK)	1.978 W/(mK)

Table 4-6 Summary of semi-floating foundation strain gage correction factors

	Gage 1	Gage 2	Gage 3	Gage 4	Gage 5	Gage 6	Gage 7
Average χ	.34	.49	.33	.43	.52	.47	.52
Average β	-25	-26	-28	-7	-4	-24	-25
Average ψ	10	16	9.3	4.0	3.8	8.0	4.8

Table 4-7 Summary of end-bearing foundation strain gage correction factors

	Gage 1	Gage 2	Gage 3	Gage 4	Gage 5	Gage 6	Gage 7
Average χ	.52	.53	.53	.51	.48	.54	.49
Average β	-24	-26	-27	-24	-26	-26	-24
Average ψ	1.0	1.5	2.5	-1.5	13	11	1.0

4.7 Example of Strain Gage Correction Steps

This section presents the procedures used to apply each of the strain gage correction factors for a typical test, along with the effects of each of the correction factors when moving from raw strain values to fully-corrected values. The correction equations are given in Eq. 4.1, Eq. 4.2 and Eq. 4.3. The data is from a Bonny silt test on the semi-floating foundation heated to a ΔT of 18 °C. The raw axial strain is shown in Figure 4.5.1-1. It can be seen that the strains respond in the negative direction during heating, but continue to become more negative when a compressive load is applied at the foundation head. This is unreasonable and must be corrected to provide a reasonable strain output. A sign change is applied to the raw strain and is shown in Figure 4.5.1-2. The mechanical factor as determined in section 4.2 is now applied to the strain data. The next step is to apply the thermal correction factor as determined in section 4.3. The thermal correction factor is applied and presented in Figure 4.5.1-4. The strain are then zeroed prior to heating for the thermal axial strain and displayed in Figure 4.5.1-5. The free expansion is also shown in the figure, and is less than the reported strains although it should act as an upper bound to the expansion strains in the foundation. These magnitudes are incorrect but the pattern and signs make logical sense.

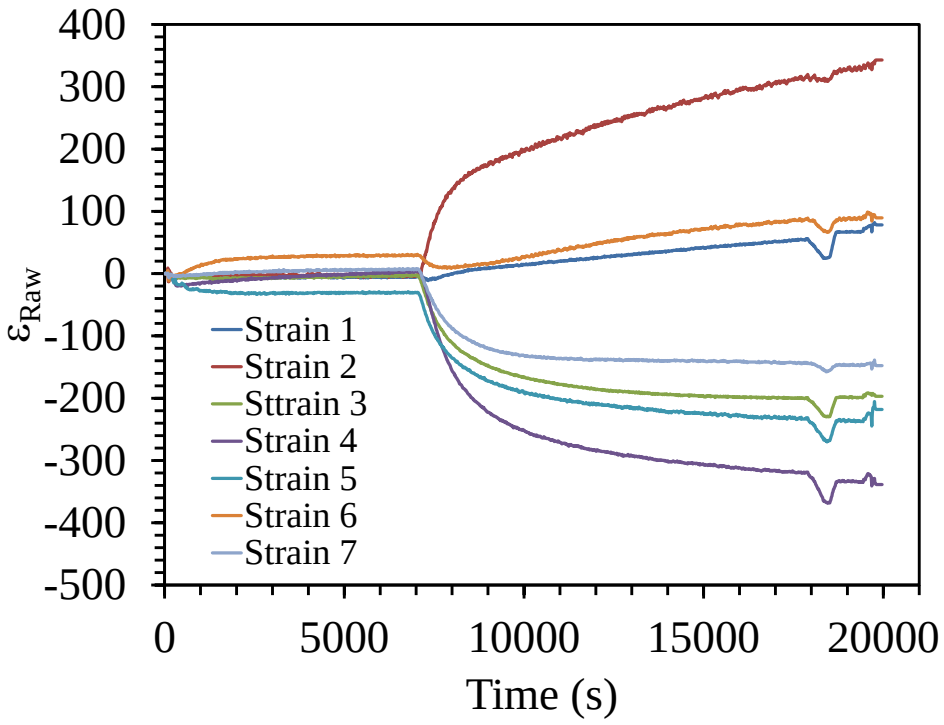

Figure 4.7.1-1 Raw axial strain.

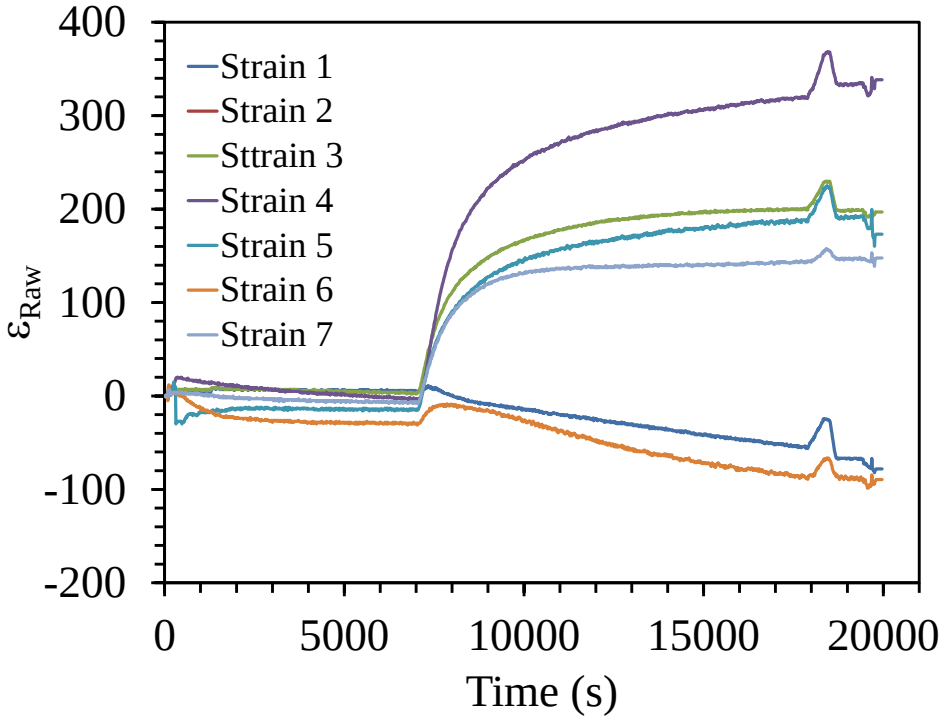

Figure 4.7.1-2 Change of sign convention for the raw strains (no other correction).

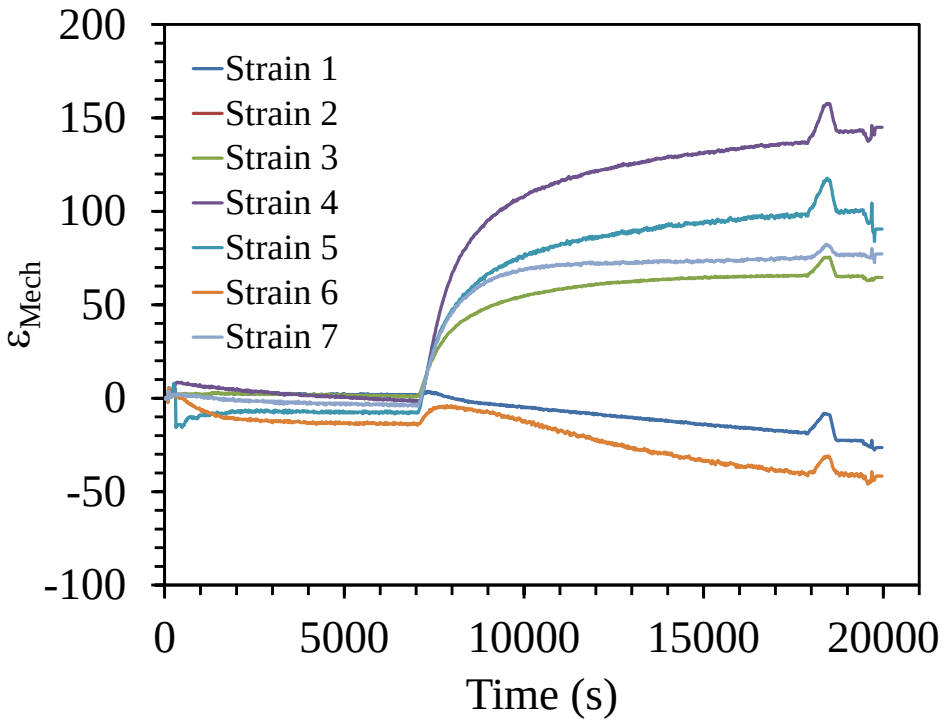

Figure 4.7.1-3 Axial strains after application of the mechanical correction factor.

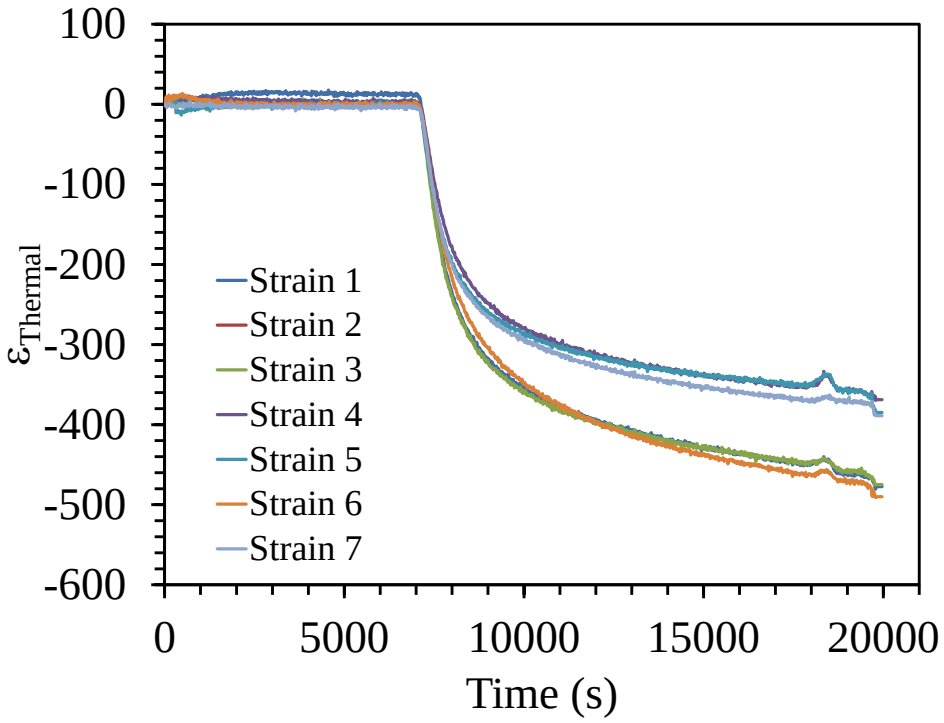

Figure 4.7.1-4 Thermally corrected axial strains.

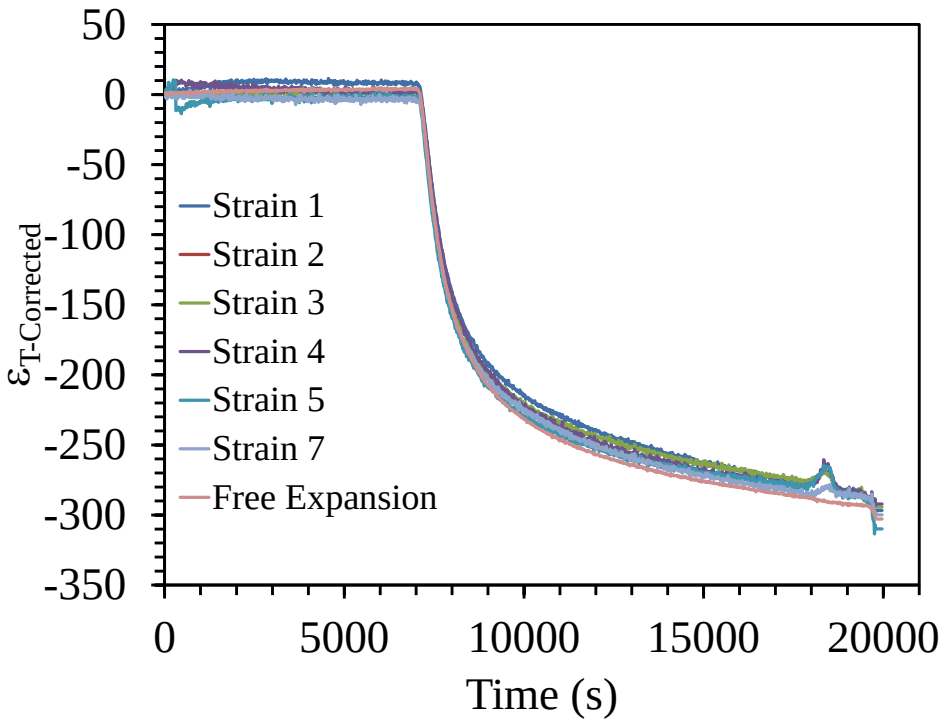

Figure 4.7.1-5 Thermal axial strains after application of the steel-concrete correction factor with the theoretical thermal axial strain corresponding to free expansion conditions.

4.8 Soil Properties

Two soil types were used for this study, dry sand and unsaturated, compacted silt. The sand used in this study is Nevada sand, which is a well-characterized material used in several other centrifuge testing projects at CU Boulder. The silt used in this study was recovered from the Bonny dam in eastern Colorado, and was used by Rosenberg (2010) and Stewart (2012) in their centrifuge testing programs on energy foundations. Both soils have an extensive database of geotechnical properties, and were selected to represent cohesionless and cohesive soil behavior during thermo-mechanical soil-structure interaction, respectively.

4.8.1 Nevada Sand

Dry Nevada sand with a relative density of 60% was used to characterize the response of energy foundations in cohesionless soil. The properties of Nevada sand are summarized in

Table 4-8. The relative density, which corresponds to a void ratio of 0.692 and a dry unit weight of 15.4 kN/m^3 was achieved through air pluviation from a height of 1.2 m. A triaxial testing program was performed by McClay (2013) to characterize the shear strength of Nevada sand. The principal stress difference as a function of strain for three different normal stresses is shown in Figure 4.6.1-1, while the volumetric strain as a function of axial strain is shown in Figure 4.6.1-2. For this range of normal stresses at this relative density the sand behaves in a dilative manner. The effective stress failure envelope for Nevada sand is shown in Figure 4.6.1-3. The friction angle of the sand was found to be 31.4°. Correlations for other variables for elastic modulus properties can be found in Popescu and Prevost (1993).

Table 4-8 Nevada Sand Properties (McClay 2013)

Property	Value
Specific Gravity, G_s	2.65
Minimum Void Ratio, e_{min}	0.586
Maximum Void Ratio, e_{max}	0.852

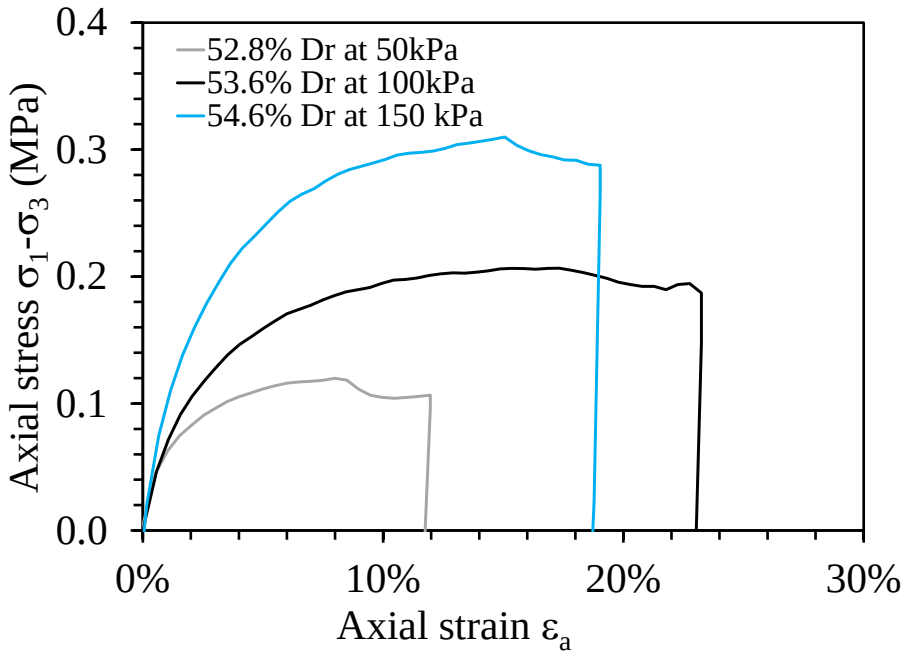

Figure 4.8.1-1 Axial stress-strain curves from drained triaxial compression tests on Nevada sand.

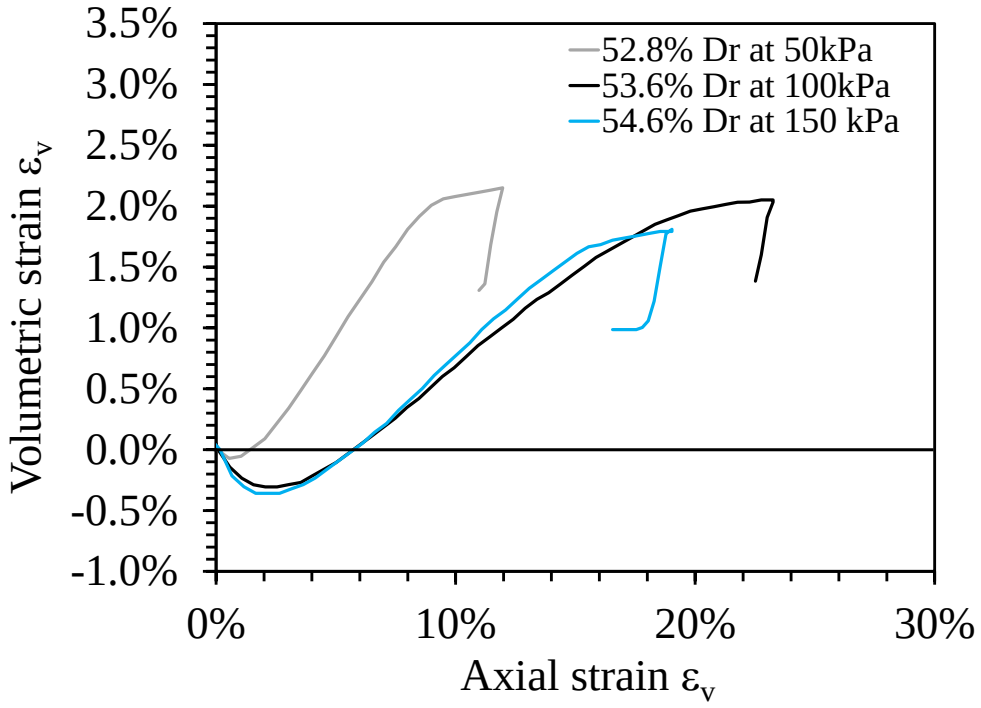

Figure 4.8.1-2 Volumetric and axial strain from drained triaxial tests on Nevada sand.

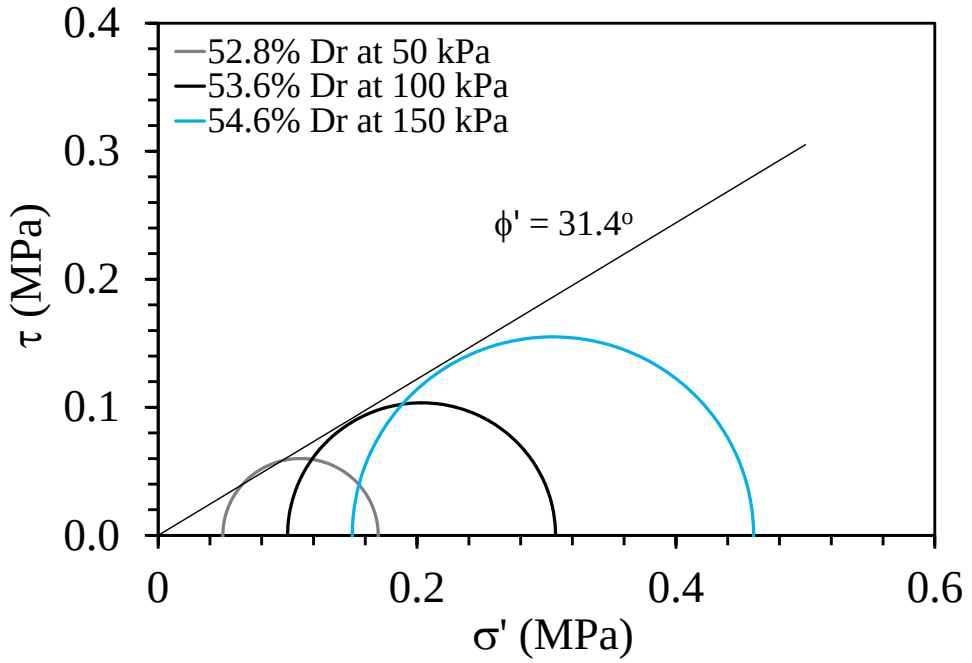

Figure 4.8.1-3 Mohr circles from drained triaxial compression tests on Nevada sand.

4.8.2 Bonny Silt

Soil from the Bonny dam located near the Colorado-Kansas border in Yuma County, Colorado, referred to as "Bonny silt", was also used in this experimental study. This soil has been characterized in previous experimental studies at the University of Colorado Boulder (El Tawati 2010; Coccia 2011). Further, it is has been used in centrifuge experiments on energy foundations which involve cycles of heating and cooling (Rosenberg 2010; Stewart 2012). This chapter summarizes the various physical properties of Bonny silt, including its particle-size distribution, Atterberg limits, specific gravity, and compaction properties, compression properties, and thermal conductivity.

The soil particle-size distribution of the Bonny silt was measured in accordance to ASTM D 422. The distribution of particle sizes larger than 75 μm (retained on the No. 200 sieve) was determined with a sieve analysis, while the distribution of particle sizes for the fraction that was finer than 75 μm was determined using a hydrometer analysis. The particle-size distribution curve is shown in Figure 4.8.1-1, and several particle size distribution characteristics are summarized on Table 4.9. Although Bonny silt has a high fines content, it has a wide range of particle sizes. Because of the high fines content, the silt is expected to behave as a low-permeability material which can retain stress history. Both of these features are common in soils which experience thermal consolidation (McCartney 2012).

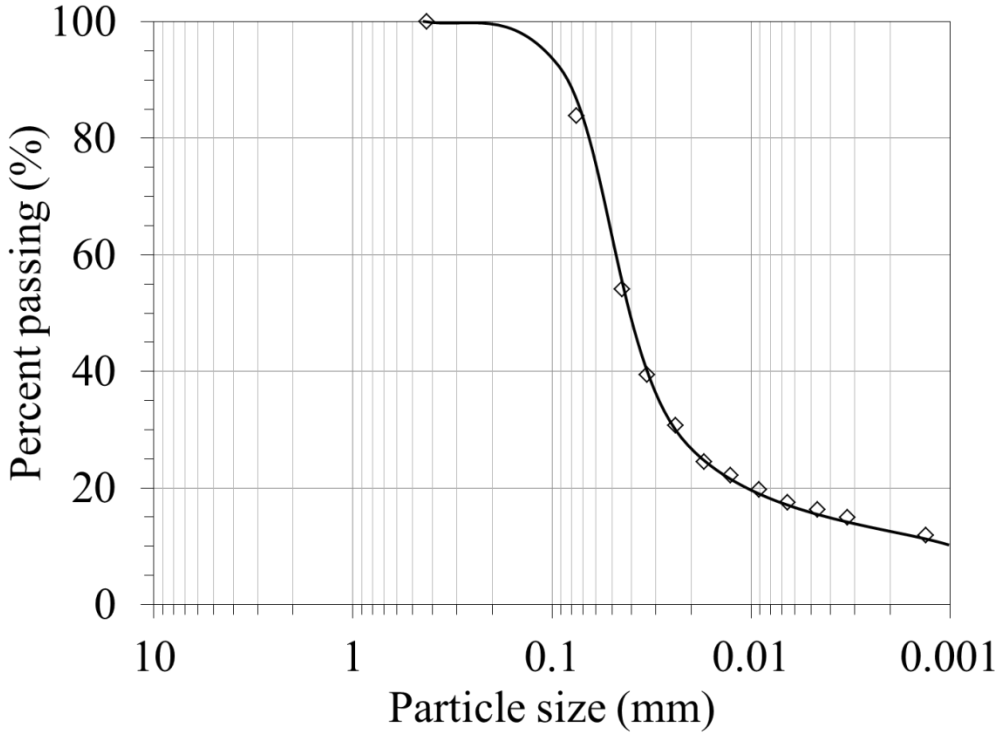

Figure 4.8.2-1 Particle-size distribution curve for Bonny silt

Table 4-9 Particle-size distribution properties of Bonny silt

Particle-Size Parameter	Value
D_{10}	< 0.0013 mm
D_{30}	0.022 mm
D_{50}	0.039 mm
% Fines (Passing No. 200 sieve)	83.9%
% Clay size	14%
% Silt size	69.9%
% Sand size	16.1%

The Atterberg limits, which include the liquid limit (LL), plastic limit (PL), and plasticity index (PI), were measured for Bonny silt in accordance with ASTM D 4318. The results of these tests are summarized in Table 4.10, including the activity A, which is defined as:

$$A = \frac{PI}{\%\ by\ weight\ of\ claysize\ fraction} \qquad \text{(Eq. 4.4)}$$

An activity of 0.29 is relatively low, which indicates that the clay size particles do not contain a significant amount of clay minerals which have a thick diffuse double layer (Mitchell and Soga 2005). Because the thickness of the diffuse double layer of some clay minerals is sensitive to temperature, high amounts of clay minerals such as Smectite may lead to complex thermo-hydro-mechanical behavior (Sultan 2002). Due to the low activity of Bonny silt, soil volume change during temperature changes is expected to occur primarily as a result of the differential thermal expansion of free water and soil particles (Mitchell and Campanella 1968). Based on the Atterberg limits and the shape of the particle size distribution, Bonny silt is classified as ML (inorganic silt) according to the Unified Soil Classification System (ASTM D 2487).

Table 4-10 Atterberg limits and activity of Bonny silt

Property	Value
Liquid Limit, LL	25
Plastic Limit, PL	21
Plasticity Index, PI	4
Activity, A	0.29

The specific gravity of soil solids, G_s, is defined as the ratio of the average density of particles to the density of distilled water. The specific gravity is an important parameter for calculating the weight-volume relationships for soils. The value of specific gravity for most natural soils falls within a range of 2.6 to 2.9. The specific gravity of solids that pass the 4.75-mm (No. 4) sieve (all of the Bonny silt particles) was determined by means of a water pycnometer in accordance to ASTM D 854, of the value of G_s for Bonny silt obtained as the average of three tests was 2.63.

The standard Proctor compaction test (ASTM D 698) and the modified Proctor compaction test (ASTM D1557) were performed on Bonny silt to define the relationship between compaction water content and dry unit weight for different compaction energies. The standard and modified Proctor compaction curves for Bonny silt are presented in Figure 4.8.1-2. With respect to the standard Proctor compaction test, the optimum water content, w_{opt}, for Bonny silt is 13.6% and the maximum dry unit weight, γ_{dry}, is 16.3 kN/m^3.

The specimens evaluated in this study were prepared using static compaction with a manual press in order to lead to similar soil conditions to those used in centrifuge tests on energy foundations by Rosenberg (2010) and Stewart (2012). The target compaction water content is 15% and the target dry unit weight is 16.6 kN/m^3, which is slightly wet of optimum.

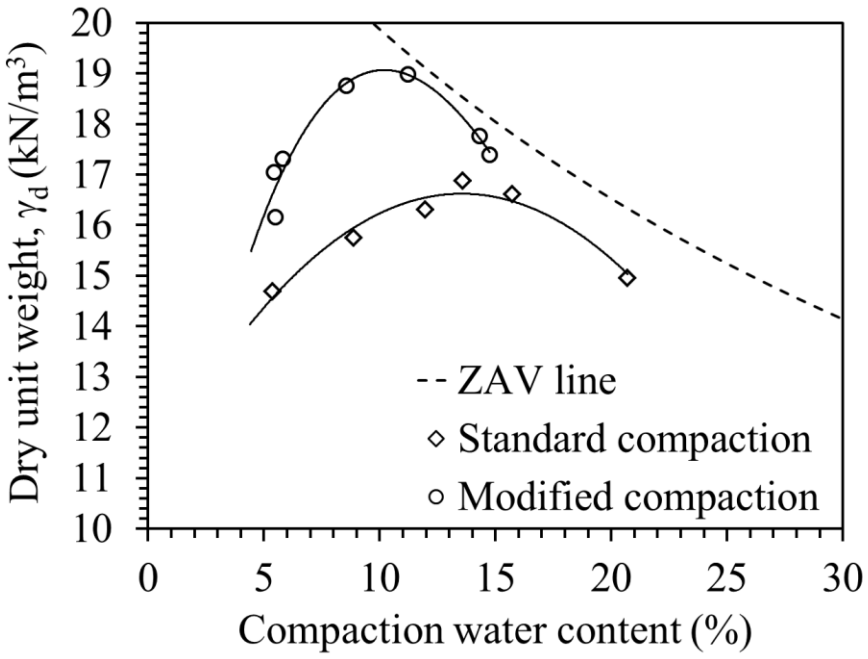

Figure 4.8.2-2 Proctor compaction curves for Bonny silt

The compression properties of Bonny silt were measured using a standard oedometer test (within the same cell used in the thermal consolidation tests) following the procedures in ASTM

D2435, although loading increments were applied only until reaching the end of primary consolidation at each stress level. The compression curve for a specimen compacted to the target conditions described in the previous section is shown in Figure 4.8.1-3. The compression curve parameters are presented in Table 4-11. A typical log-time settlement curves for Bonny silt during a stress increment of 400 kPa is shown in Figure 4.8.1-4. In general, specimen was observed to reach 90% consolidation after approximately 4.41 minutes. This corresponds to a coefficient of consolidation c_v of 1.32 cm^2/min. The value of c_v will of course vary as a function of the loading increment and void ratio.

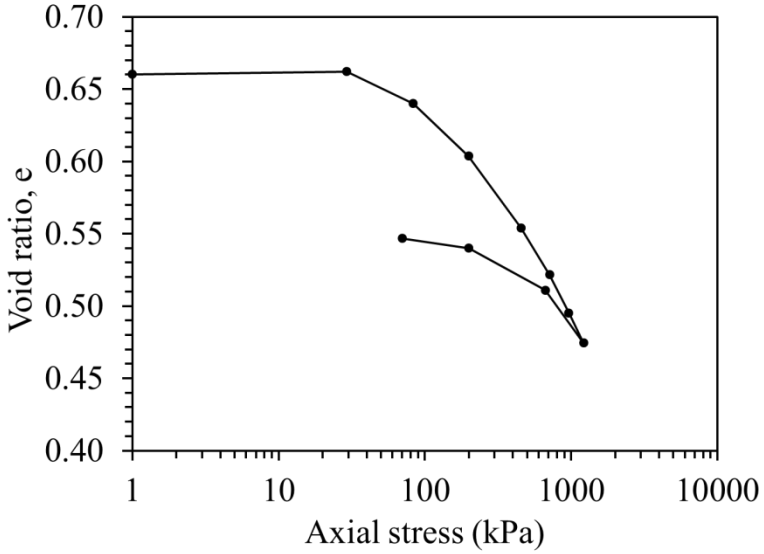

Figure 4.8.2-3 Compression curve for compacted Bonny silt

Table 4-11 Compression curve parameters

Compression Property	Value
Compression Index (C_c)	0.20
Recompression Index (C_r)	0.034

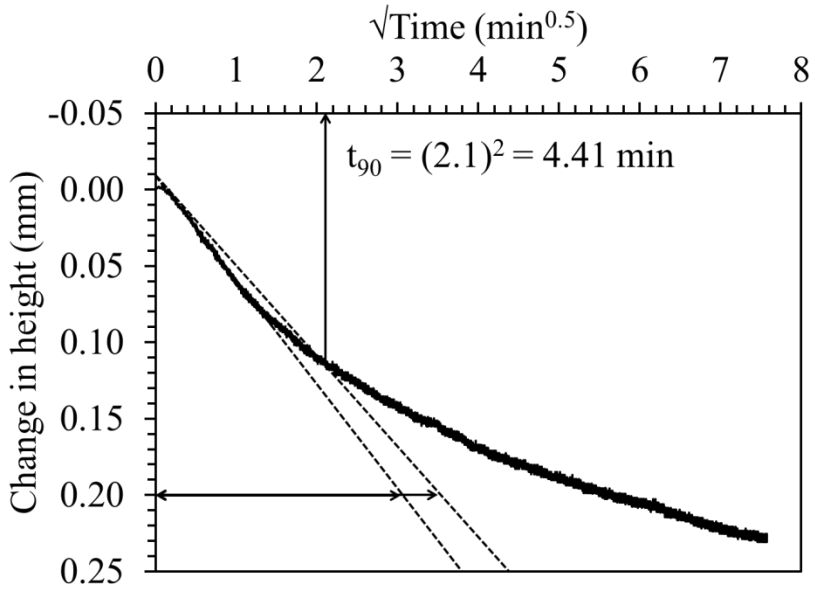

Figure 4.8.2-4 Typical time settlement curve for Bonny silt on a root-time

Thermal conductivity for unsaturated Bonny silt was measured using a thermal needle test during testing indicated a value of 1.24 W/(m°C). Table 4-12 shows the results from each test. The tests were performed by taking periodic measurements during the tests. The thermal needle was placed in the free field portion of the soil.

Table 4-12 Thermal Conductivity for Unsaturated Bonny Silt

Test	Thermal Conductivity W/(m°C).
S-BS-ML-0	1.234
S-BS-ML-10	1.237
S-BS-ML-18	1.253
S-BS-CL	1.222
S-BS-CL	1.246

The stress paths obtained from three consolidated undrained (CU) triaxial tests performed in accordance with ASTM standard D4767 on saturated Bonny silt specimens are shown in Figure 4.8.1-5. These stress paths indicate that for this range of mean effective stress, Bonny silt

exhibited behavior similar to over-consolidated soils. Specifically, compacted Bonny silt exhibits a dilative soil behavior with negative excess pore water pressure generation during shearing. The slope of the critical state line is 1.305, corresponding to a drained friction angle of 32.4°.

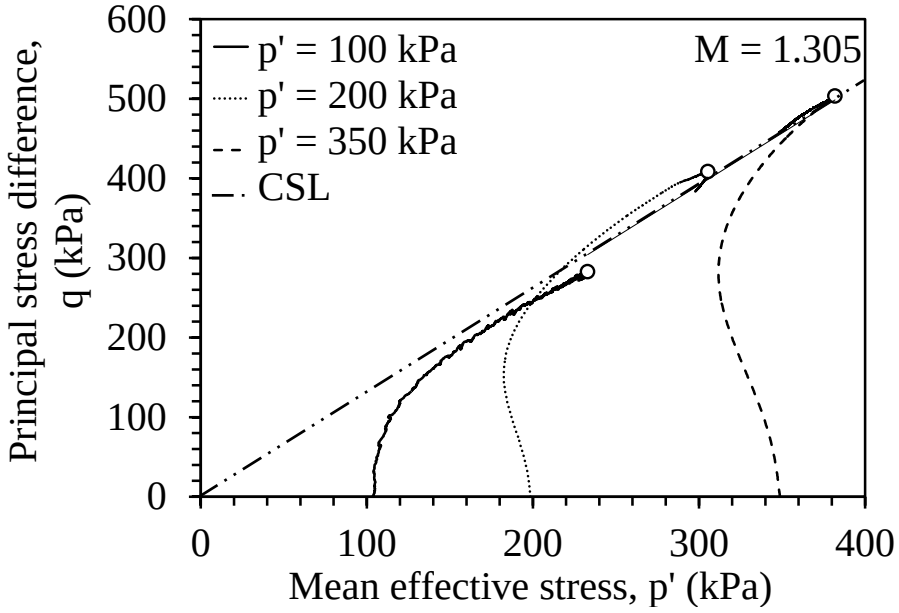

Figure 4.8.2-5 Effective stress paths for compacted Bonny silt plotted for initial consolidation effective stresses of 100, 200 and 350 kPa

The small-strain shear modulus (G_{max}) was measured for a variety of net stresses and plotted as a function of mean effective stress with the model (described below) in Figure 4.8.1-6. The small strain shear modulus can be represented according the following equation:

$$G_{max} = AP_a \log\left(\frac{p'}{P_a}\right)^n \quad \text{(Eq 4.4)}$$

where P_a is the atmospheric pressure used for normalization, and the fitting parameters A and n for this data set are 0.42 and 0.52, respectively.

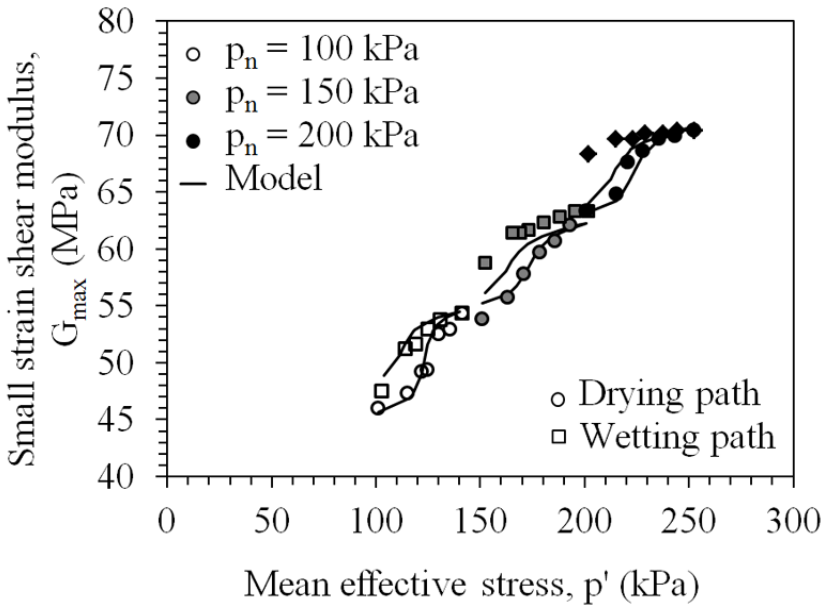

Figure 4.8.2-6 Changes in small strain shear modulus with mean effective stress

The hydraulic properties of Bonny silt were measured using the flow pump technique developed by Aiban and Znidarcic (1989). This technique was used to define the saturated hydraulic conductivity using a constant flow rate approach, and was later combined with the axis-translation technique to measure the soil-water retention curve (SWRC) and hydraulic conductivity function (HCF) of unsaturated soils. A plot of saturated hydraulic conductivity for a variety of void ratios is presented in Figure 4.8.1-7. The data for this plot was taken from previous literature published using this technique. The hydraulic conductivity of saturated specimens having initial void ratios ranging from 0.5 to 0.8 ranges from $1x10^{-9}$ to $1x10^{-7}$ m/s. The SWRC for Bonny silt specimen having an initial void ratio of 0.69 under a range of net stresses are shown in Figure 4.8.1-8.

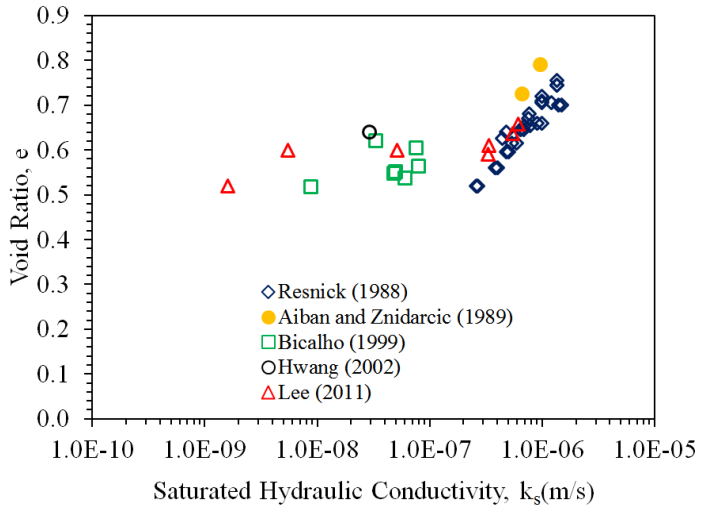

Figure 4.8.2-7 Hydraulic conductivity as a function of void ratio for a variety of tests performed on Bonny silt

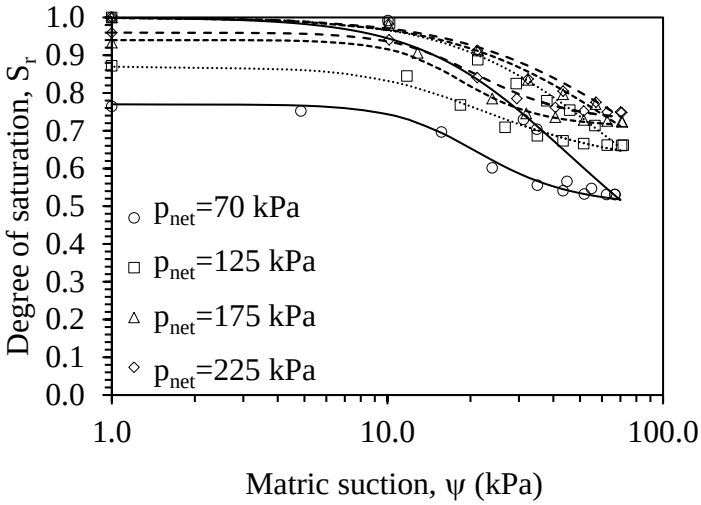

Figure 4.8.2-8 SWRCs for Bonny silt specimens having an initial void ratio of 0.69 under a range of net stresses

CHAPTER 5 Centrifuge Testing Procedures

5.1 Sample Preparation

A total of 14 tests were performed as part of this study, including eight on foundations in Nevada sand and six on foundations in Bonny silt. The procedures used to prepare the soil layers and for placement of the scale model energy-foundations are described in the next two sections.

5.1.1 Preparation of Tests involving Nevada Sand

Nevada sand layers were prepared to achieve parameters mentioned in Section 3.9. To start, clean Nevada sand stored in 55-gallon drums was moved to the sample preparation area, which was covered with clean plastic drop tarps used only for Nevada sand raining. The sand was then transferred to a large hopper for sand raining. The hopper was then raised to a height of 1.2 m for air pluviation. When preparing the semi-floating foundation samples, the first 190.5 mm of the container were filled with sand before stopping the sand raining for placing of the foundation. The foundations were centered using cross strings and leveled. Once the foundation was level and centered sand raining continued. The sand hopper was continuously raised to keep a constant height above the current soil level. This height was measured with a string of appropriate length and monitored by the lab assistant in charge of raising and lowering the hopper. Once the sand reached the desired level at the top of the container the container was cleaned off and transported to the basket of the centrifuge. Figures 5.1.1-1 and 5.1.1-2 show the air pluviation process taking place.

Figure 5.1.1-1 Air pluviation using a sand hopper.

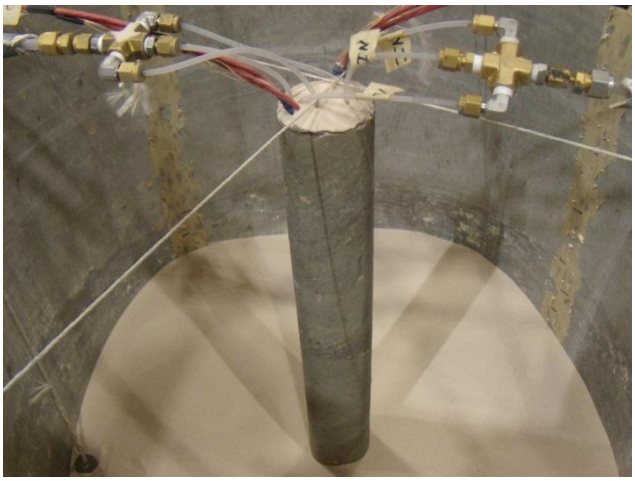

Figure 5.1.1-2 End-bearing foundation during sample preparation.

5.1.2 Preparation of tests involving Bonny Silt

The Bonny silt layers were prepared using impact compaction in order to create a uniform layer of soil with a consistent dry unit weight of 17 kN/m^3. The soil was passed through a 13 mm sieve to break up large clods, and then further broken up using a rubber mallet. Once the crushed soil was passed through a number 40 sieve, the soil was wetted gradually using a pressurized water sprayer to achieve a water content of approximately 12.5%. The soil was then moisture conditioned in a closed bucket to homogenize the water content through the soil.

During compaction, the soil was placed in fourteen 38.1 mm-thick lifts to reach the final height of the container. A total of 18.7 kg was placed into each lift to reach the target dry unit weight of 17 kN/m^3. For the semi-floating foundation, 18.9 kg were placed in the bottom 5 lifts to account for the fact that the foundation was not present. Once a level base was created at the depth corresponding to the toe of the semi-floating foundation, the semi-floating foundation was placed in the container then centered and leveled. Scarification of lifts was used to ensure that the lifts were well bonded. When it was required for placement of the dielectric sensors some soil from the next lift was placed in the container and spread evenly. The dielectric sensors were

placed on a thin amount of loose soil so that after compaction they would be horizontal at the desired depth and radial location from the foundation. The soil around the sensor was first compacted by hand to minimize damage to the sensor, after which additional soil was placed and impact compaction was used for the remainder of the lift. Compaction was performed using a 27 kg square weight having a surface area of 0.03 m^2, with a drop height of approximately .25 m. Compaction around the foundation and edges of the soil container was performed using a rubber mallet to permit more precision in soil placement. The rubber mallet has an area of 63.5 mm. Each layer was carefully weighed out to the appropriate weight and measured to 38.1 mm after compaction effort was completed. Figure 5.1.2-1 shows the Bonny silt compaction process.

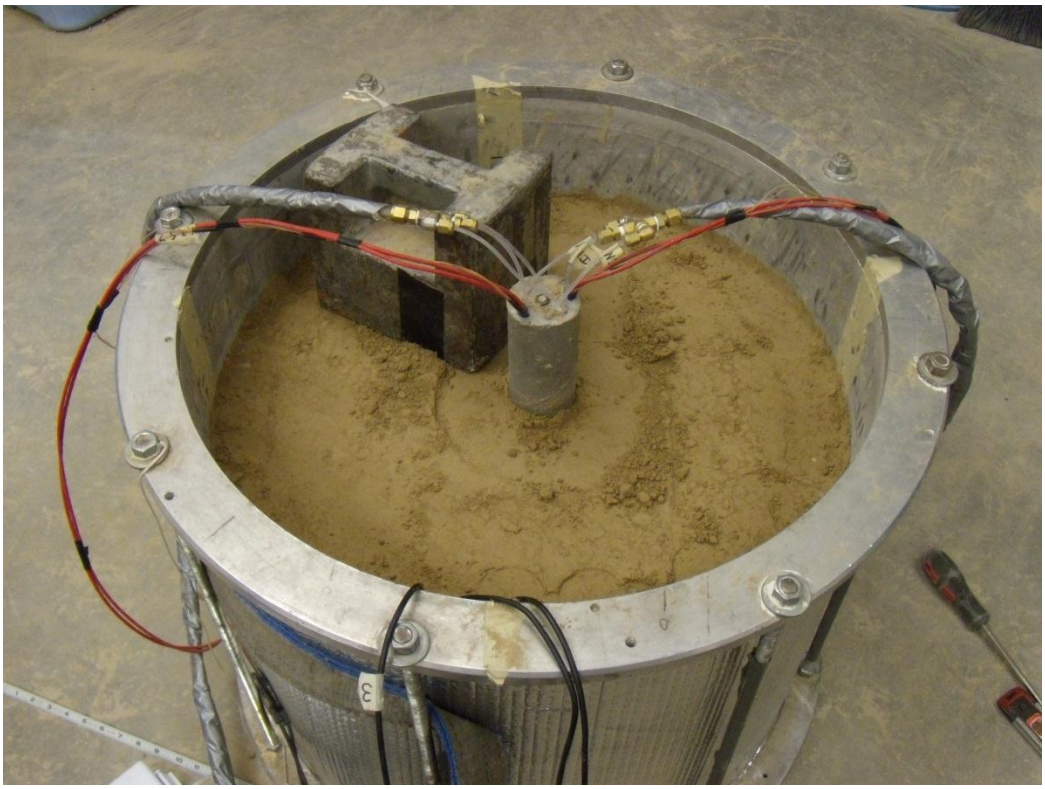

Figure 5.1.2-1 Bonny silt compaction in progress, the square weight is shown in this photo.

5.2 Testing Procedure

Each of the 14 tests performed in this study had different temperature conditions, foundation types, soil types, and top loading conditions. Because of the difference in testing conditions, different sets of testing procedures were used throughout the study. The semi-floating foundations were heated under a constant axial load, after which they were loaded to failure. The end-bearing foundations were heated under a constant axial load as well, but were loaded elastically after each change in temperature to evaluate changes in side shear resistance.

5.2.1 General Centrifuge Procedure

Once the soil container was ready for spinning it was lowered into the centrifuge chamber using the overhead crane. While lowering the full container, it was weighed using a hanging scale for the purposes of balancing the centrifuge. The soil container was lowered to a roller cart and then transferred to the centrifuge spinning basket. In order to minimize the time required to heat the foundations during centrifugation, the heat exchange fluid was pre-heated in the heat pump to 90 °C approximately two hours prior to centrifugation. Strain gages, thermocouples, LVDTs and load cell were all plugged in and checked to ensure that they were working properly. The air pressure supply was turned on and the lid to the centrifuge chamber was set in place. All centrifuge tests were performed at 24 g. After finishing the general centrifuge preparation was completed, the protocol for the rest of the test was changed based on each individual test. A picture of the soil container being lowered is shown in Figure 5.2.1-1 the soil container in the testing frame on the centrifuge is shown in Figure 5.2.1-2.

Figure 5.2.1-1 Lowering of the soil container onto the roller cart in the centrifuge chamber with hanging scale.

Figure 5.2.1-2 Soil container in place with all instrumentation prepared for testing.

5.2.2 Semi-floating Foundation Test Procedures

After completing the general procedure applicable to all tests the individual procedure based on the test type was carried out. For a semi-floating foundation test the first phase after spin-up allowed for the system to equilibrate, including the strain gages and settlements. Creep settlement would continue throughout the test but it was important to wait for the primary settlement stage to finish. The foundation was then loaded to approximately 600 N in model scale indicating a building load. After application of the building load more time was allowed for the foundations strain gages and settlements to stabilize. At this time a heating load was applied to the foundation, when the target temperature was reached more time was given for the temperatures to stabilize. This temperature control was performed by the project engineer during centrifugation by controlling the servo valves through the National Instruments LabView data

acquisition program. A picture of the servo-controlled valves setup is shown in Figure 3.5.1-2. Once the target temperature was stable the peak load was applied to the foundation. The peak load was increased in stages at a rate of 1.38 kPa/second to a maximum load of 4220 N. After 2 minutes the foundation load was decreased prior to spin down. An ideal loading program of load and temperature with time is shown in Figure 5.2.2-1.

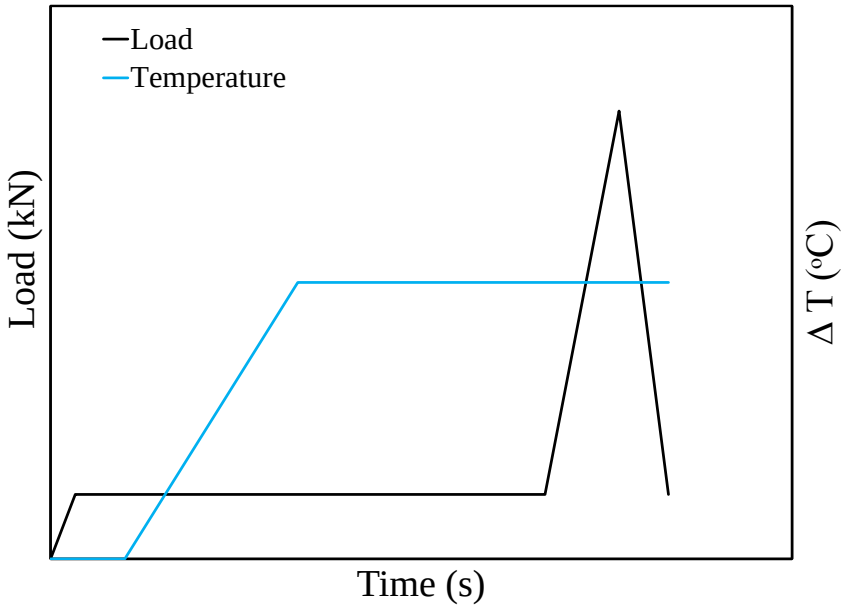

Figure 5.2.2-1 Idealized load and temperature application stages for monotonic loading of the semi-floating foundation.

5.2.3 Top End Restraint Condition Test Procedures

Two top load conditions were tested on the end-bearing foundation load control conditions as well as stiffness control. The load control condition was achieved through the same loading system used for all other tests. The stiffness boundary condition required fabrication of a new loading technique. The first test performed was the load condition test. After achieving the target g-level and all elements and stabilized a 2,200 N load was applied to the foundation. After the load stabilized the foundation was heated to 33 °C. An ideal test procedure schematic is shown in Figure 5.2.3-1.

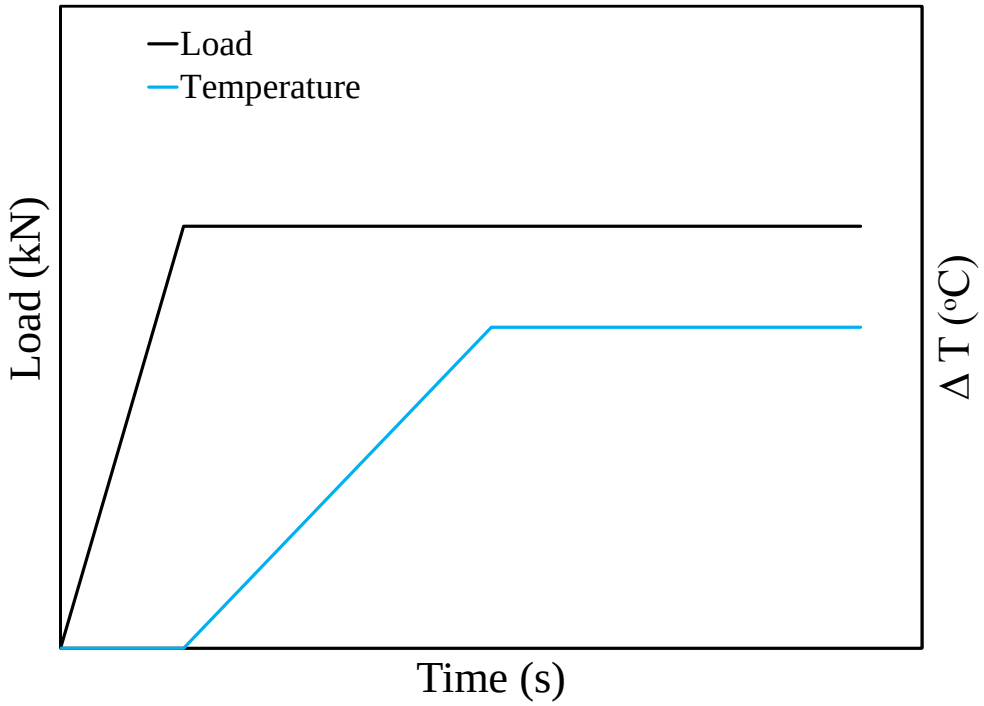

Figure 5.2.3-1 Typical load and temperature during a test on the end-bearing foundation with different end-restraint boundary conditions.

The test for stiffness control was performed on the same soil sample as the load control. After finishing the previous test the pneumatic piston was removed and the stiffness setup was installed. This stiffness technique as mentioned in Section 2.3.1 was replaced on the frame prior to spin up was loaded to 2840 N. After spin up, the initial load was 2350 N. Once the foundation stabilized the foundation was headed to 33.5 °C.

5.2.4 End-Bearing Foundation Test Procedures

The end-bearing foundation tests were slightly different than the semi-floating foundation test because the end-bearing foundation rests on a stiff bottom there will be no change in toe bearing stress. For this reason for each end-bearing foundation sample multiple temperatures were used in succession. The procedure follows that the semi-floating foundation outlined in 4.2.1, but with additions at the end. After the foundation was loaded it and held stable for 2 minutes the load was decreased at a rate of 3.45 kPa/second to 600 N. After a stabilization

period heating was applied to reach the second target temperature. At this time the same peak loading procedure was followed. This carried on until all target temperature and respective loadings took place. Figure 5.2.4-1 shows an ideal test program for a end-bearing foundation test, with a cyclic cooling at the end of the test.

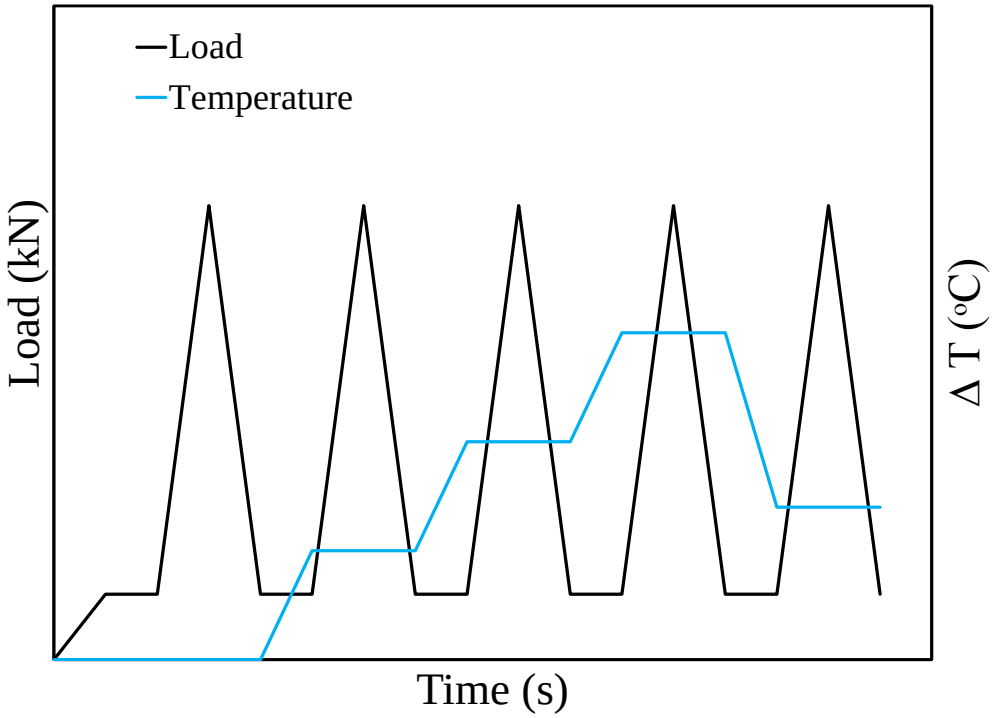

Figure 5.2.4-1 Typical load and temperature with time for and end-bearing foundation staged loading test.

CHAPTER 6 Centrifuge Test Results

6.1 Overview of Results Layout

6.1.1 Summary Tables

A nomenclature was created for identification of the different tests. The test ID format is (Foundation type)-(Soil type)-(Heating and Load type)-(Temperature Change). The foundation type is indicated as either S for the semi-floating foundation (semi-floating) or L for the end-bearing foundation (end-bearing). The soil type will be indicated by NS or BS for Nevada sand and Bonny silt respectively. The heating types are monotonic heating M, staged heating S, cyclic heating C, and staged heating followed by cooling SC. The loading type is indicated as either L for load control or S for stiffness control. The change in temperature for monotonic loading is noted in the test ID as the temperature change at loading. Basic descriptions of each test a presented in Table 6-1. The properties of the soil layer in each test are summarized in Table 6-2. The temperature loading program used in each test is presented in Table 6-3. The mechanical loading details of each test are presented in Table 6-4.

Table 6-1 Summary of all tests performed with description.

Test ID	Soil type	Foundation	Test Description
S-NS-ML-0	Nevada	Short	Ambient loading test on short foundation
S-NS-ML-7	Nevada	Short	Loading test on short foundation at elevated temperature
S-NS-ML-11	Nevada	Short	Loading test on short foundation at elevated temperature
S-NS-ML-18	Nevada	Short	Loading test on short foundation at elevated temperature
L-NS-ML-11	Nevada	Long	Load-control heating test on long foundation
L-NS-MS-12	Nevada	Long	Stiffness-control heating test on long foundation
S-NS-SCL	Nevada	Long	Staged loading test on long foundation after cyclic heating-cooling
L-NS-SCL	Nevada	Long	Staged loading test on long foundation after cyclic heating-cooling
S-BS-ML-0	Bonny	Short	Loading test on short foundation at elevated temperature
S-BS-ML-10	Bonny	Short	Loading test on short foundation at elevated temperature
S-BS-ML-18	Bonny	Short	Loading test on short foundation at elevated temperature
S-BS-CL	Bonny	Short	Loading test on short foundation after cyclic heating-cooling
S-BS-CL	Bonny	Short	Loading test on short foundation after cyclic heating-cooling
L-BS-SCL	Bonny	Long	Staged loading test on long foundation after cyclic heating-cooling

Table 6-2 Summary of tests soil properties.

Test ID	Soil type	Foundation	Tambient	Temperature at mechanical loading	DT	Heating ramp time	Total heating duration
			(^{o}C)	**(^{o}C)**	**(^{o}C)**	**(min)**	**(min)**
S-NS-ML-0	Nevada	Short	18	23.0	3	-	-
S-NS-ML-7	Nevada	Short	18	30.2	7	34	81
S-NS-ML-11	Nevada	Short	18	35.3	11	61	77
S-NS-ML-18	Nevada	Short	18	40.3	18	52	93
L-NS-ML-11	Nevada	Long	18	33.4	11	66	118
L-NS-MS-12	Nevada	Long	18	33.3	12	67	103
S-NS-SCL	Nevada	Long	18	23.7	Multiple	-	107
L-NS-SCL	Nevada	Long	18	35.6	Multiple	-	277
S-BS-ML-0	Bonny	Short	18	21.4	1	-	-
S-BS-ML-10	Bonny	Short	18	30.5	10	77	87
S-BS-ML-18	Bonny	Short	18	38.0	18	65	181
S-BS-CL	Bonny	Short	18	36.6	16	26	265
S-BS-CL	Bonny	Short	18	34.8	15	-	187
L-BS-SCL	Bonny	Long	18	21.2	Multiple	-	257

Table 6-3 Summary of tests and temperature loading program.

Test ID	Soil type	Foundation	G-level	Seating mechanical load on foundation	Maximum applied mechanical load on foundation
				(kN)	**(kN)**
S-NS-ML-0	Nevada	Short	24	365	2440
S-NS-ML-7	Nevada	Short	24	365	2440
S-NS-ML-11	Nevada	Short	24	365	2440
S-NS-ML-18	Nevada	Short	24	365	2440
L-NS-ML-11	Nevada	Long	24	1265	1265
L-NS-MS-12	Nevada	Long	24	1340	1510
S-NS-SCL	Nevada	Long	24	365	2440
L-NS-SCL	Nevada	Long	24	365	2440
S-BS-ML-0	Bonny	Short	24	365	2440
S-BS-ML-10	Bonny	Short	24	365	2440
S-BS-ML-18	Bonny	Short	24	365	2440
S-BS-CL	Bonny	Short	24	365	2330
S-BS-CL	Bonny	Short	24	365	2440
L-BS-SCL	Bonny	Long	24	365	2440

Table 6-4 Mechanical details of all tests.

Test ID	Soil type	Foundation	Soil unit weight	Pre-test soil thermal conductivity	Pre-test gravimetric water content	Post-test gravimetric water content (at foundation)	Post-test gravimetric water content (at foundation)	Post-test gravimetric water content (away from foundation)
			(kN/m^3)	**(W/(mK))**	**(%)**	**(%)**	**(%)**	**(%)**
S-NS-ML-0	Nevada	Short	15.5	-	-	-	-	-
S-NS-ML-7	Nevada	Short	15.5	-	-	-	-	-
S-NS-ML-11	Nevada	Short	15.5	0.265	-	-	-	-
S-NS-ML-18	Nevada	Short	15.5	-	-	-	-	-
L-NS-ML-11	Nevada	Long	15.5	-	-	-	-	-
L-NS-MS-12	Nevada	Long	15.5	-	-	-	-	-
S-NS-SCL	Nevada	Long	15.5	-	-	-	-	-
L-NS-SCL	Nevada	Long	15.5	0.248	-	-	-	-
S-BS-ML-0	Bonny	Short	17.0	1.234	12.3	-	-	12.3
S-BS-ML-10	Bonny	Short	17.0	1.237	12.6	12.1	11.4	12.2
S-BS-ML-18	Bonny	Short	17.0	1.252	12.5	11.7	12.0	12.5
S-BS-CL	Bonny	Short	17.0	1.222	12.5	12.0	-	-
S-BS-CL	Bonny	Short	17.0	1.246	12.5	11.1	11.4	11.9
L-BS-SCL	Bonny	Long	17.0	1.150	12.2	11.4	11.8	12.1

6.1.2 Figure Layout

The raw results from each of the tests are relatively similar, so to avoid repetition in the text, a system for presenting the figures in a consistent manner was developed. In the section for each test, up to 18 figures are presented. The contents of each figure are as follows (where X denotes the section number corresponding to each test):

- The key temperatures during tests are shown in Figure X-1: inlet fluid, outlet fluid, average foundation temperature, and the ambient temperature. The inlet fluid temperature was closely monitored along the foundation temperature during heating for adjustments to keep the change in temperature at a desired value.
- Radial temperatures in the soil surrounding the energy foundation are shown in Figure X-2. The impact of soil type can be seen in this particular figure as heat propagates through the foundation and soil strata.
- The foundation temperatures with depth are then shown in Figure X-3.
- Model scale settlements are then shown with the spin up of the centrifuge for Figure X-4. The spin up stage of the test caused a large amount of settlement due to the increase in g-level. This is captured in Figure X-4, and will be subtracted out in subsequent figures for further analysis.
- The prototype displacements of the foundation are shown in Figure X-5, with the spin-up stage of testing zeroed out. Specifically this shows any displacements after the primary settlement due to settlement was completed. The foundation settlements as well as the free field soil settlements are shown.
- The zeroed displacements of the foundation and free field soil are shown in Figure X-6. The results in this figure are different from those in X-6 as they focus on heating portion of each

test. The creep settlement of the soil is subtracted out of the settlement to show the actual thermal settlement of the foundation. The temperature is also displayed on a secondary axis.

- The prototype foundation head load and foundation settlement on separate axes in a time series are shown in Figure X-7.
- The prototype load settlement curve is shown in Figure X-8 where the prototype settlement is shown as positive (+) downwards on the y axis and the axial load in kN is shown on the abscissa.
- Time series of the axial strains in the foundation are shown in Figure X-9, with the strains zeroed prior to application of the seating mechanical load to the foundation.
- The axial strains zeroed at the beginning of heating are defined as the thermal axial strains, and are shown in Figure X-10.
- The axial strains during the loading test are shown in Figure X-11, with the strains zeroed just prior to final mechanical loading.
- The profile of temperature with depth is shown in Figure X-12.
- The prototype-scale thermal axial strain with depth at various temperatures are shown in Figure X-13.
- The associated thermal axial stress profiles with depth at various temperatures are shown in Figure X-14.
- The integrated thermal axial displacements are shown in Figure X-15. The thermal axial displacement was derived by integrating the thermal strains and defining the foundation heads displacement as the LVDT displacement at that point in time.
- The prototype mechanical axial strain profiles corresponding to different axial loads applied to the foundation head during the final loading test are shown in Figure X-16.

- Two additional figures are presented for tests performed on Bonny silt to show the data from the dielectric sensors. The temperature readings at radial locations are shown in Figure X-17 and the changes in volumetric water content are shown in Figure X-18.

Note: The tests performed at ambient temperature do not show the figures associated with the heating portions of the test and only the foundation temperature time series is shown.

6.2 Semi-Floating Foundation Tests in Nevada Sand

Four tests were used to determine the impact of various temperature heating programs on the semi-floating foundation. The four temperatures were 23, 30, 35, and 40 °C. This gave a wide range of temperatures to investigate the trends during heating and loading. The four tests were performed in a similar manner although it takes more time to achieve a much higher temperature so a longer heating period was necessary for the tests with a higher load temperature. The radial temperatures show little to no temperature change during the dry sand tests. It can be noted in the foundation temperature profile that the top and deepest foundation temperature reading is often less than the majority of the temperatures in the foundation. This can be attributed to the proximity to the air at the top of the foundation and the thermocouple at the base of the foundation is slightly further from the heat exchange loops. The settlement profiles show very small settlements after the initial settlement is finished due to spin up. It can be seen in the semi-floating foundation profiles that the foundation sheds load along the length of the foundation as expected.

6.2.1 Results from Test S-NS-ML-0

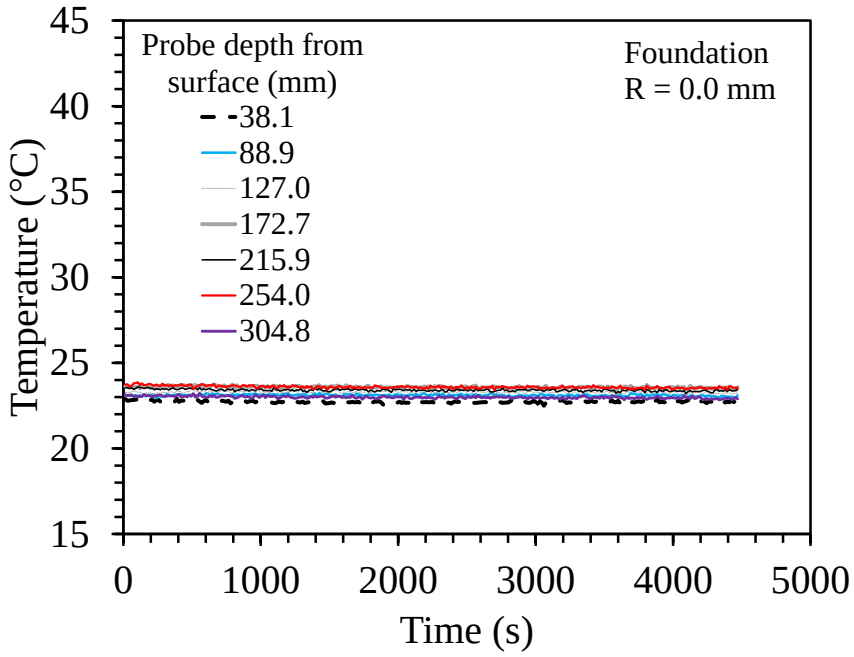

Figure 6.2.1-1 Foundation temperatures during the ambient-temperature (ΔT = 0 °C) loading test on the semi-floating foundation in Nevada sand.

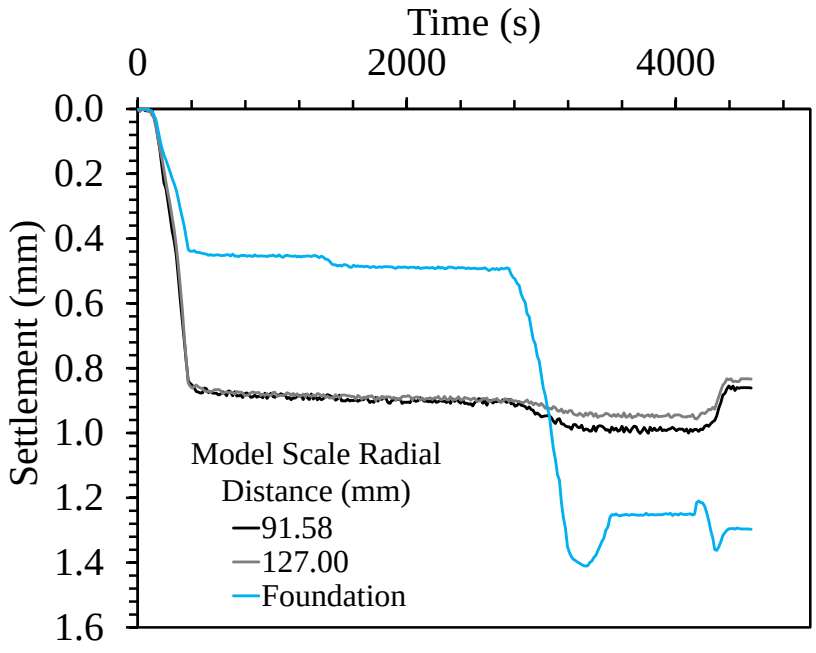

Figure 6.2.1-2 Model-scale settlements during spin up and testing for the ambient-temperature (ΔT = 0 °C) loading test on the semi-floating foundation in Nevada sand.

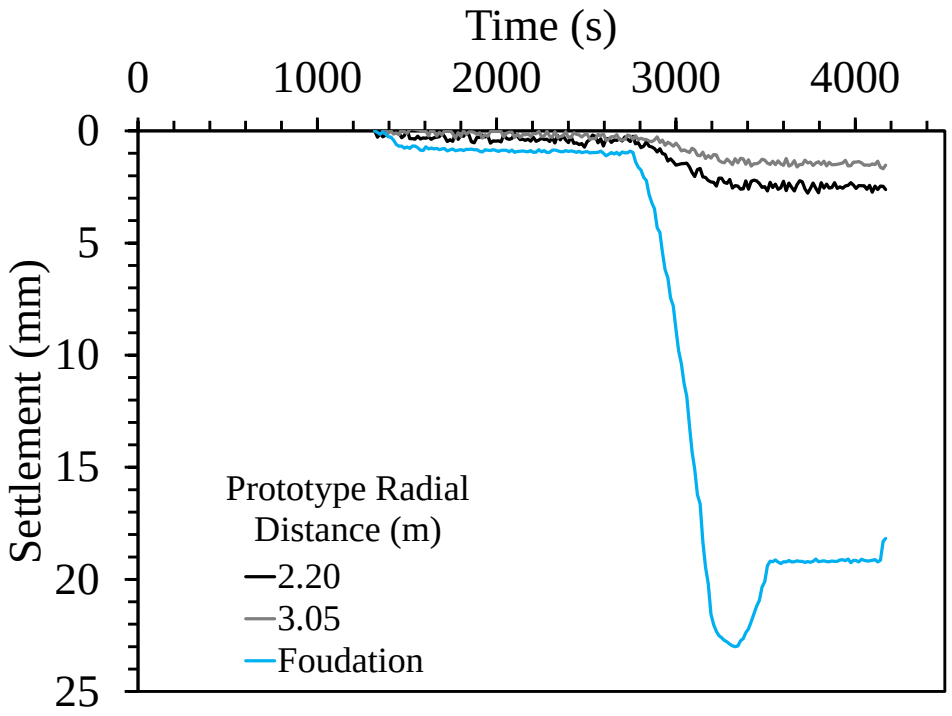

Figure 6.2.1-3 Prototype settlements after spin up during the ambient-temperature (ΔT = 0 °C) loading test on the semi-floating foundation in Nevada sand.

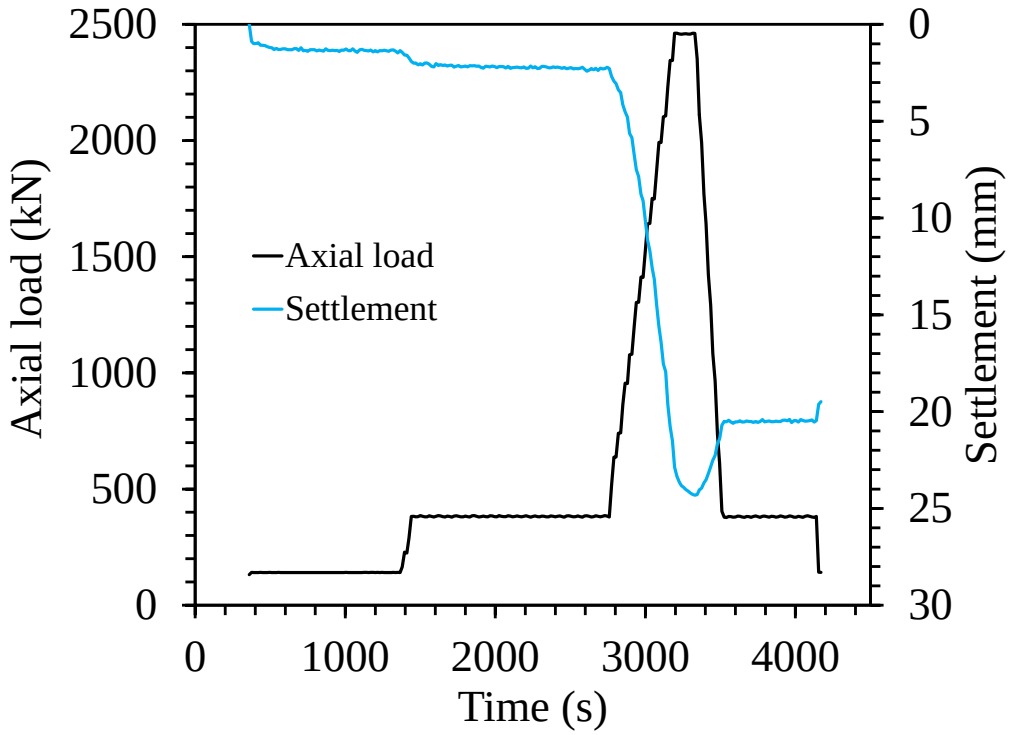

Figure 6.2.1-4 Prototype foundation settlement and associated applied axial load during the ambient-temperature (ΔT = 0 °C) loading test on the semi-floating foundation in Nevada sand.

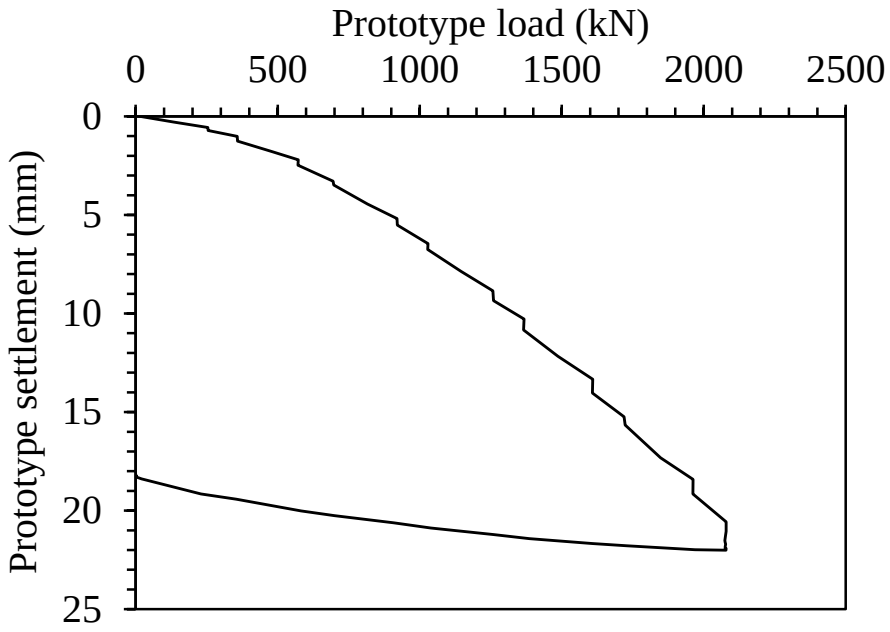

Figure 6.2.1-5 Prototype load settlement curve for the ambient-temperature (ΔT = 0 °C) loading test on the semi-floating foundation in Nevada sand.

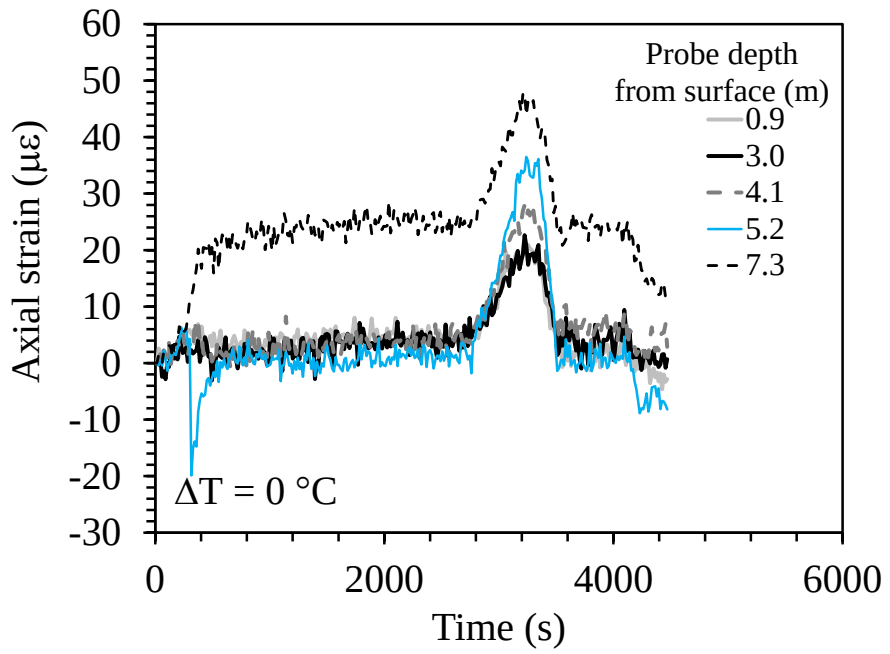

Figure 6.2.1-6 Axial strain time series for the ambient-temperature (ΔT = 0 °C) loading test on the semi-floating foundation in Nevada sand.

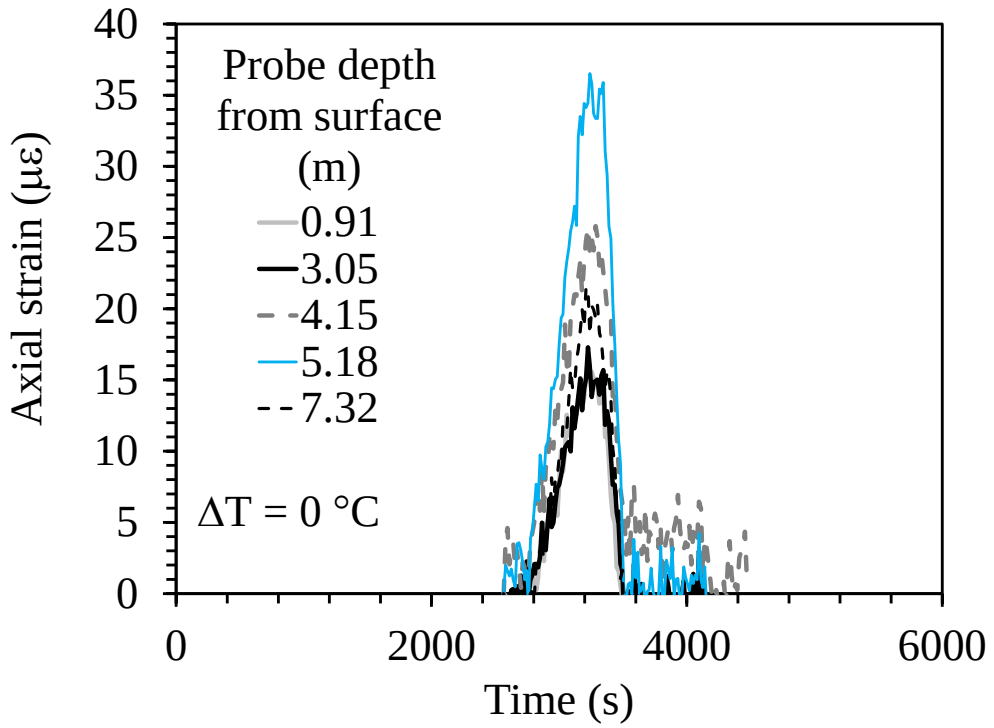

Figure 6.2.1-7 Axial strains during load test for the ambient-temperature (ΔT = 0 °C) loading test on the semi-floating foundation in Nevada sand.

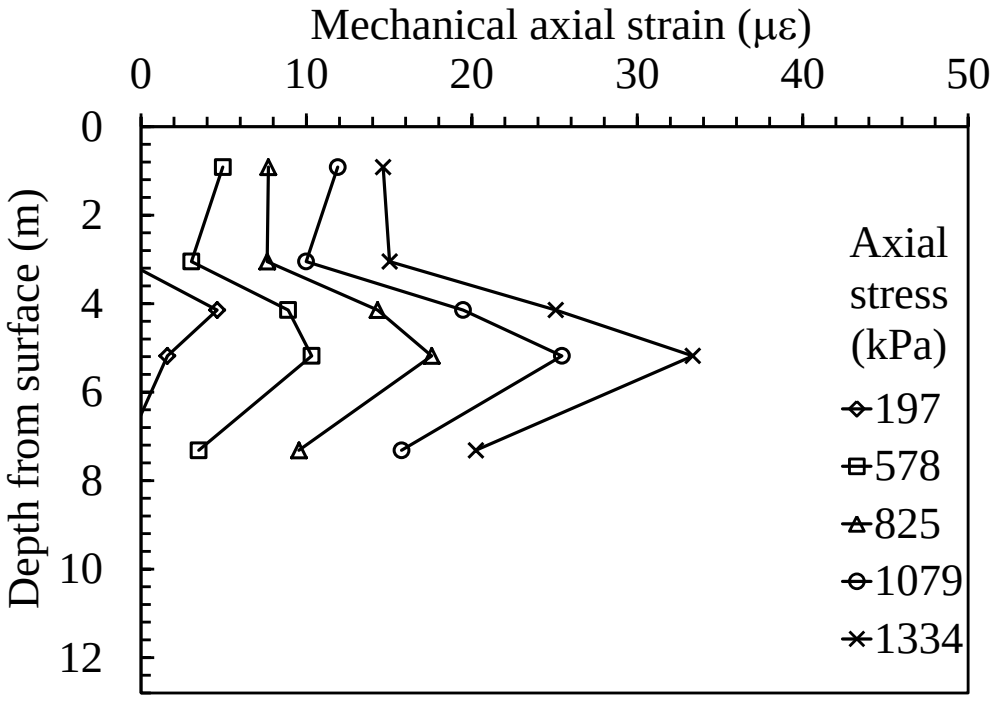

Figure 6.2.1-8 Prototype strain profile during load test for the ambient-temperature (ΔT = 0 °C) loading test on the semi-floating foundation in Nevada sand.

6.2.2 Results from Test S-NS-ML-7

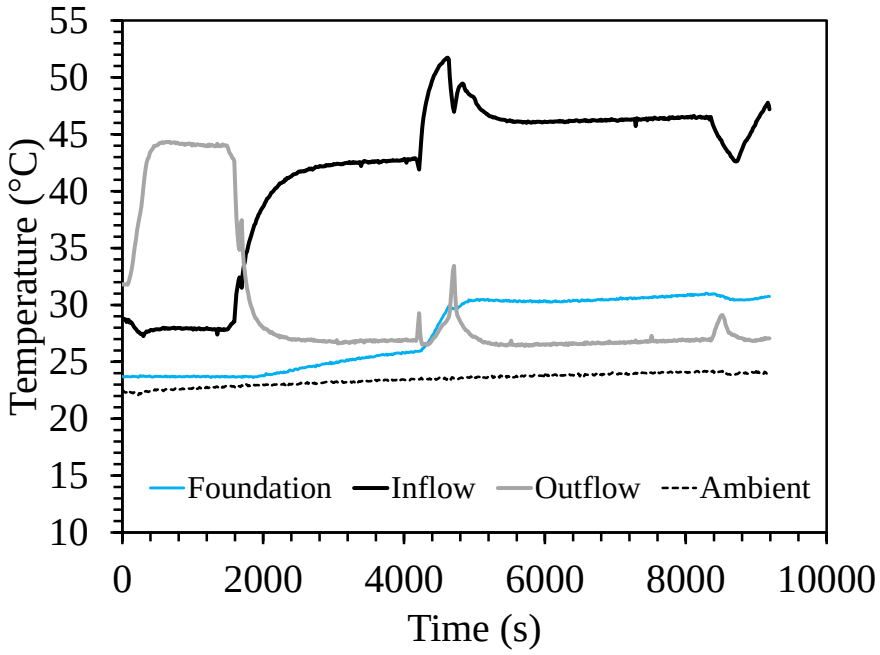

Figure 6.2.2-1 Temperatures for the heated (ΔT = 7 °C) loading test on the semi-floating foundation in Nevada sand.

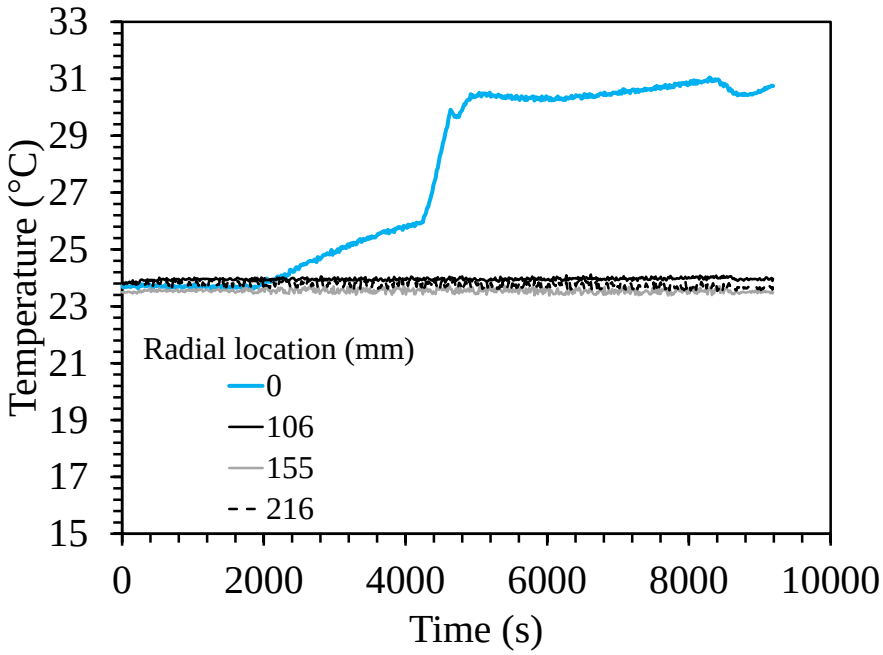

Figure 6.2.2-2 Average temperatures of foundation and four thermal probes for the heated (ΔT = 7 °C) loading test on the semi-floating foundation in Nevada sand.

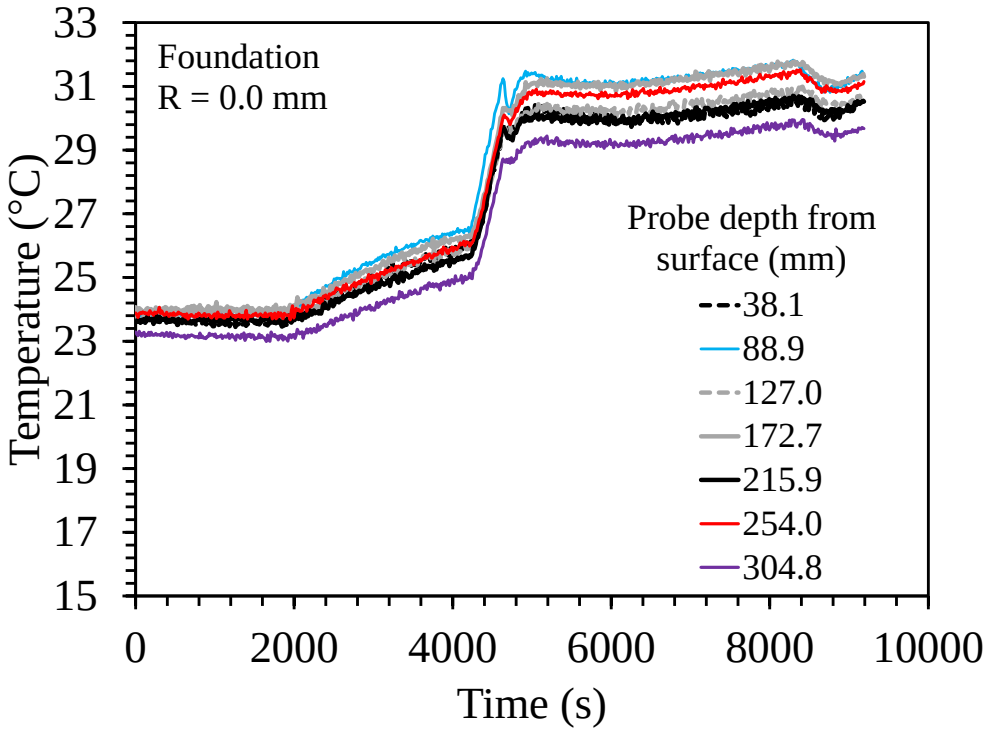

Figure 6.2.2-3 Foundation temperatures for the heated (ΔT = 7 °C) loading test on the semi-floating foundation in Nevada sand.

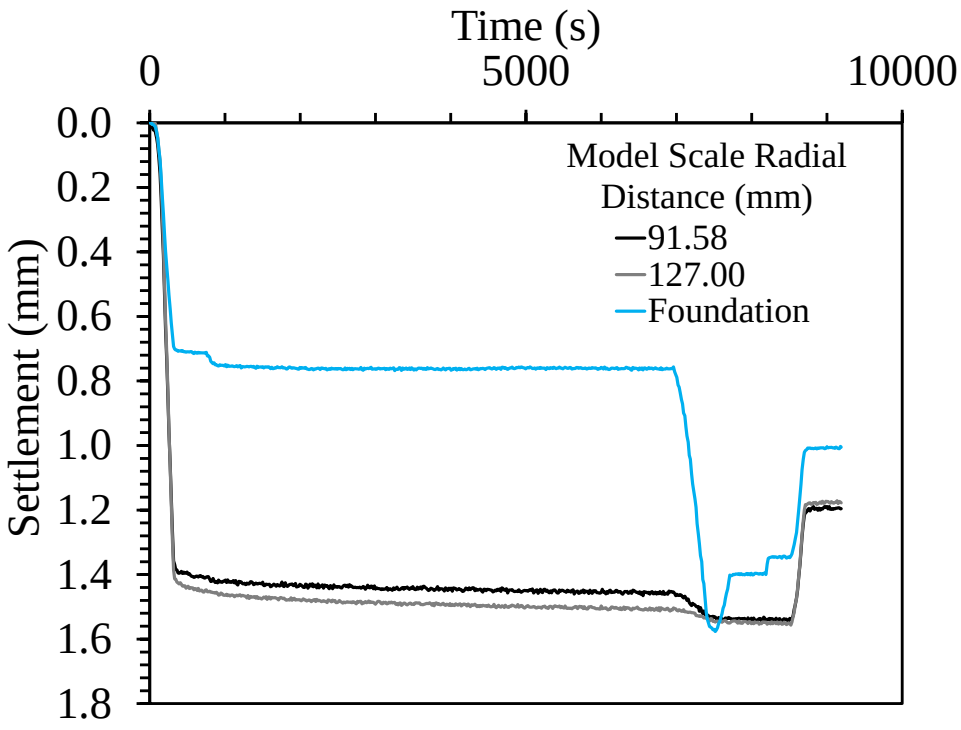

Figure 6.2.2-4 Model scale settlements with spin up for the heated (ΔT = 7 °C) loading test on the semi-floating foundation in Nevada sand.

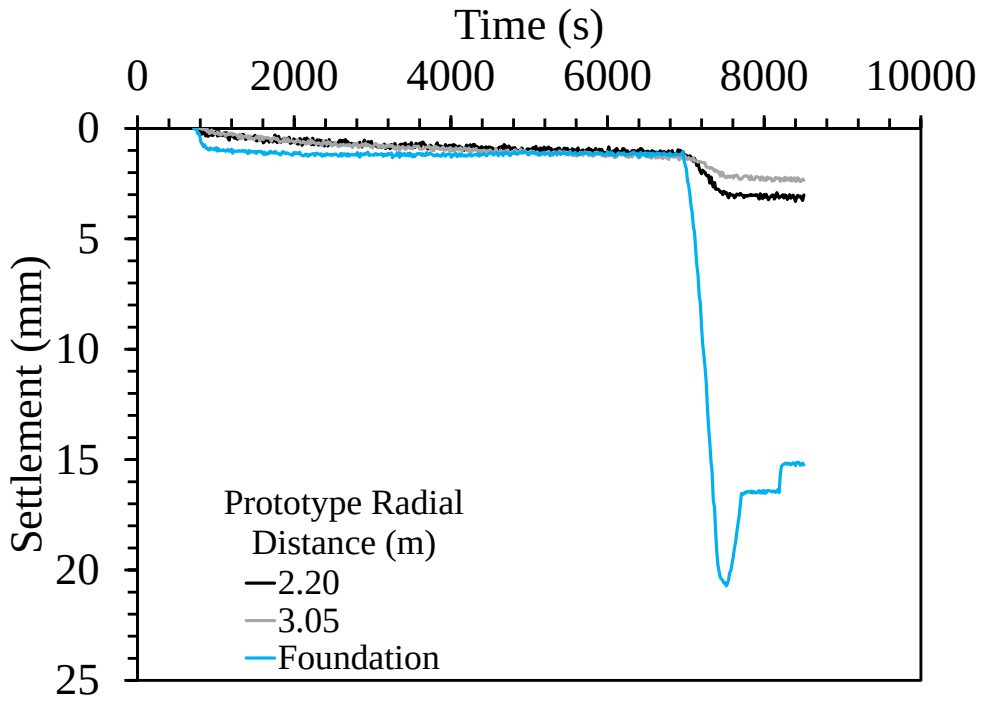

Figure 6.2.2-5 Prototype settlements after spin up for the heated (ΔT = 7 °C) loading test on the semi-floating foundation in Nevada sand.

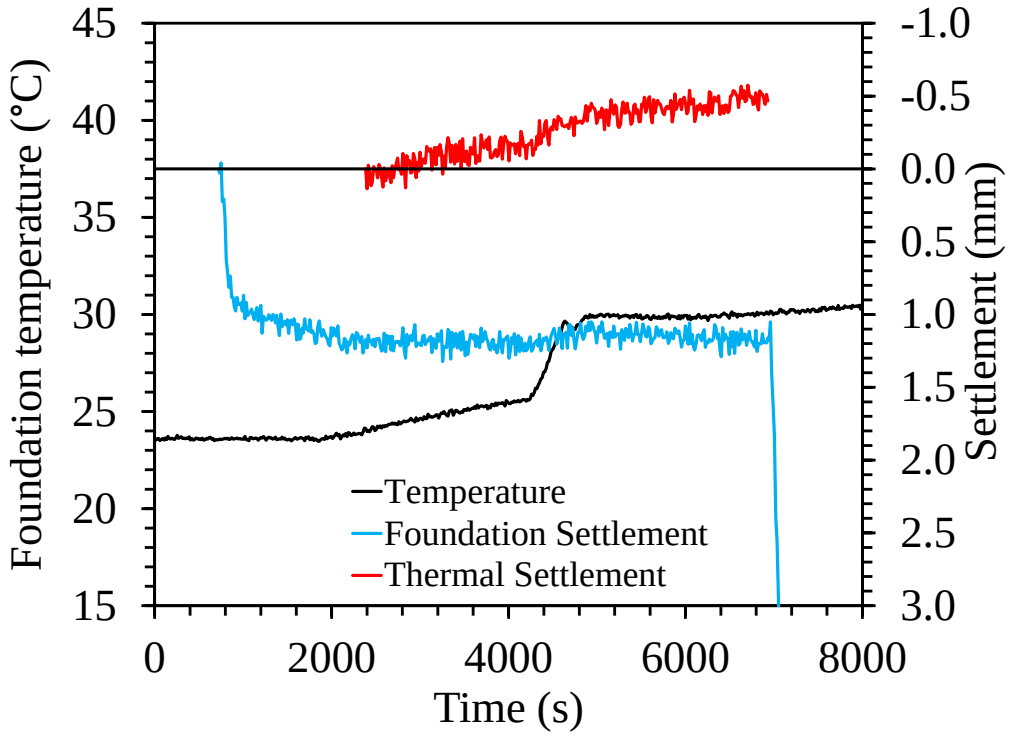

Figure 6.2.2-6 Foundation temperature, overall foundation settlement, and thermal settlement for the heated (ΔT = 7 °C) loading test on the semi-floating foundation in Nevada sand.

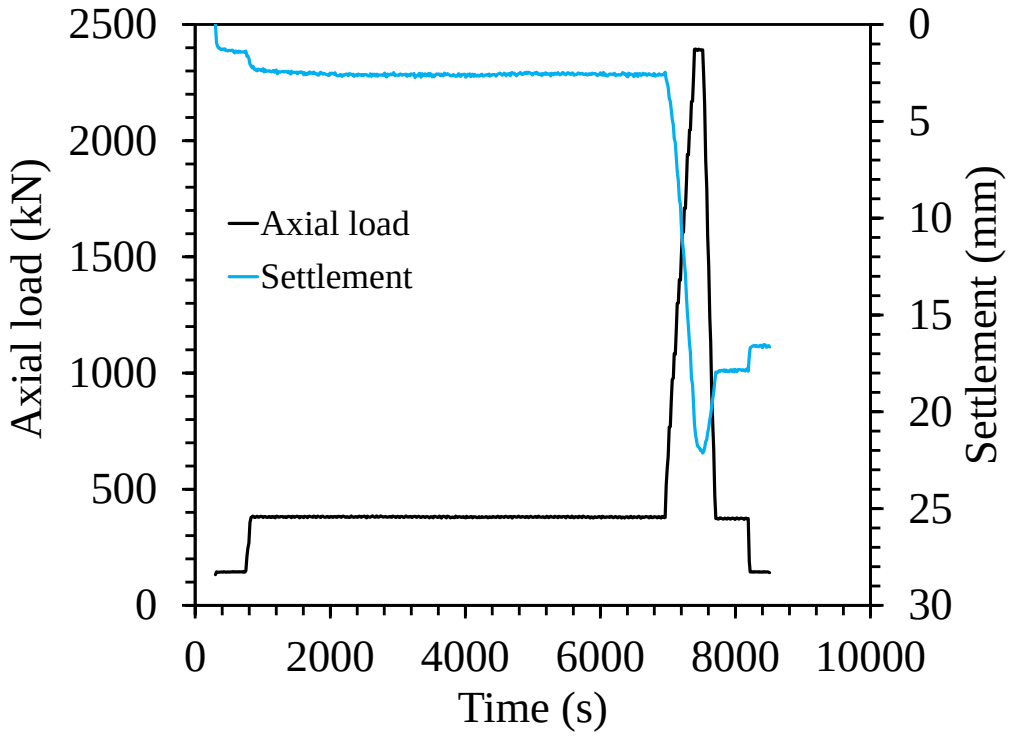

Figure 6.2.2-7 Prototype foundation settlement and associated applied axial load for the heated (ΔT = 7 °C) loading test on the semi-floating foundation in Nevada sand.

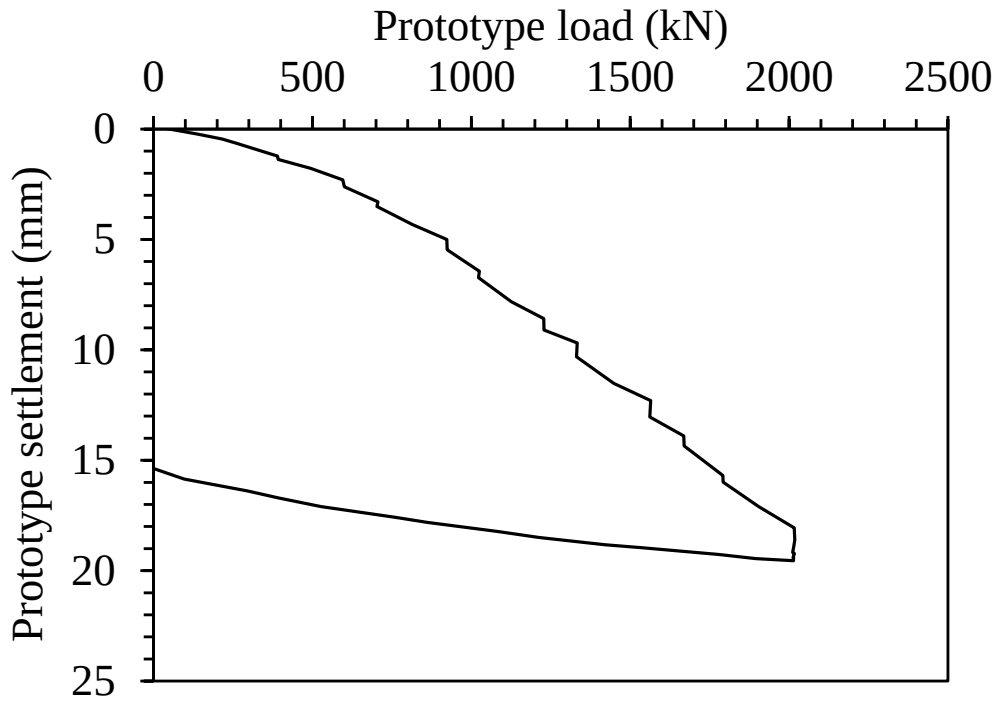

Figure 6.2.2-8 Prototype load settlement curve for the heated (ΔT = 7 °C) loading test on the semi-floating foundation in Nevada sand.

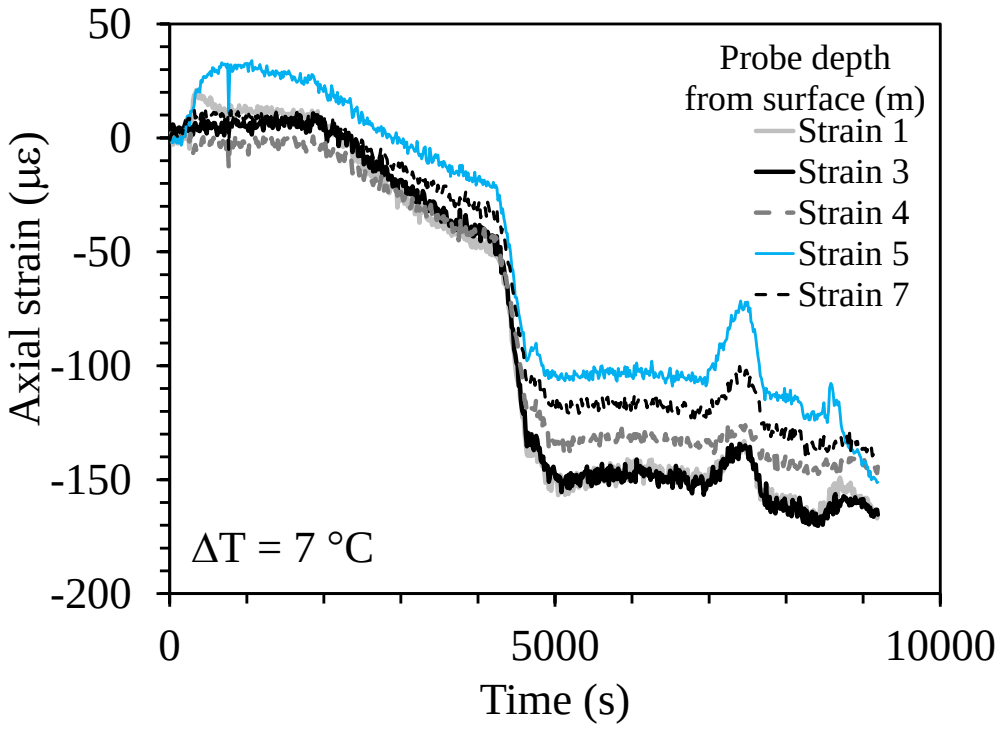

Figure 6.2.2-9 Axial strain time series for the heated (ΔT = 7 °C) loading test on the semi-floating foundation in Nevada sand.

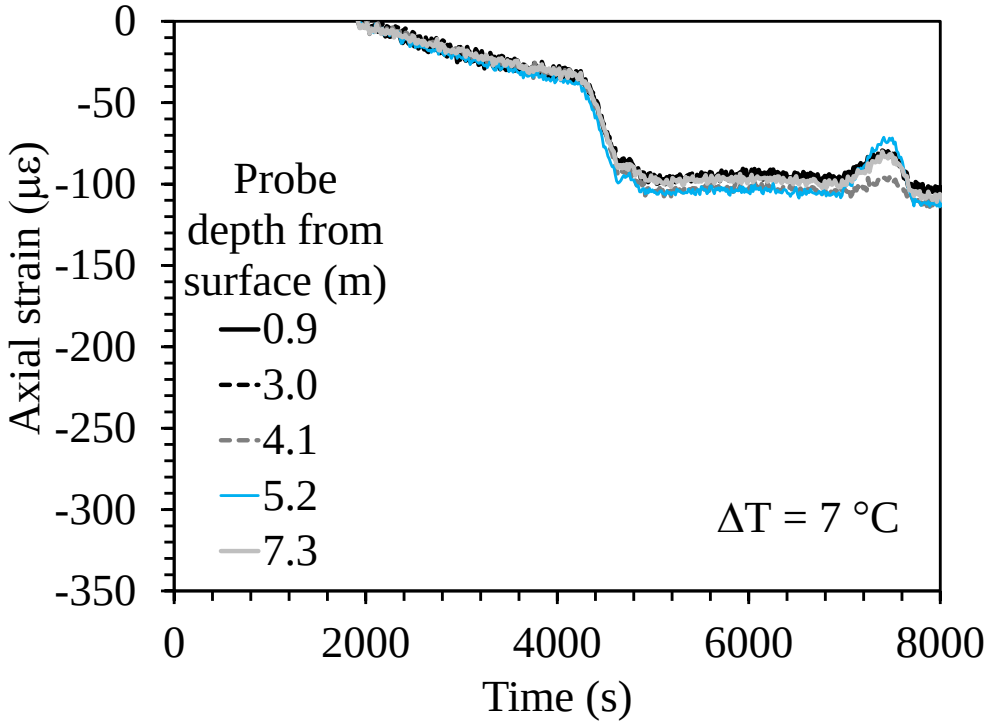

Figure 6.2.2-10 Axial strain during heating for the heated (ΔT = 7 °C) loading test on the semi-floating foundation in Nevada sand.

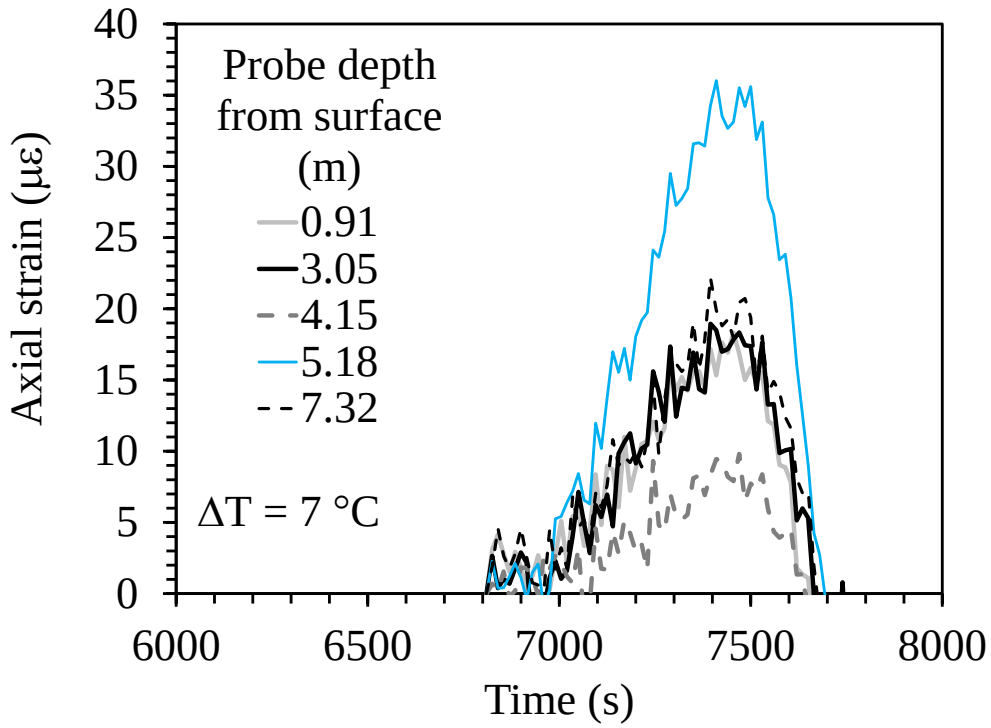

Figure 6.2.2-11 Axial strain during loading for the heated (ΔT = 7 °C) loading test on the semi-floating foundation in Nevada sand.

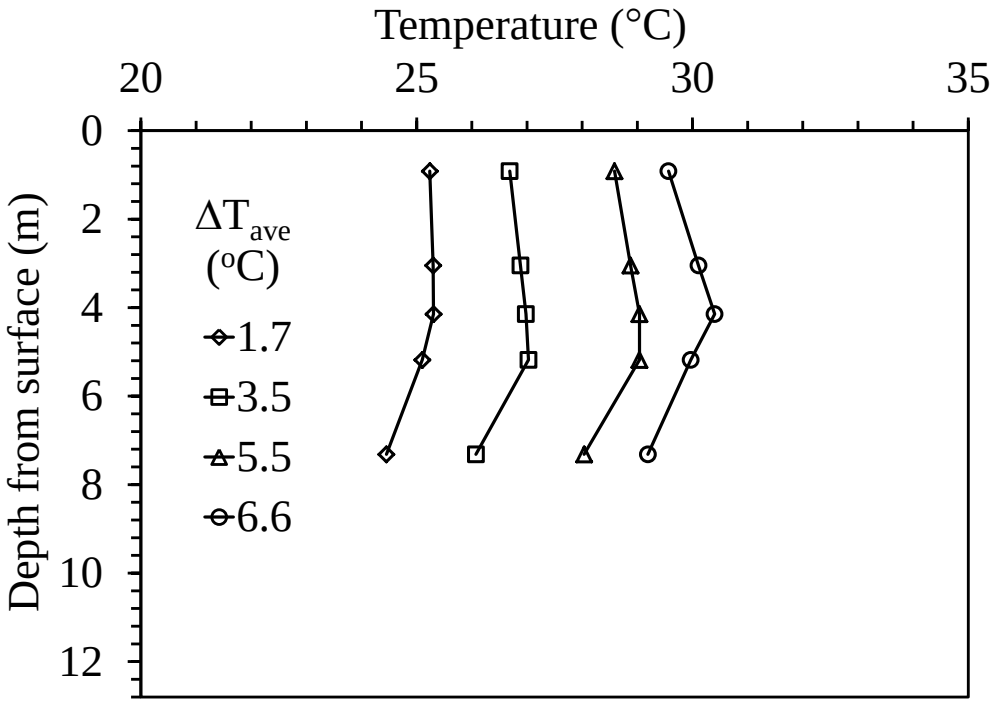

Figure 6.2.2-12 Temperature profiles for the heated (ΔT = 7 °C) loading test on the semi-floating foundation in Nevada sand.

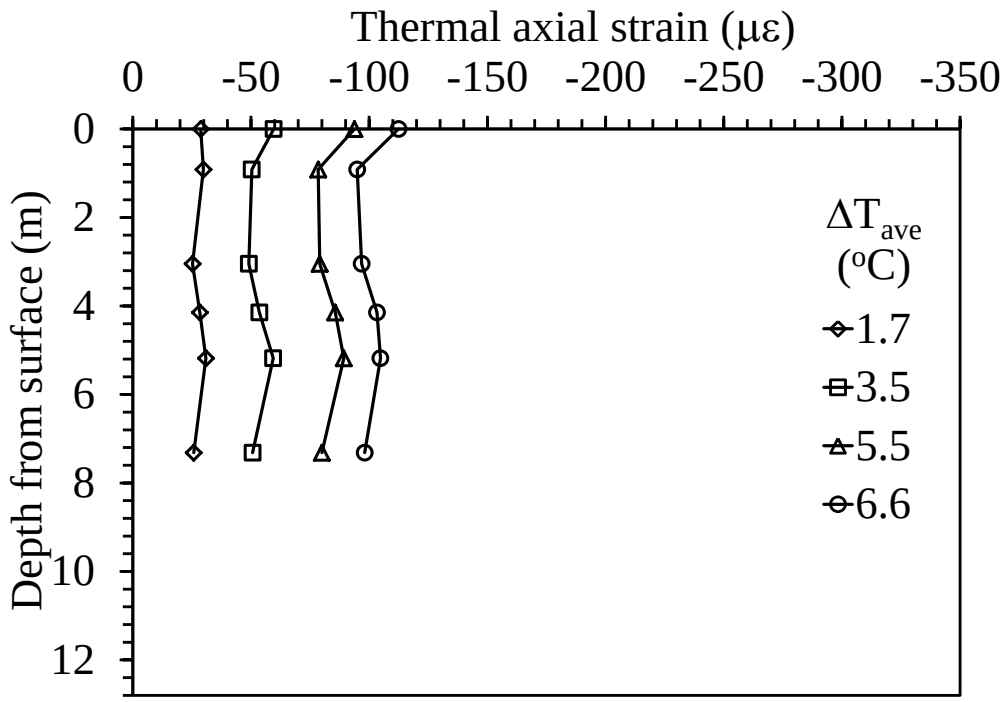

Figure 6.2.2-13 Prototype strain profile during heating for the heated (ΔT = 7 °C) loading test on the semi-floating foundation in Nevada sand.

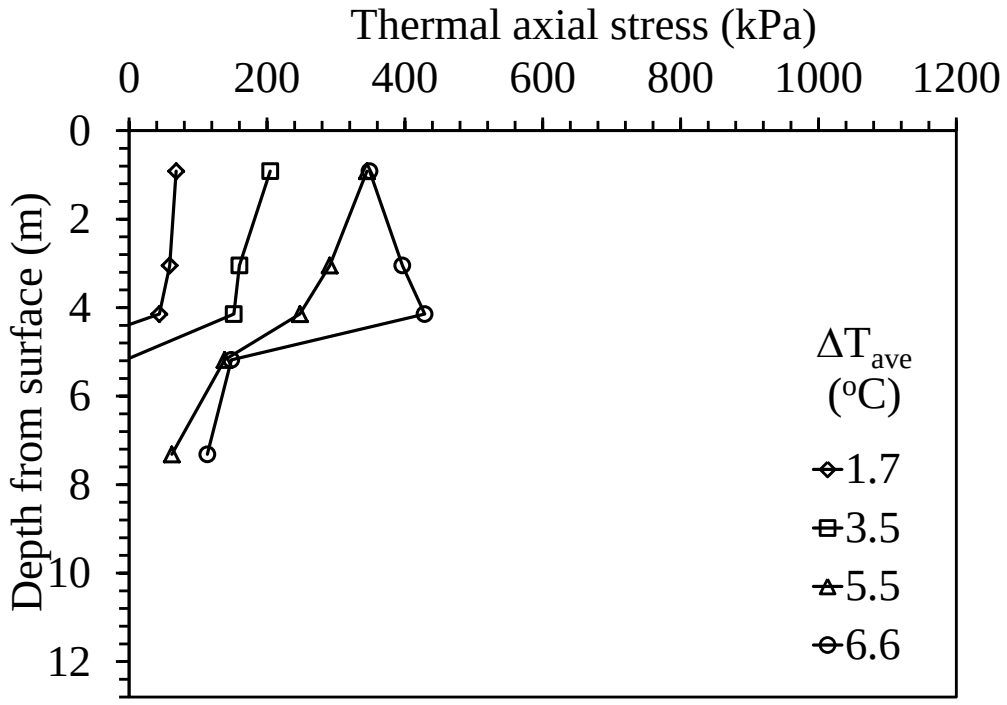

Figure 6.2.2-14 Prototype thermal stress profile for the heated (ΔT = 7 °C) loading test on the semi-floating foundation in Nevada sand.

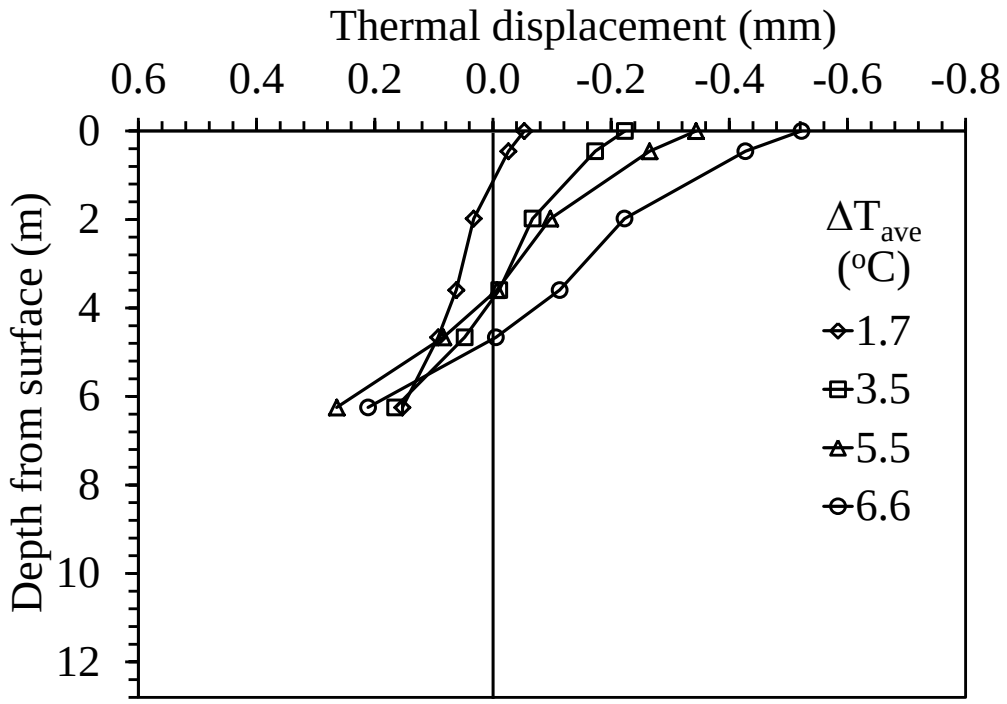

Figure 6.2.2-15 Thermal axial displacement profile for the heated (ΔT = 7 °C) loading test on the semi-floating foundation in Nevada sand.

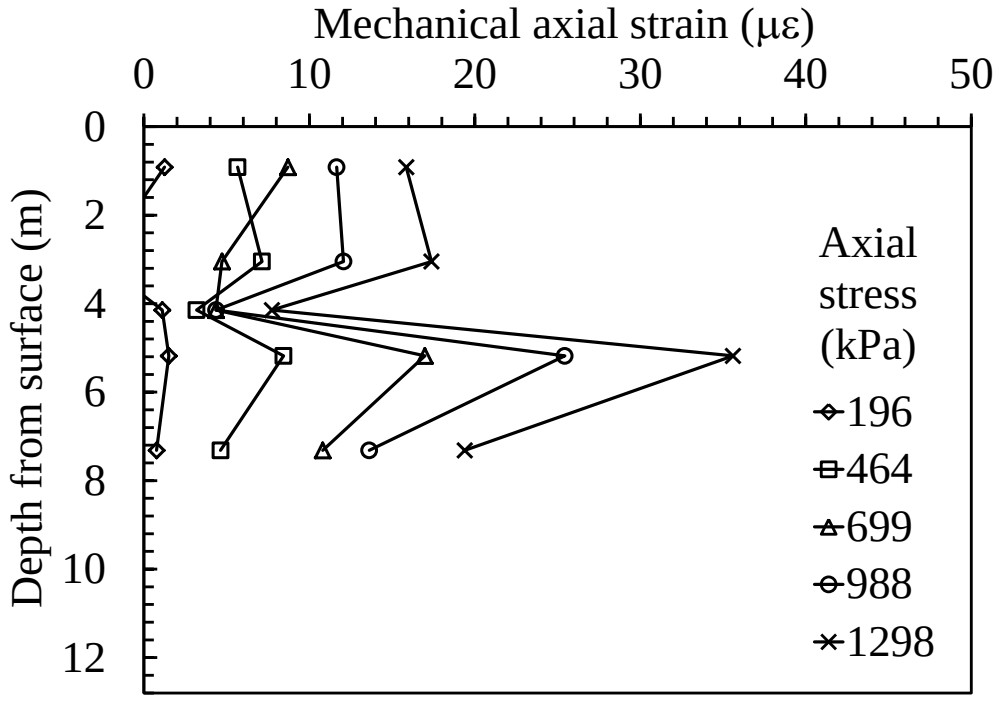

Figure 6.2.2-16 Prototype mechanical strain profile for the heated (ΔT = 7 °C) loading test on the semi-floating foundation in Nevada sand.

6.2.3 Results from Test S-NS-ML-11

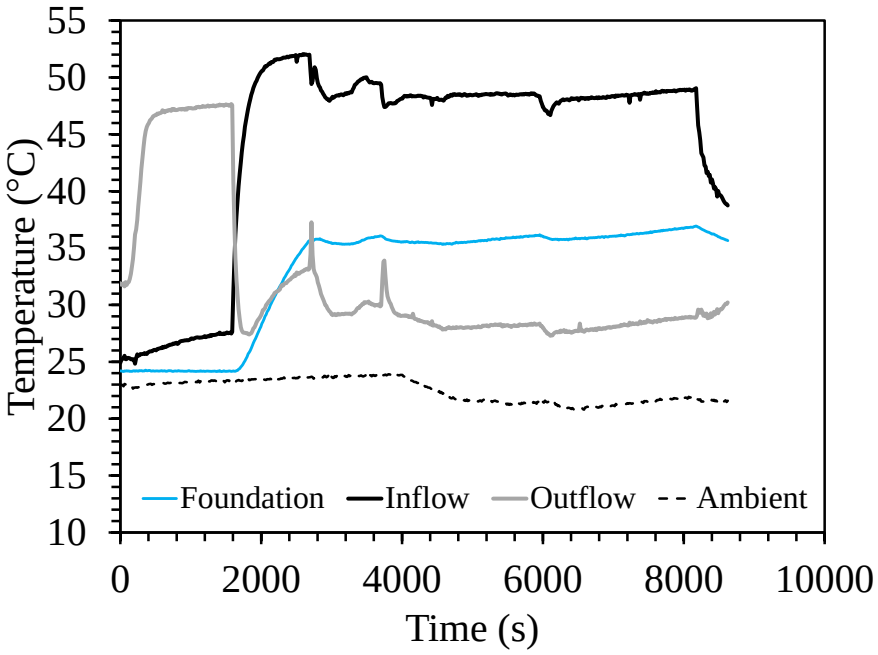

Figure 6.2.3-1 Temperatures during testing for the heated (ΔT = 11 °C) loading test on the semi-floating foundation in Nevada sand.

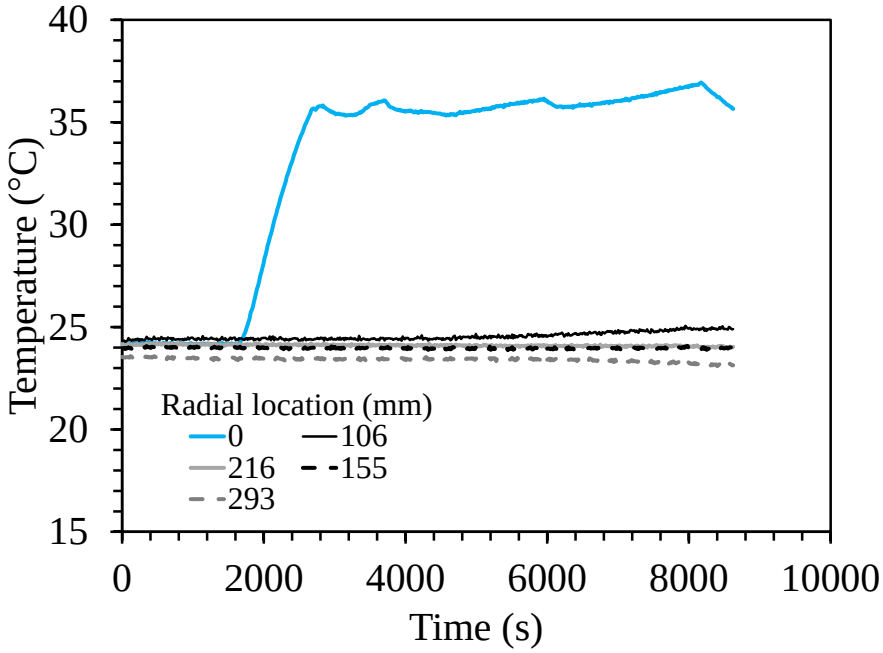

Figure 6.2.3-2 Average temperatures of foundation and four thermal probes for the heated (ΔT = 11 °C) loading test on the semi-floating foundation in Nevada sand.

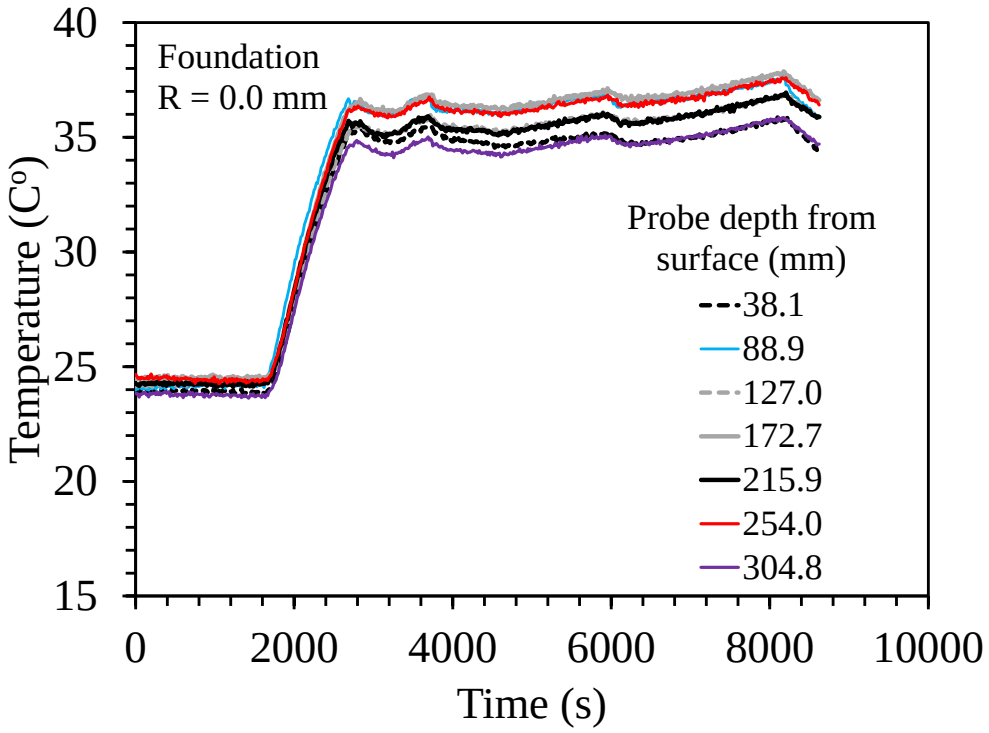

Figure 6.2.3-3 Foundation temperatures for the heated (ΔT = 11 °C) loading test on the semi-floating foundation in Nevada sand.

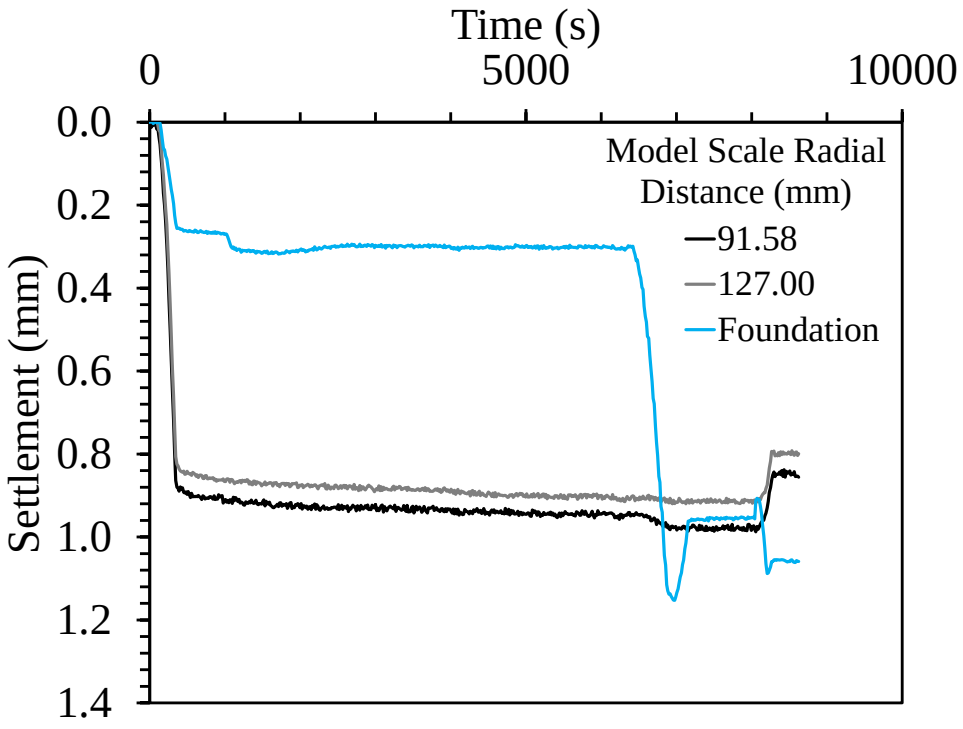

Figure 6.2.3-4 Model scale settlements with spin up for the heated (ΔT = 11 °C) loading test on the semi-floating foundation in Nevada sand.

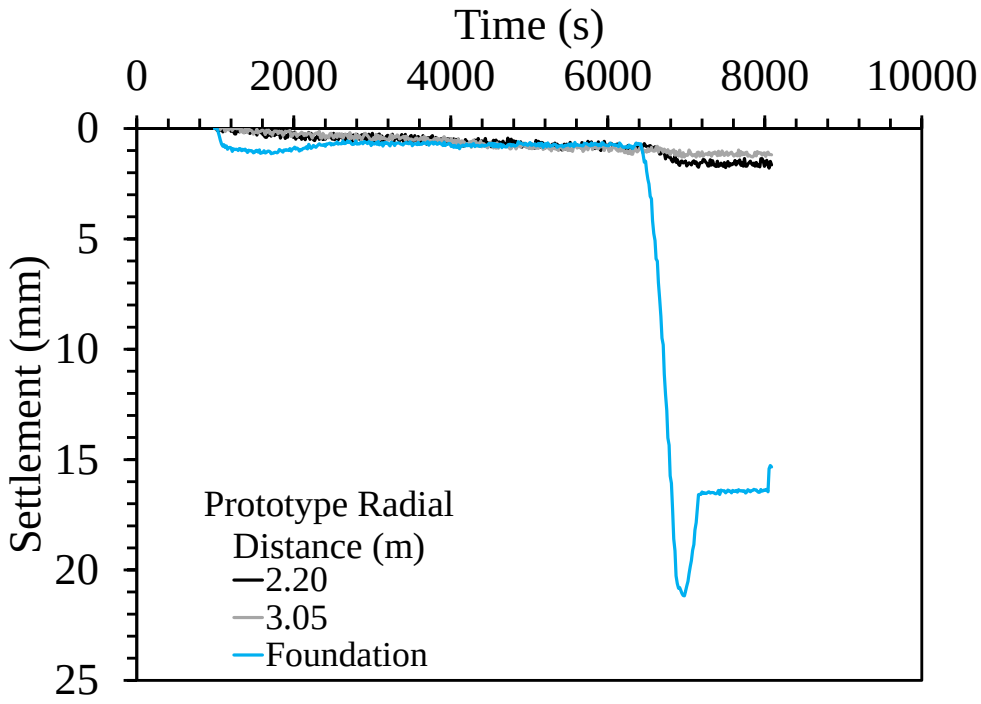

Figure 6.2.3-5 Prototype settlements after spin up for the heated (ΔT = 11 °C) loading test on the semi-floating foundation in Nevada sand.

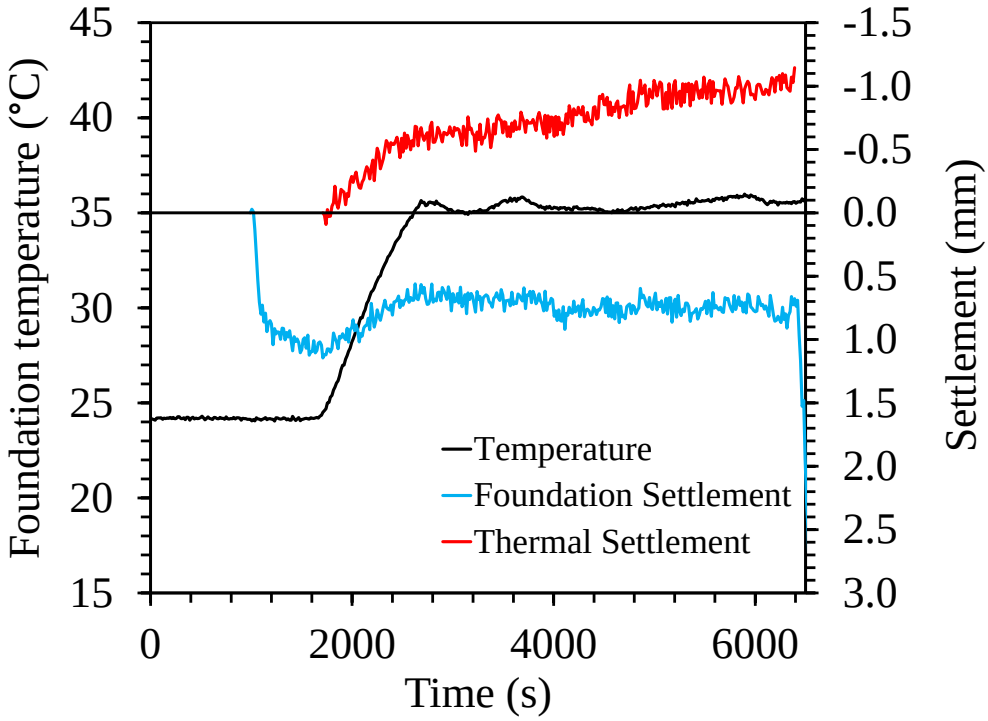

Figure 6.2.3-6 Foundation temperature, overall foundation settlement, and thermal settlement for the heated (ΔT = 11 °C) loading test on the semi-floating foundation in Nevada sand.

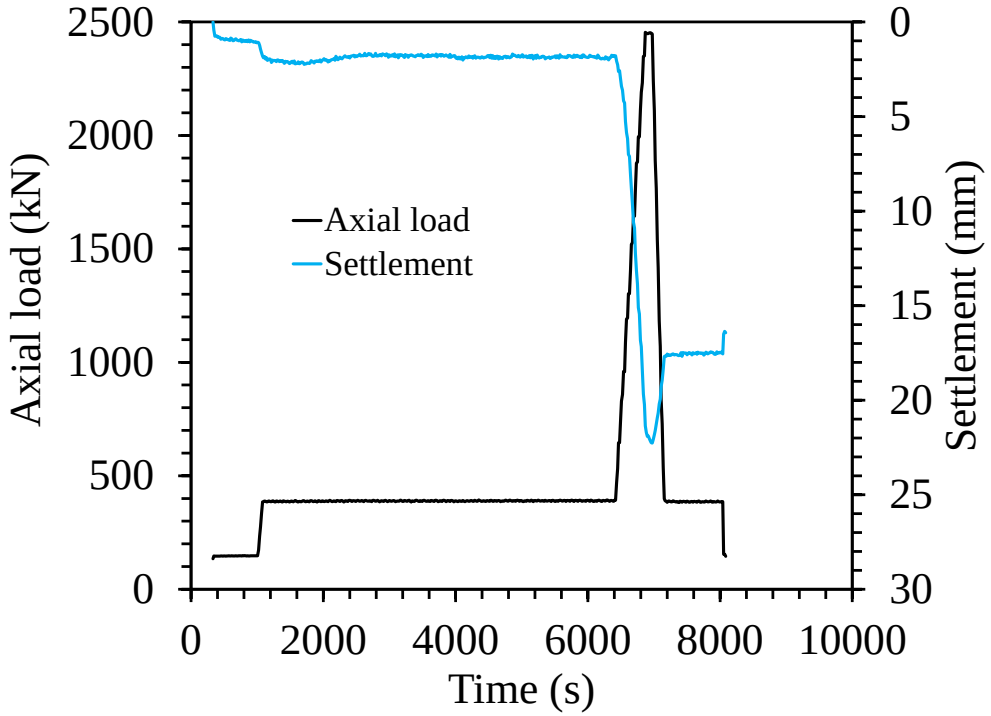

Figure 6.2.3-7 Prototype foundation settlement and associated applied axial load for the heated (ΔT = 11 °C) loading test on the semi-floating foundation in Nevada sand.

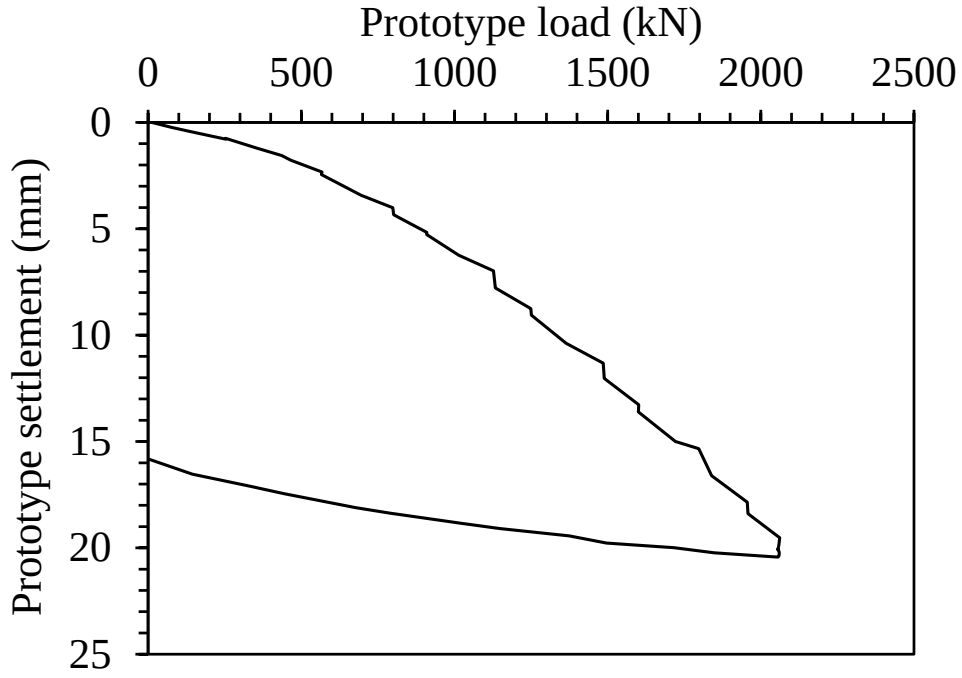

Figure 6.2.3-8 Prototype load settlement curve for the heated (ΔT = 11 °C) loading test on the semi-floating foundation in Nevada sand.

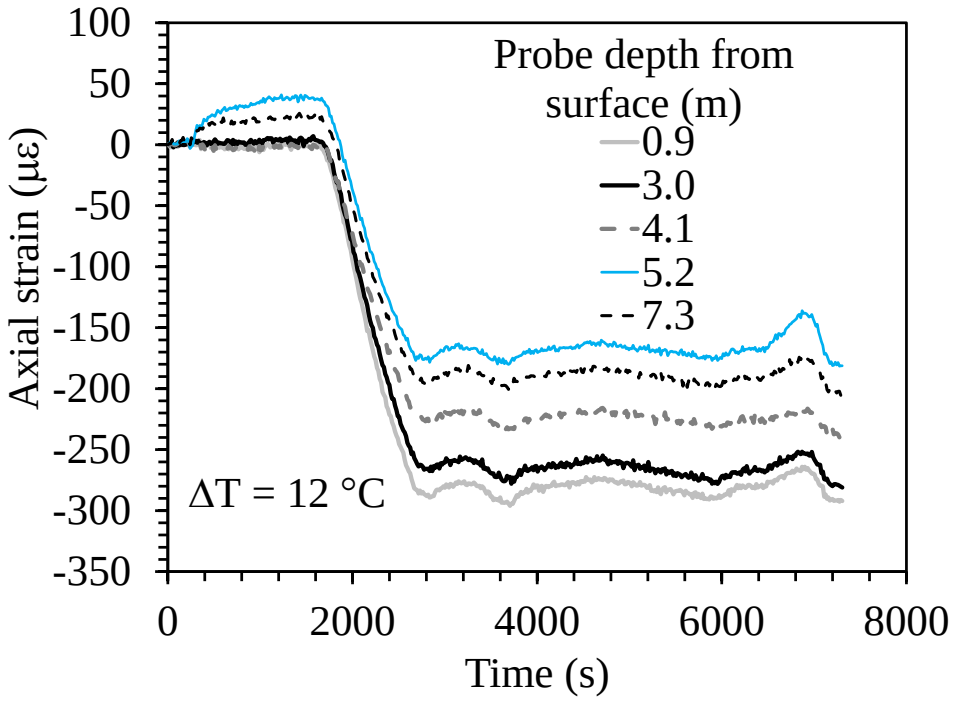

Figure 6.2.3-9 Axial strain time series for the heated (ΔT = 11 °C) loading test on the semi-floating foundation in Nevada sand.

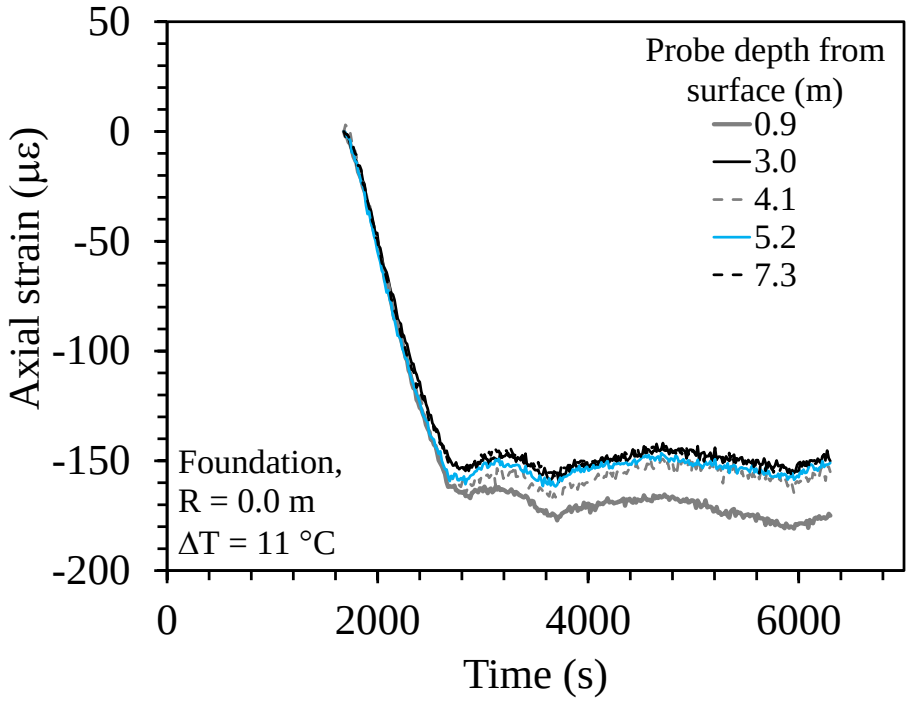

Figure 6.2.3-10 Axial strain during heating for the heated (ΔT = 11 °C) loading test on the semi-floating foundation in Nevada sand.

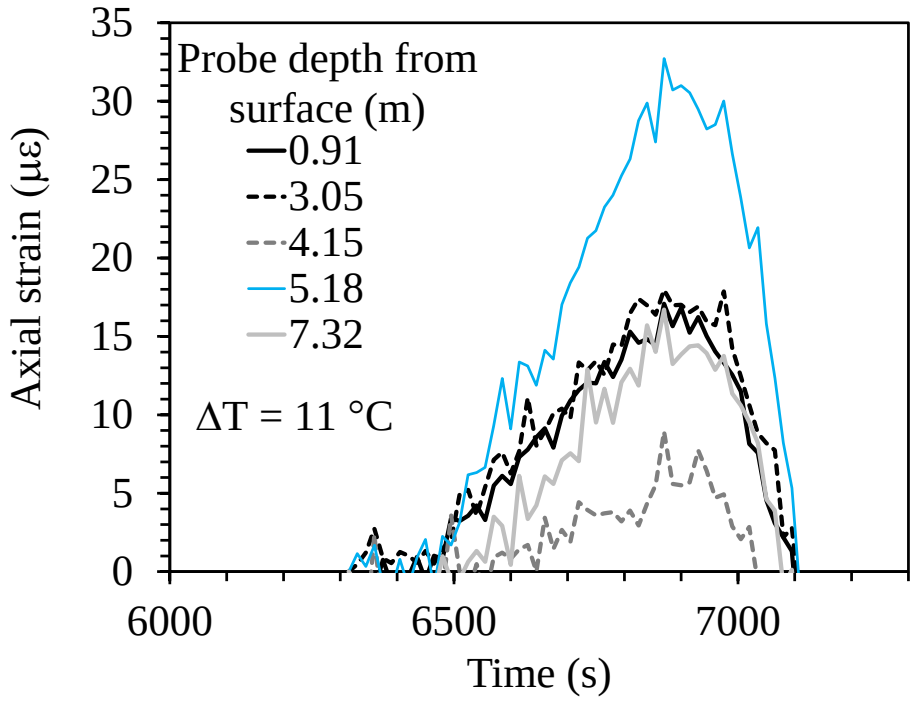

Figure 6.2.3-11 Axial strains during load test for the heated (ΔT = 11 °C) loading test on the semi-floating foundation in Nevada sand.

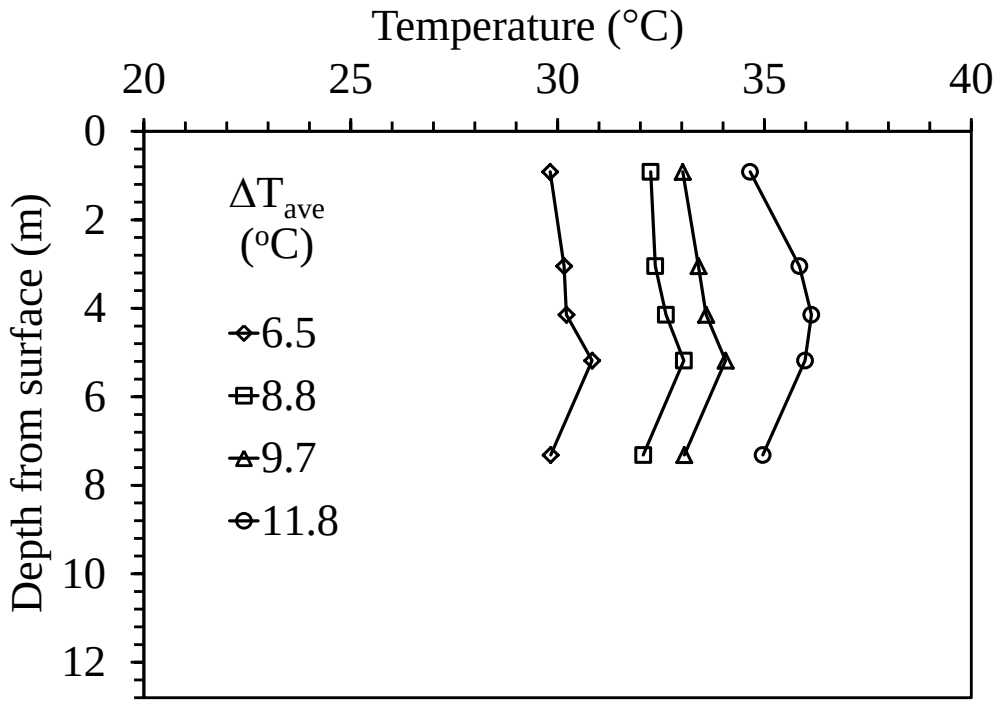

Figure 6.2.3-12 Temperature profiles for the heated (ΔT = 11 °C) loading test on the semi-floating foundation in Nevada sand.

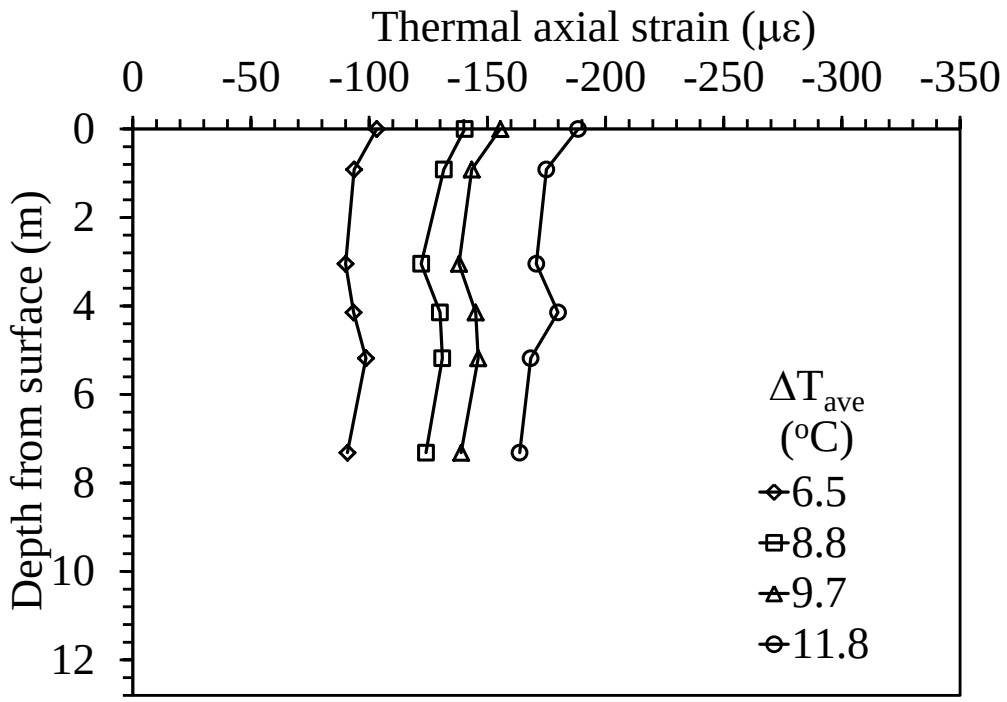

Figure 6.2.3-13 Prototype strain profile during heating for the heated (ΔT = 11 °C) loading test on the semi-floating foundation in Nevada sand.

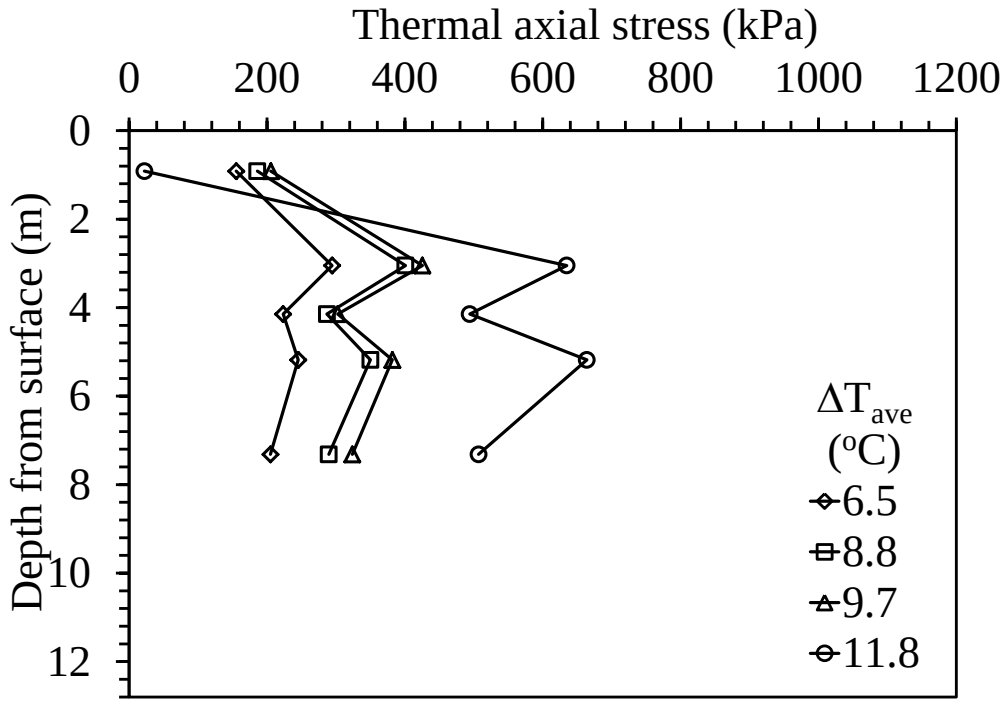

Figure 6.2.3-14 Prototype thermal stress profile for the heated (ΔT = 11 °C) loading test on the semi-floating foundation in Nevada sand.

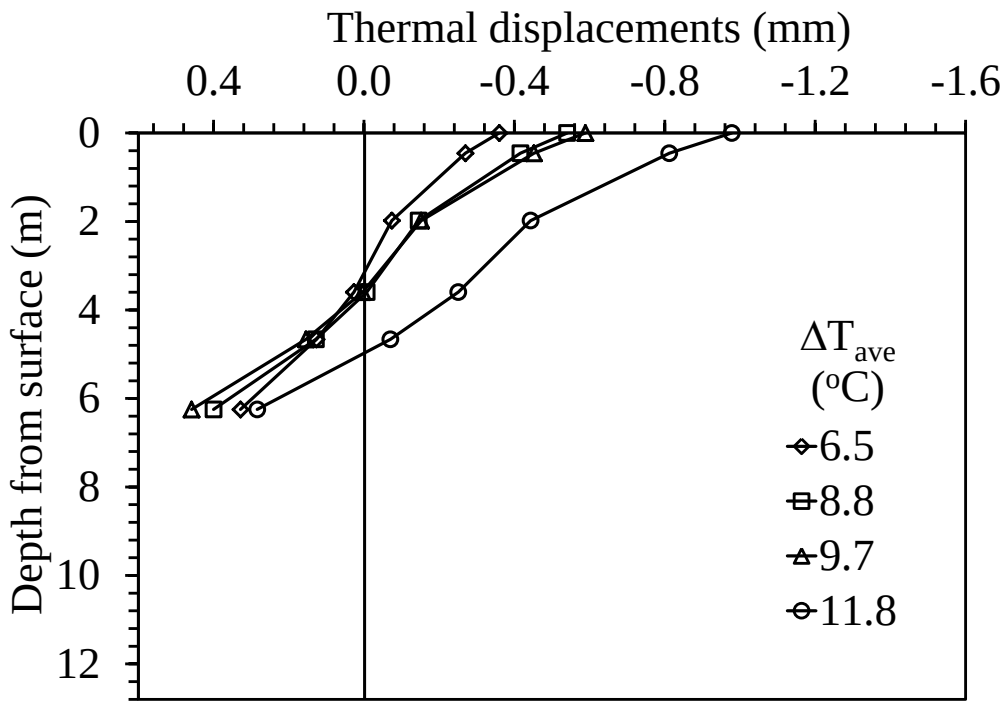

Figure 6.2.3-15 Thermal axial displacement profiles for the heated (ΔT = 11 °C) loading test on the semi-floating foundation in Nevada sand.

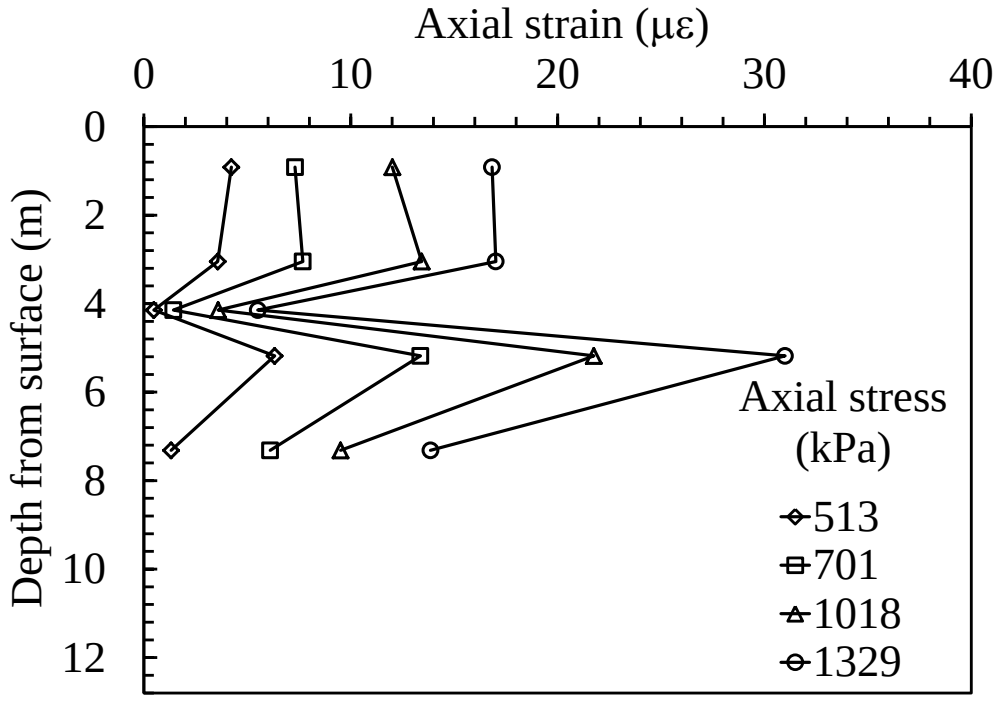

Figure 6.2.3-16 Prototype mechanical strain profile for the heated (ΔT = 11 °C) loading test on the semi-floating foundation in Nevada sand.

6.2.4 Results from Test S-NS-ML-18

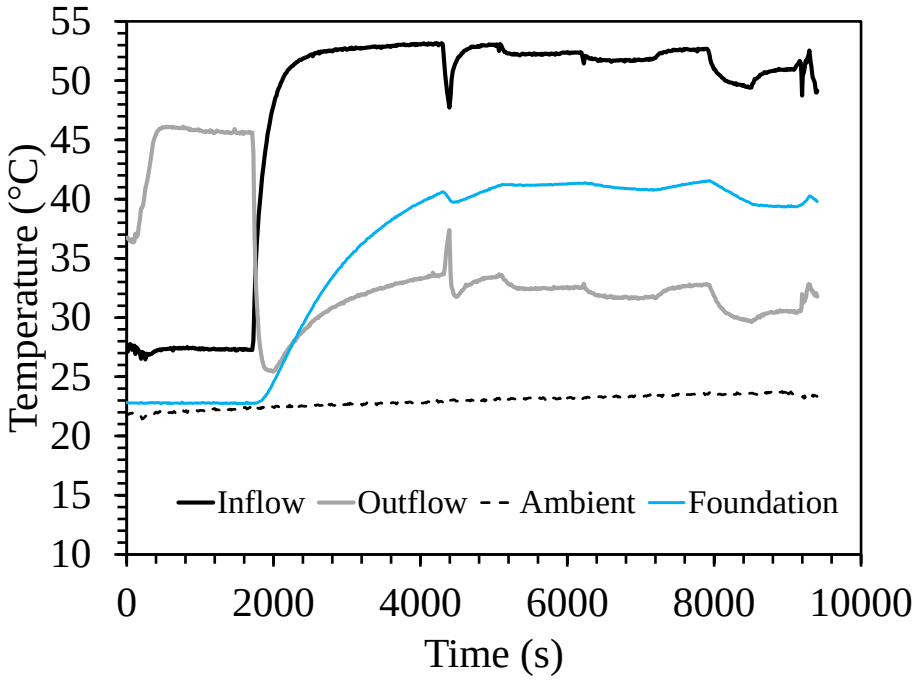

Figure 6.2.4-1 Temperatures during testing for the heated (ΔT = 18 °C) loading test on the semi-floating foundation in Nevada sand.

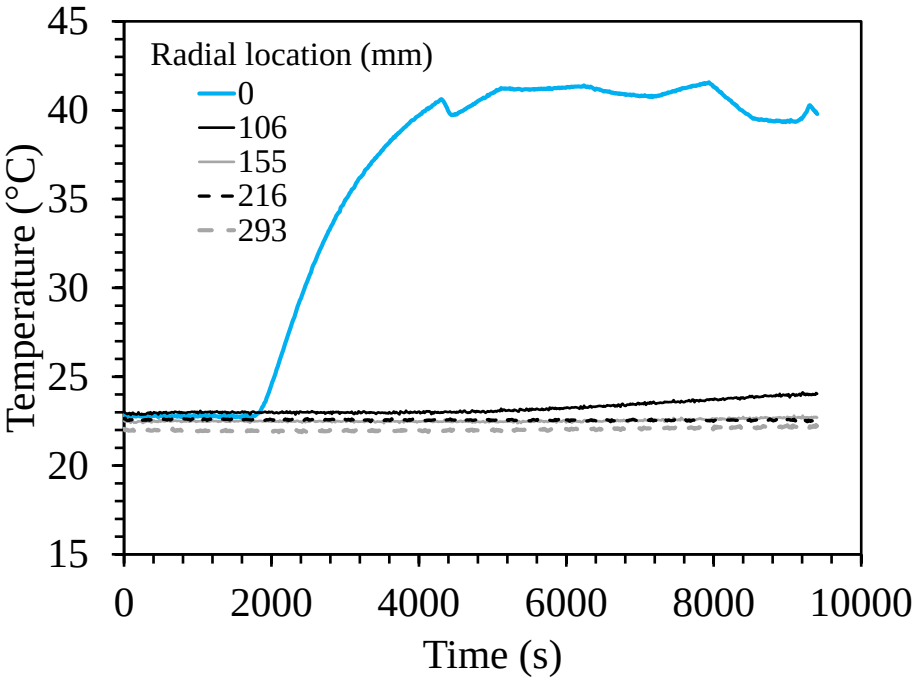

Figure 6.2.4-2 Average temperatures of foundation and four thermal probes for the heated (ΔT = 18 °C) loading test on the semi-floating foundation in Nevada sand.

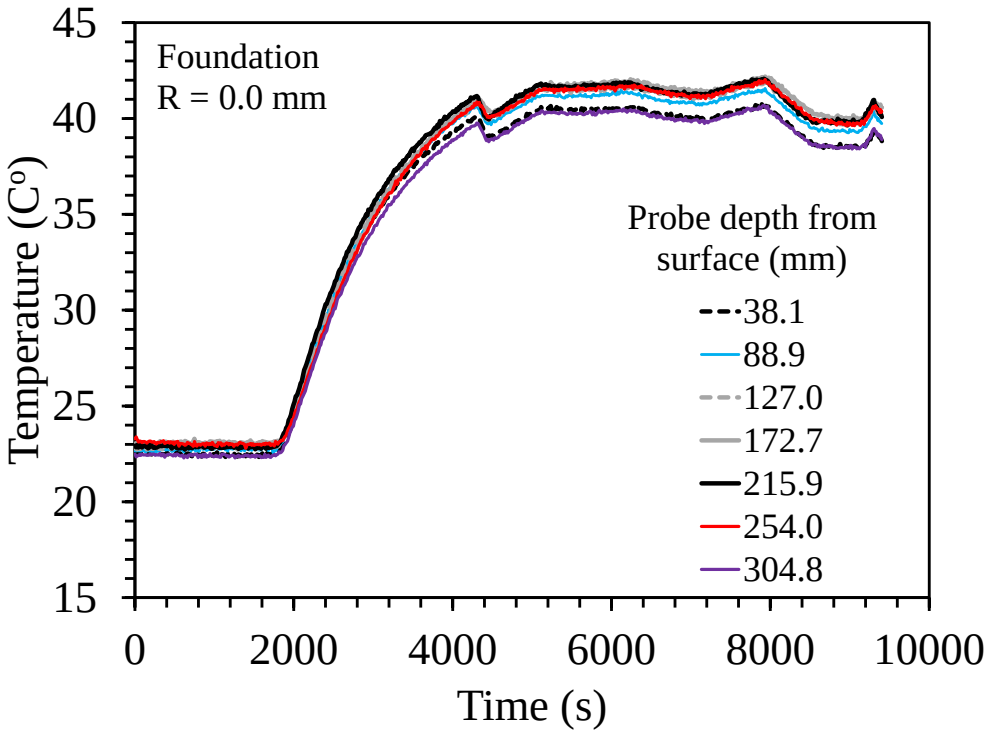

Figure 6.2.4-3 Foundation temperatures for the heated (ΔT = 18 °C) loading test on the semi-floating foundation in Nevada sand.

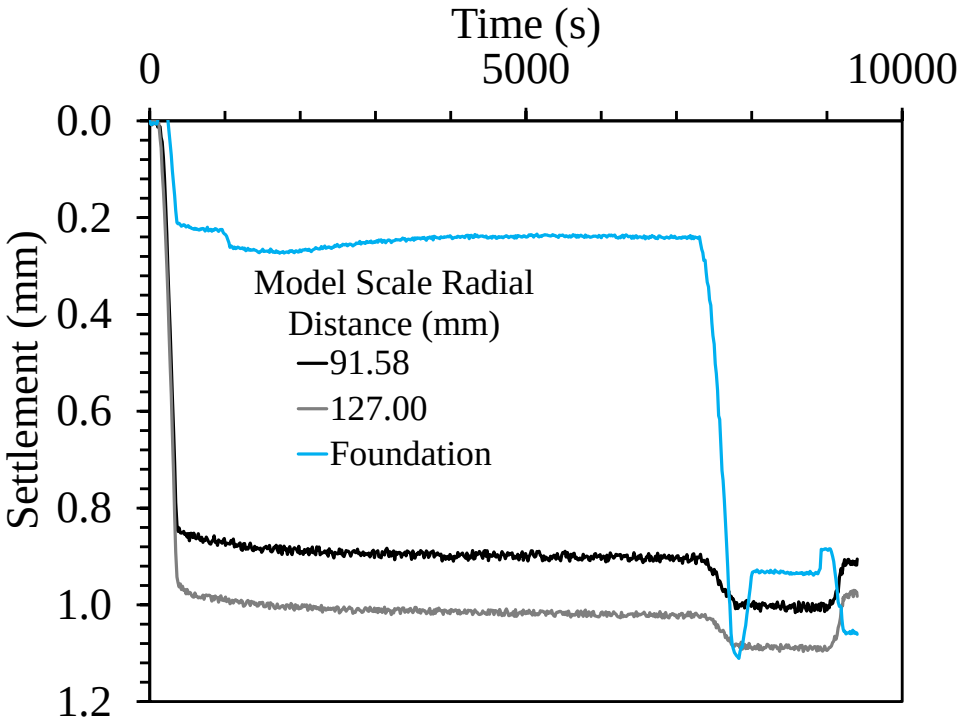

Figure 6.2.4-4 Model scale settlements with spin up for the heated (ΔT = 18 °C) loading test on the semi-floating foundation in Nevada sand.

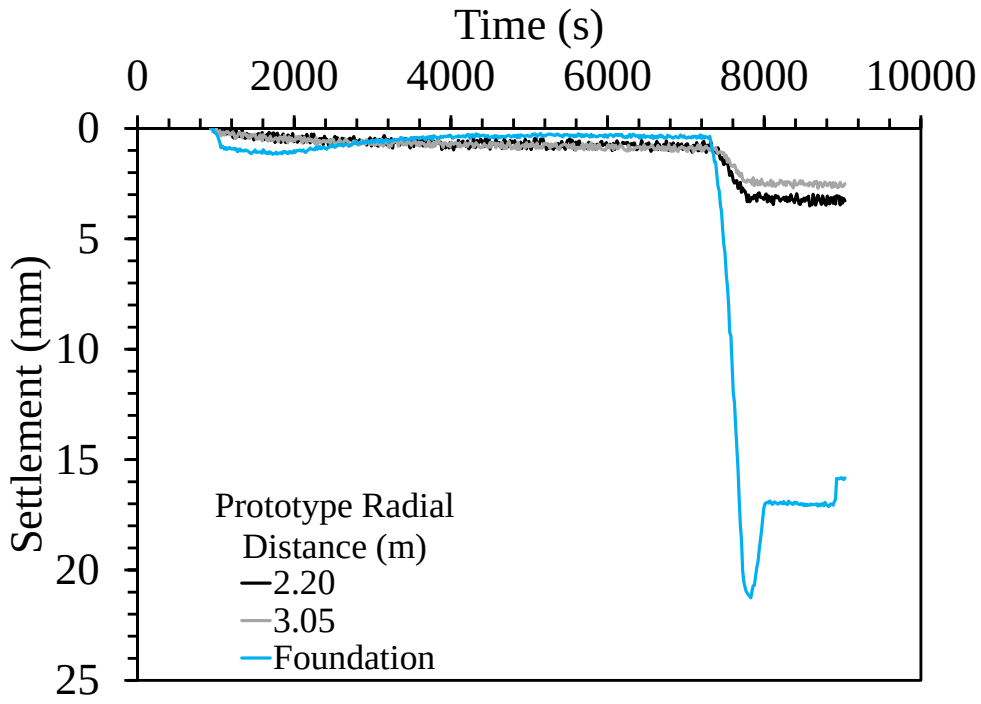

Figure 6.2.4-5 Prototype settlements after spin up for the heated (ΔT = 18 °C) loading test on the semi-floating foundation in Nevada sand.

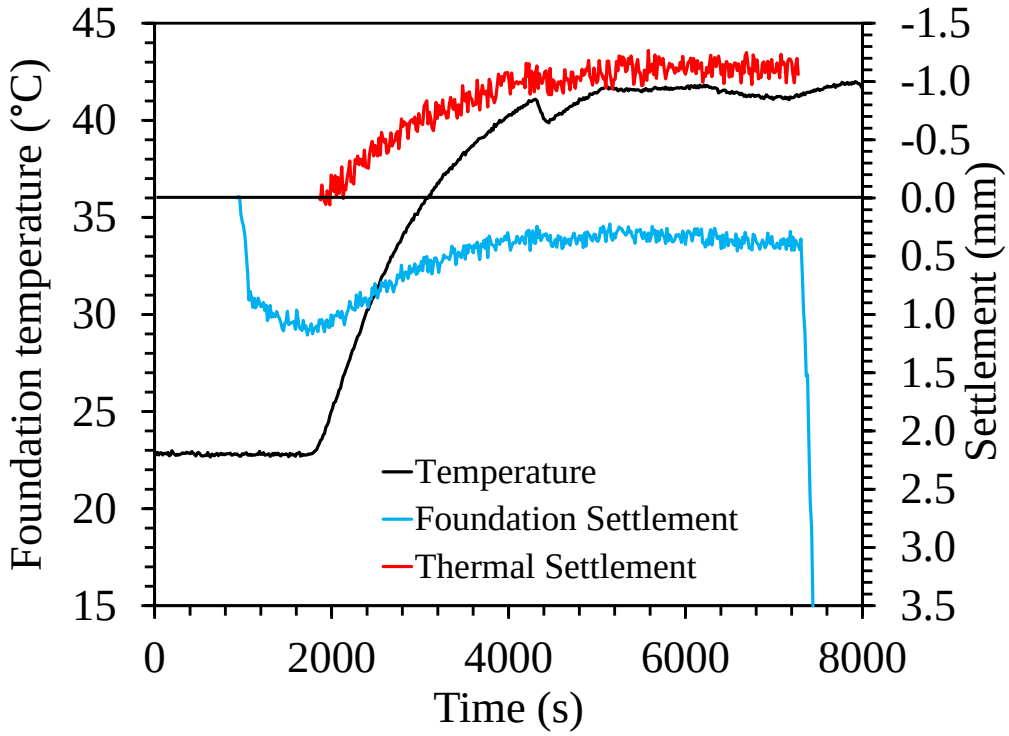

Figure 6.2.4-6 Foundation temperature, overall foundation settlement, and thermal settlement for the heated (ΔT = 18 °C) loading test on the semi-floating foundation in Nevada sand.

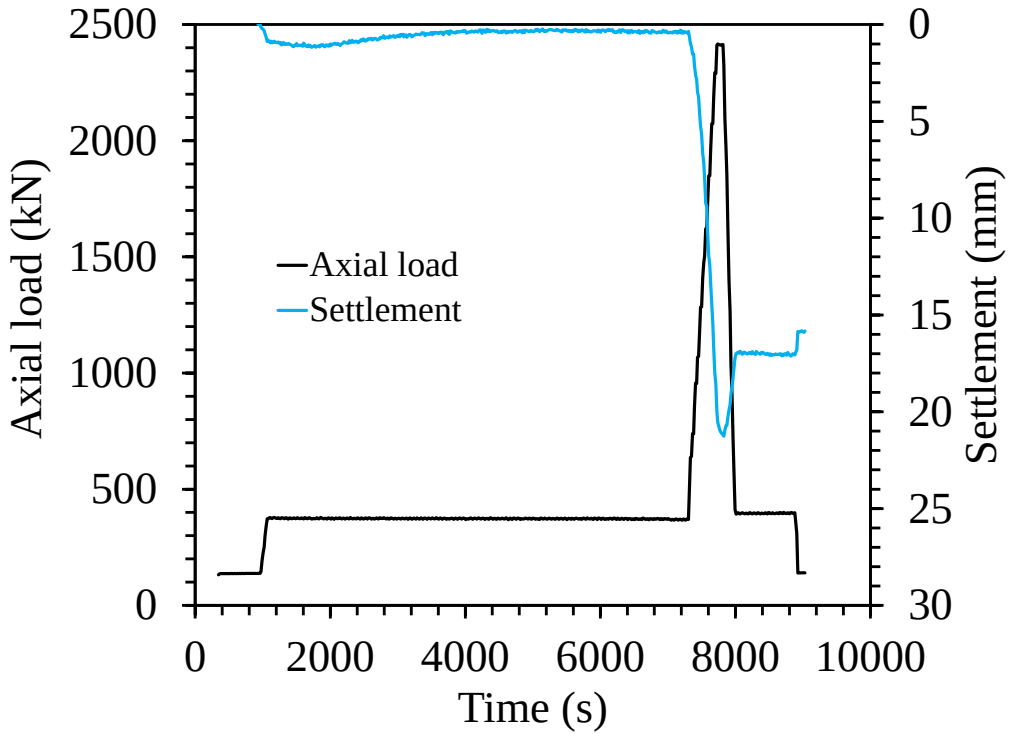

Figure 6.2.4-7 Prototype foundation settlement and associated applied axial load for the heated (ΔT = 18 °C) loading test on the semi-floating foundation in Nevada sand.

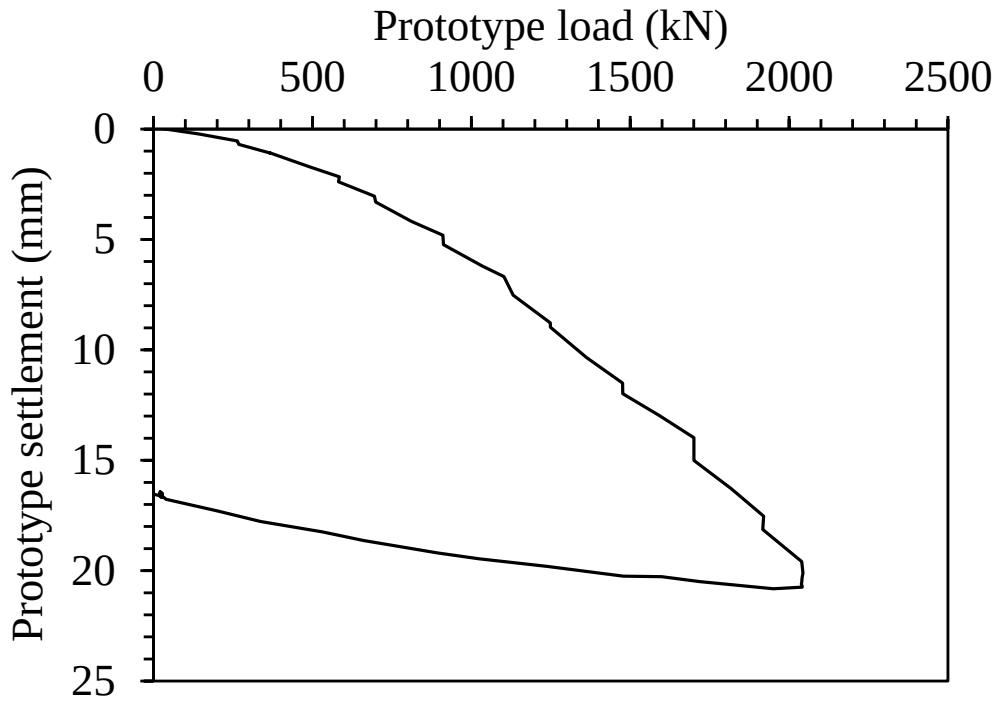

Figure 6.2.4-8 Prototype load settlement curve for the heated (ΔT = 18 °C) loading test on the semi-floating foundation in Nevada sand.

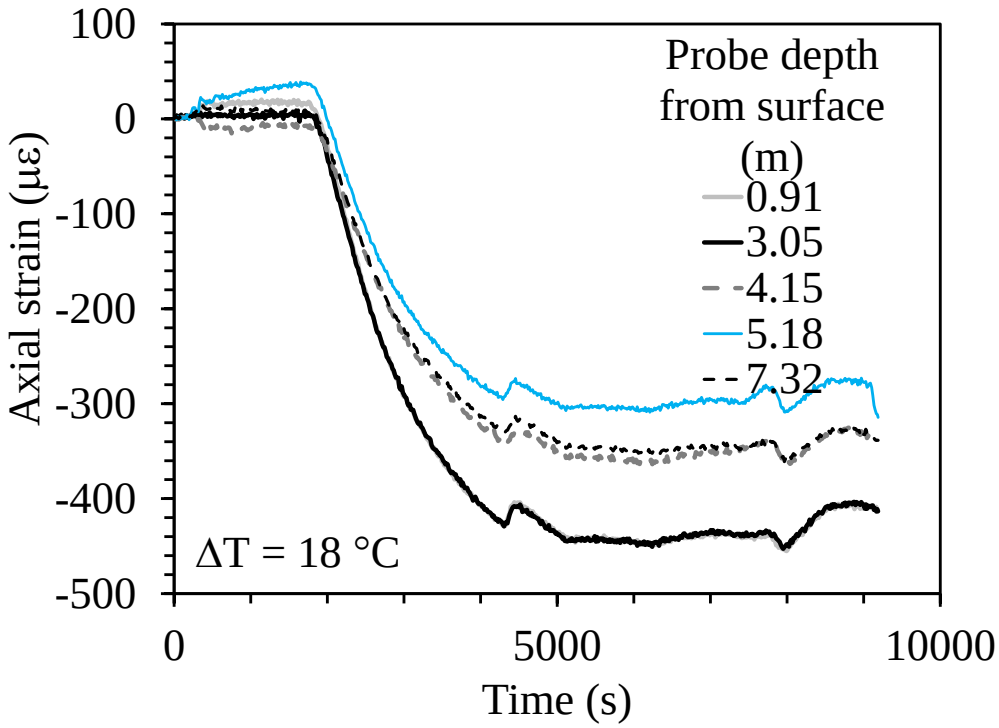

Figure 6.2.4-9 Axial strain time series for the heated (ΔT = 18 °C) loading test on the semi-floating foundation in Nevada sand.

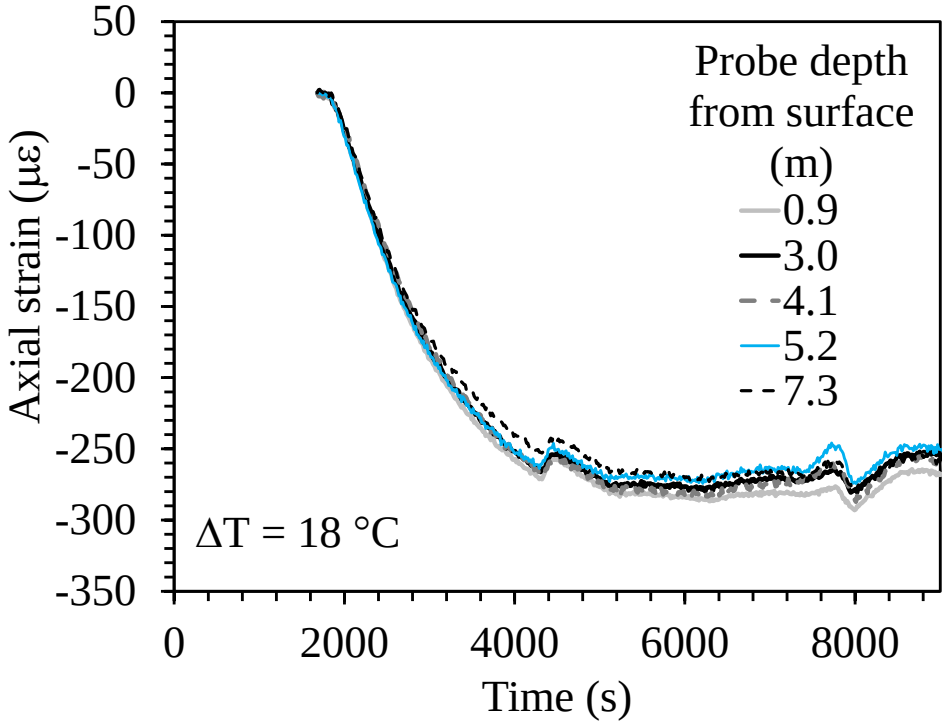

Figure 6.2.4-10 Axial strain during heating for the heated (ΔT = 18 °C) loading test on the semi-floating foundation in Nevada sand.

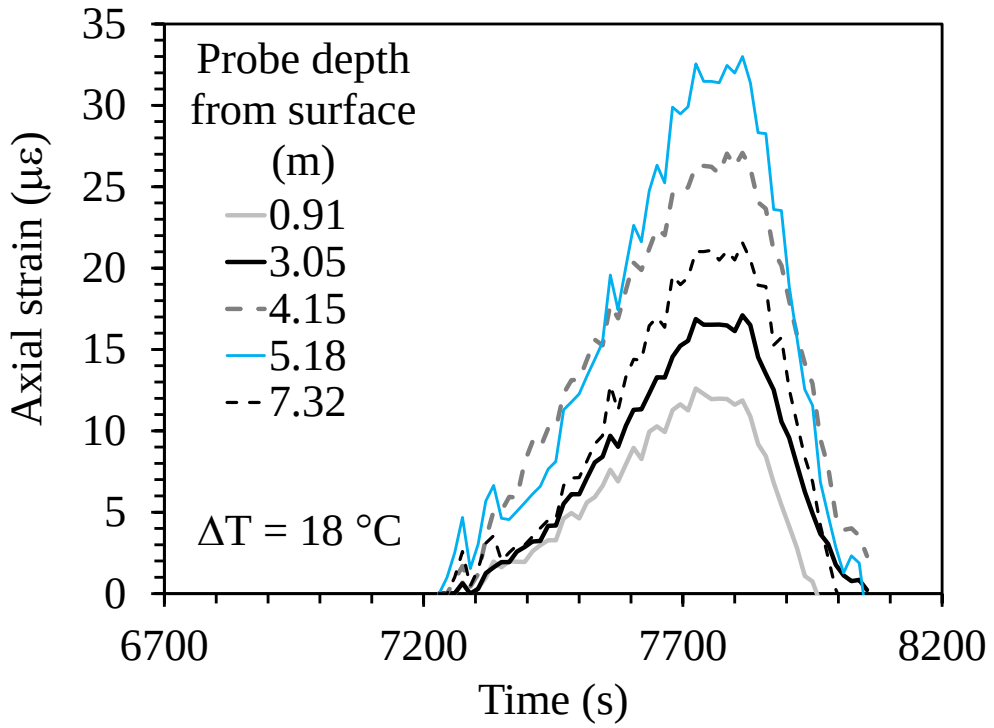

Figure 6.2.4-11 Axial strains during load test for the heated (ΔT = 18 °C) loading test on the semi-floating foundation in Nevada sand.

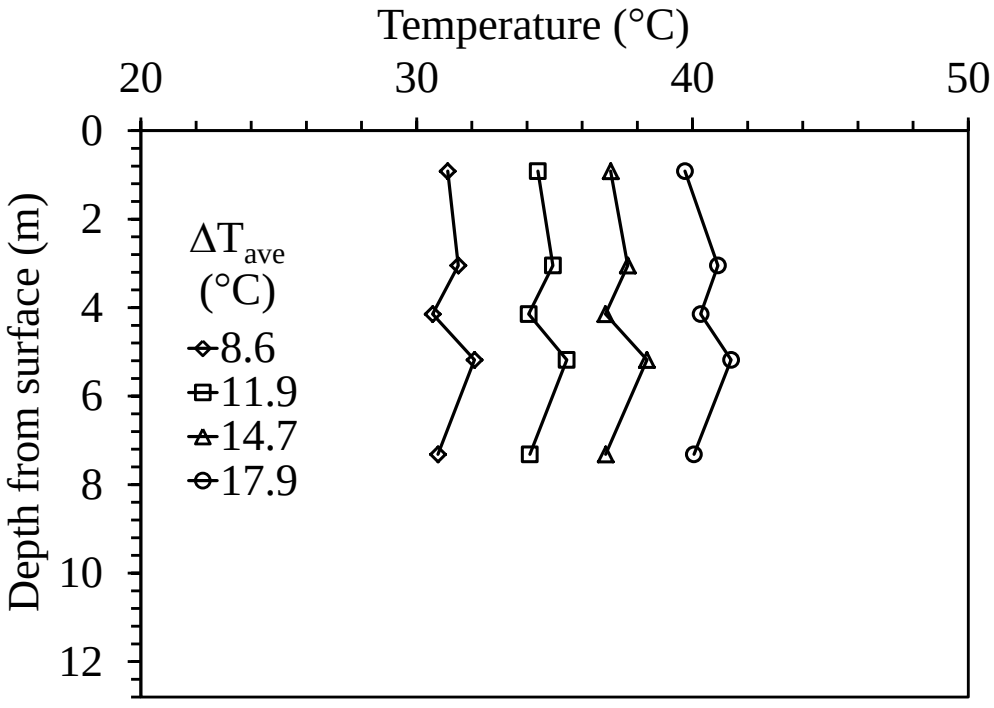

Figure 6.2.4-12 Temperature profiles for the heated (ΔT = 18 °C) loading test on the semi-floating foundation in Nevada sand.

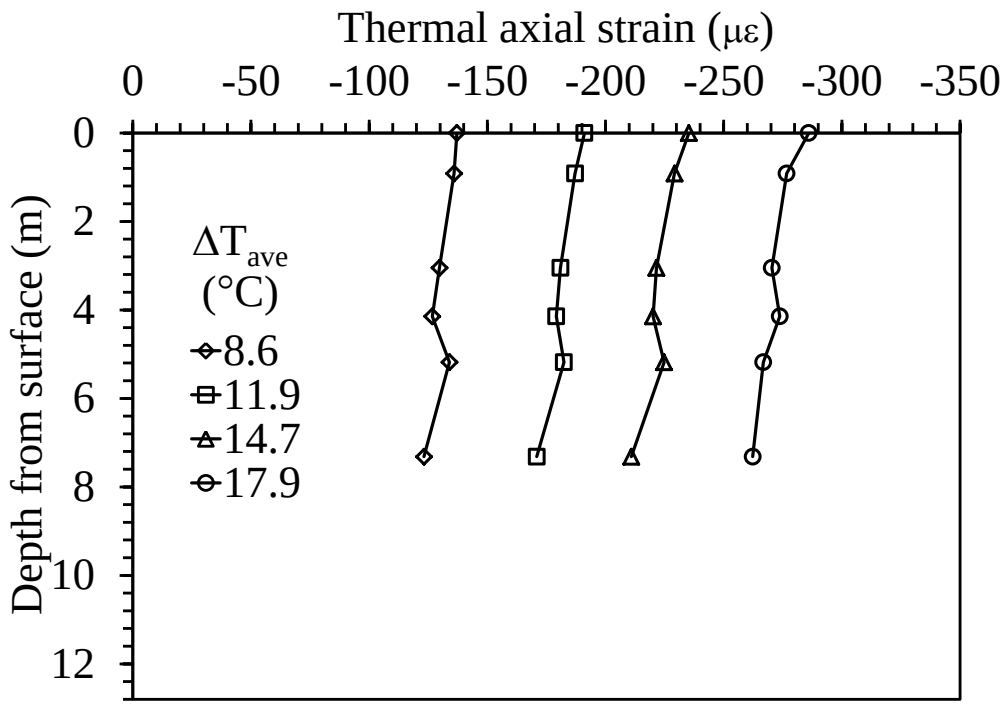

Figure 6.2.4-13 Prototype strain profile during heating for the heated (ΔT = 18 °C) loading test on the semi-floating foundation in Nevada sand.

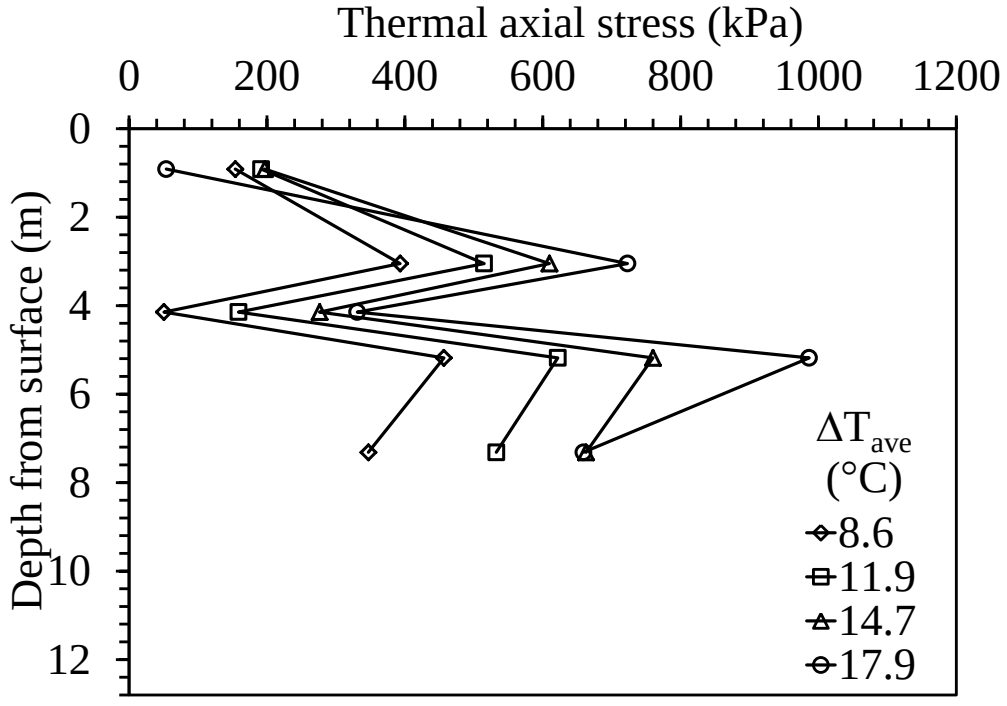

Figure 6.2.4-14 Prototype thermal stress profile for the heated (ΔT = 18 °C) loading test on the semi-floating foundation in Nevada sand.

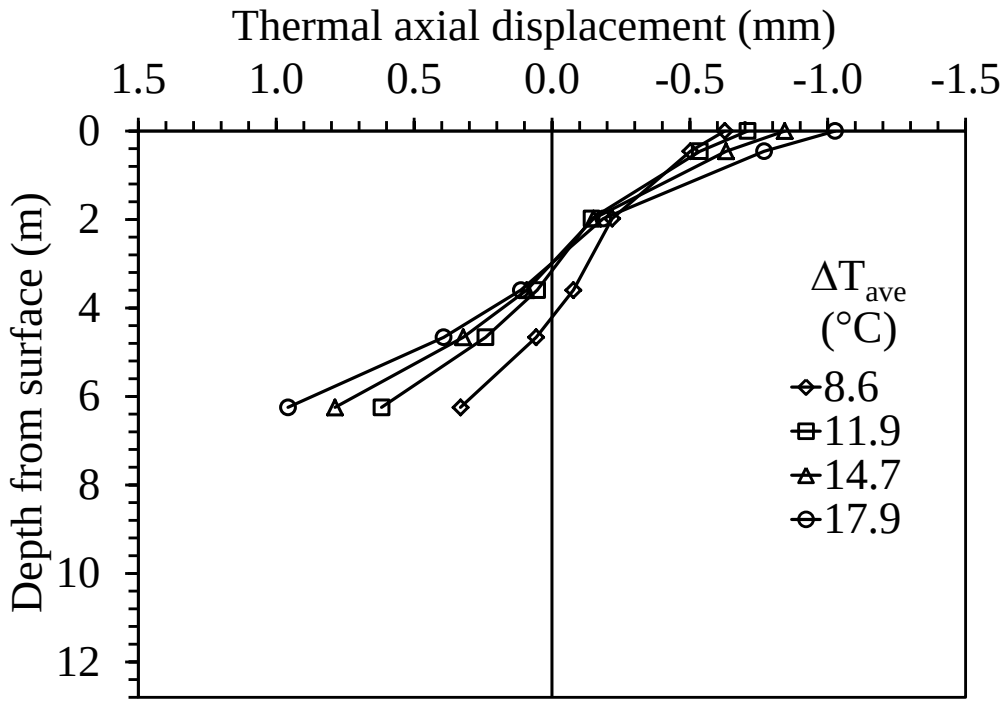

Figure 6.2.4-15 Thermal axial displacement profiles for the heated (ΔT = 18 °C) loading test on the semi-floating foundation in Nevada sand.

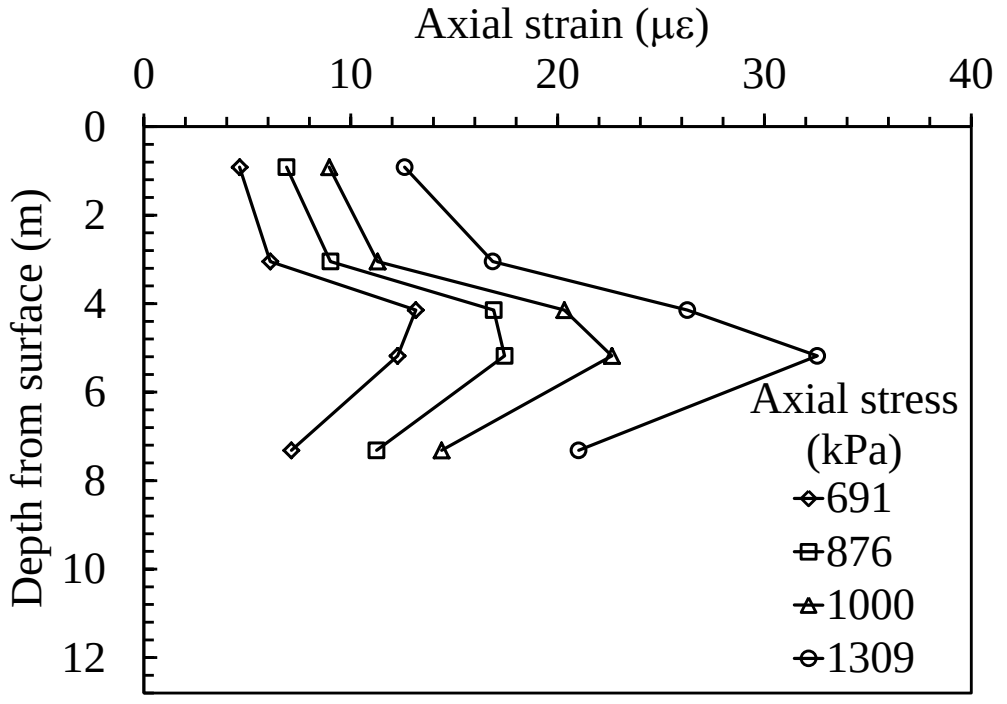

Figure 6.2.4-16 Prototype mechanical strains for the heated (ΔT = 18 °C) loading test on the semi-floating foundation in Nevada sand.

6.3 Semi-Floating Foundation Tests in Bonny Silt

Three tests were performed on the semi-floating foundation in Bonny silt to compare the effects that loading temperature had on the foundation. The final testing temperatures used for the three tests were ambient temperature, 30 °C, and 38 °C. The figures for the Bonny silt tests are displayed in the following sections, and follows the same outline presented in Section 6.1.2. The Bonny silt was observed to settle significantly more than the dry sand tests, although the testing portions of the test are only experiencing creep settlements after the primary settlements occur during and directly after spin up. Heat flow is much more pronounced as expected due to the significantly higher thermal conductivity. An additional plot of temperature is shown in the following sections, with the data from the dielectric sensors. This data provides radial distances and respective temperatures with different radial distances than the thermo probes. The moisture content sensors were able to be placed much closer to the foundation. An addition figure is shown at the end of the two heated tests which displays the foundation temperature of the left axis and the change in gravimetric water content at increasing radial locations on the right axis. The two tests were performed to investigate the role of cyclic heating on the foundation are presented here. The cooled test provides a foundation that was heated, held constant and then cooled before loading as can be seen in the temperature figures.

6.3.1 Results from Test S-BS-ML-0

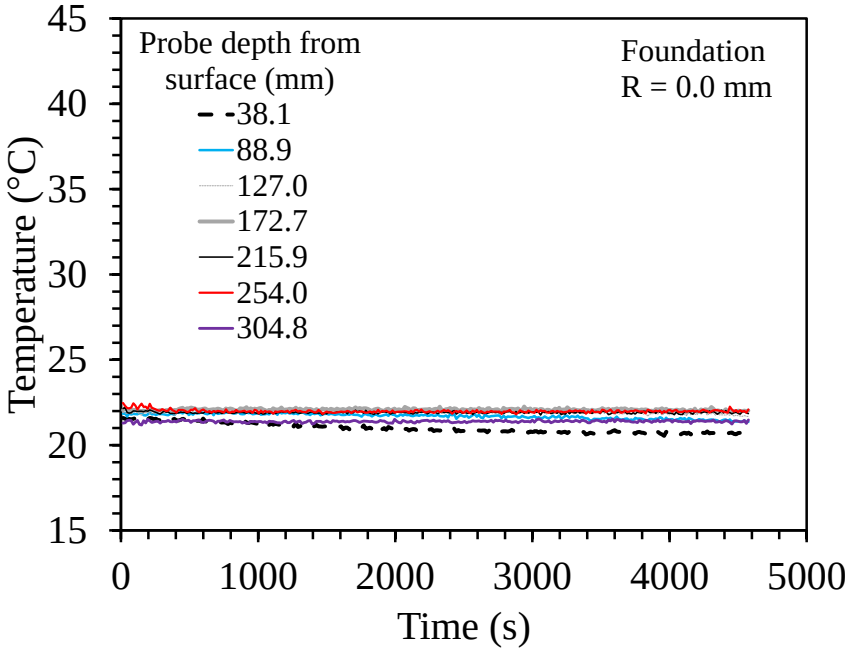

Figure 6.3.1-1 Foundation temperatures for the ambient (ΔT = 0 °C) loading test on the semi-floating foundation in Bonny silt.

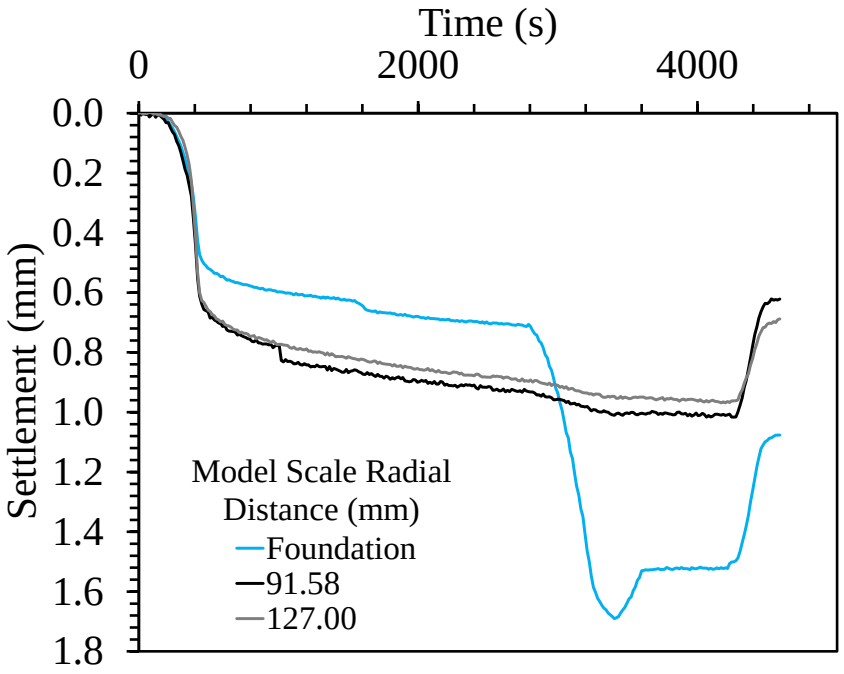

Figure 6.3.1-2 Model scale settlements with spin up for the ambient (ΔT = 0 °C) loading test on the semi-floating foundation in Bonny silt.

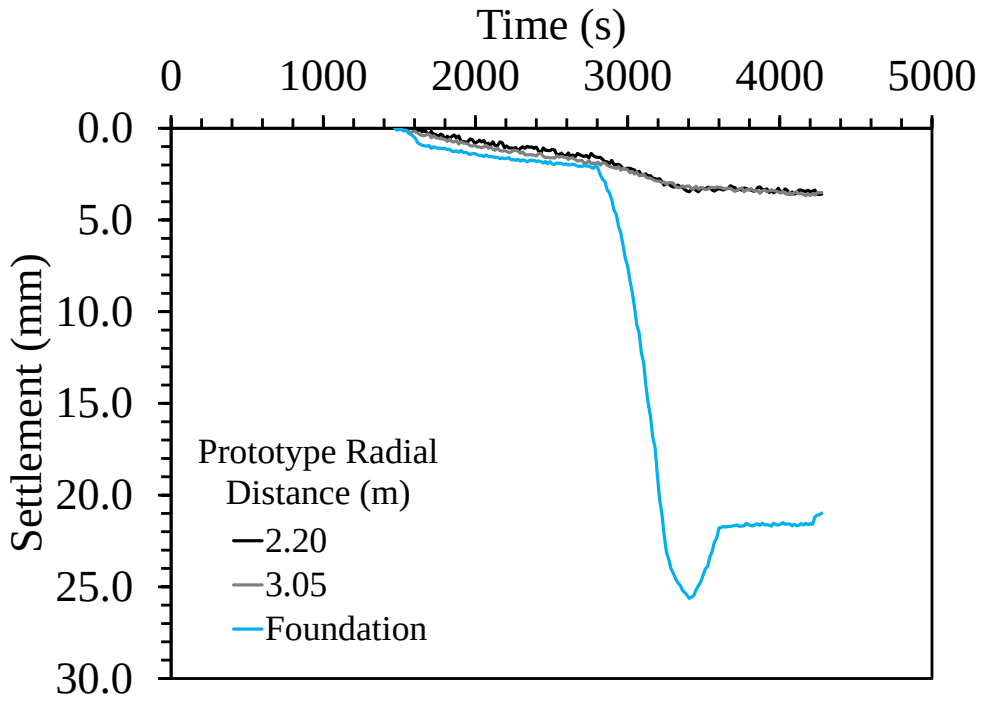

Figure 6.3.1-3 Prototype settlements after spin up for the ambient (ΔT = 0 °C) loading test on the semi-floating foundation in Bonny silt.

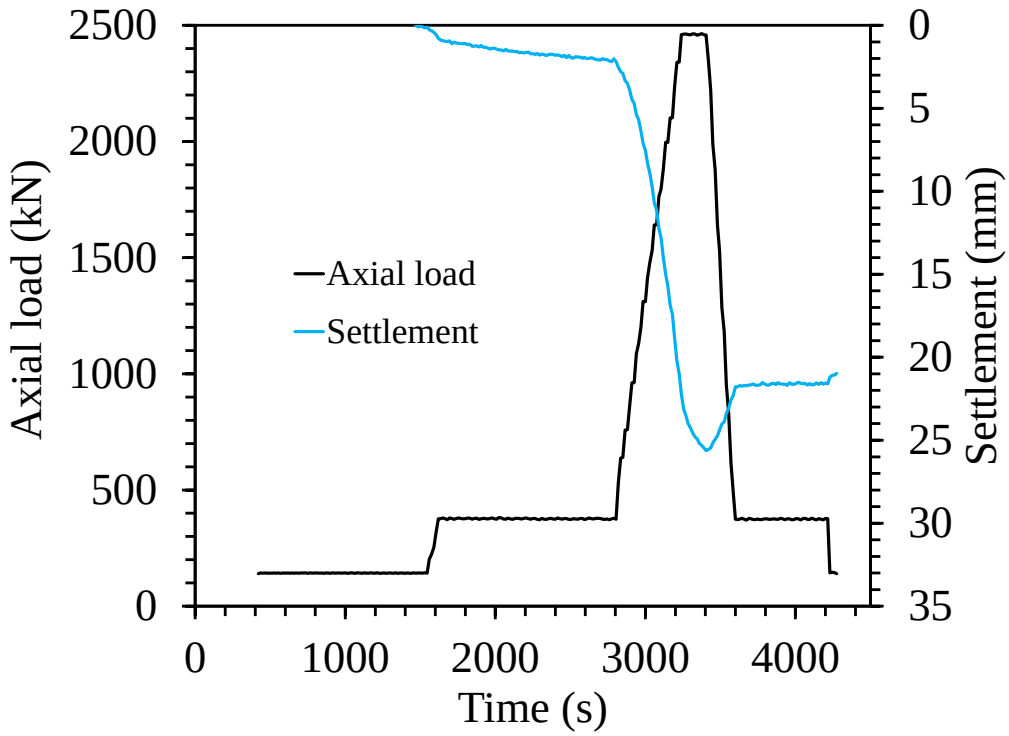

Figure 6.3.1-4 Foundation settlement and associated applied axial load for the ambient (ΔT = 0 °C) loading test on the semi-floating foundation in Bonny silt.

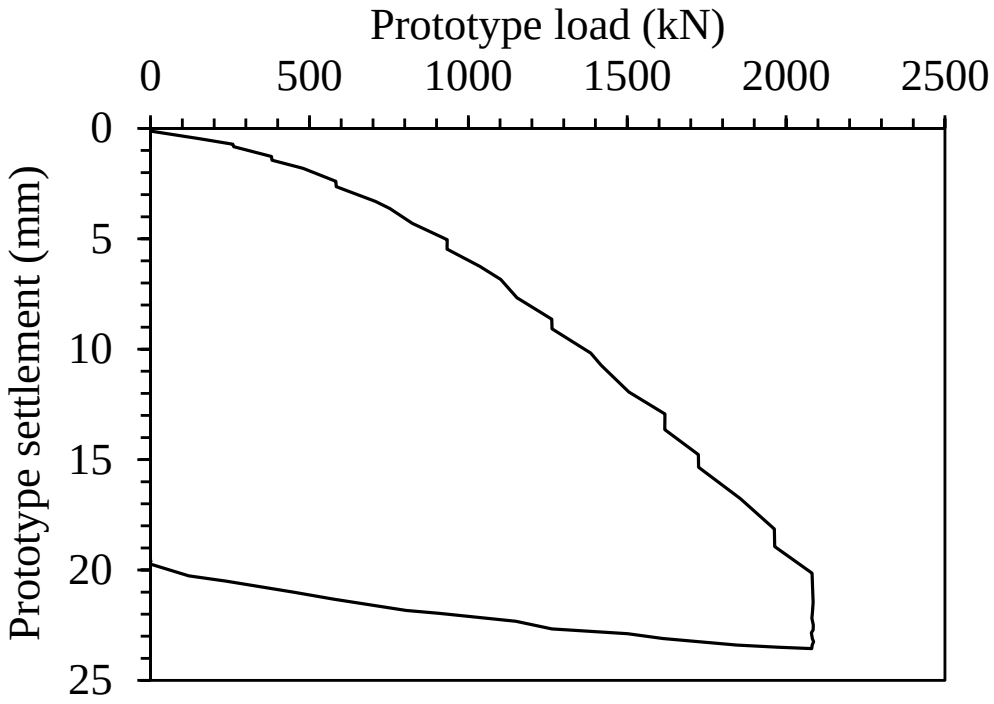

Figure 6.3.1-5 Prototype load settlement curve for the ambient (ΔT = 0 °C) loading test on the semi-floating foundation in Bonny silt.

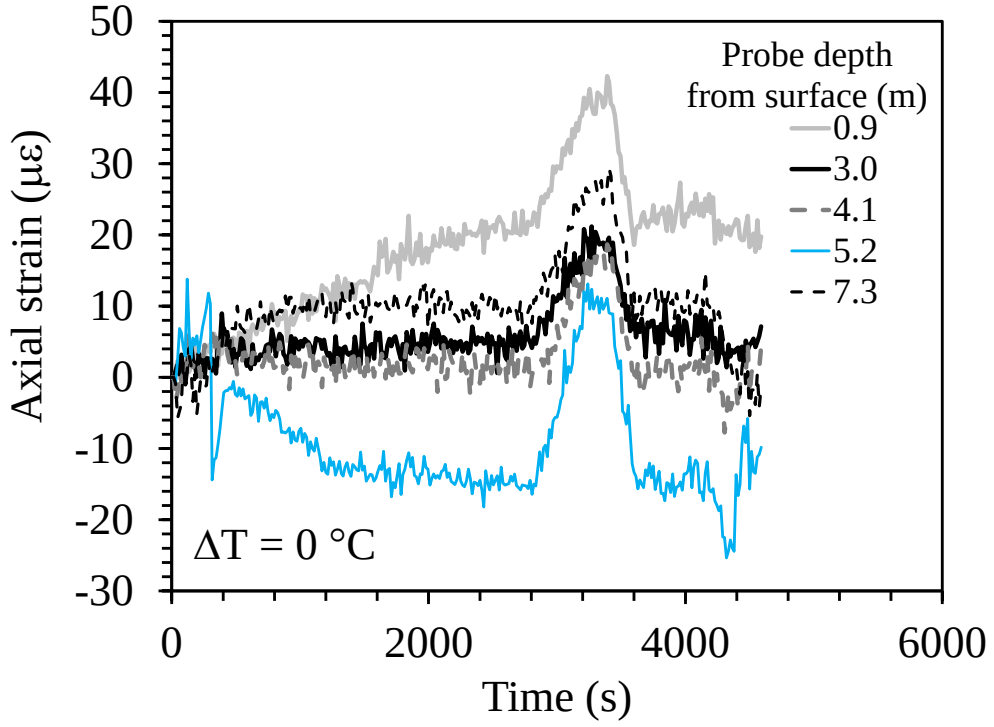

Figure 6.3.1-6 Axial strain time series for the ambient (ΔT = 0 °C) loading test on the semi-floating foundation in Bonny silt.

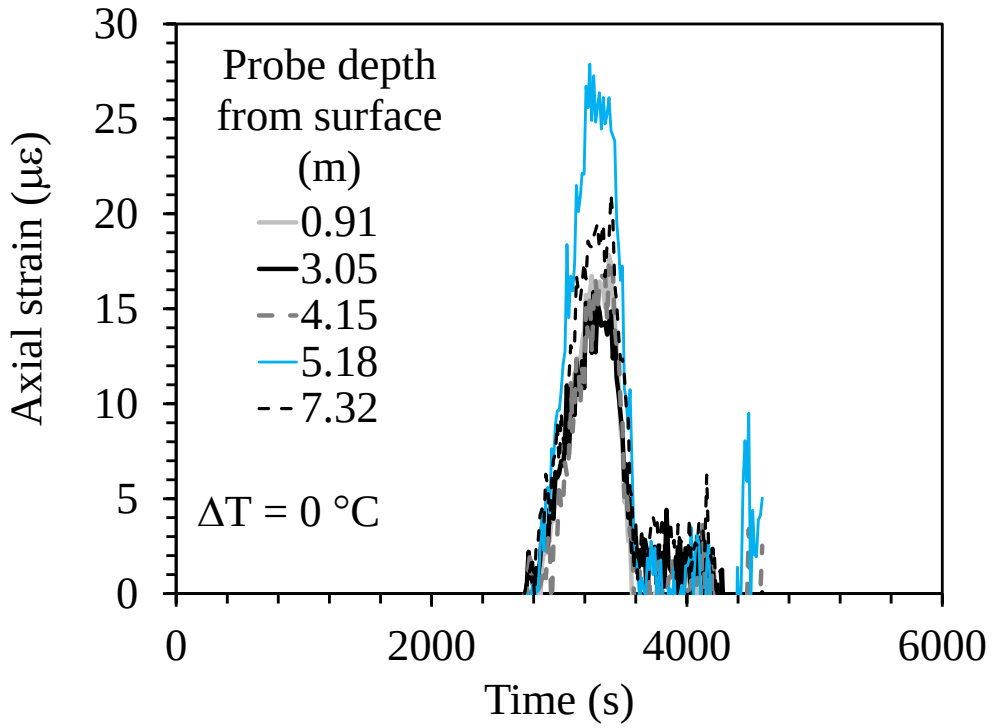

Figure 6.3.1-7 Axial strains during load test for the ambient (ΔT = 0 °C) loading test on the semi-floating foundation in Bonny silt.

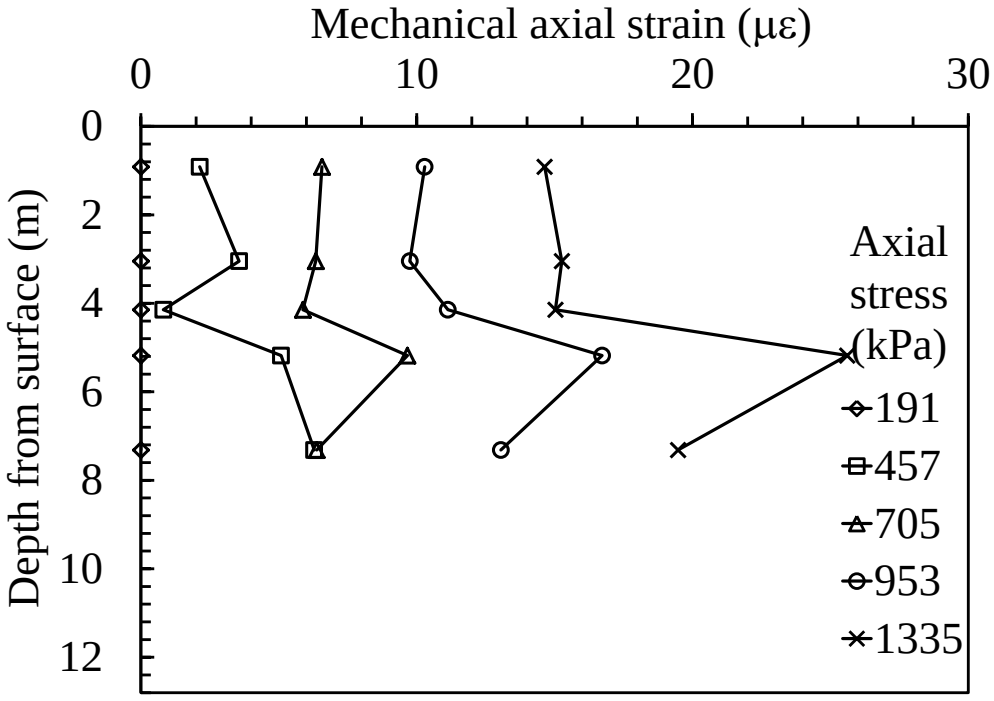

Figure 6.3.1-8 Prototype strain profile during loading for the ambient (ΔT = 0 °C) loading test on the semi-floating foundation in Bonny silt.

6.3.2 Results from Test S-BS-ML-10

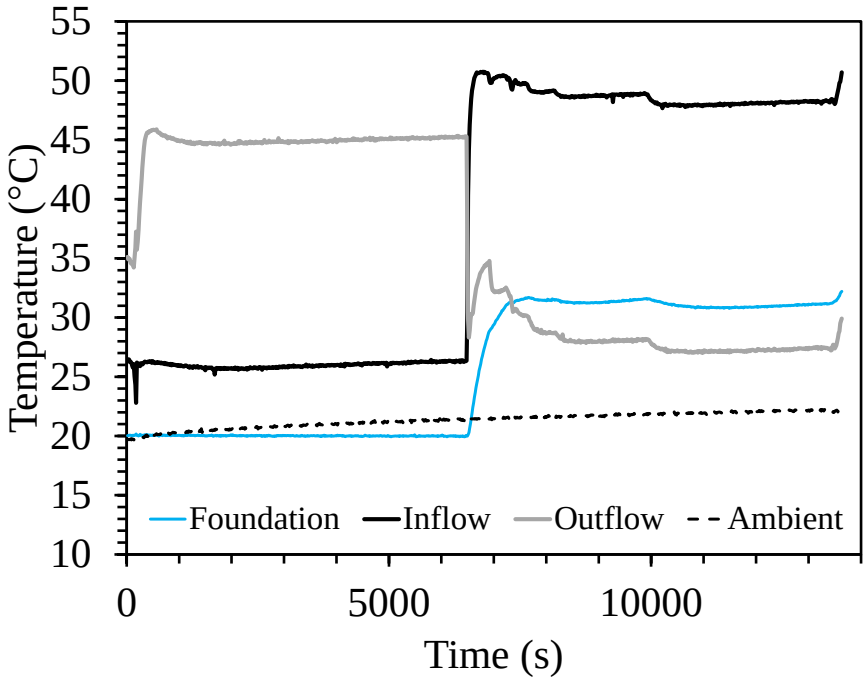

Figure 6.3.2-1 Temperatures during testing for the heated (ΔT = 10 °C) loading test on the semi-floating foundation in Bonny silt.

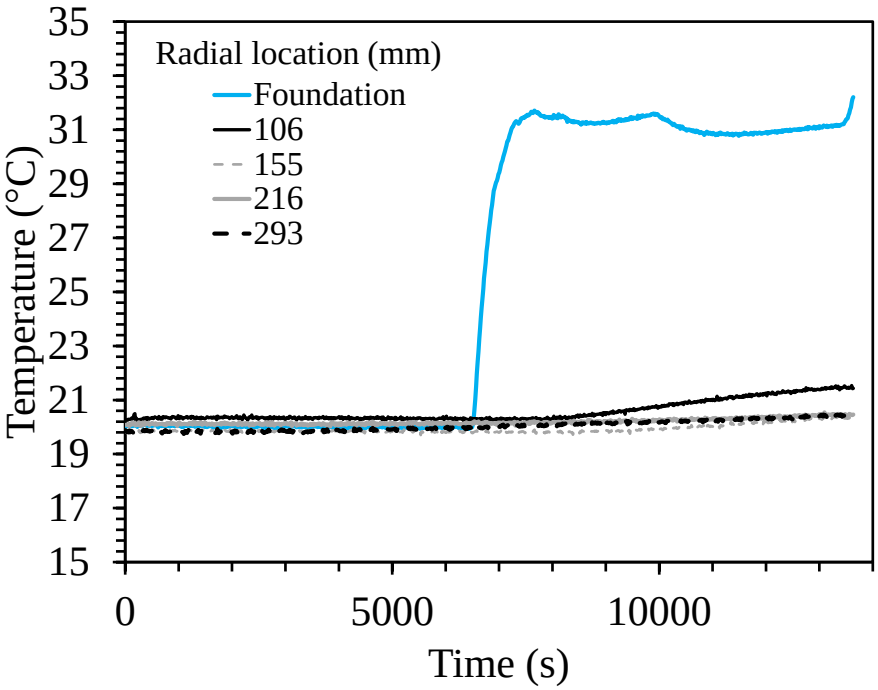

Figure 6.3.2-2 Average temperatures of foundation and four thermal probes for the heated (ΔT = 10 °C) loading test on the semi-floating foundation in Bonny silt.

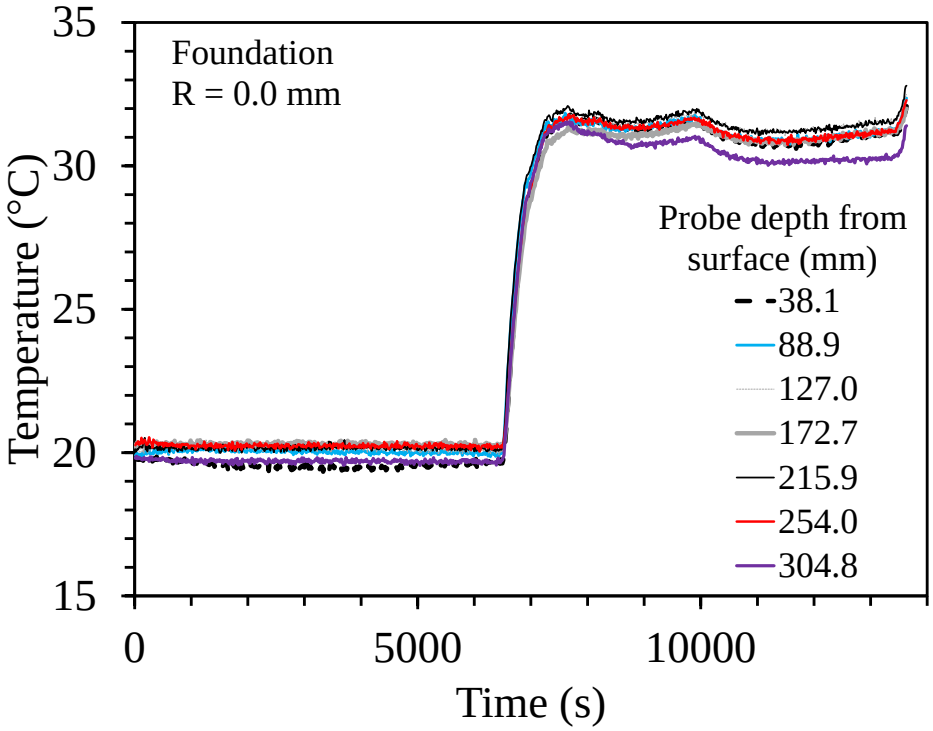

Figure 6.3.2-3 Foundation temperatures for the heated (ΔT = 10 °C) loading test on the semi-floating foundation in Bonny silt.

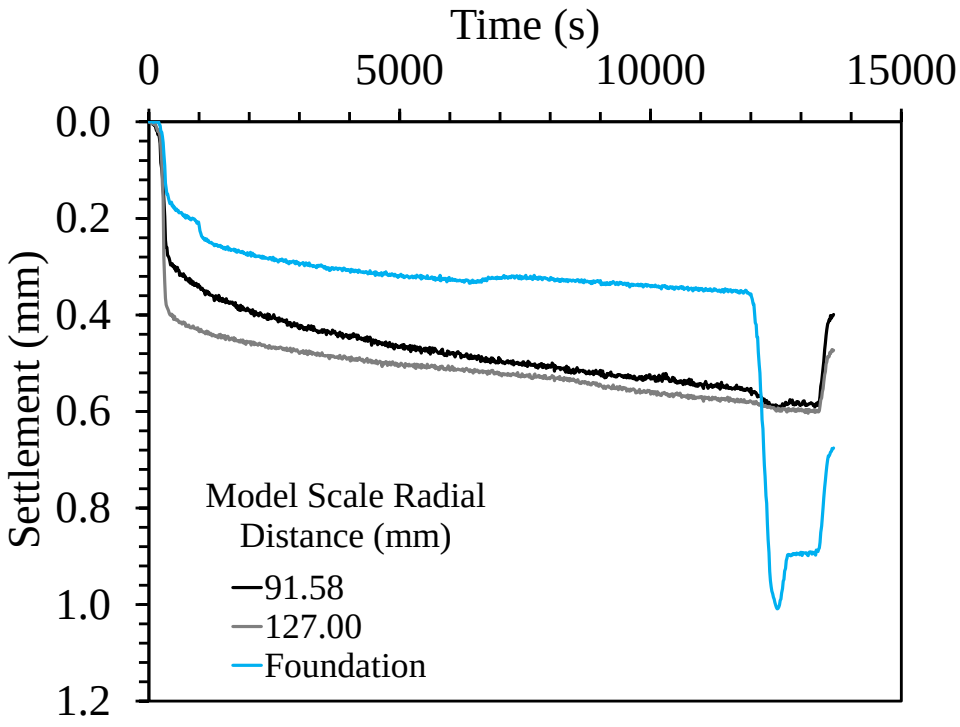

Figure 6.3.2-4 Model scale settlements with spin up for the heated (ΔT = 10 °C) loading test on the semi-floating foundation in Bonny silt.

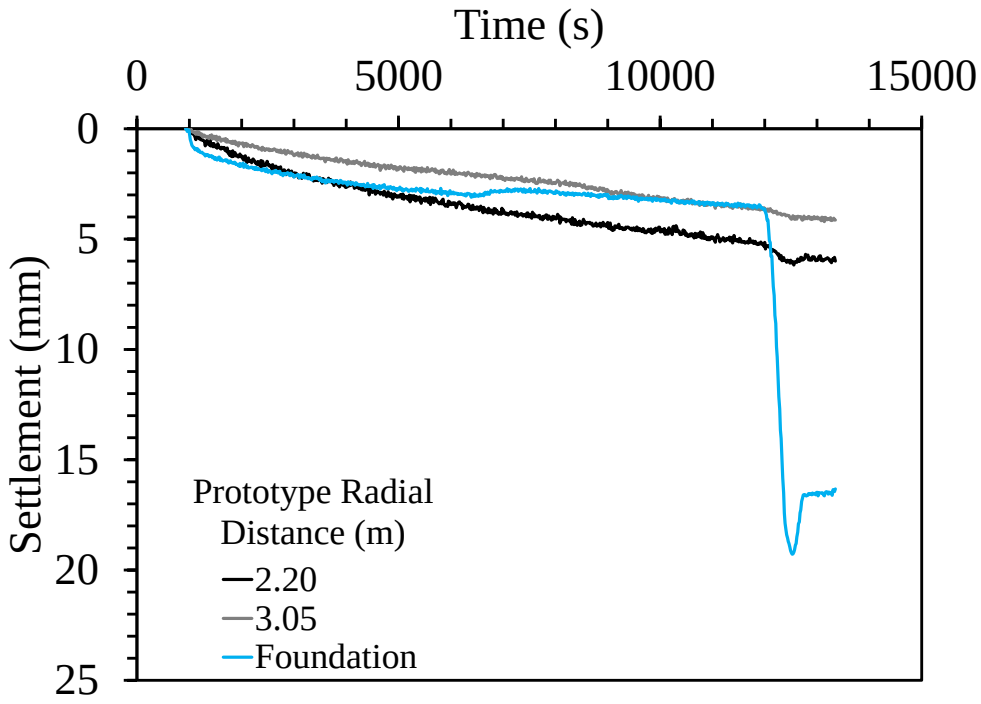

Figure 6.3.2-5 Prototype settlements after spin up for the heated (ΔT = 10 °C) loading test on the semi-floating foundation in Bonny silt.

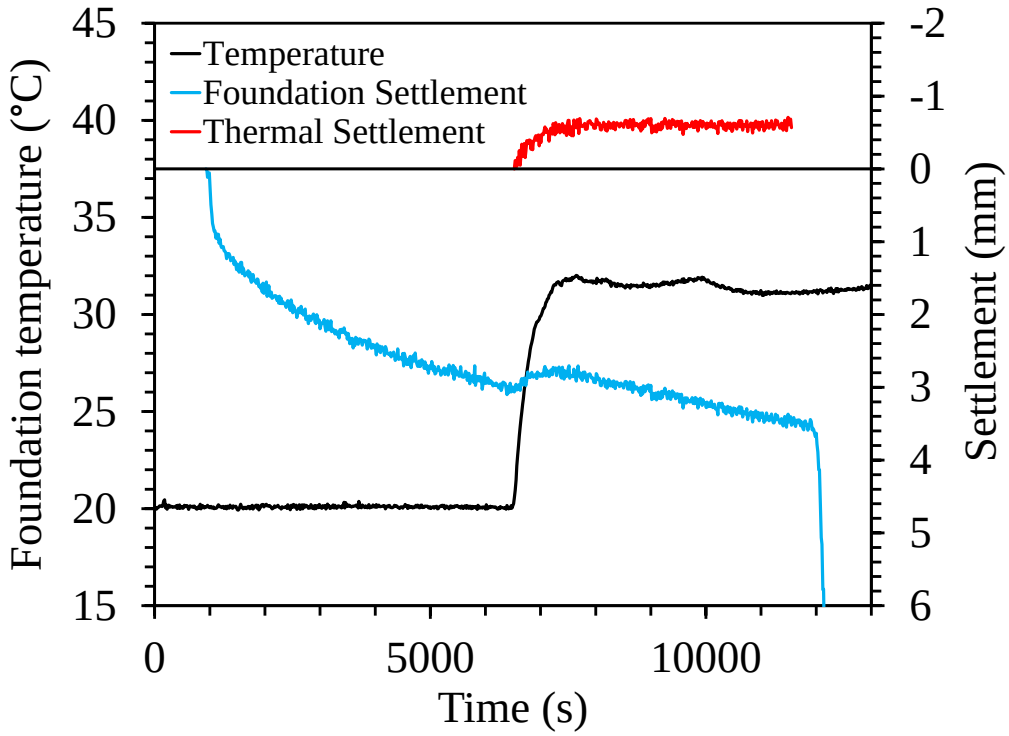

Figure 6.3.2-6 Foundation temperature, overall foundation settlement, and thermal settlement for the heated (ΔT = 10 °C) loading test on the semi-floating foundation in Bonny silt.

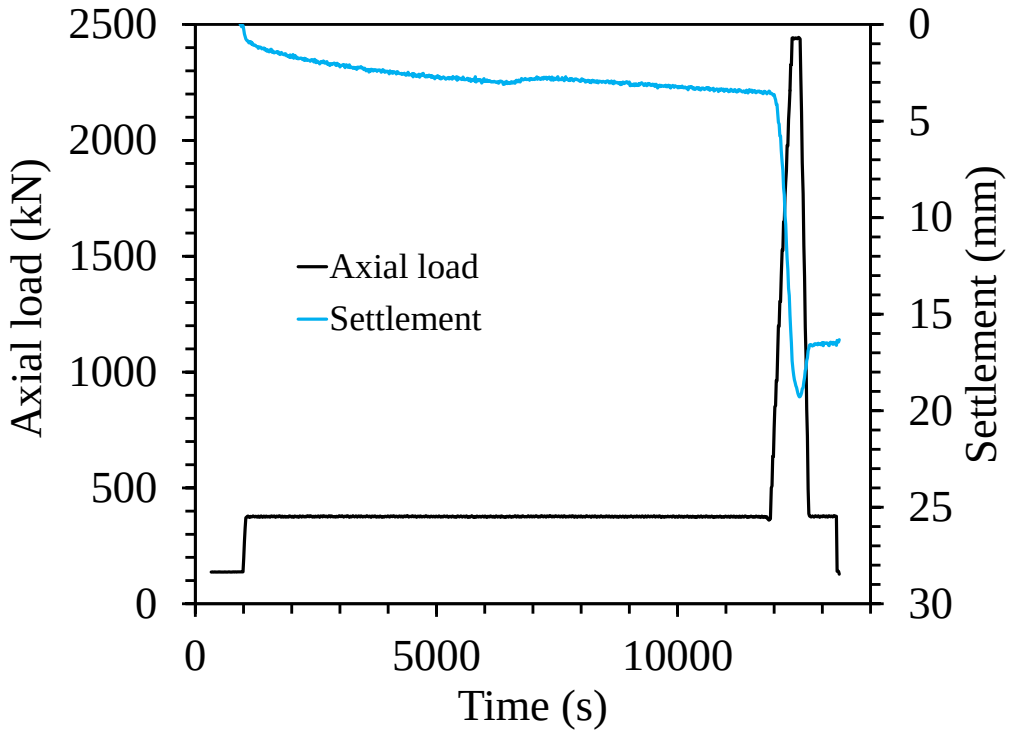

Figure 6.3.2-7 Prototype foundation settlement and associated applied axial load for the heated (ΔT = 10 °C) loading test on the semi-floating foundation in Bonny silt.

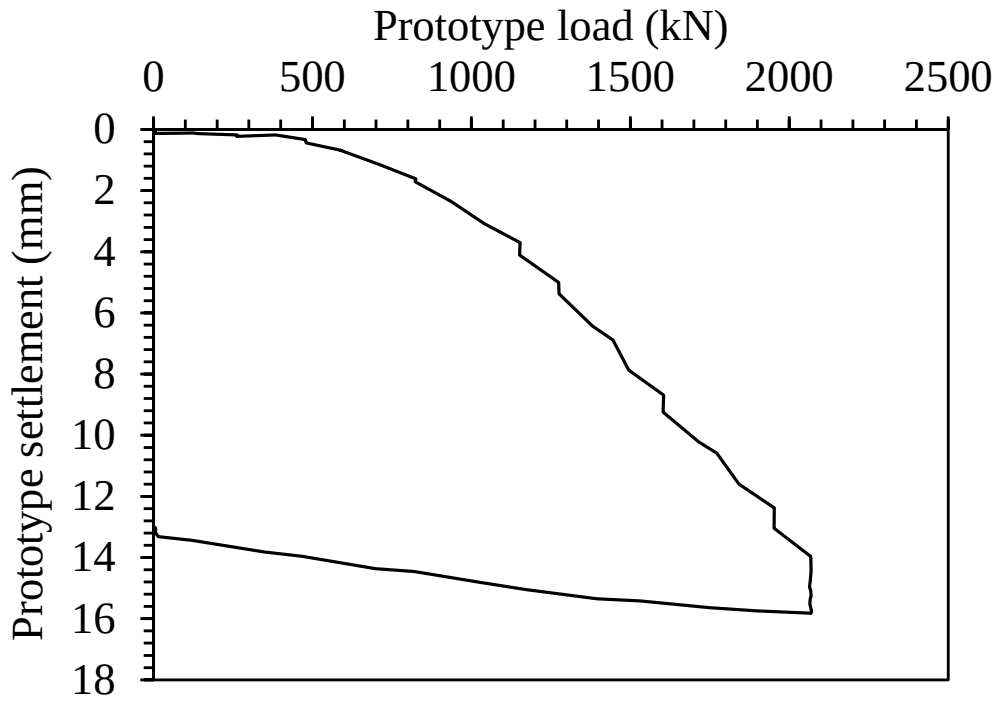

Figure 6.3.2-8 Prototype load settlement curve for the heated (ΔT = 10 °C) loading test on the semi-floating foundation in Bonny silt.

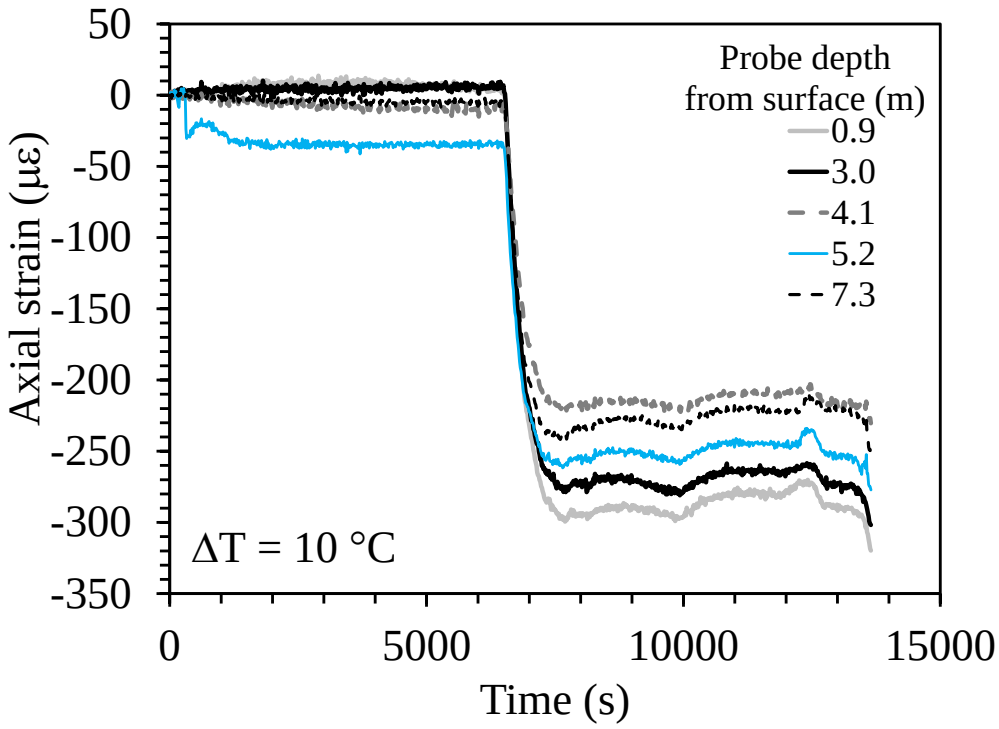

Figure 6.3.2-9 Axial strain time series for the heated (ΔT = 10 °C) loading test on the semi-floating foundation in Bonny silt.

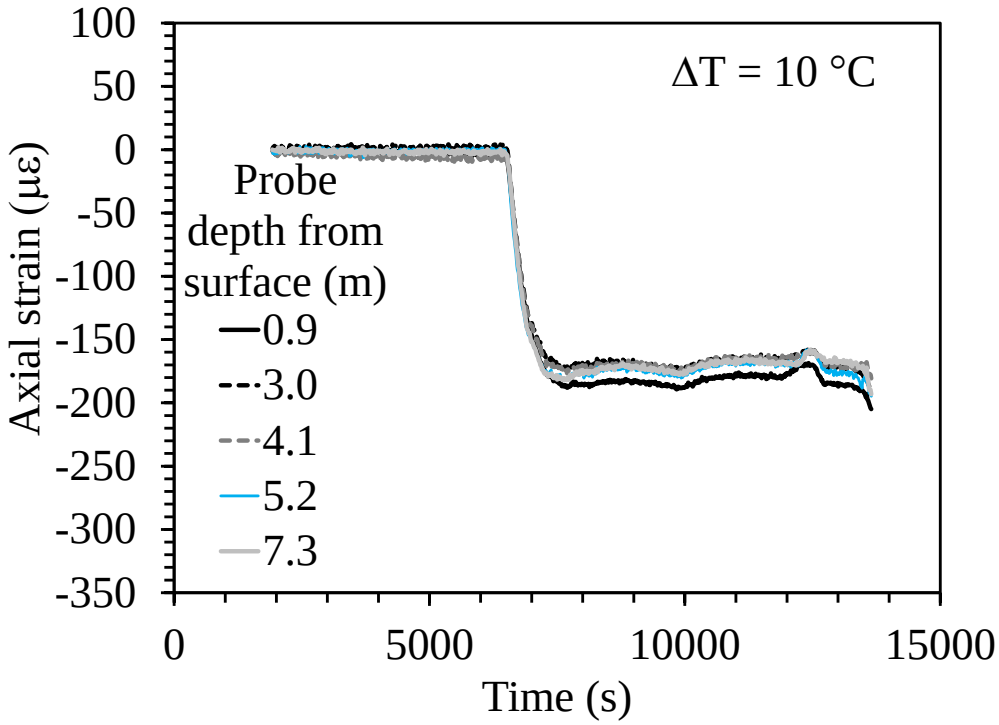

Figure 6.3.2-10 Axial strains during heating for the heated (ΔT = 10 °C) loading test on the semi-floating foundation in Bonny silt.

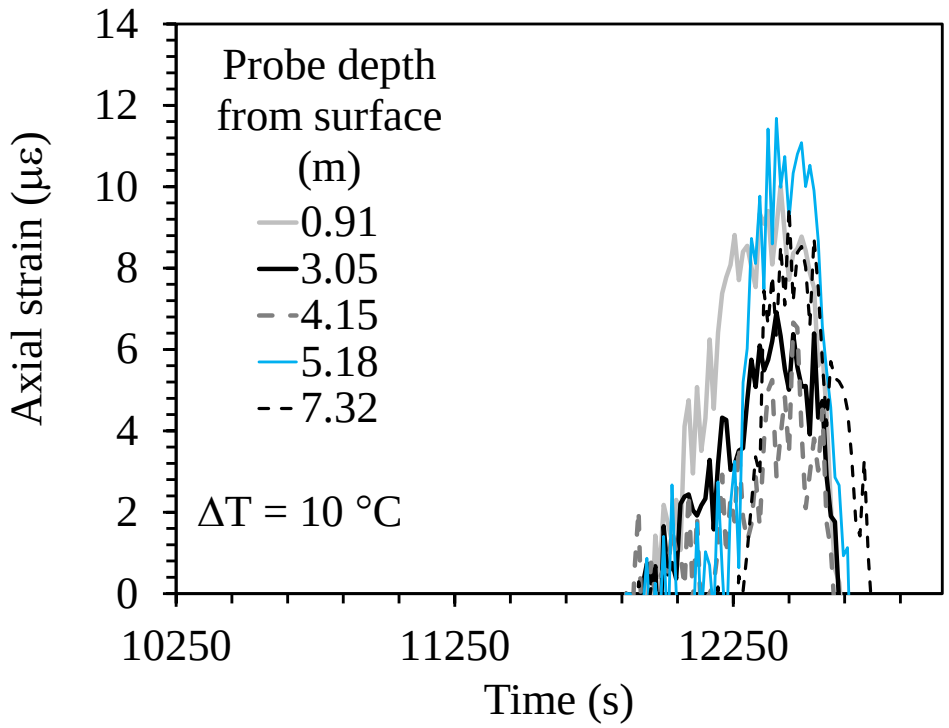

Figure 6.3.2-11 Axial strains during load test for the heated (ΔT = 10 °C) loading test on the semi-floating foundation in Bonny silt.

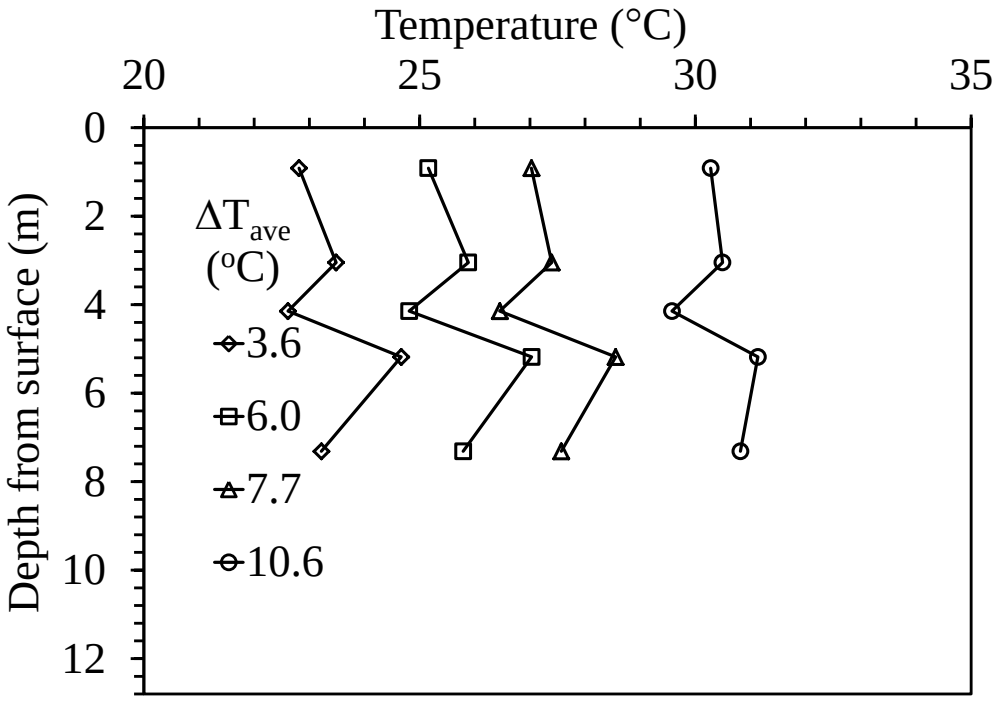

Figure 6.3.2-12 Temperature profiles for the heated (ΔT = 10 °C) loading test on the semi-floating foundation in Bonny silt.

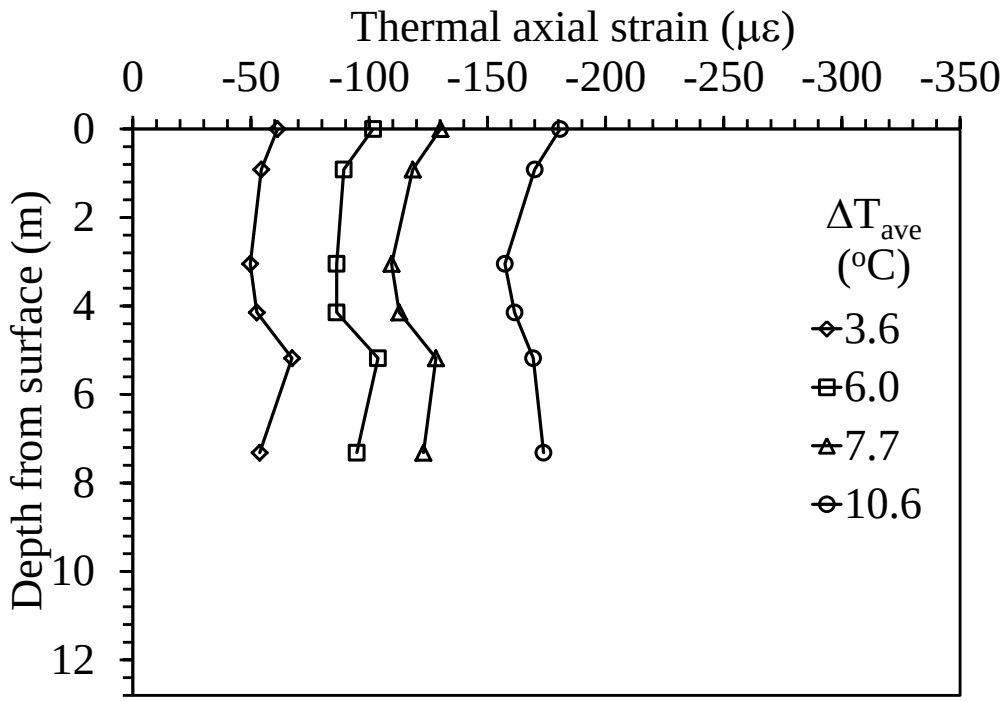

Figure 6.3.2-13 Prototype thermal axial strain profile for the heated (ΔT = 10 °C) loading test on the semi-floating foundation in Bonny silt.

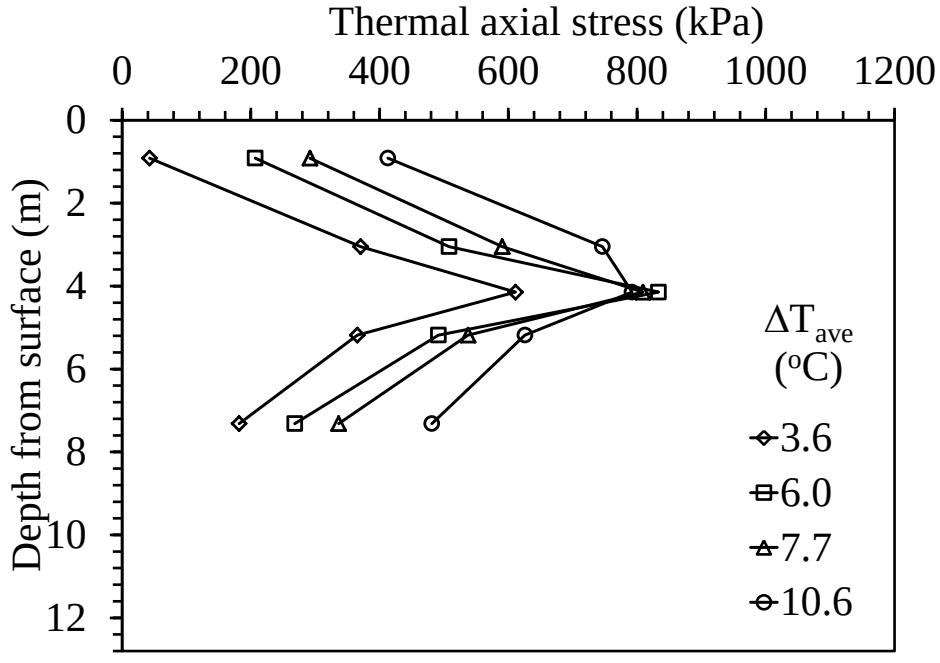

Figure 6.3.2-14 Prototype thermal stress profile for the heated (ΔT = 10 °C) loading test on the semi-floating foundation in Bonny silt.

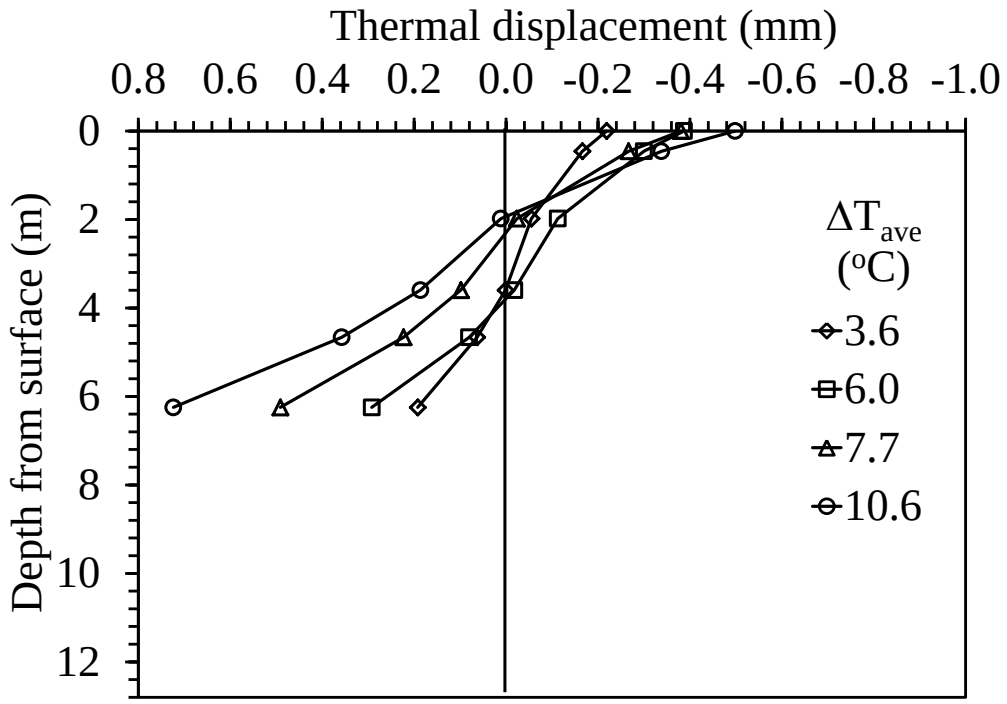

Figure 6.3.2-15 Thermal axial displacement profiles for the heated (ΔT = 10 °C) loading test on the semi-floating foundation in Bonny silt.

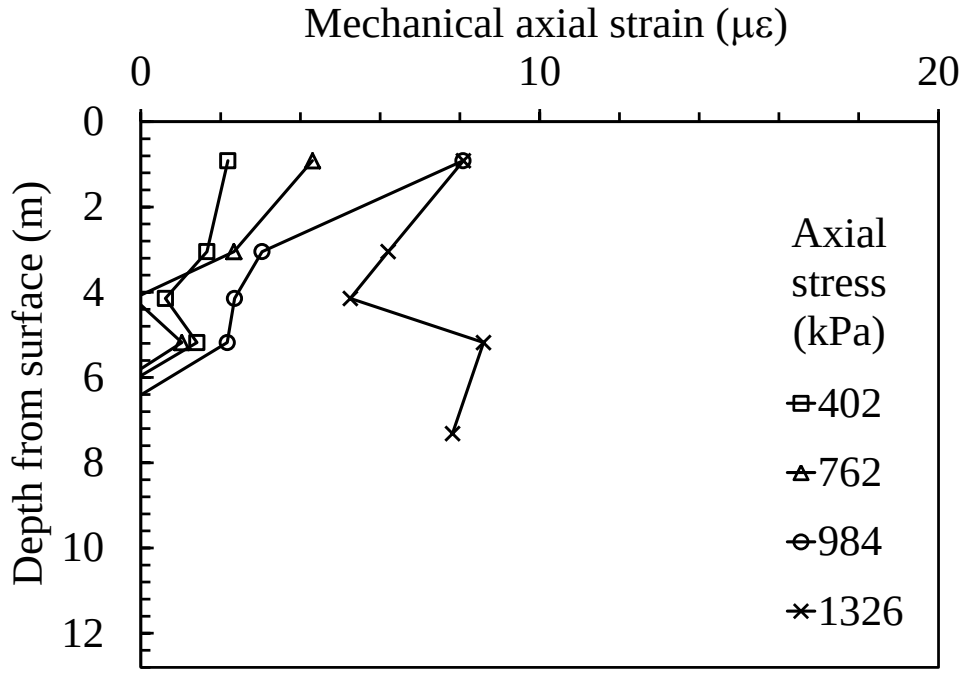

Figure 6.3.2-16 Prototype strain profile during load test for the heated (ΔT = 10 °C) loading test on the semi-floating foundation in Bonny silt.

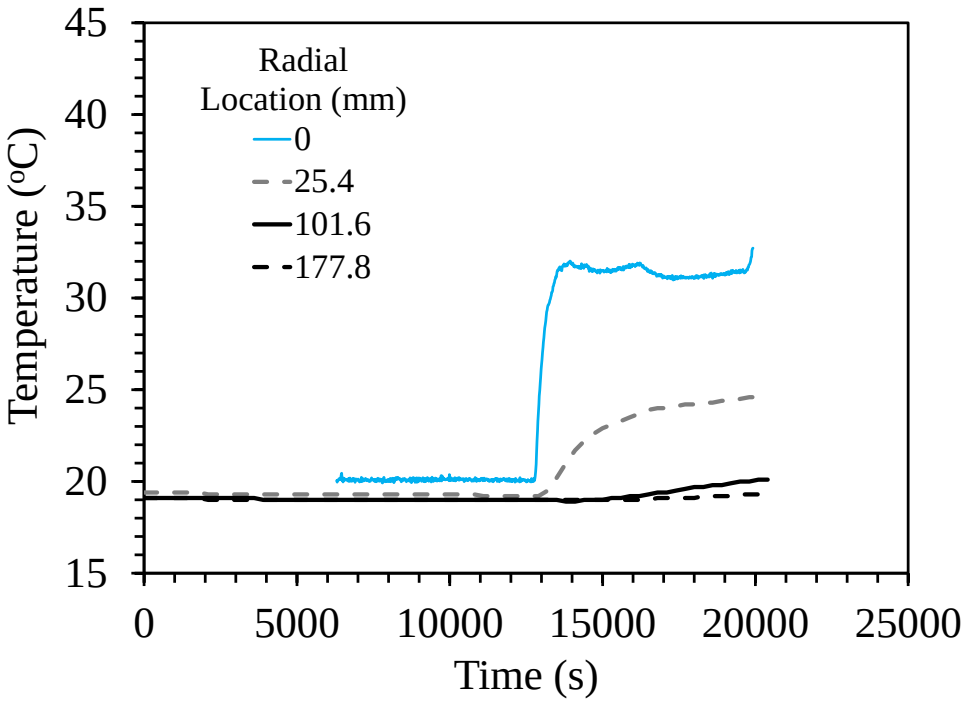

Figure 6.3.2-17 Temperature readings from dielectric sensors at radial locations for the heated (ΔT = 10 °C) loading test on the semi-floating foundation in Bonny silt.

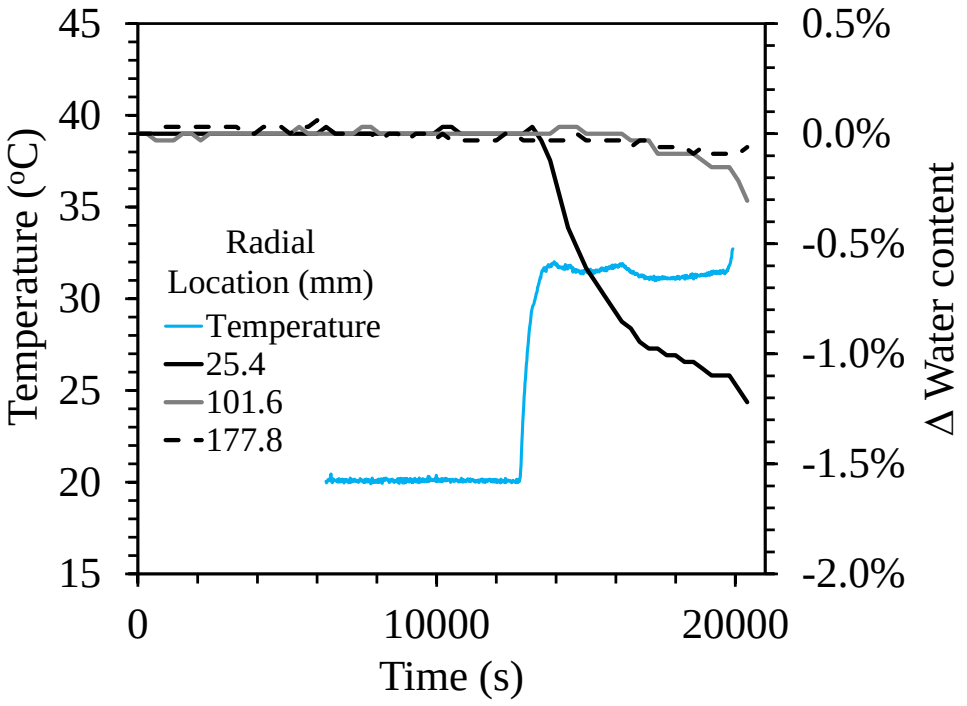

Figure 6.3.2-18 Change in water content at radial locations along with foundation temperature for the heated (ΔT = 10 °C) loading test on the semi-floating foundation in Bonny silt.

6.3.3 Results from Test S-BS-ML-18

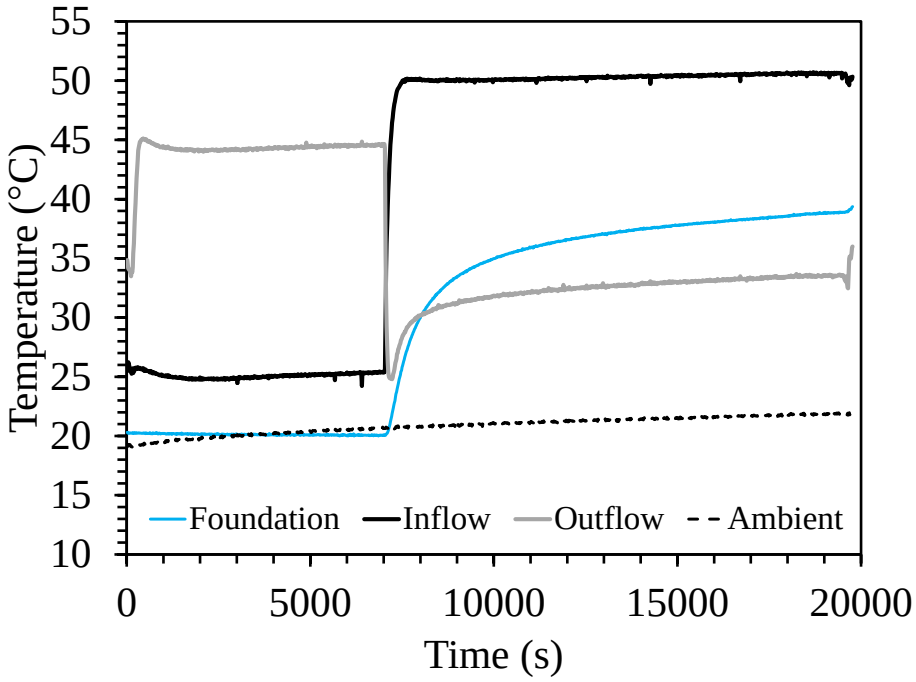

Figure 6.3.3-1 Temperatures during testing for the heated (ΔT = 18 °C) loading test on the semi-floating foundation in Bonny silt.

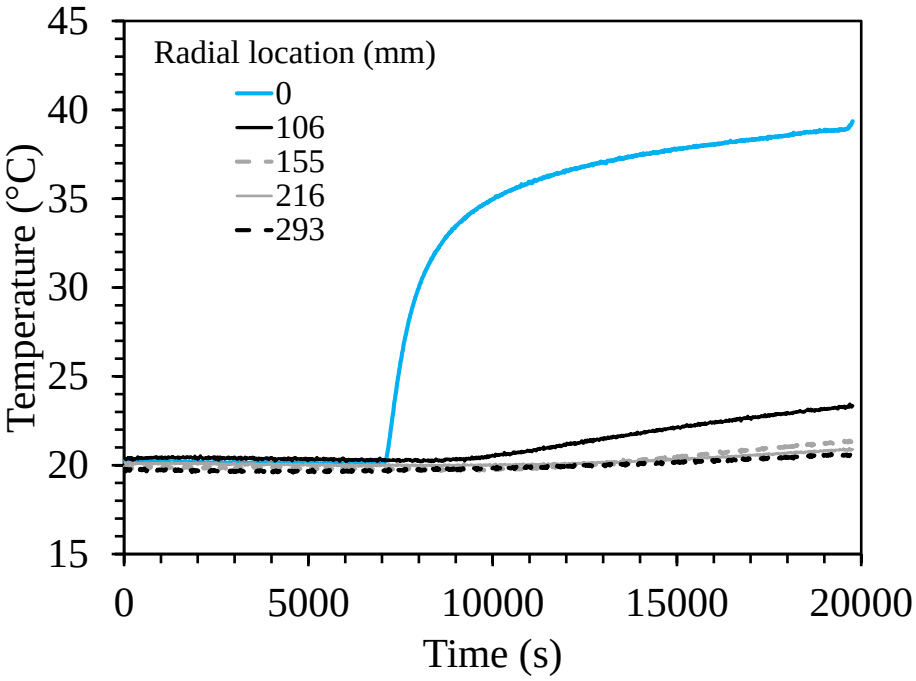

Figure 6.3.3-2 Average temperatures of foundation and four thermal probes for the heated (ΔT = 18 °C) loading test on the semi-floating foundation in Bonny silt.

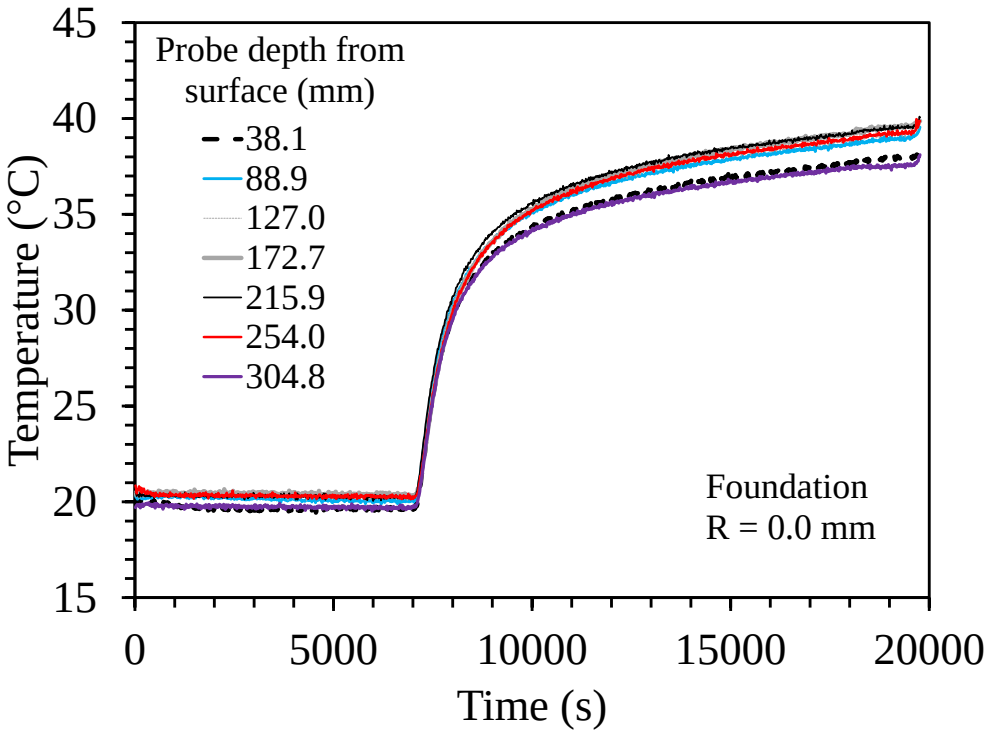

Figure 6.3.3-3 Foundation temperatures for the heated (ΔT = 18 °C) loading test on the semi-floating foundation in Bonny silt.

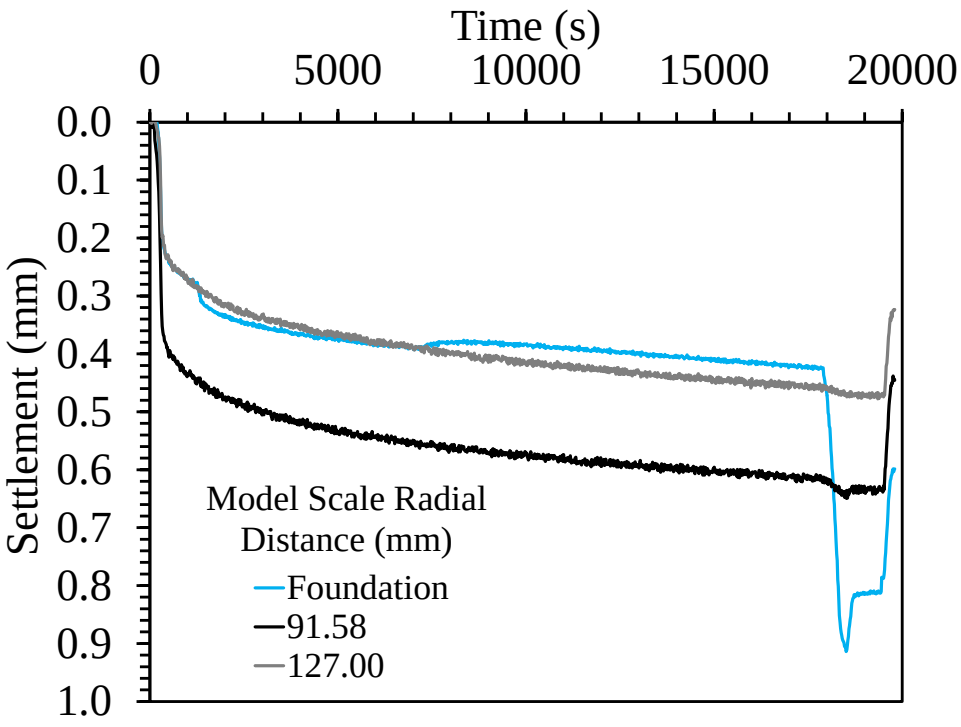

Figure 6.3.3-4 Model scale settlements with spin up for the heated (ΔT = 18 °C) loading test on the semi-floating foundation in Bonny silt.

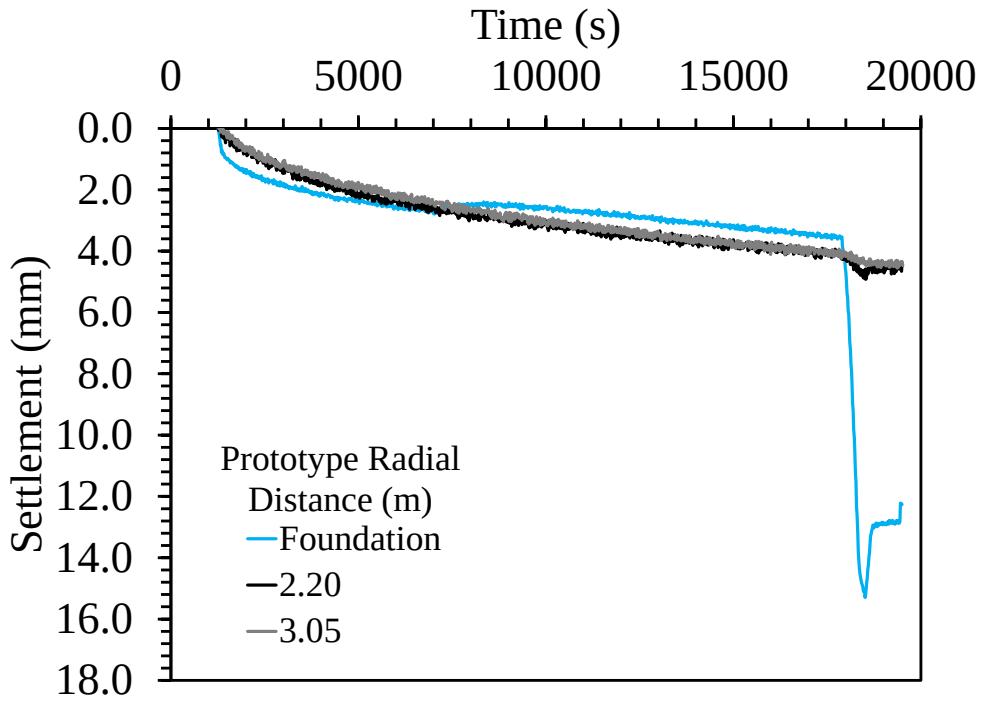

Figure 6.3.3-5 Prototype settlements after spin up for the heated (ΔT = 18 °C) loading test on the semi-floating foundation in Bonny silt.

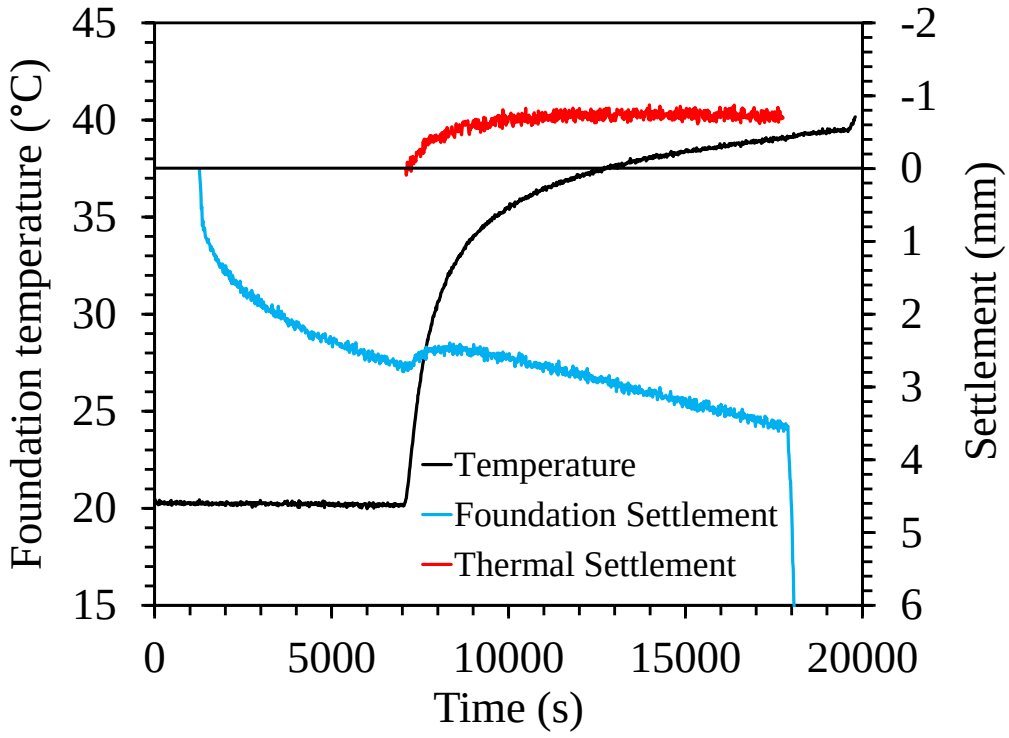

Figure 6.3.3-6 Foundation temperature, overall foundation settlement, and thermal settlement for the heated (ΔT = 18 °C) loading test on the semi-floating foundation in Bonny silt.

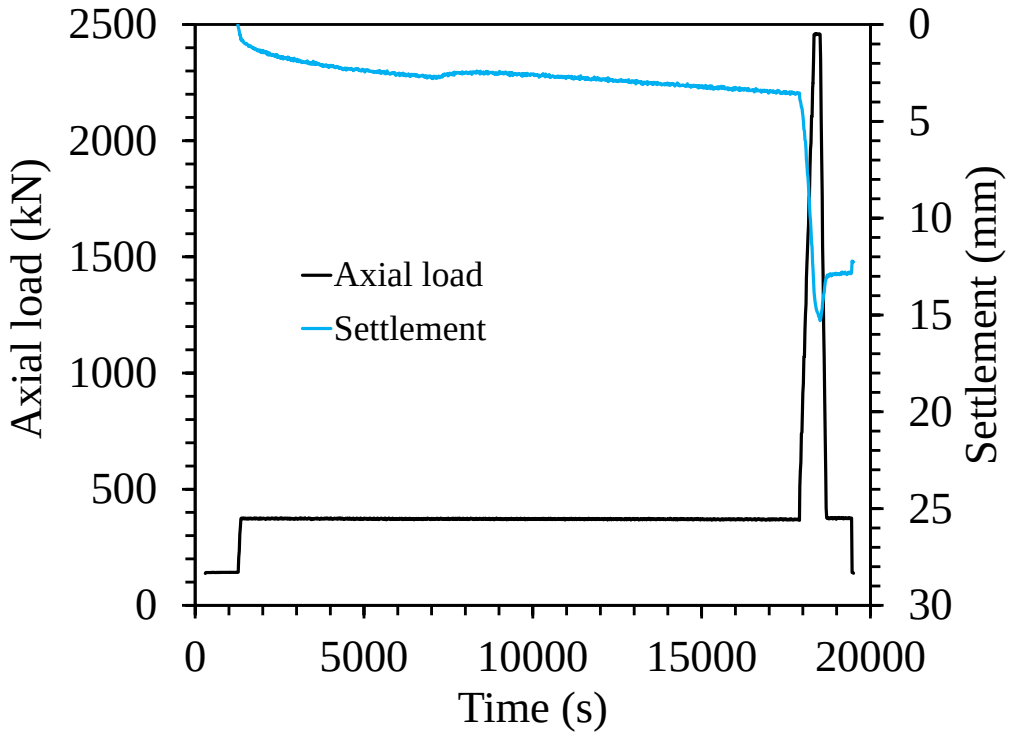

Figure 6.3.3-7 Prototype foundation settlement and associated applied axial load for the heated (ΔT = 18 °C) loading test on the semi-floating foundation in Bonny silt.

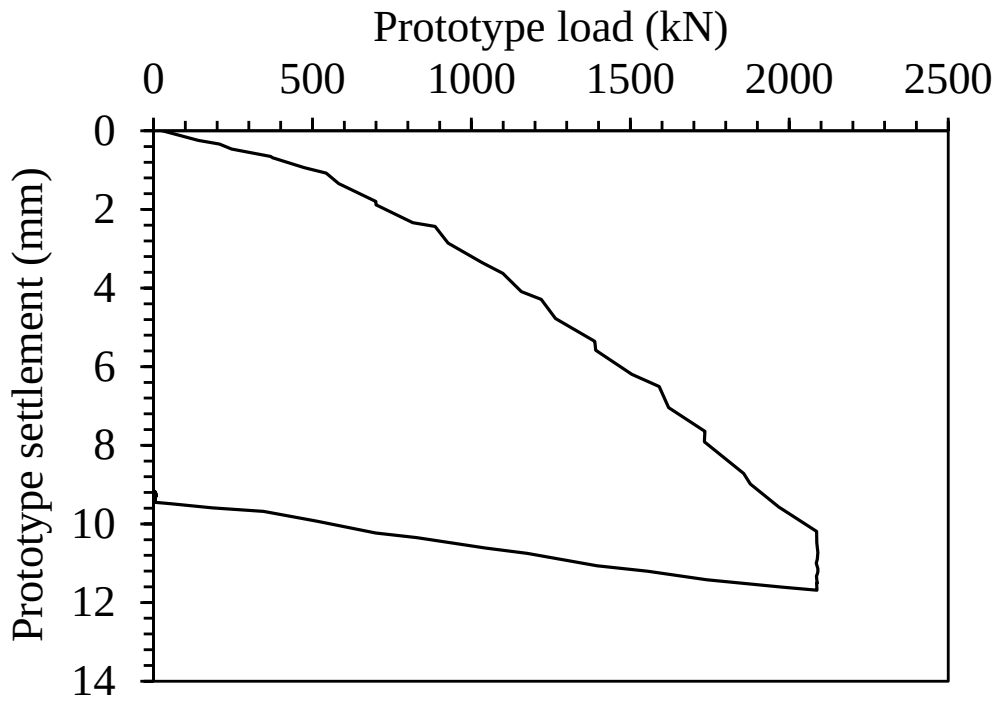

Figure 6.3.3-8 Prototype load settlement curve for the heated (ΔT = 18 °C) loading test on the semi-floating foundation in Bonny silt.

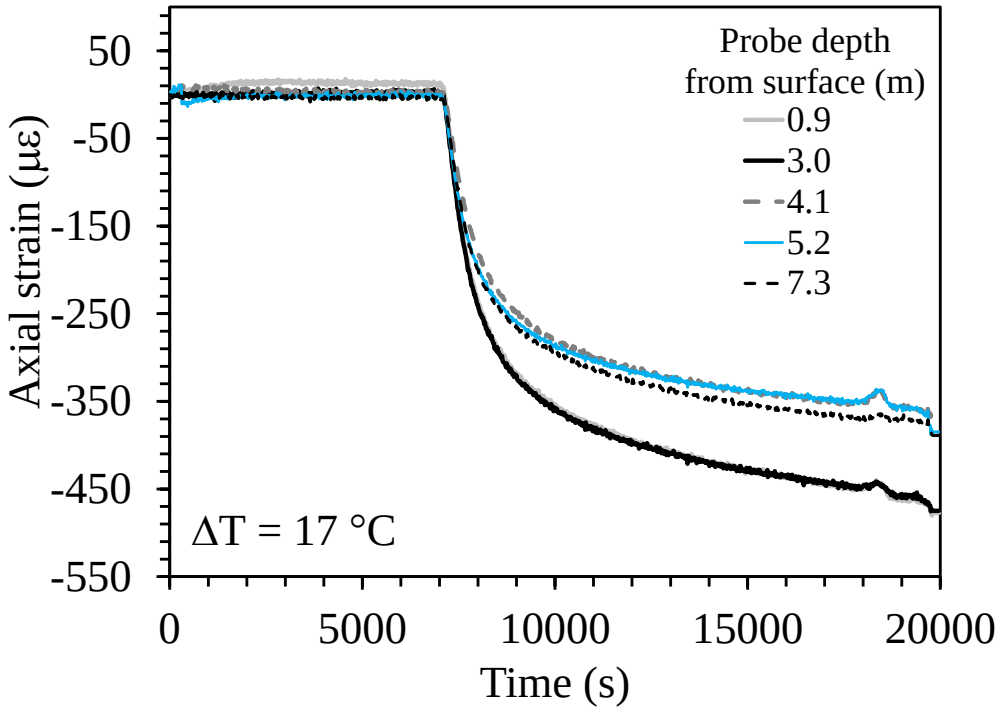

Figure 6.3.3-9 Axial strain time series for the heated (ΔT = 18 °C) loading test on the semi-floating foundation in Bonny silt.

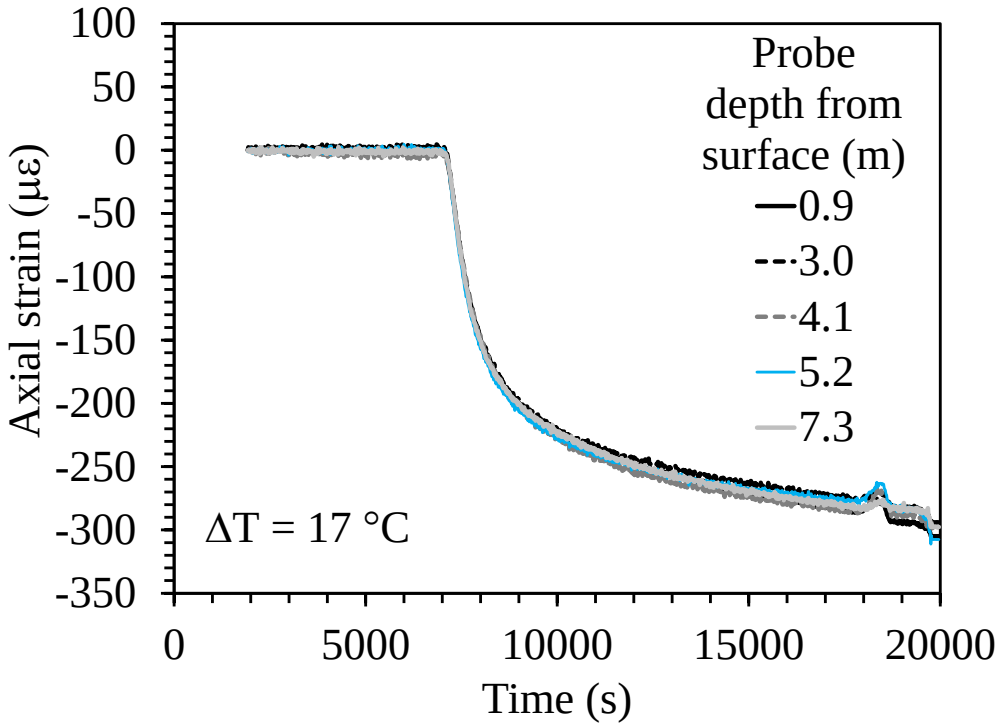

Figure 6.3.3-10 Axial strains during heating for the heated (ΔT = 18 °C) loading test on the semi-floating foundation in Bonny silt.

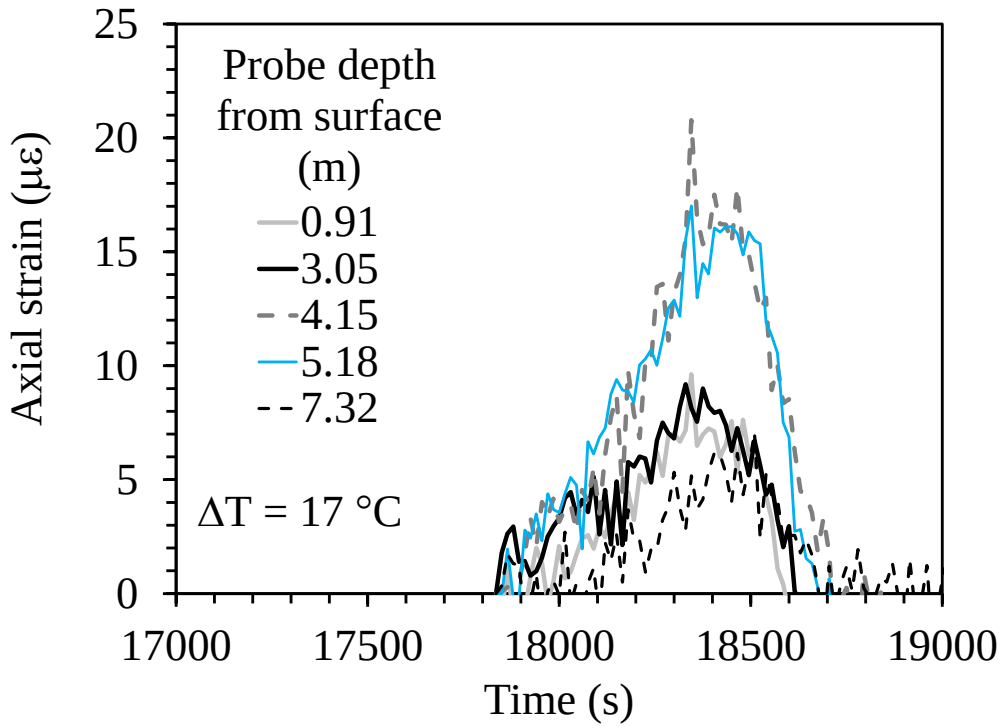

Figure 6.3.3-11 Axial strains during load test for the heated (ΔT = 18 °C) loading test on the semi-floating foundation in Bonny silt.

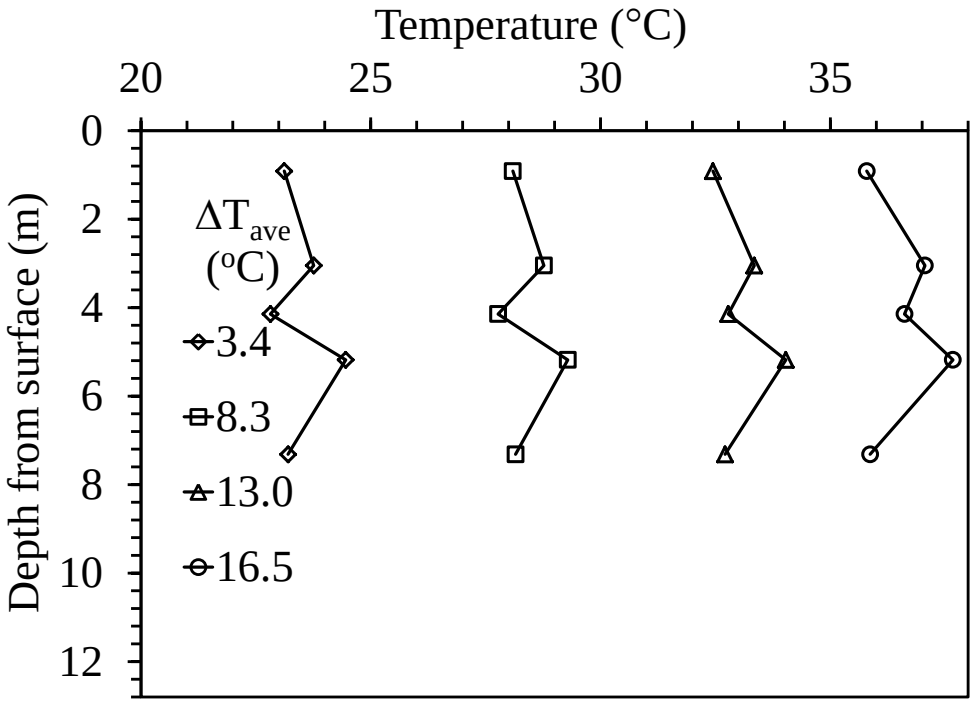

Figure 6.3.3-12 Temperature profiles for the heated (ΔT = 18 °C) loading test on the semi-floating foundation in Bonny silt.

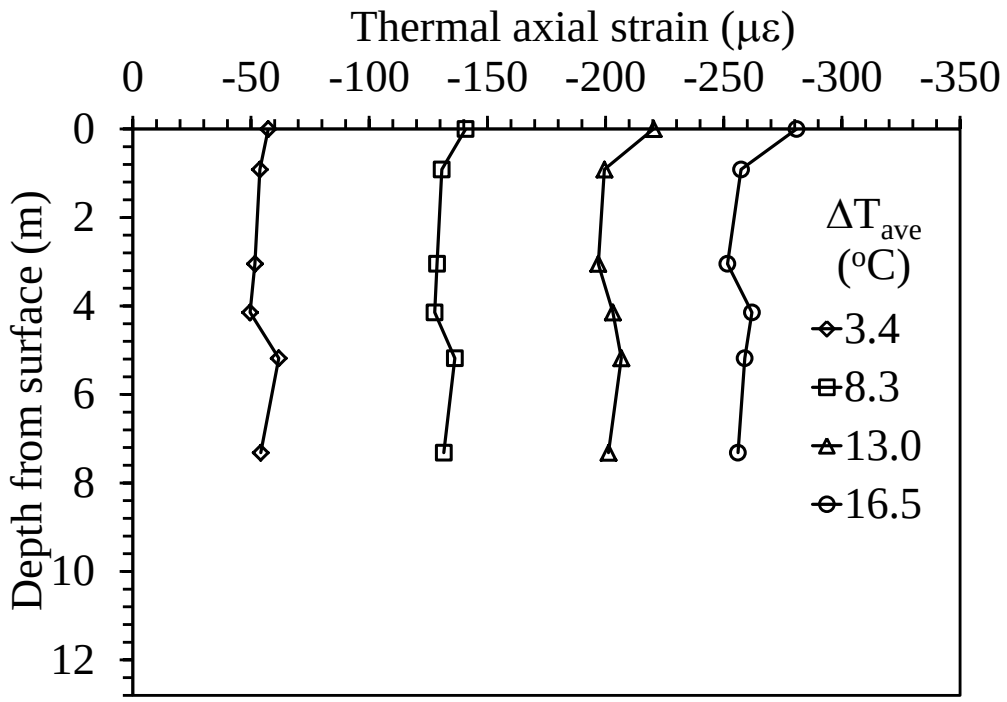

Figure 6.3.3-13 Prototype thermal axial strain profile for the heated (ΔT = 18 °C) loading test on the semi-floating foundation in Bonny silt.

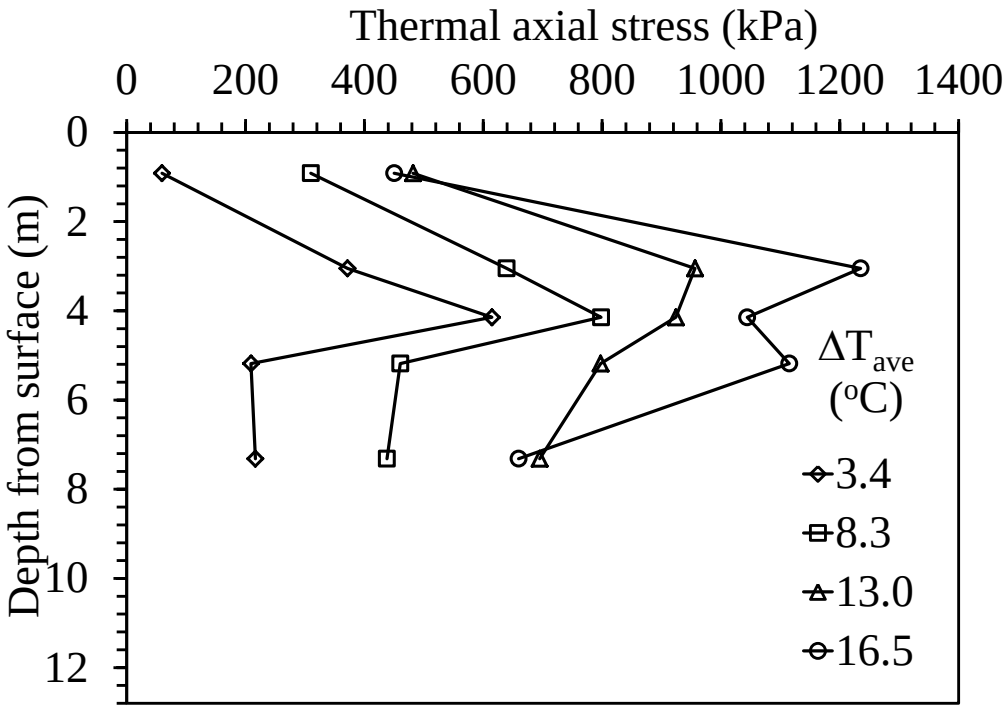

Figure 6.3.3-14 Prototype thermal stress profile for the heated (ΔT = 18 °C) loading test on the semi-floating foundation in Bonny silt.

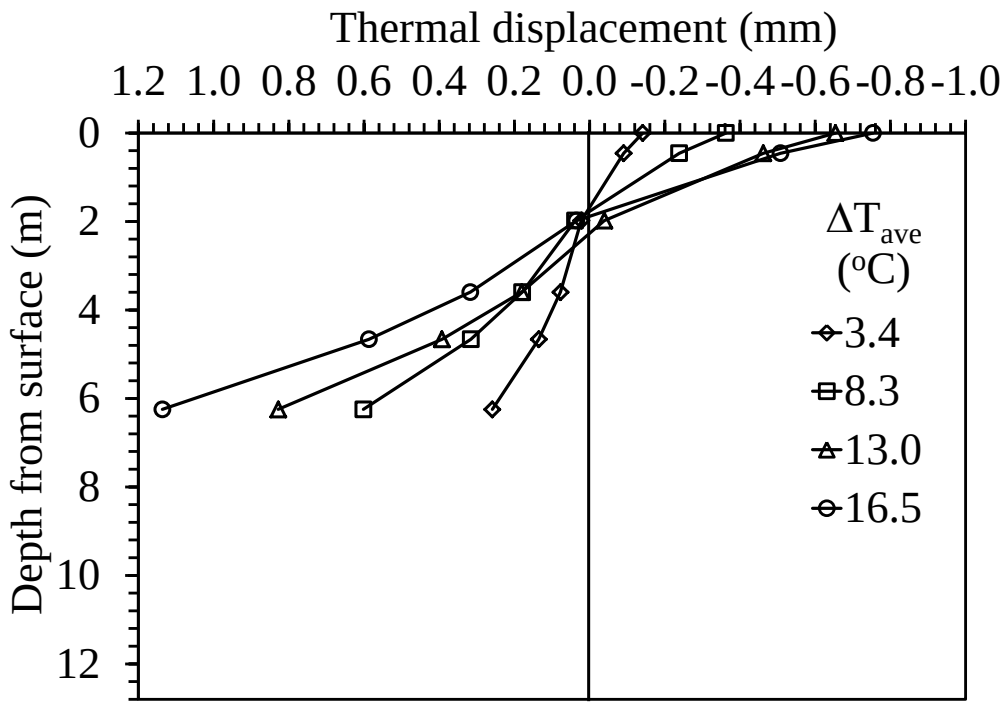

Figure 6.3.3-15 Thermal axial displacement profiles for the heated (ΔT = 18 °C) loading test on the semi-floating foundation in Bonny silt.

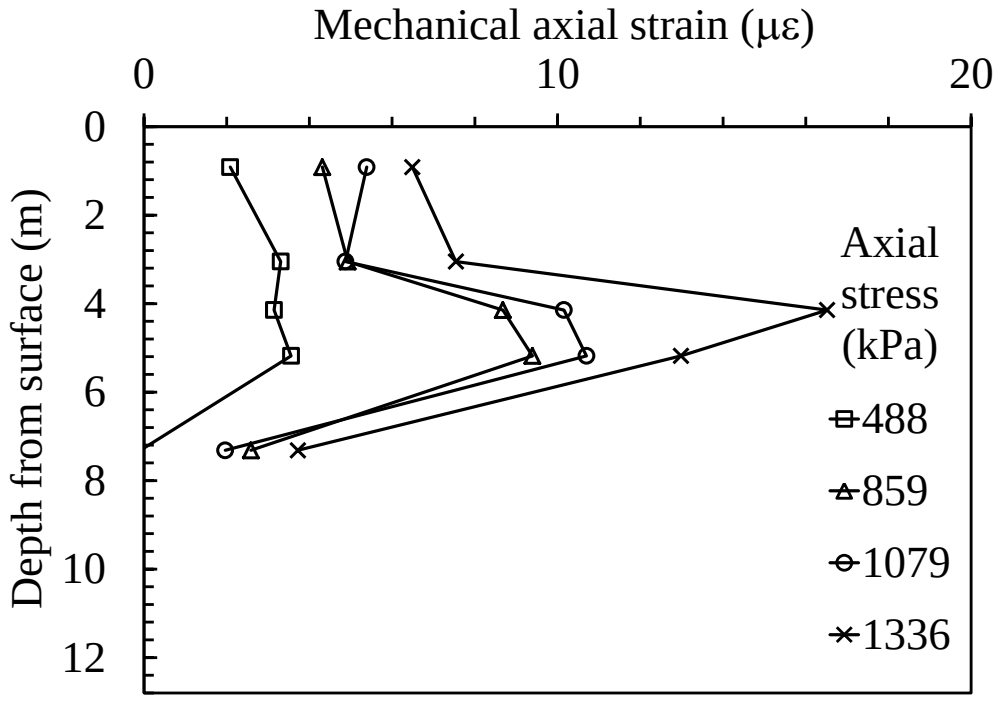

Figure 6.3.3-16 Prototype strain profile during loading for the heated (ΔT = 18 °C) loading test on the semi-floating foundation in Bonny silt.

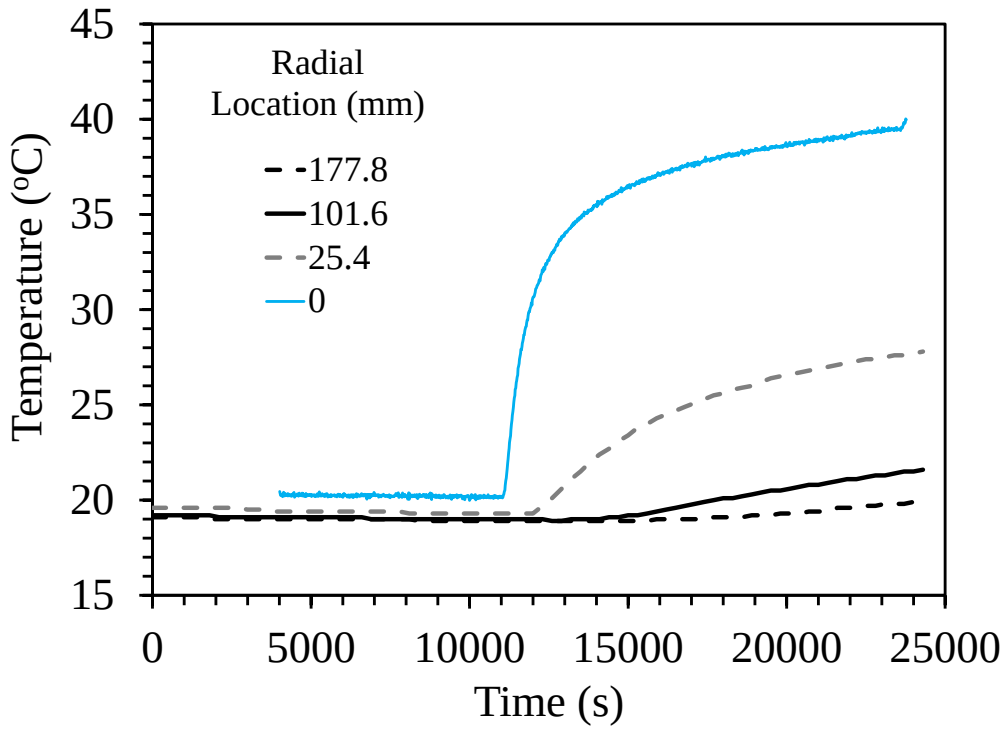

Figure 6.3.3-17 Temperature readings from dielectric sensors at radial locations for the heated (ΔT = 18 °C) loading test on the semi-floating foundation in Bonny silt.

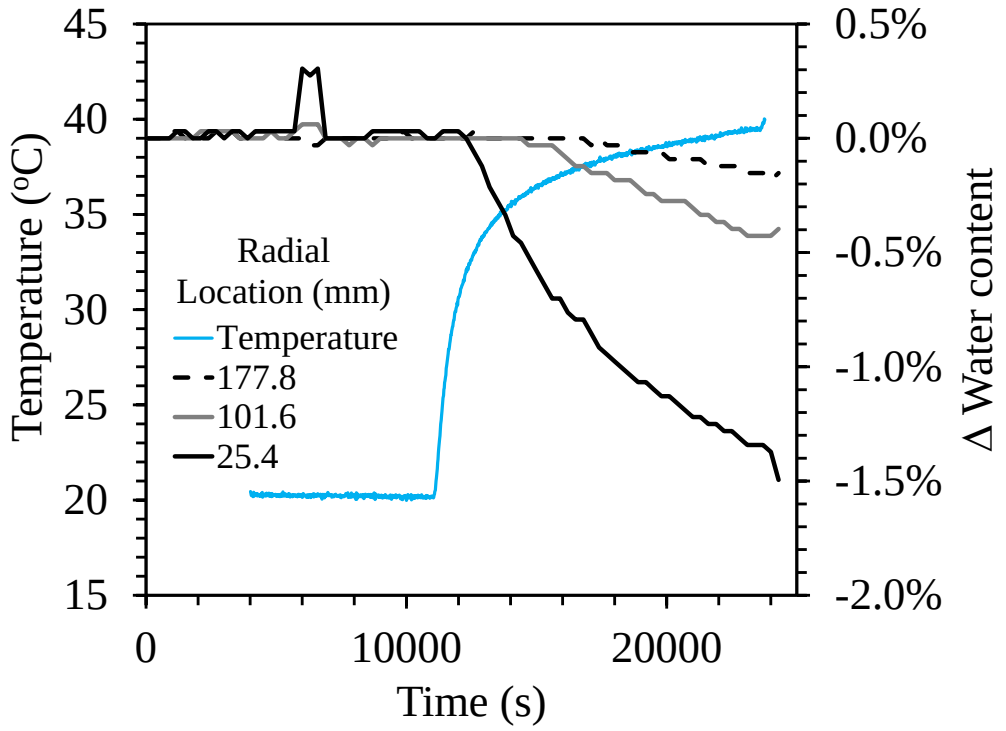

Figure 6.3.3-18 Change in water content at radial locations along with foundation temperature for the heated (ΔT = 18 °C) loading test on the semi-floating foundation in Bonny silt.

6.3.4 Results from Test S-BS-CL-Cooled

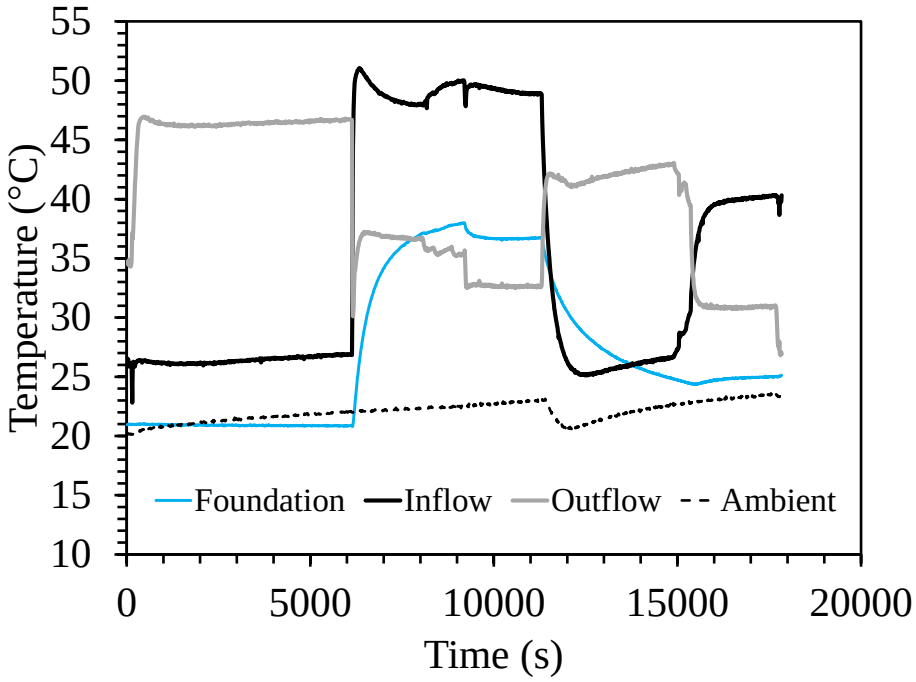

Figure 6.3.4-1 Temperatures during testing for the cooled loading test on the semi-floating foundation in Bonny silt.

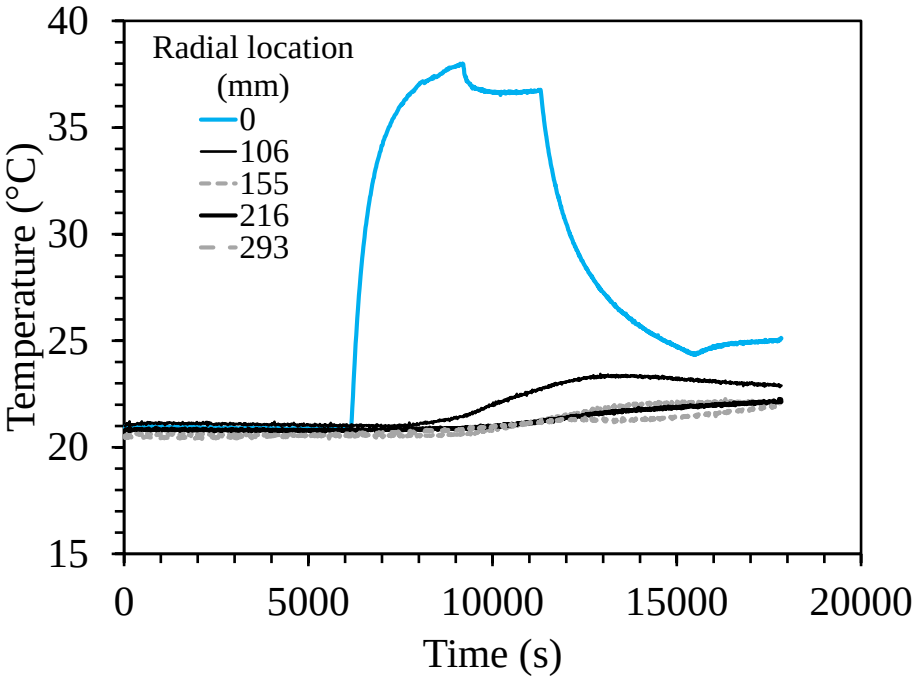

Figure 6.3.4-2 Average temperatures of foundation and four thermal probes for the cooled loading test on the semi-floating foundation in Bonny silt.

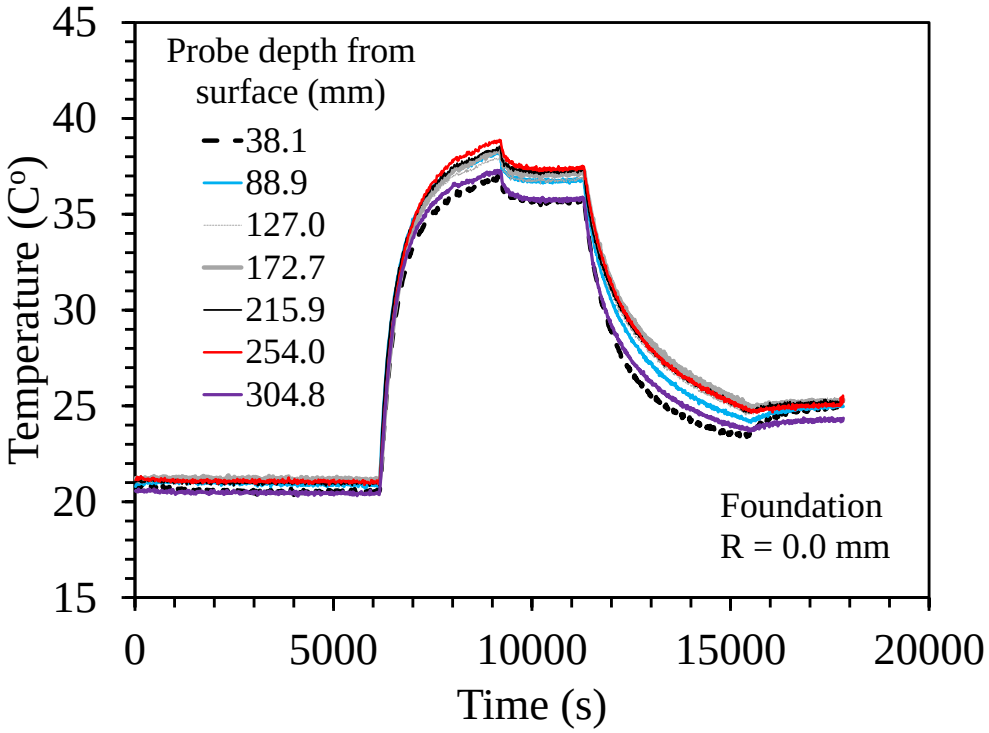

Figure 6.3.4-3 Foundation temperatures for the cooled loading test on the semi-floating foundation in Bonny silt.

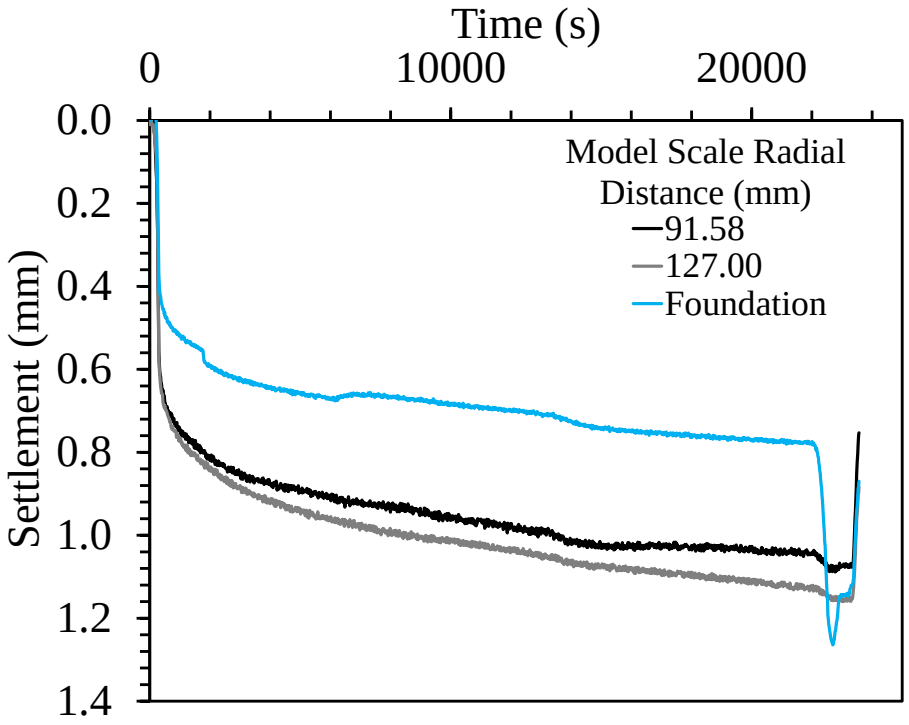

Figure 6.3.4-4 Model scale settlements with spin up for the cooled loading test on the semi-floating foundation in Bonny silt.

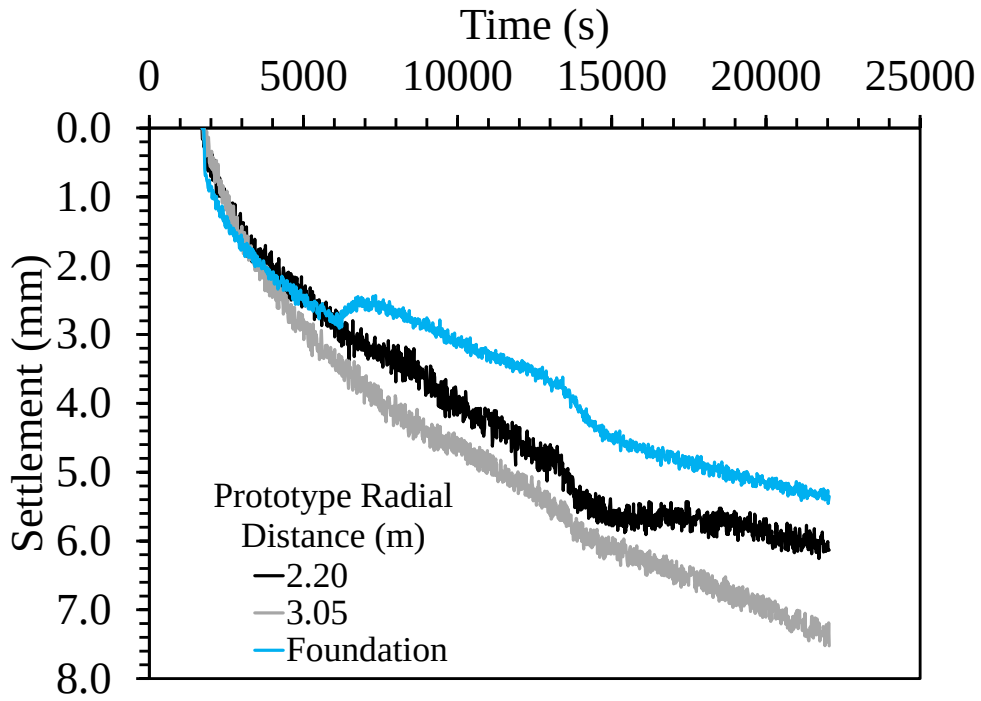

Figure 6.3.4-5 Prototype settlements after spin up for the cooled loading test on the semi-floating foundation in Bonny silt.

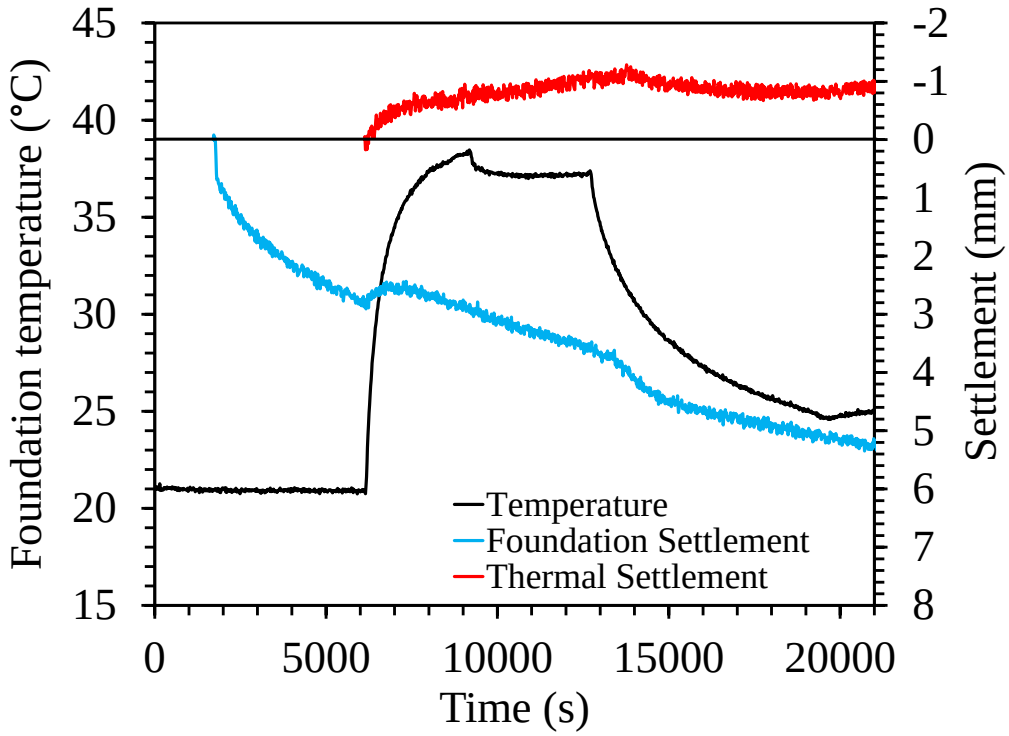

Figure 6.3.4-6 Foundation temperature, overall foundation settlement, and thermal settlement for the cooled loading test on the semi-floating foundation in Bonny silt.

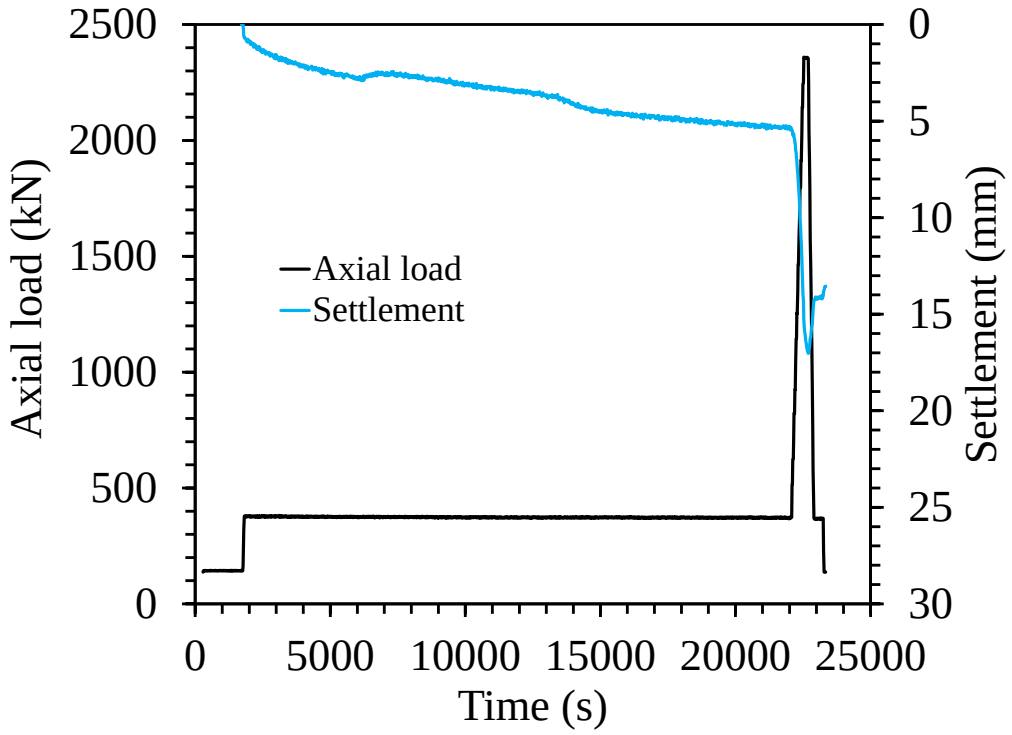

Figure 6.3.4-7 Prototype foundation settlement and associated applied axial load for the cooled loading test on the semi-floating foundation in Bonny silt.

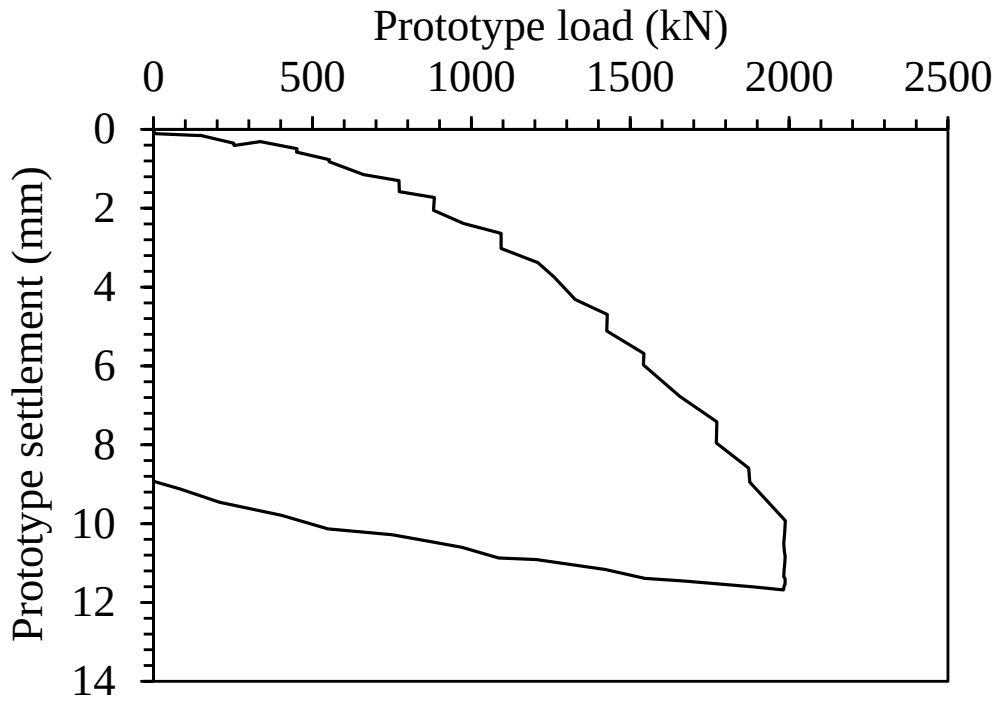

Figure 6.3.4-8 Prototype load settlement curve for the cooled loading test on the semi-floating foundation in Bonny silt.

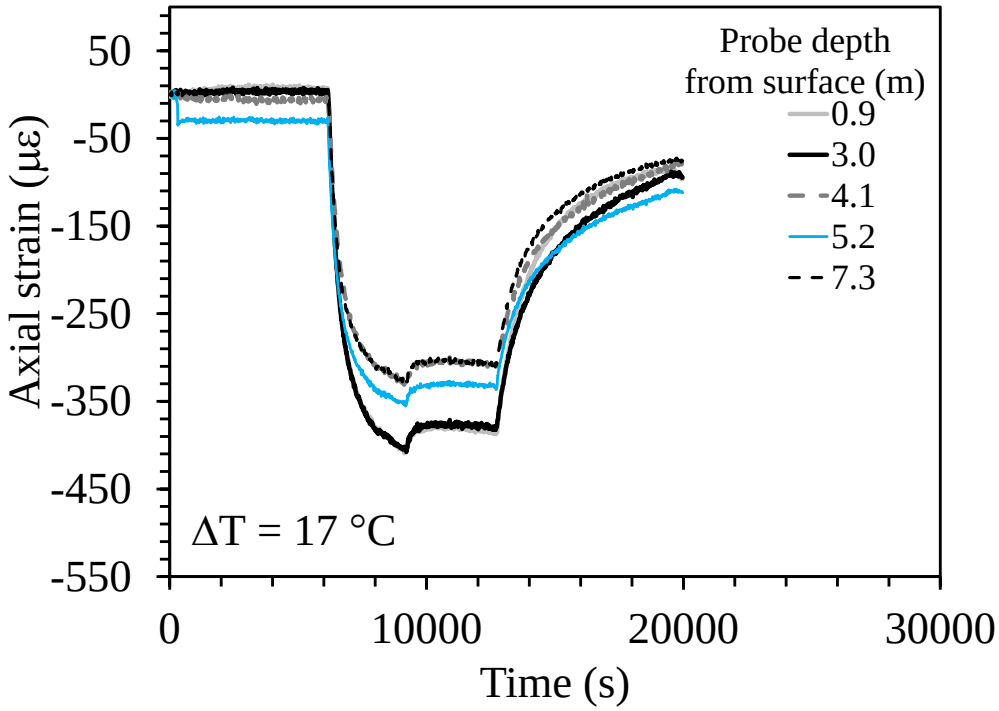

Figure 6.3.4-9 Axial strain time series for the cooled loading test on the semi-floating foundation in Bonny silt.

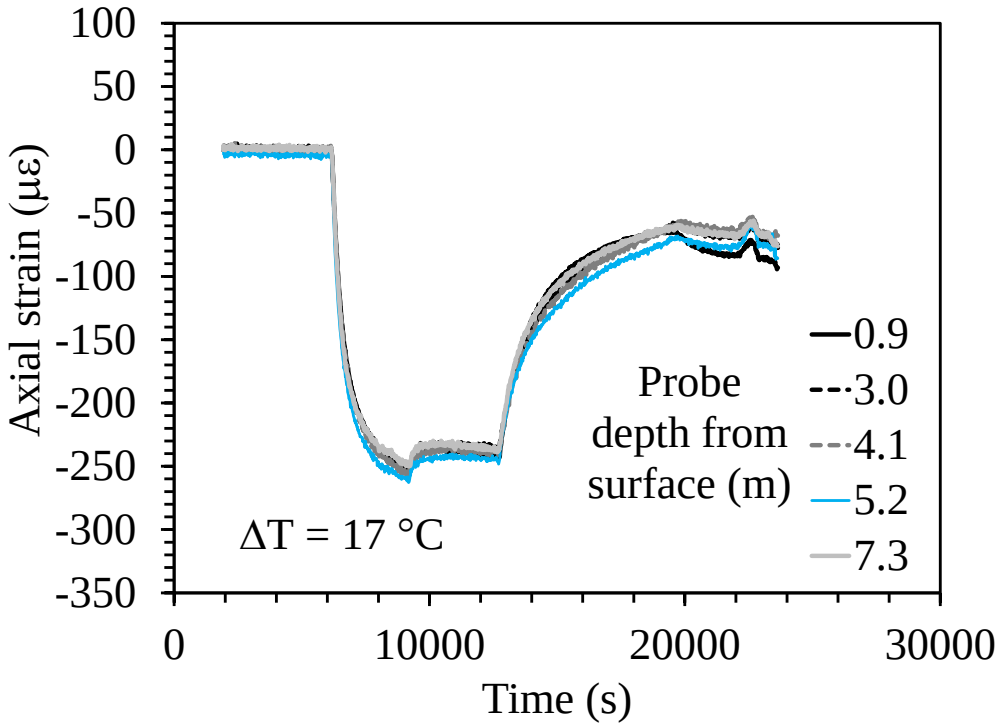

Figure 6.3.4-10 Axial strains during heating and cooling for the cooled loading test on the semi-floating foundation in Bonny silt.

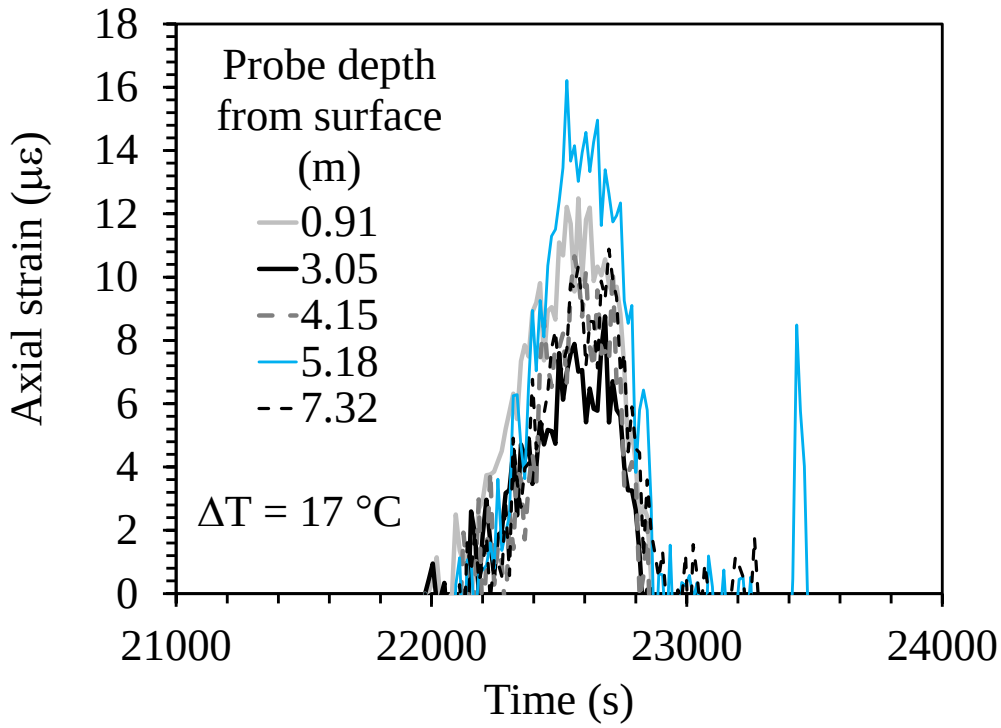

Figure 6.3.4-11 Axial strain during load test for the cooled loading test on the semi-floating foundation in Bonny silt.

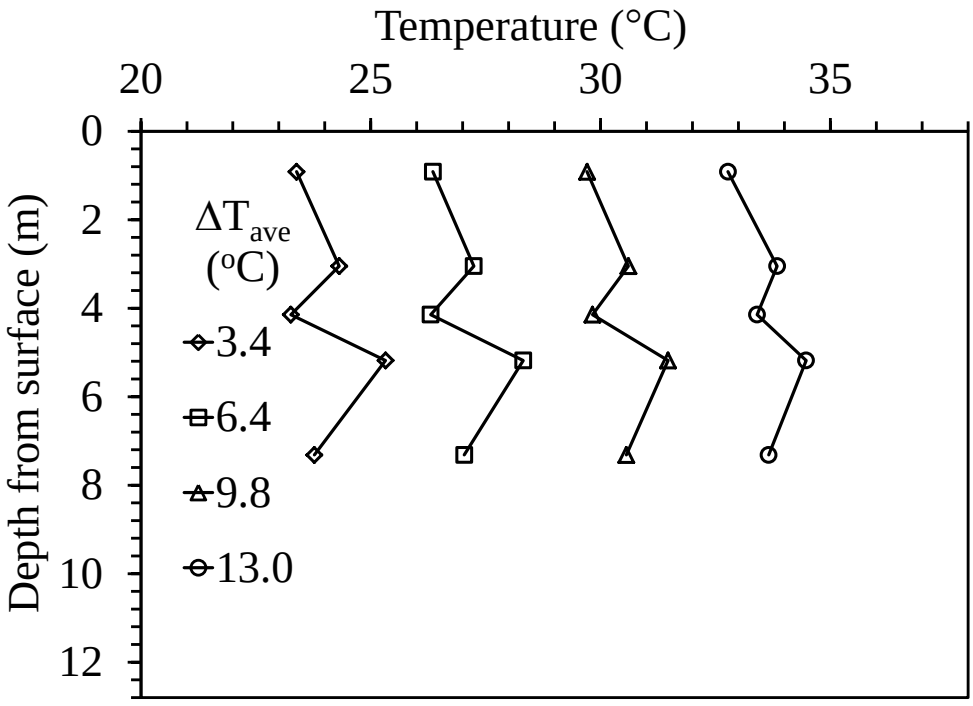

Figure 6.3.4-12 Temperature profiles for the cooled loading test on the semi-floating foundation in Bonny silt.

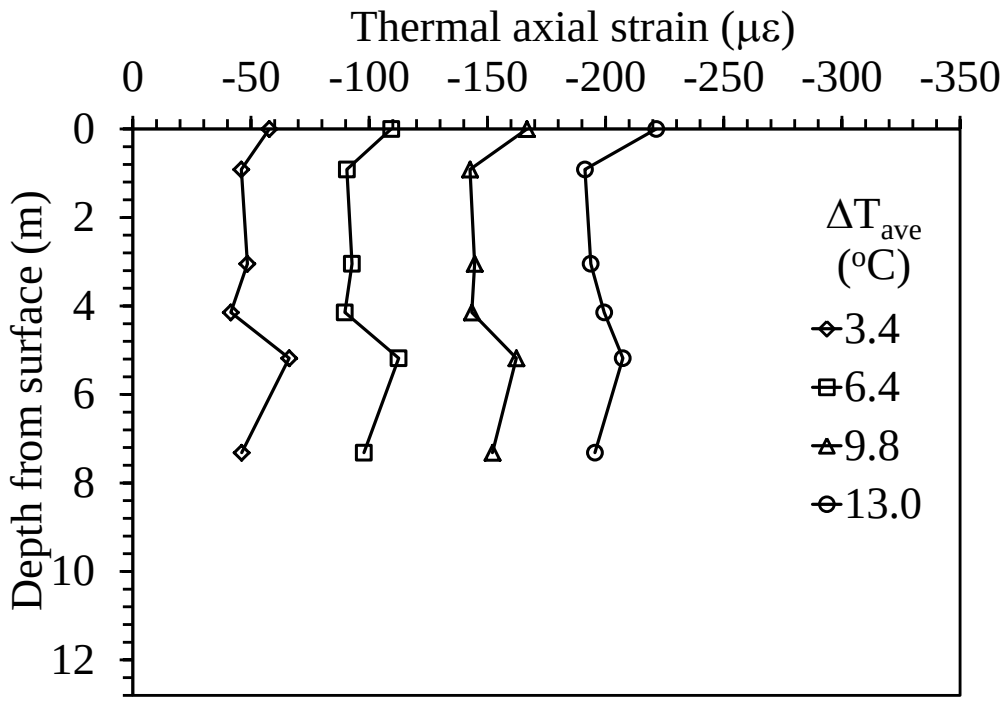

Figure 6.3.4-13 Prototype thermal axial strain profile for the cooled loading test on the semi-floating foundation in Bonny silt.

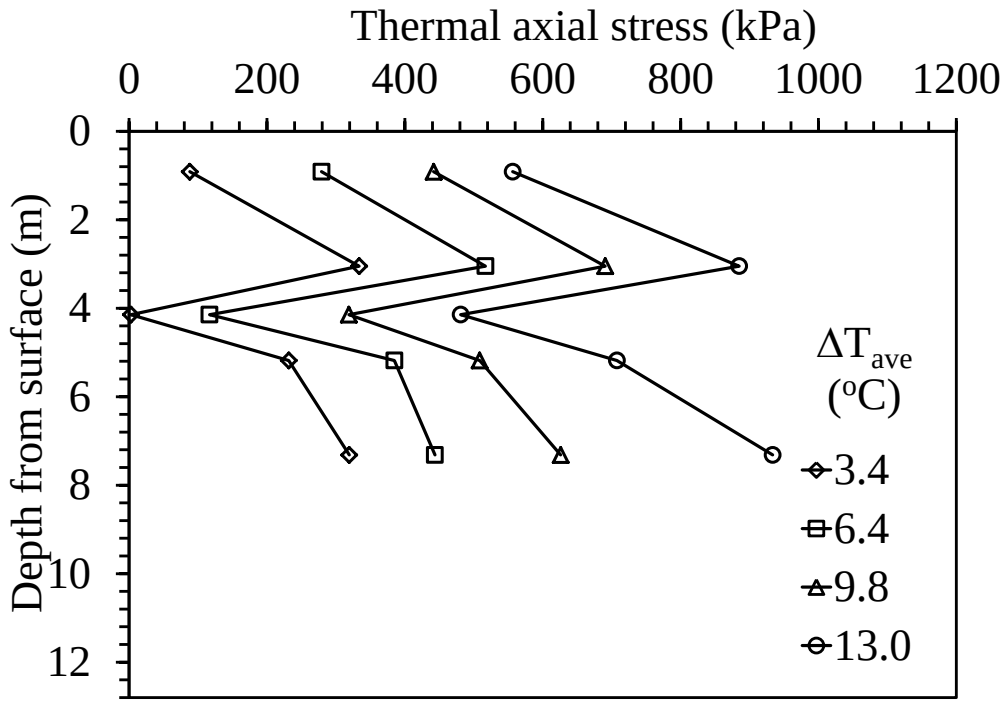

Figure 6.3.4-14 Prototype thermal stress profile for the cooled loading test on the semi-floating foundation in Bonny silt.

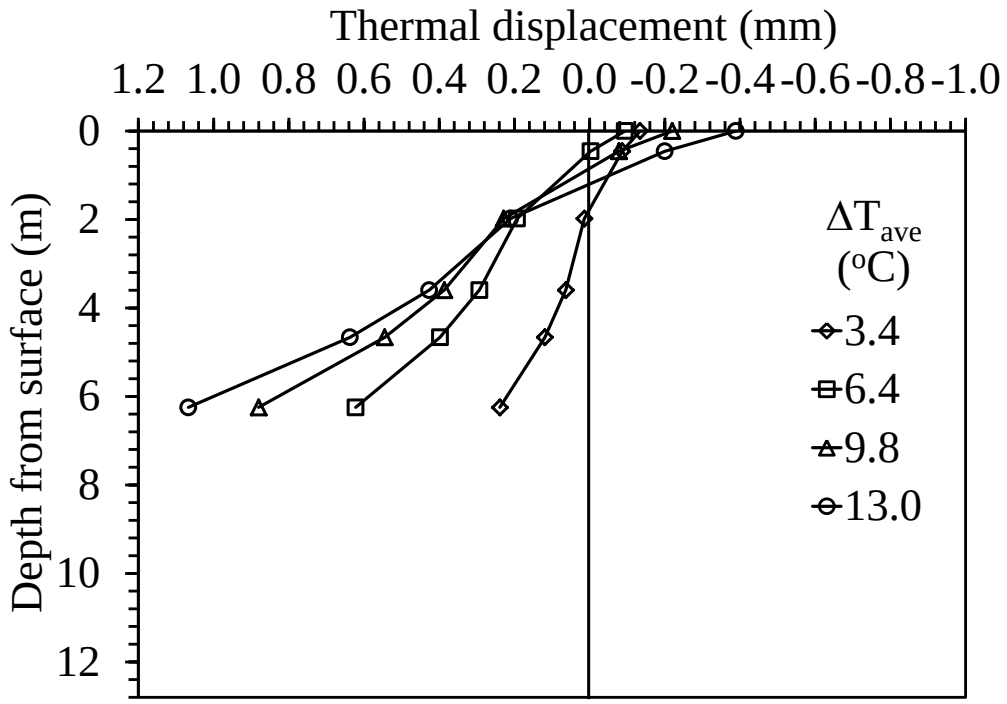

Figure 6.3.4-15 Thermal axial displacements for the cooled loading test on the semi-floating foundation in Bonny silt.

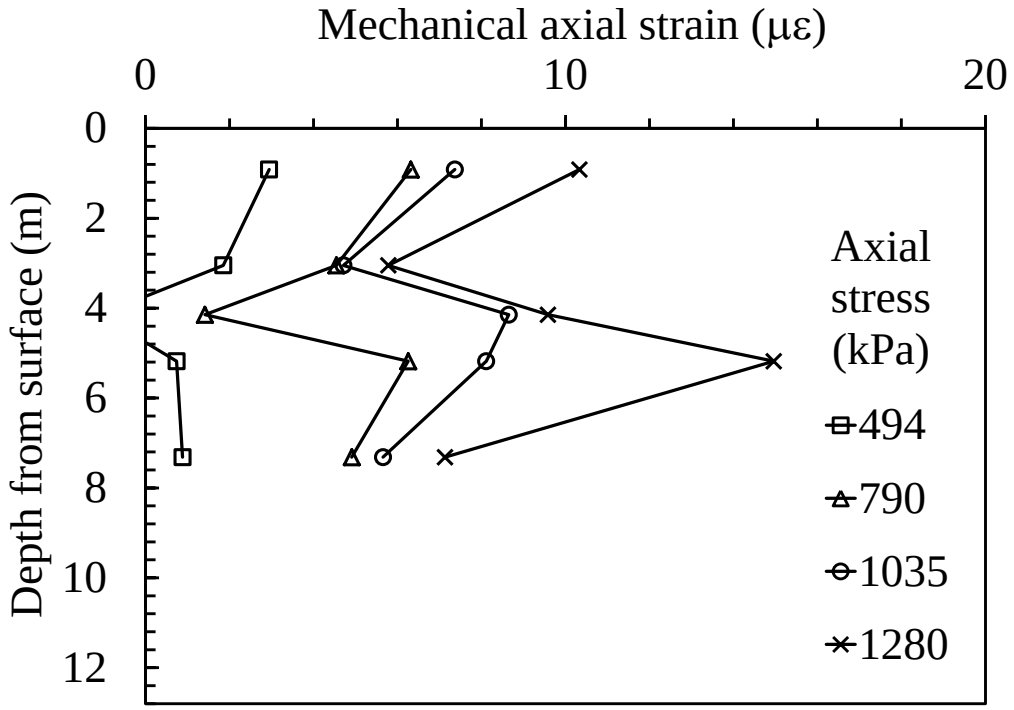

Figure 6.3.4-16 Prototype strain profile during loading for the cooled loading test on the semi-floating foundation in Bonny silt.

6.3.5 Results from Test S-BS-CL Cyclic

Table 6-5 Summary of S-BS-CL heat cycles.

Heat Cycle	Final Temperature	ΔT	Total Heat Time	Initial Load	Final Load
	(°C)	(°C)	(min)	(kN)	(kN)
1	34.8	14.7	61	365	No Load
2	27.1	-7.7	32	365	No Load
3	35	7.9	13	365	No Load
4	27.3	-7.7	29	365	No Load
5	36.1	8.8	17	365	No Load
6	27.4	-8.7	35	365	No Load
7	35.4	8	77	365	2440

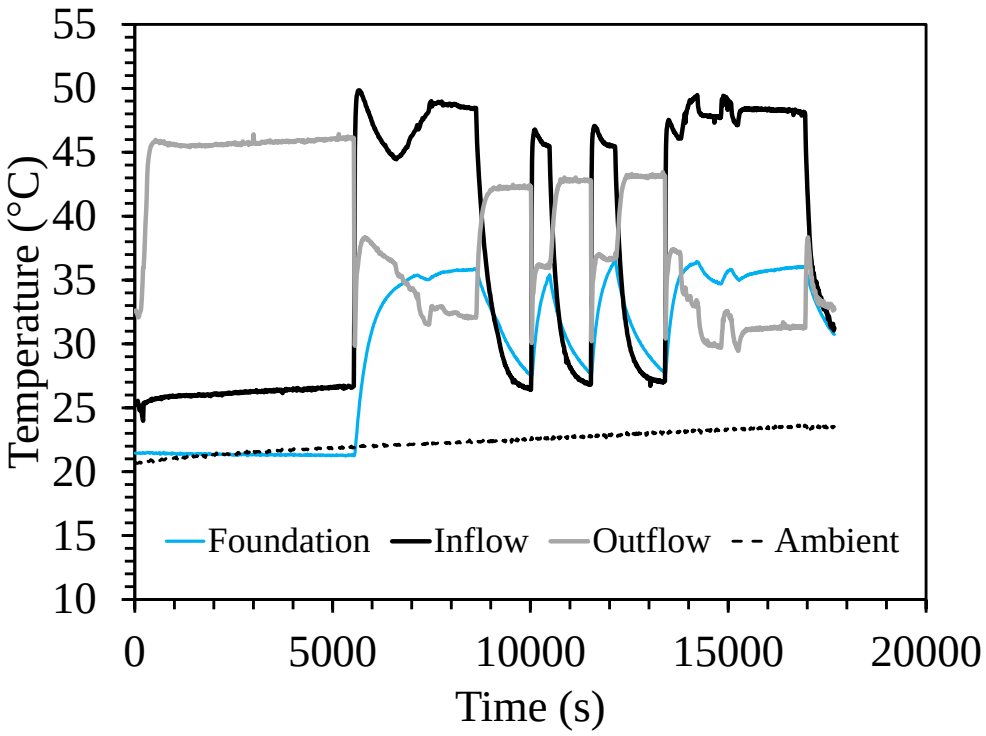

Figure 6.3.5-1 Temperatures during testing for the cyclic loading test on the semi-floating foundation in Bonny silt.

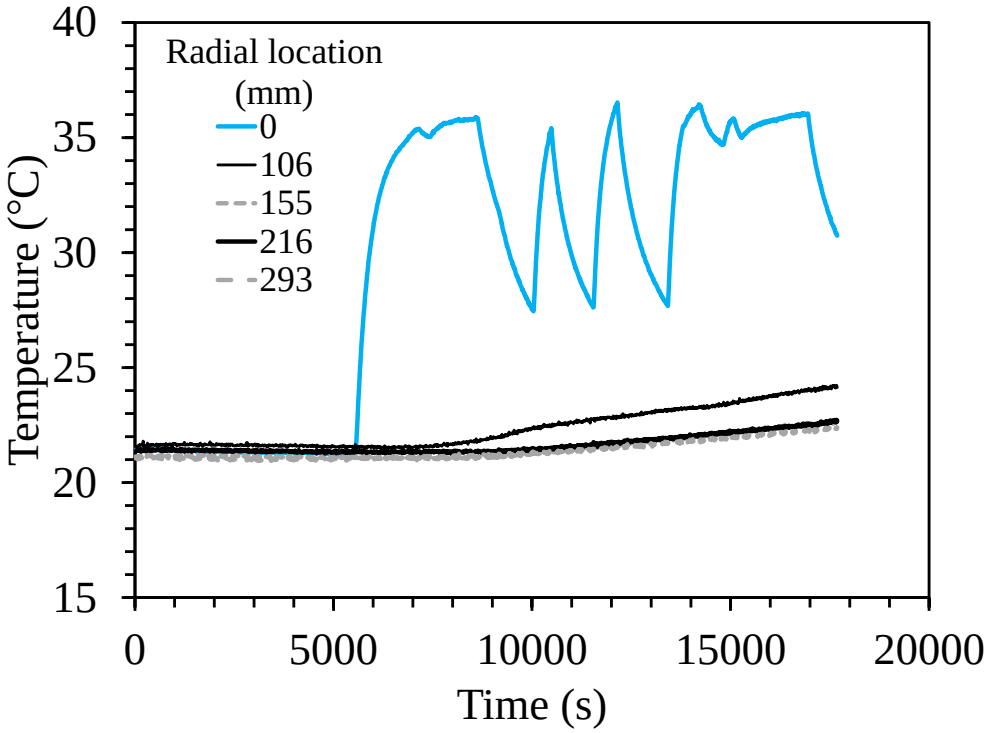

Figure 6.3.5-2 Average temperatures of foundation and four thermal probes for the cyclic loading test on the semi-floating foundation in Bonny silt.

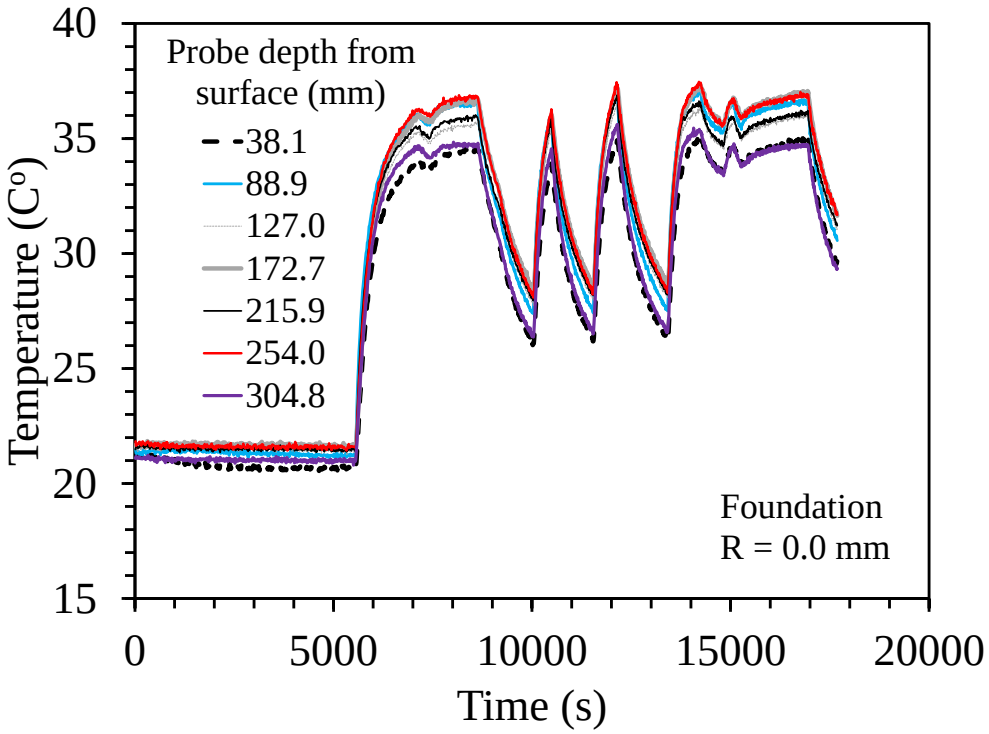

Figure 6.3.5-3 Foundation temperatures for the cyclic loading test on the semi-floating foundation in Bonny silt.

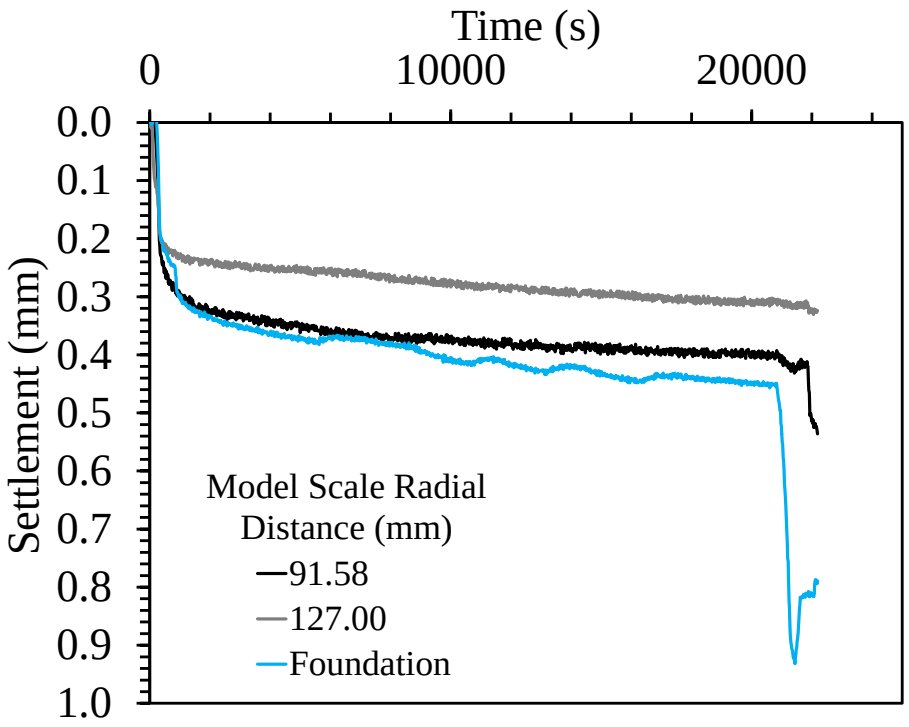

Figure 6.3.5-4 Model scale settlements with spin up for the cyclic loading test on the semi-floating foundation in Bonny silt.

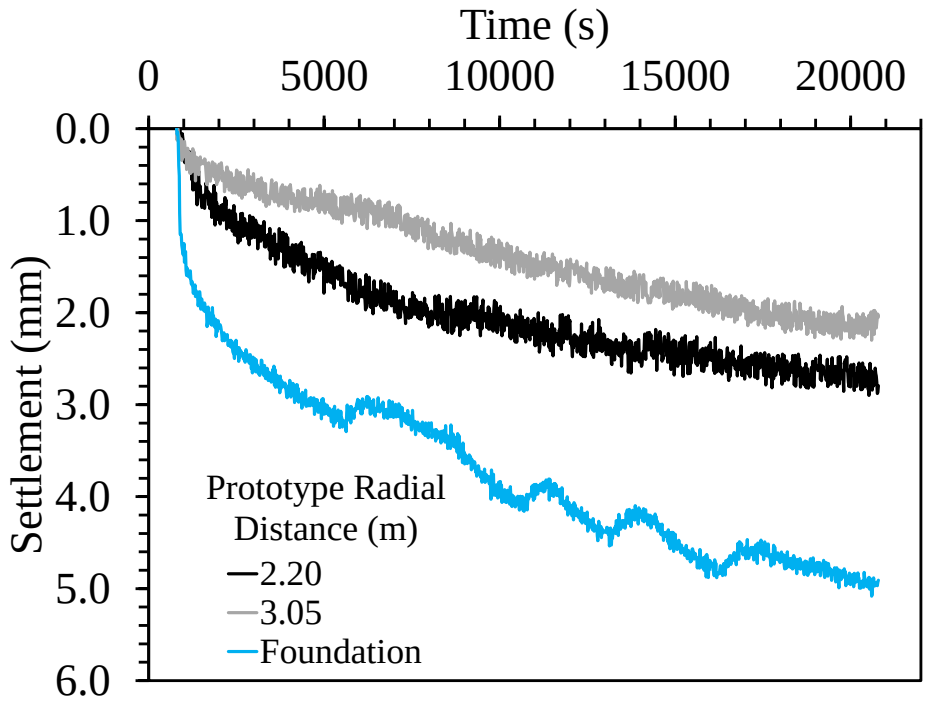

Figure 6.3.5-5 Prototype settlements after spin up for the cyclic loading test on the semi-floating foundation in Bonny silt.

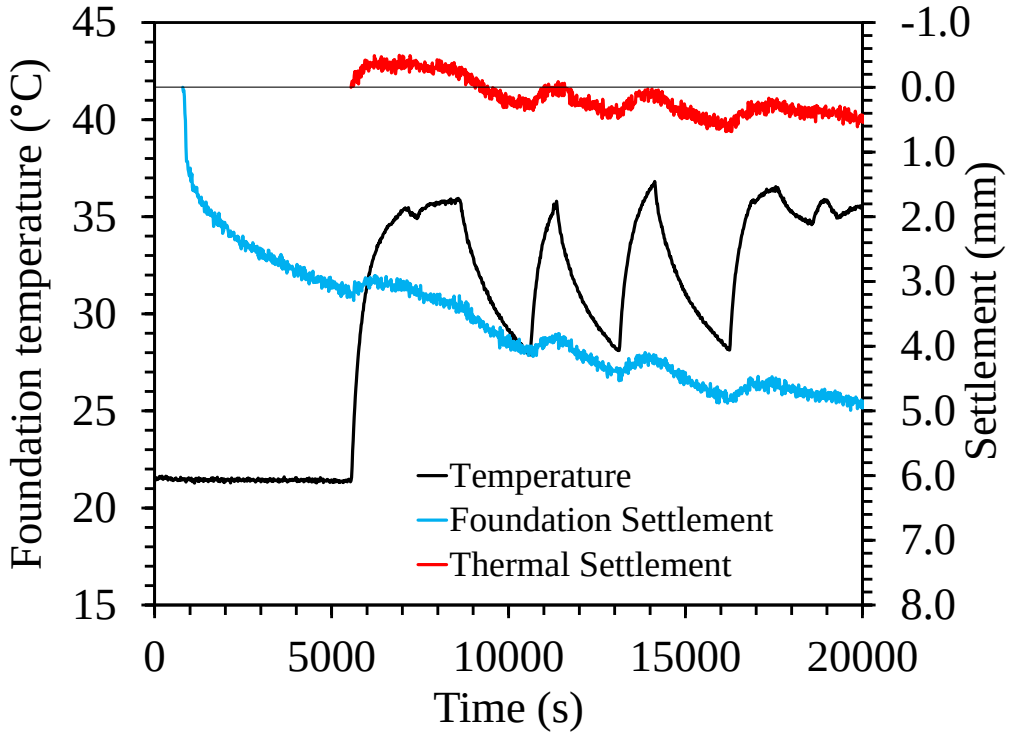

Figure 6.3.5-6 Foundation temperature, overall foundation settlement, and thermal settlement for the cyclic loading test on the semi-floating foundation in Bonny silt.

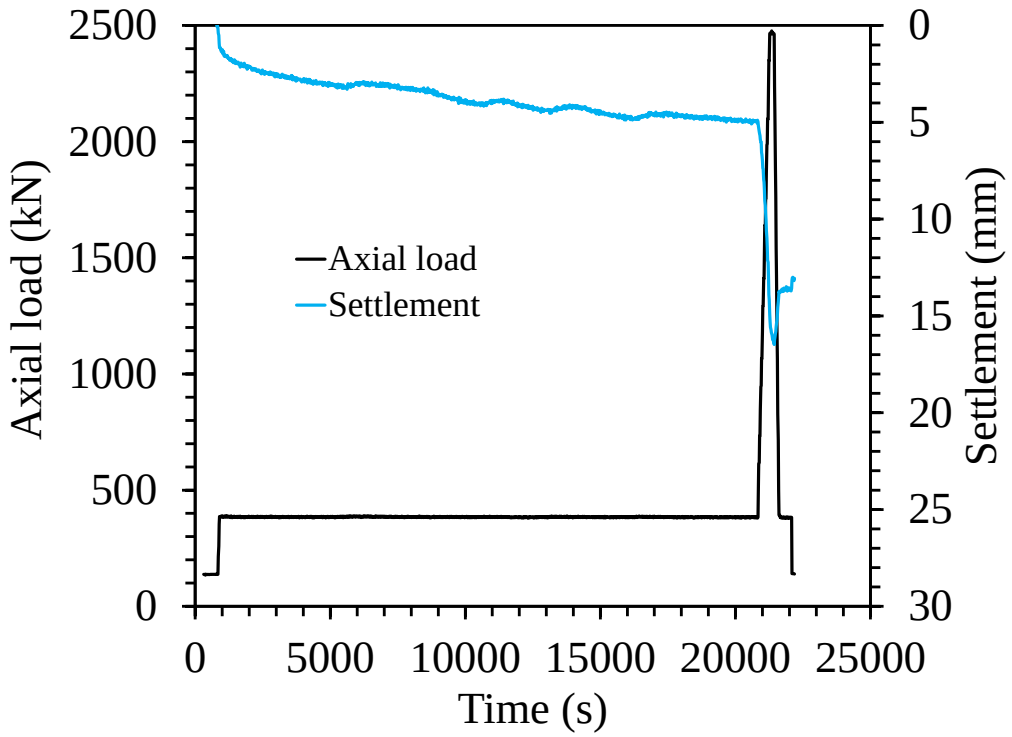

Figure 6.3.5-7 Prototype axial load and settlement for the cyclic loading test on the semi-floating foundation in Bonny silt.

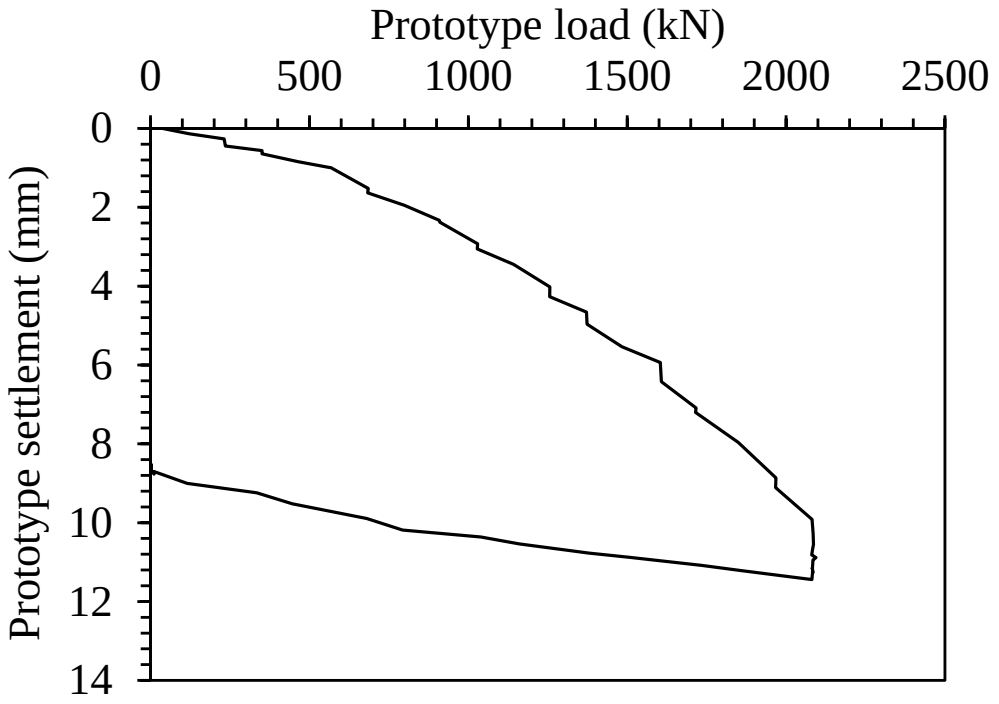

Figure 6.3.5-8 Prototype load settlement curve for the cyclic loading test on the semi-floating foundation in Bonny silt.

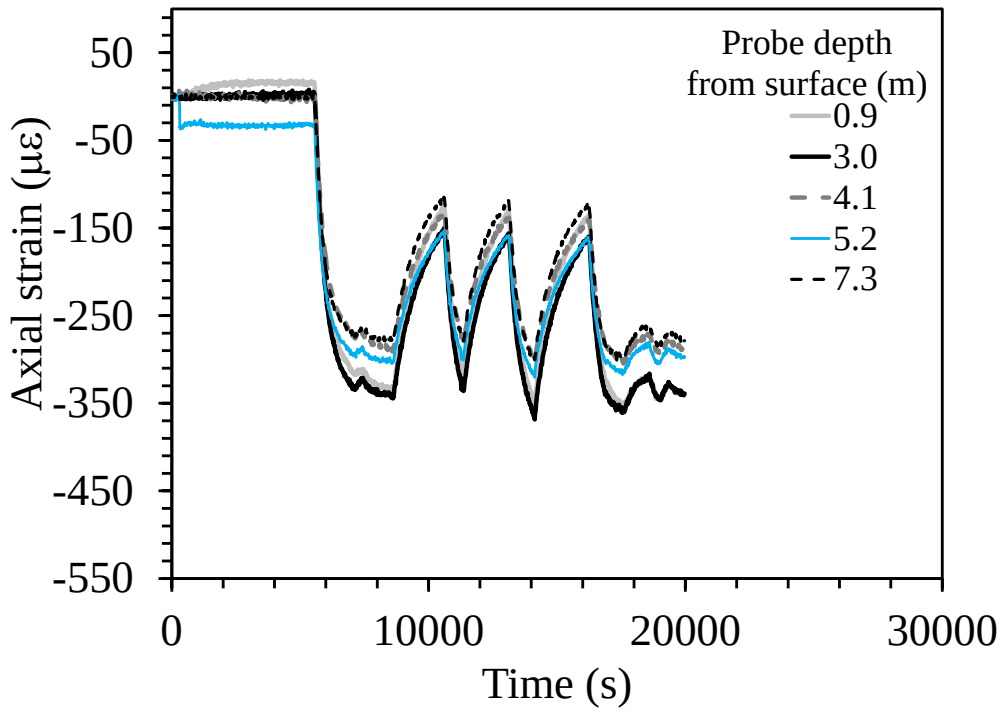

Figure 6.3.5-9 Axial strain time series for the cyclic loading test on the semi-floating foundation in Bonny silt.

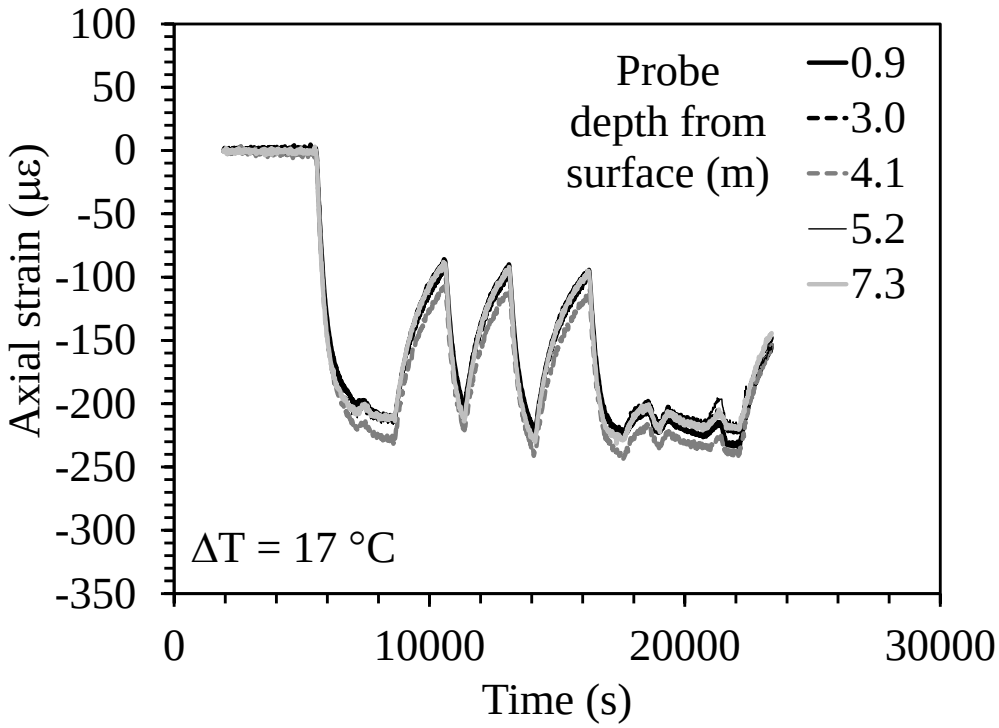

Figure 6.3.5-10 Axial strains during heating for the cyclic loading test on the semi-floating foundation in Bonny silt.

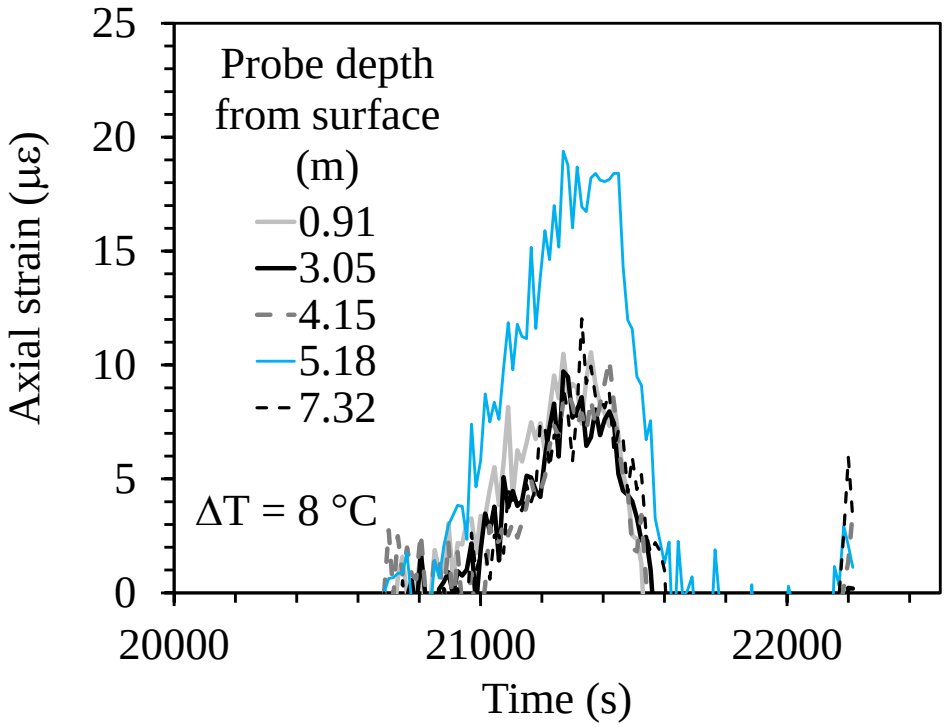

Figure 6.3.5-11 Axial strains during load test for the cyclic loading test on the semi-floating foundation in Bonny silt.

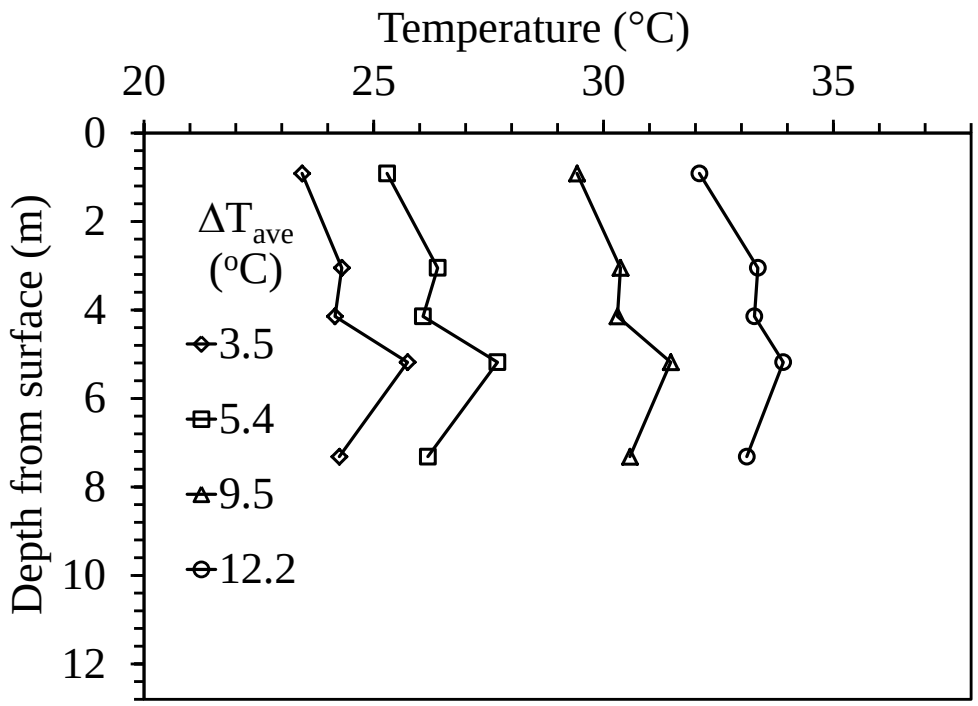

Figure 6.3.5-12 Temperature profiles for the cyclic loading test on the semi-floating foundation in Bonny silt.

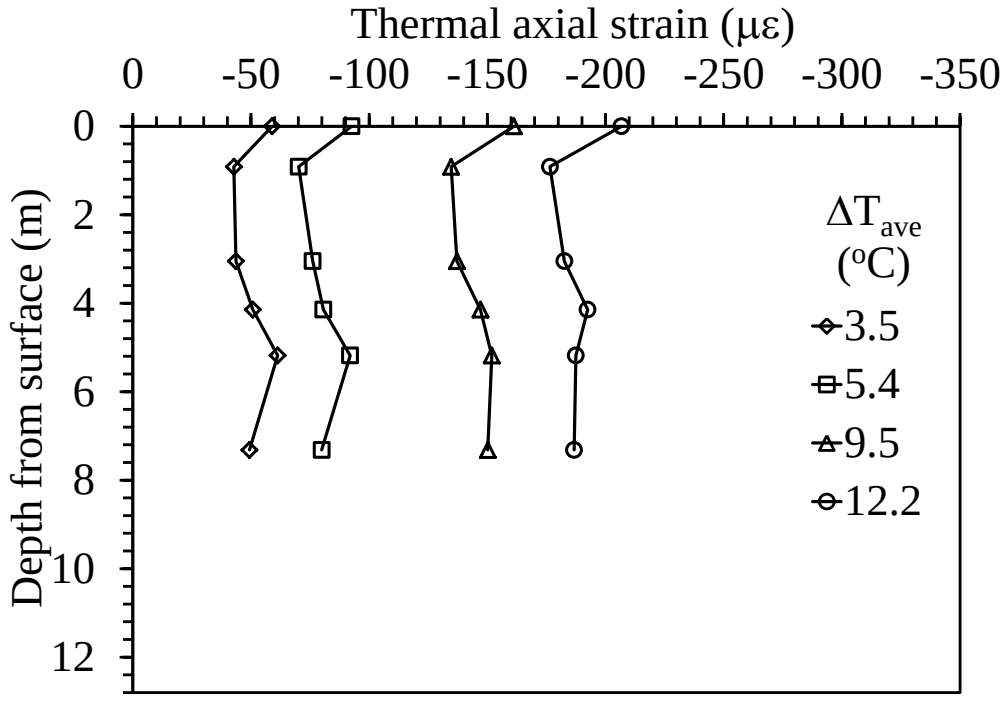

Figure 6.3.5-13 Prototype thermal axial strain profile for the cyclic loading test on the semi-floating foundation in Bonny silt.

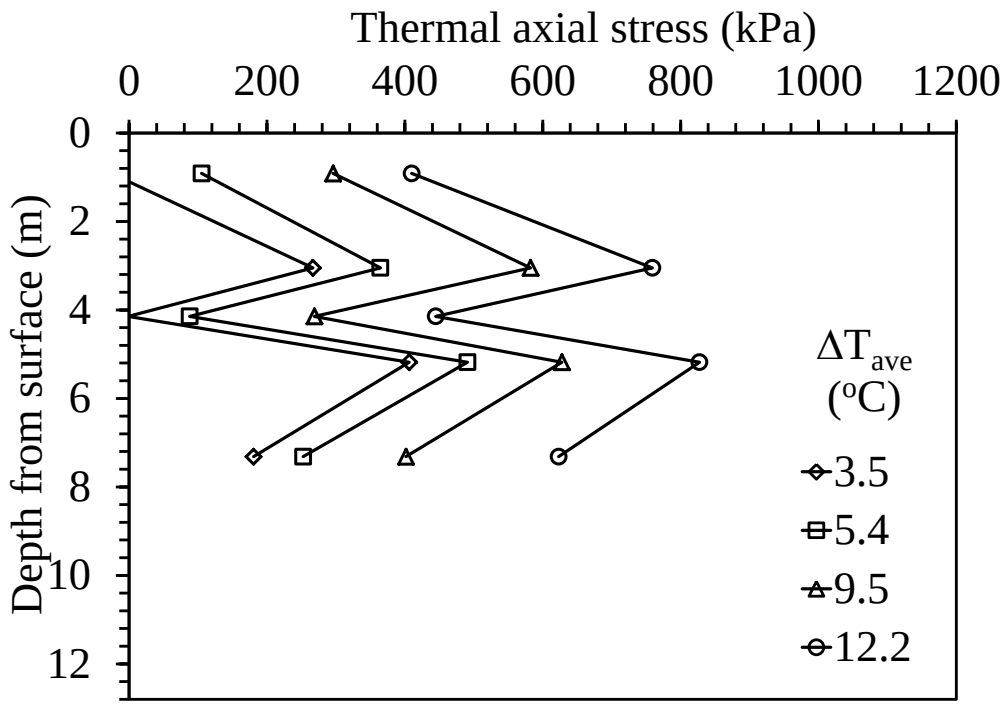

Figure 6.3.5-14 Prototype thermal stress profile for the cyclic loading test on the semi-floating foundation in Bonny silt.

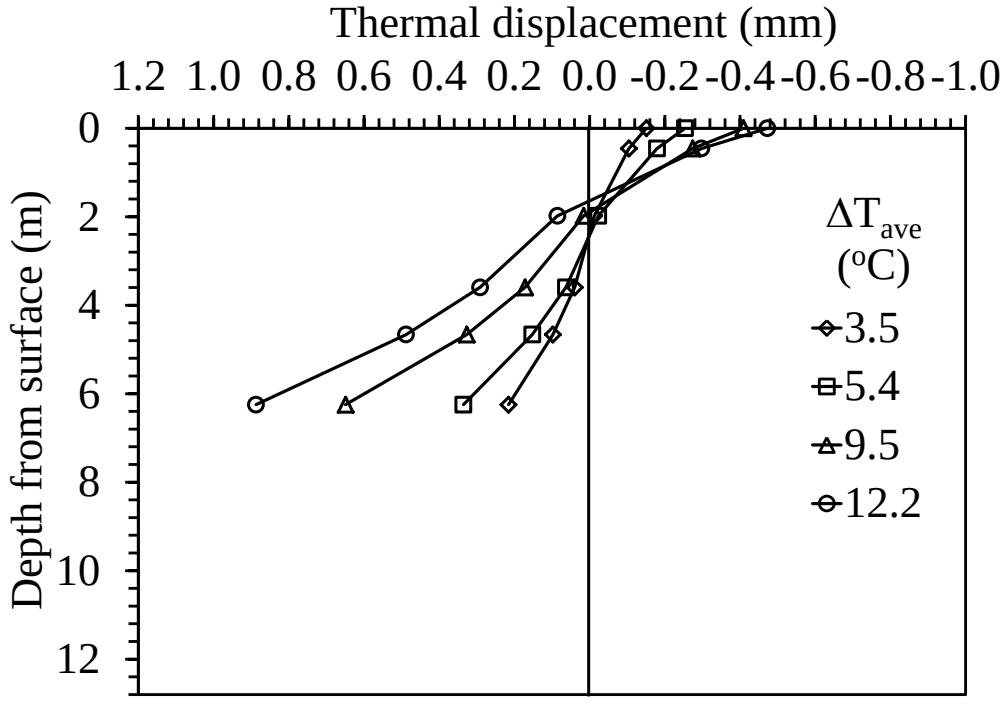

Figure 6.3.5-15 Thermal axial displacement profiles for the cyclic loading test on the semi-floating foundation in Bonny silt.

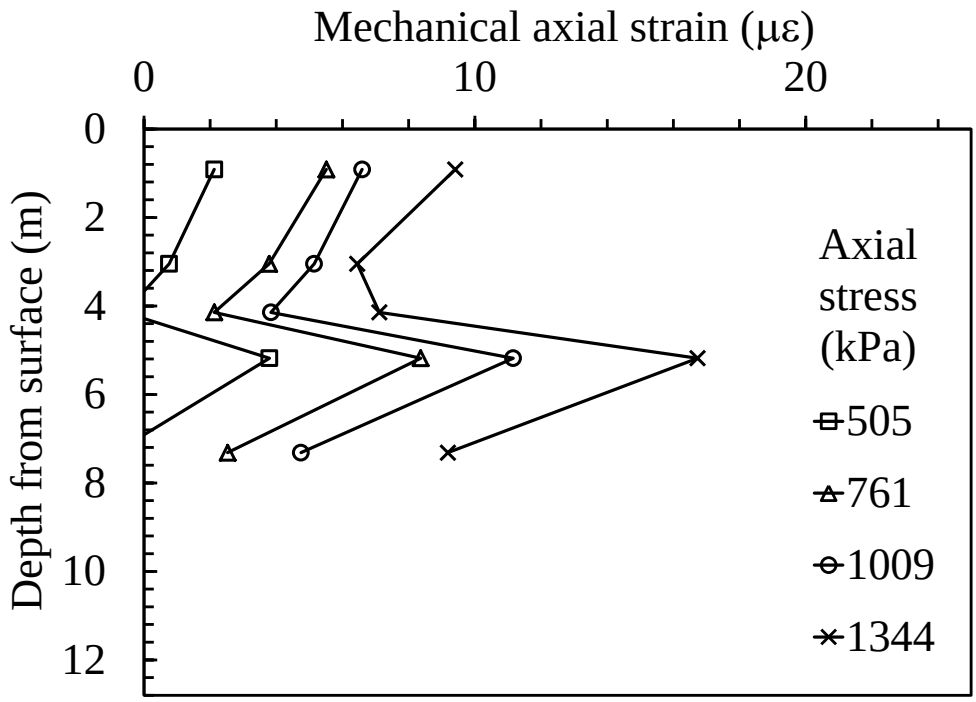

Figure 6.3.5-16 Prototype strain profile during loading for the cyclic loading test on the semi-floating foundation in Bonny silt.

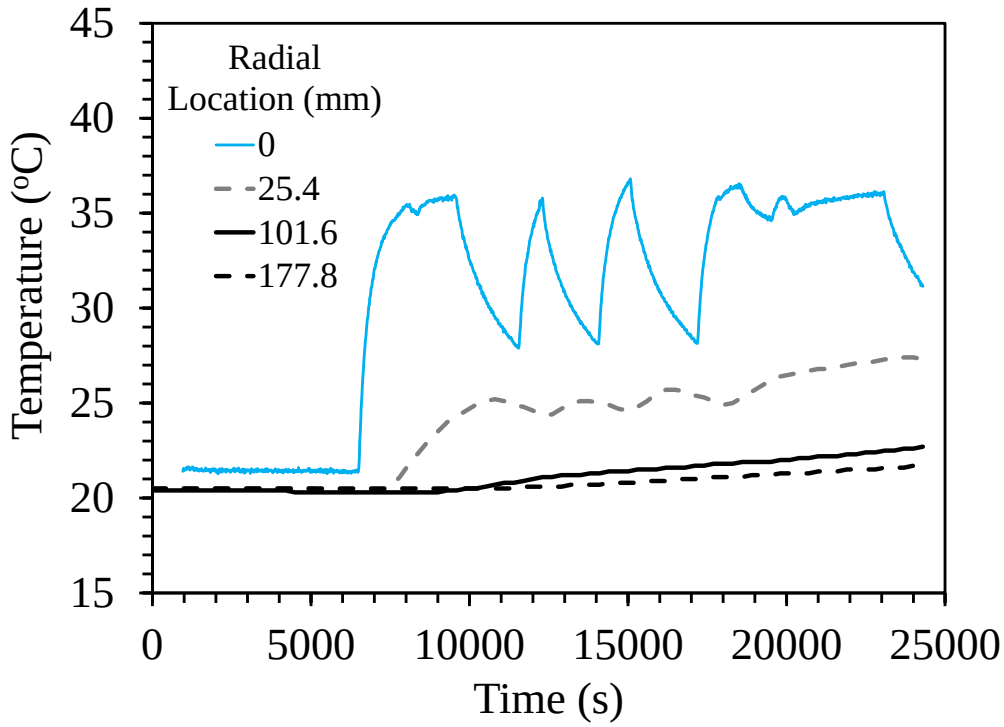

Figure 6.3.5-17 Temperature readings from dielectric sensors at radial locations for the cyclic loading test on the semi-floating foundation in Bonny silt.

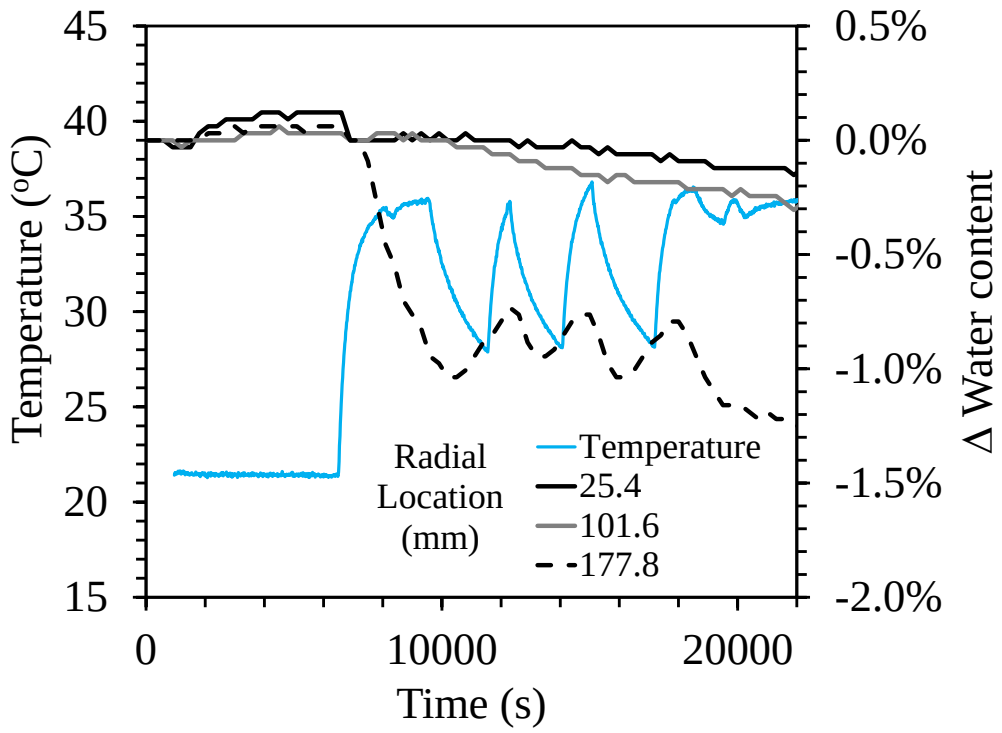

Figure 6.3.5-18 Change in water content at radial locations with foundation temperature for the cyclic loading test on the semi-floating foundation in Bonny silt.

6.4 End-Bearing Foundation Tests

A total five tests were performed on the end-bearing foundation. The first two tests presented investigate the impact of the end restraint boundary conditions. The staged loading tests investigate multiple loadings at various temperatures in both Nevada sand and Bonny silt. The effects of head end restraint conditions comparisons are presented in the following two sections. The load-control head restraint boundary conditions (used in all other tests) were compared with stiffness-control head restraint boundary conditions. The figures in this section also follow the format presented in Section 6.1.2. As discussed in Section 5.2.3, there is no ultimate load applied to the following two tests (as they are end-bearing foundations). A building load was applied followed by thermal loading. Both tests were tested a similar initial loads, but the stiffness control setup proved difficult to provide a precise load value. The thermal heating reached was also aimed to be similar and came within one degree of each other. It can be

seen in Figure 6.4.2-7 that the load increases as the foundation is heated for stiffness control as opposed to the load control condition in which the load remains at a constant value throughout the test as expected.

The end-bearing foundation tests were performed in staged and cyclic stages. Thus the plot layout is slightly different than those for the semi-floating foundations. Zeroed thermal settlement is zeroed at points before heating or cooling and is shown with the associated foundation temperature. The load settlement curve is shown for all of the loading instances of each tests and show equal stiffness regardless of the loading temperature.

6.4.1 Results from Test L-NS-ML-11

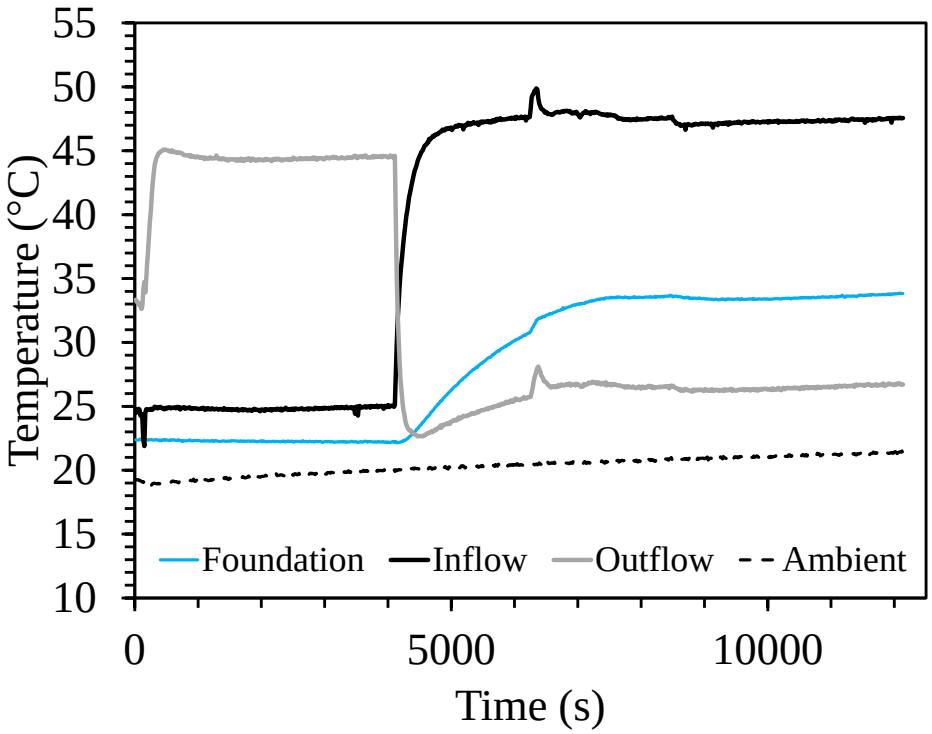

Figure 6.4.1-1 Temperatures during testing for the heated (ΔT = 11 °C) load control test on the end-bearing foundation in Nevada sand.

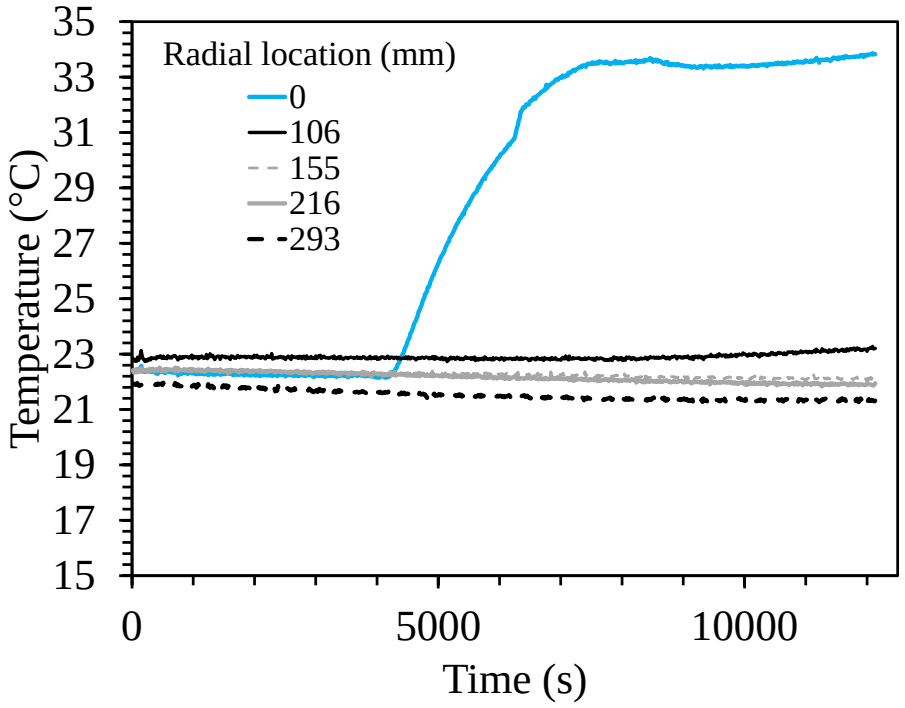

Figure 6.4.1-2 Average temperatures of foundation and four thermal probes for the heated (ΔT = 11 °C) load control test on the end-bearing foundation in Nevada sand.

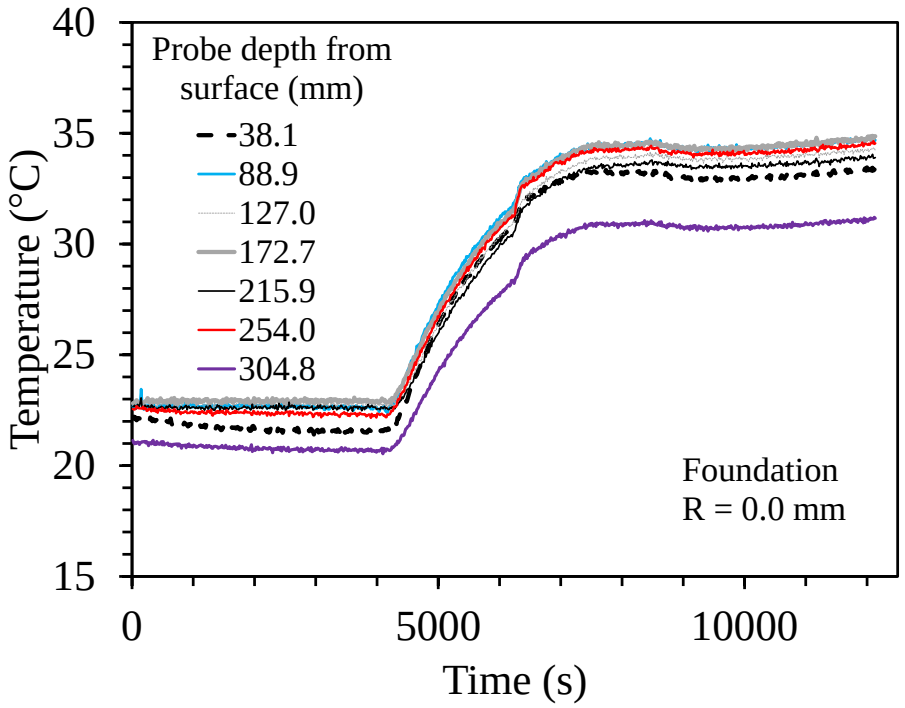

Figure 6.4.1-3 Foundation temperatures for the heated (ΔT = 11 °C) load control test on the end-bearing foundation in Nevada sand.

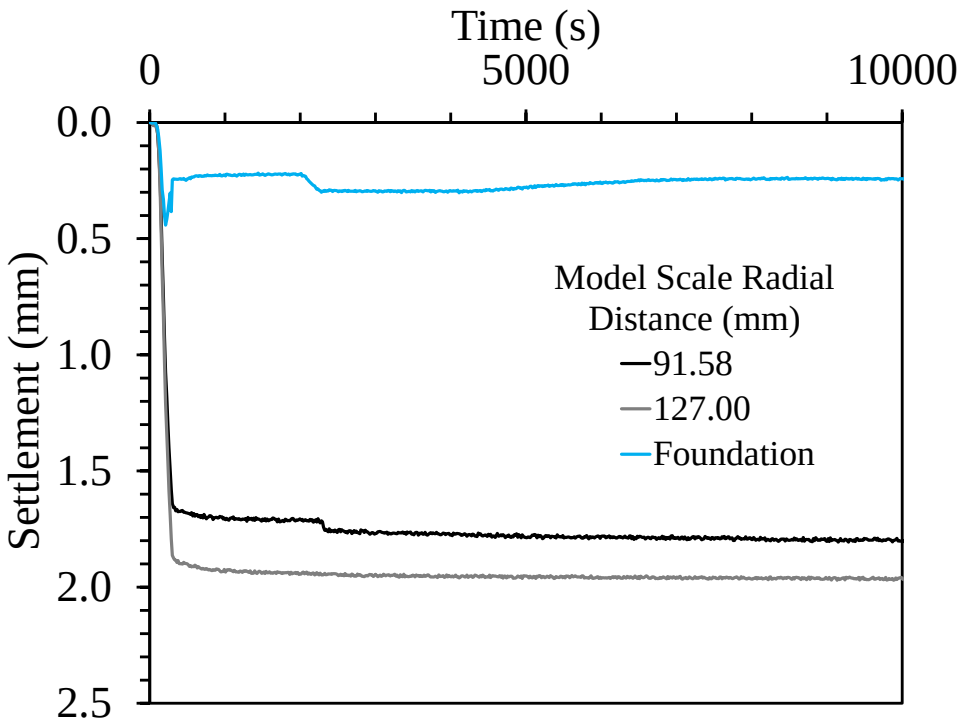

Figure 6.4.1-4 Model scale settlements with spin up for the heated (ΔT = 11 °C) load control test on the end-bearing foundation in Nevada sand.

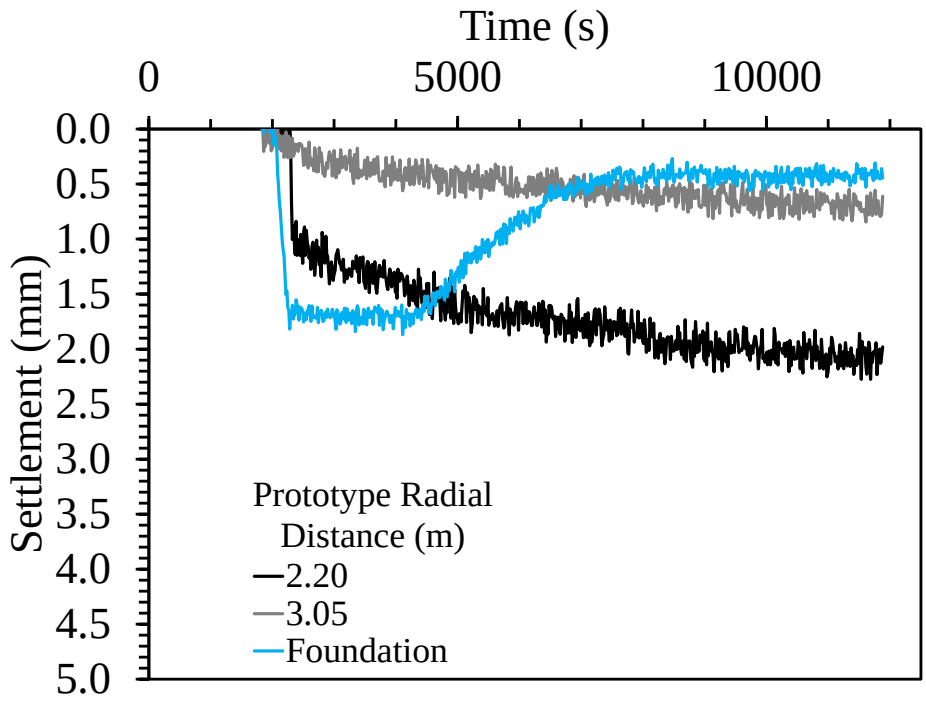

Figure 6.4.1-5 Prototype settlements after spin up for the heated (ΔT = 11 °C) load control test on the end-bearing foundation in Nevada sand.

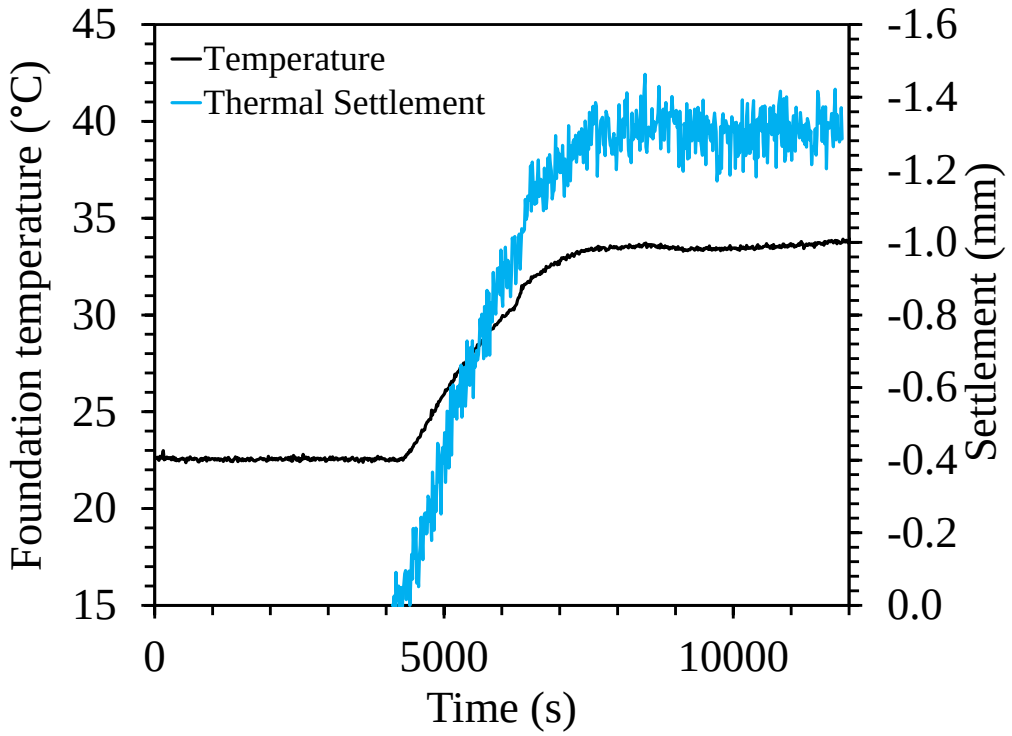

Figure 6.4.1-6 Prototype thermal expansion and temperature for the heated (ΔT = 11 °C) load control test on the end-bearing foundation in Nevada sand.

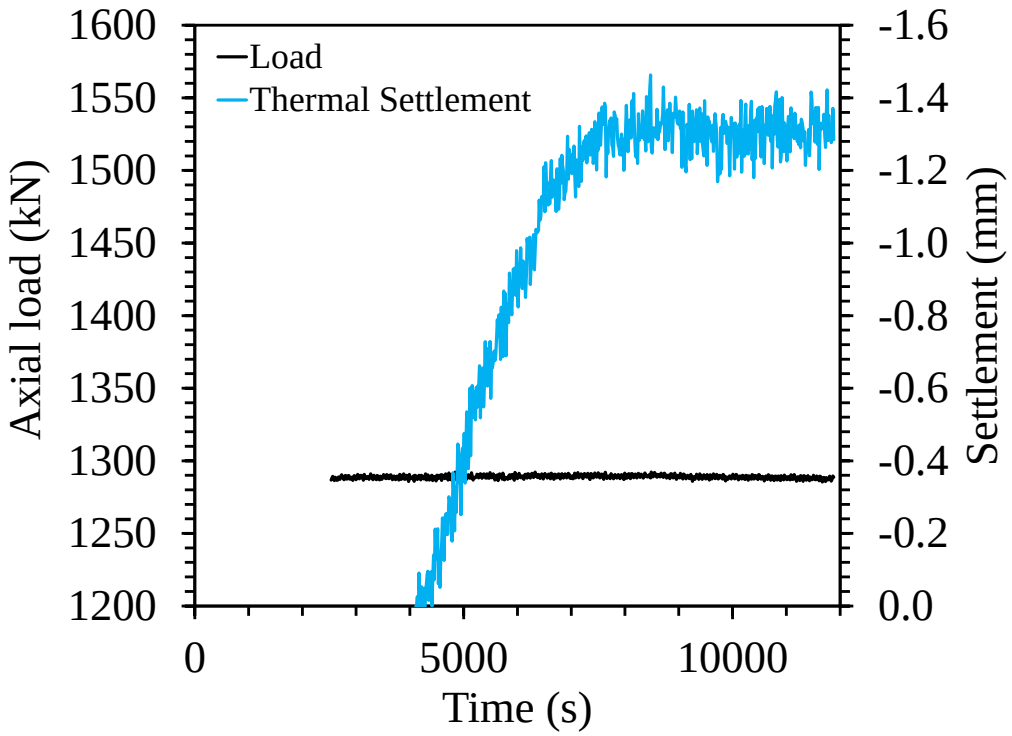

Figure 6.4.1-7 Prototype load and thermal expansion for the heated (ΔT = 11 °C) load control test on the end-bearing foundation in Nevada sand.

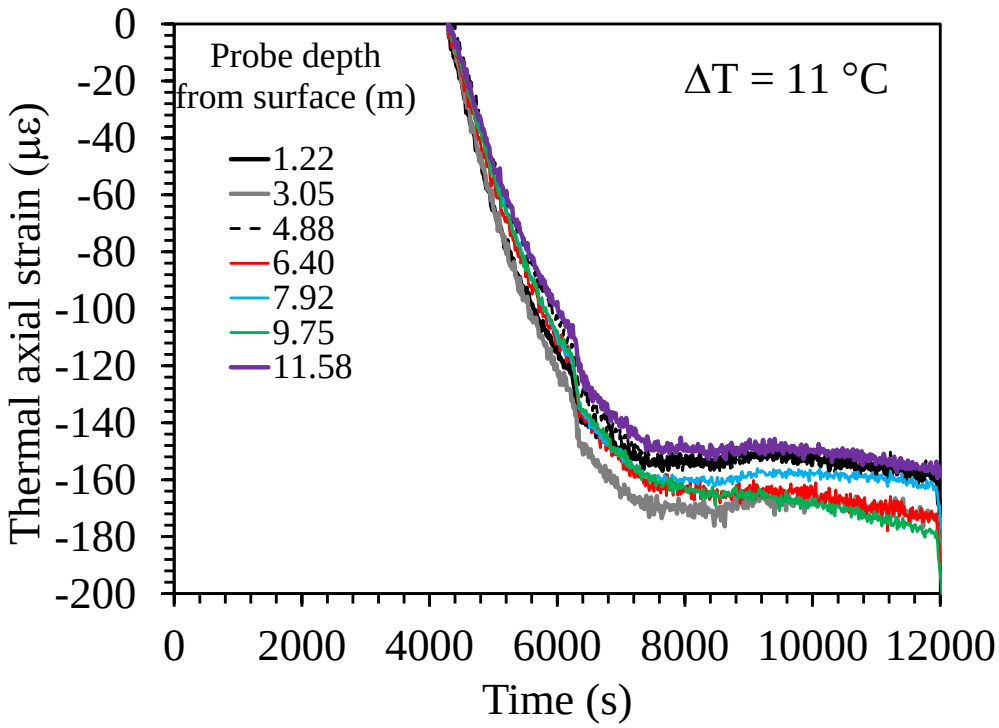

Figure 6.4.1-8 Axial strains during heating for the heated (ΔT = 11 °C) load control test on the end-bearing foundation in Nevada sand.

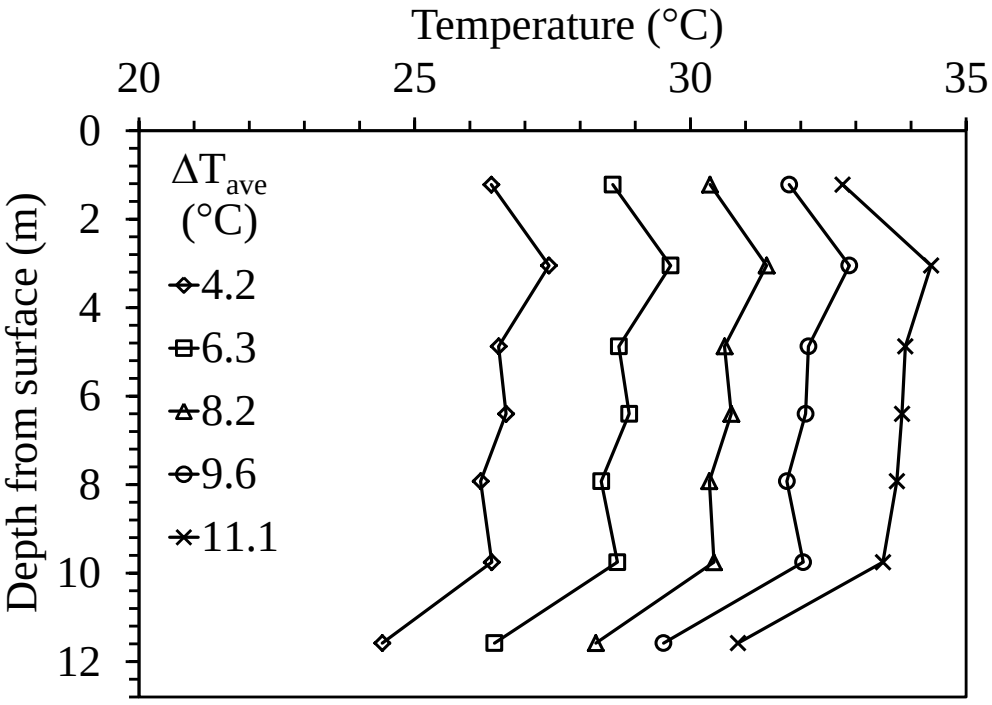

Figure 6.4.1-9 Temperature profiles for the heated (ΔT = 11 °C) load control test on the end-bearing foundation in Nevada sand.

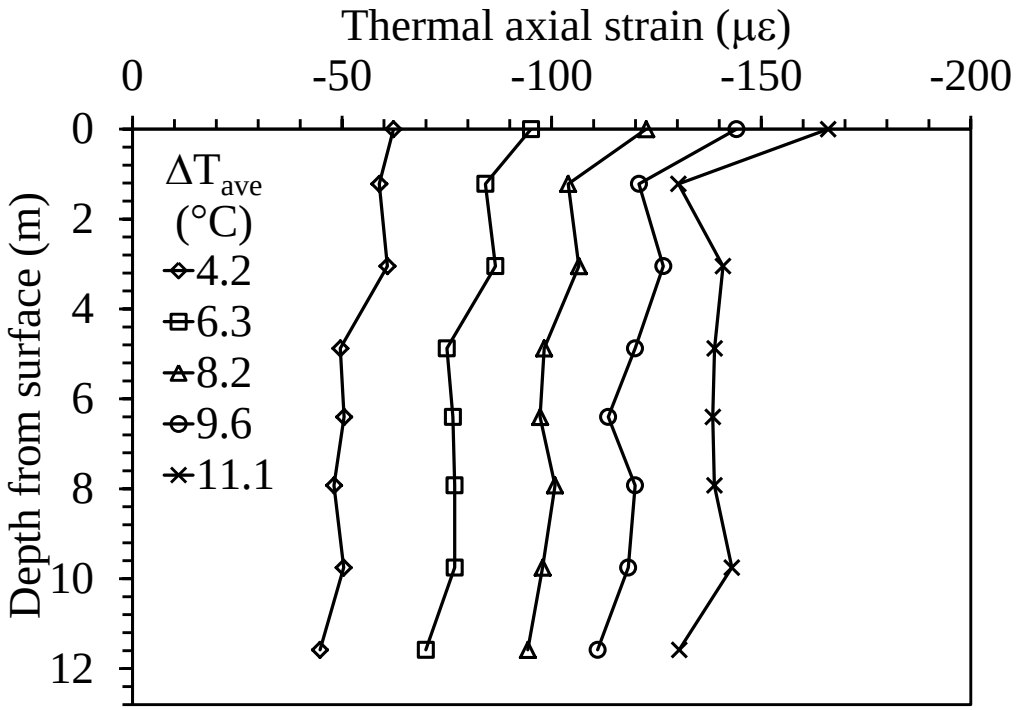

Figure 6.4.1-10 Thermal axial strain profile during heating for the heated (ΔT = 11 °C) load control test on the end-bearing foundation in Nevada sand.

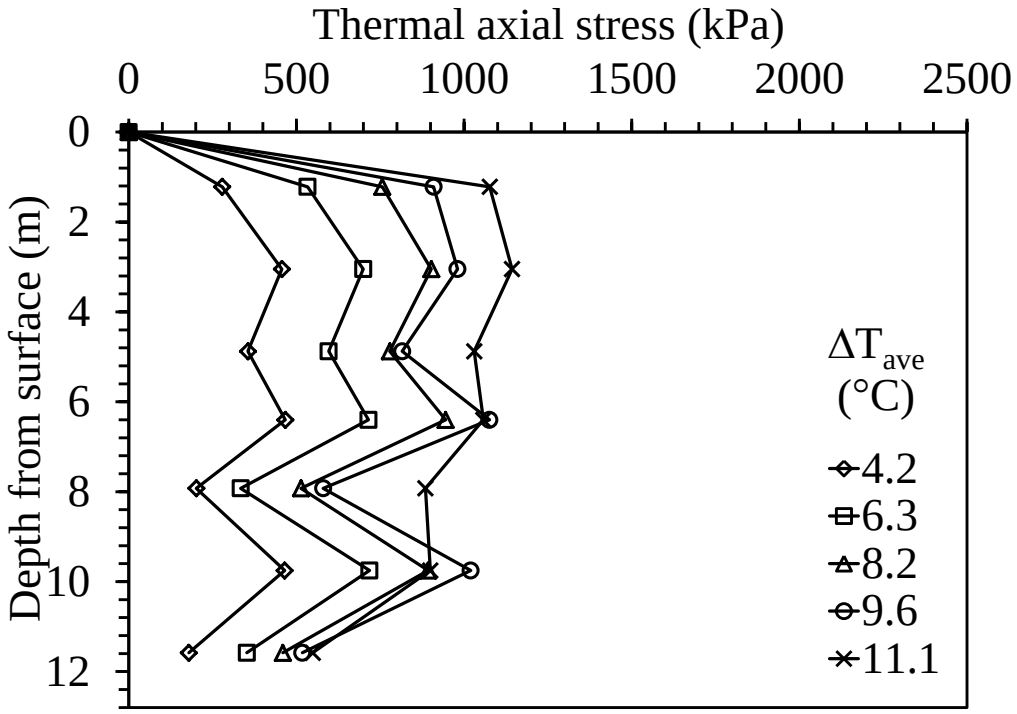

Figure 6.4.1-11 Prototype thermal stress profile for the heated (ΔT = 11 °C) load control test on the end-bearing foundation in Nevada sand.

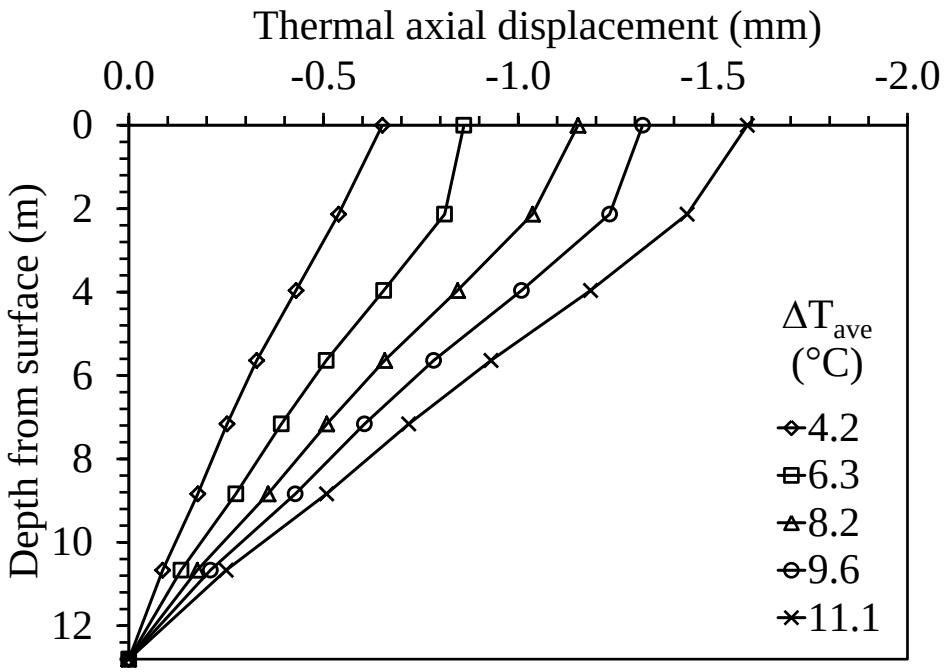

Figure 6.4.1-12 Thermal axial displacement profiles for the heated (ΔT = 11 °C) load control test on the end-bearing foundation in Nevada sand.

6.4.2 Results from Test L-NS-MS-12

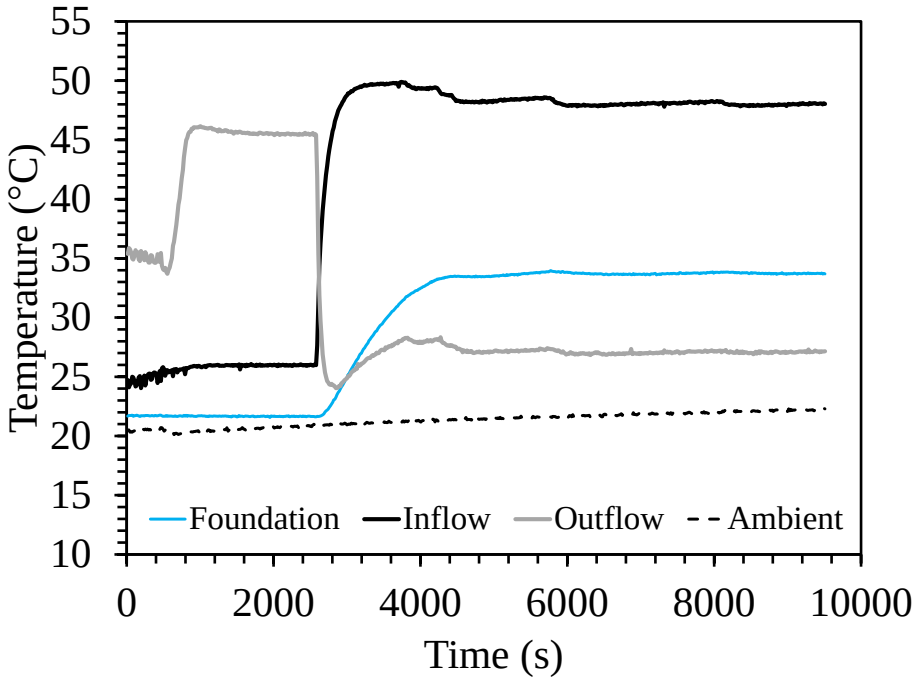

Figure 6.4.2-1 Temperatures during testing for the heated (ΔT = 12 °C) stiffness control test on the end-bearing foundation in Nevada sand.

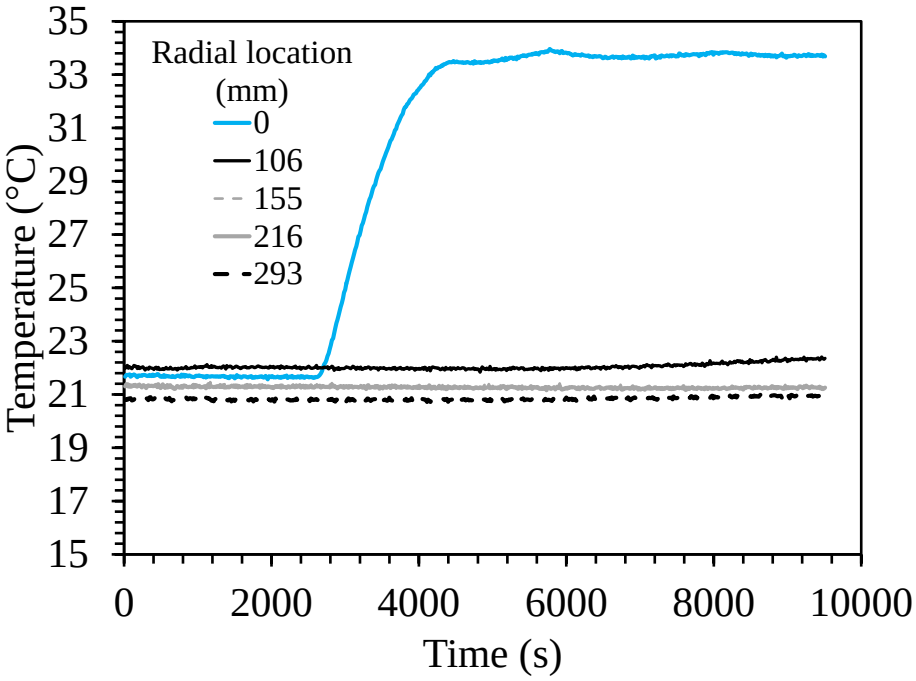

Figure 6.4.2-2 Average temperatures of foundation and four thermal probes for the heated (ΔT = 12 °C) stiffness control test on the end-bearing foundation in Nevada sand.

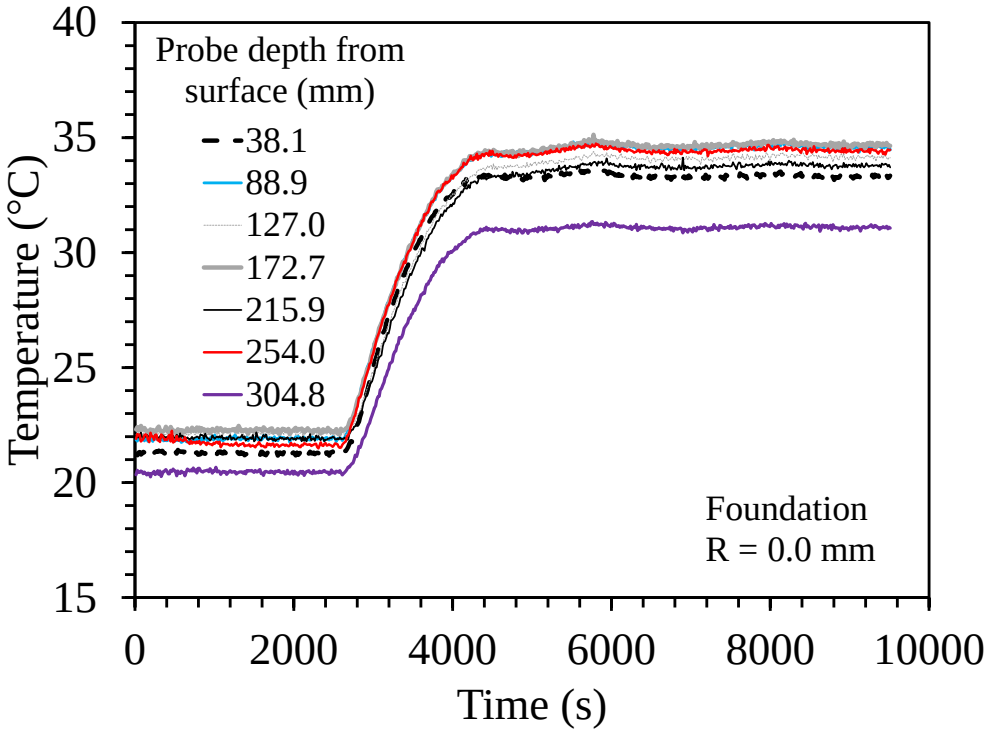

Figure 6.4.2-3 Foundation temperatures for the heated (ΔT = 12 °C) stiffness control test on the end-bearing foundation in Nevada sand.

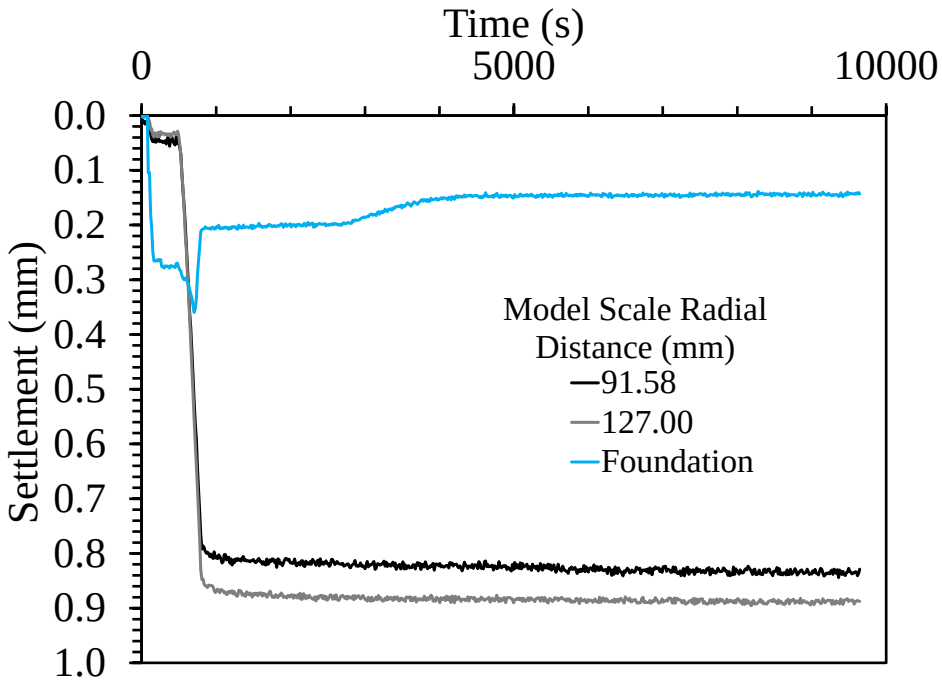

Figure 6.4.2-4 Model scale settlements with spin up for the heated (ΔT = 12 °C) stiffness control test on the end-bearing foundation in Nevada sand.

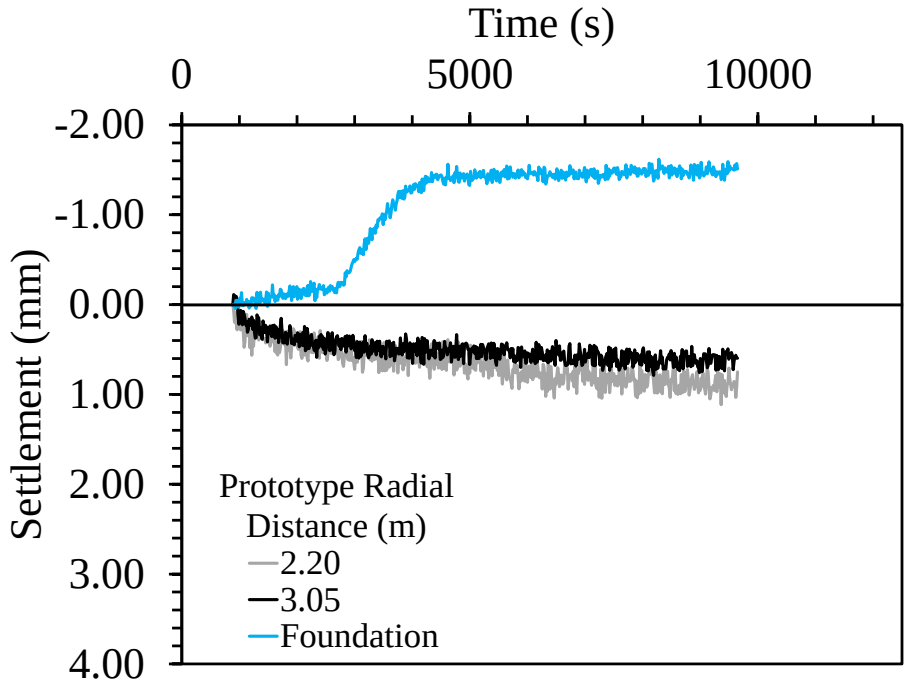

Figure 6.4.2-5 Prototype settlements after spin up for the heated (ΔT = 12 °C) stiffness control test on the end-bearing foundation in Nevada sand.

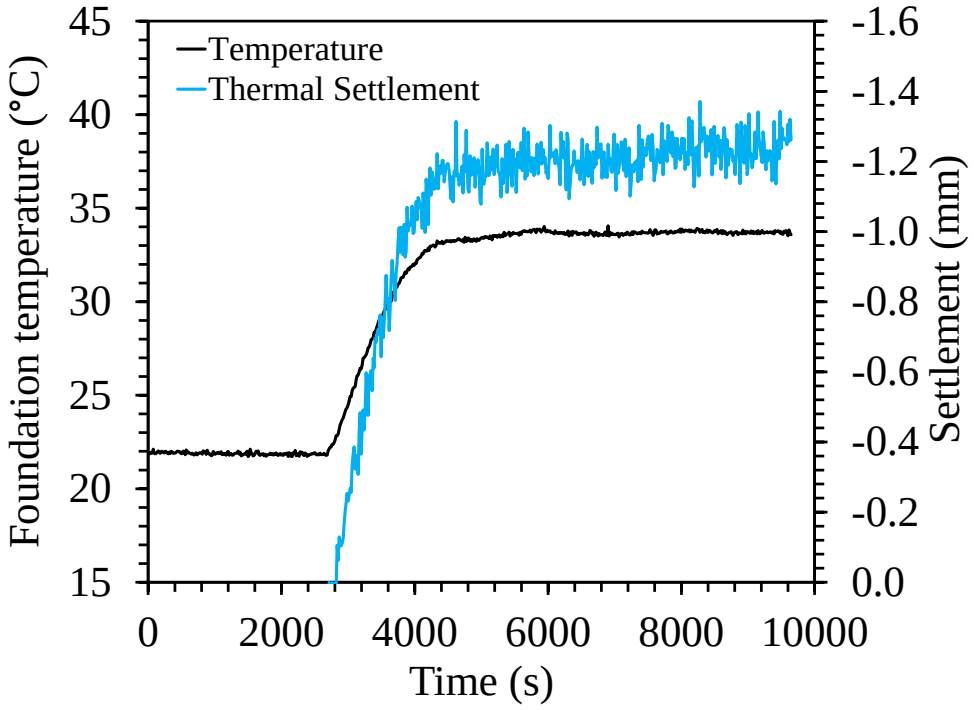

Figure 6.4.2-6 Prototype thermal expansion and temperature for the heated (ΔT = 12 °C) stiffness control test on the end-bearing foundation in Nevada sand.

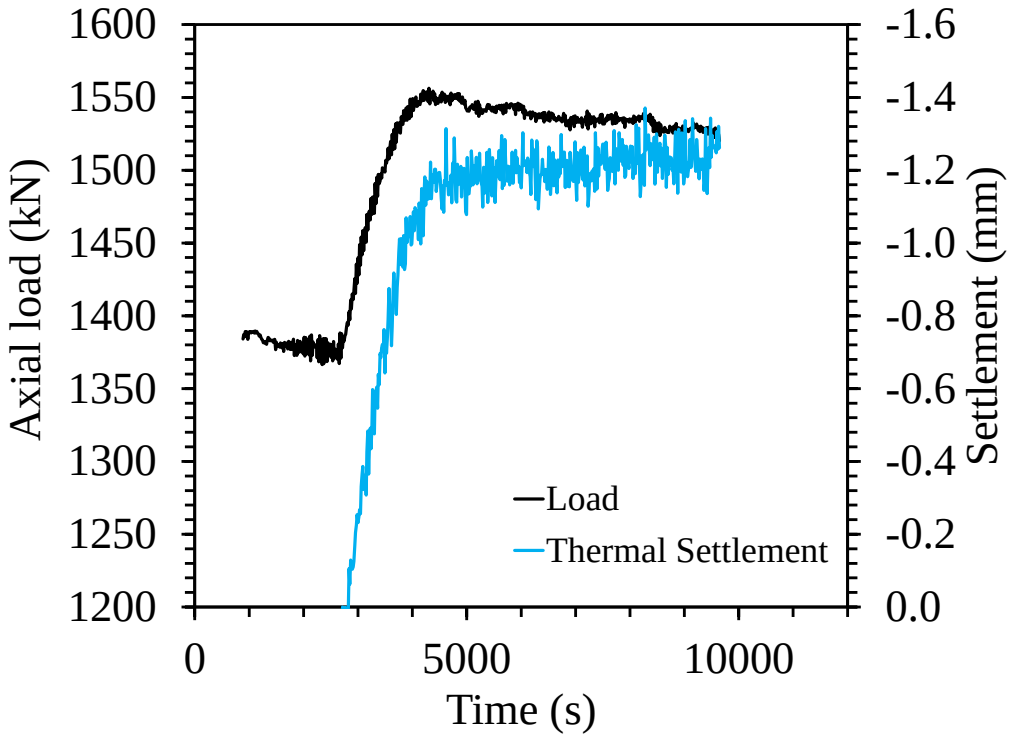

Figure 6.4.2-7 Prototype load and thermal expansion for the heated (ΔT = 12 °C) stiffness control test on the end-bearing foundation in Nevada sand.

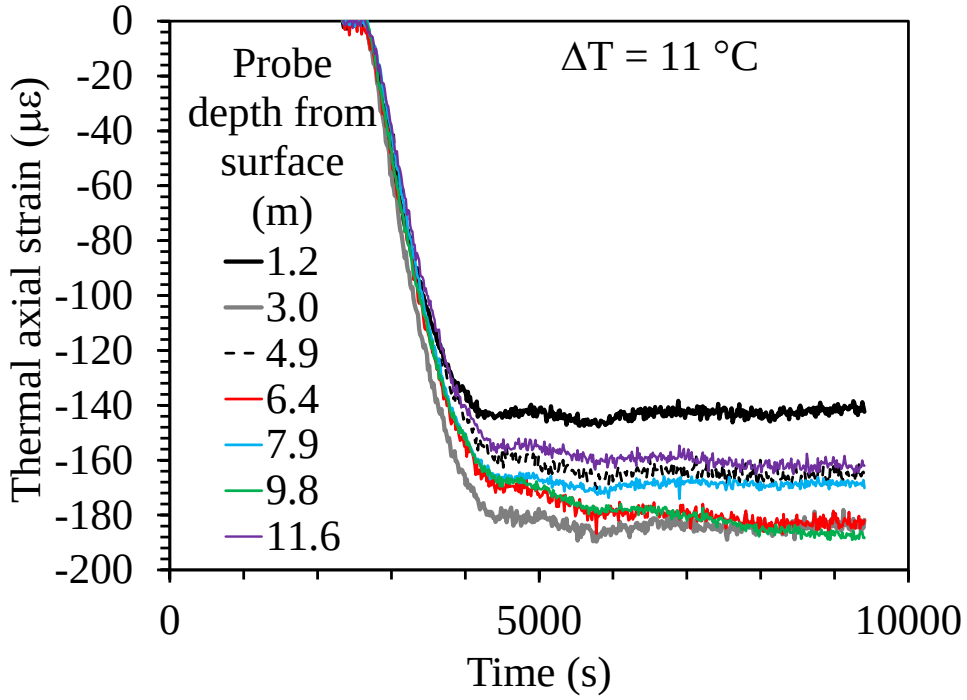

Figure 6.4.2-8 Axial strains during heating for the heated (ΔT = 12 °C) stiffness control test on the end-bearing foundation in Nevada sand.

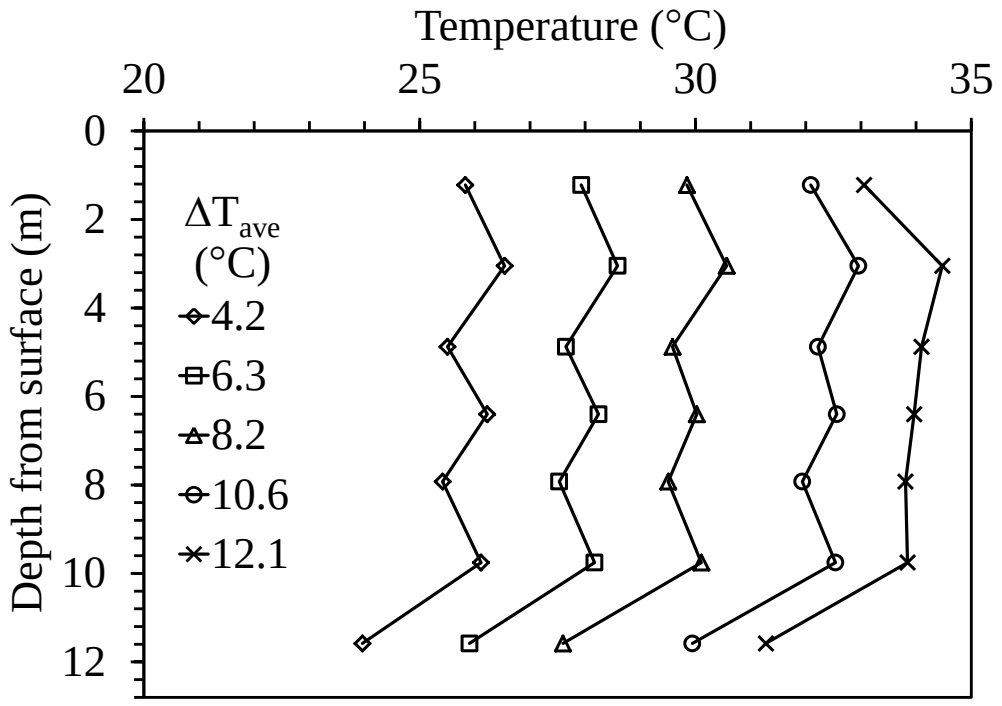

Figure 6.4.2-9 Temperature profiles for the heated (ΔT = 12 °C) stiffness control test on the end-bearing foundation in Nevada sand.

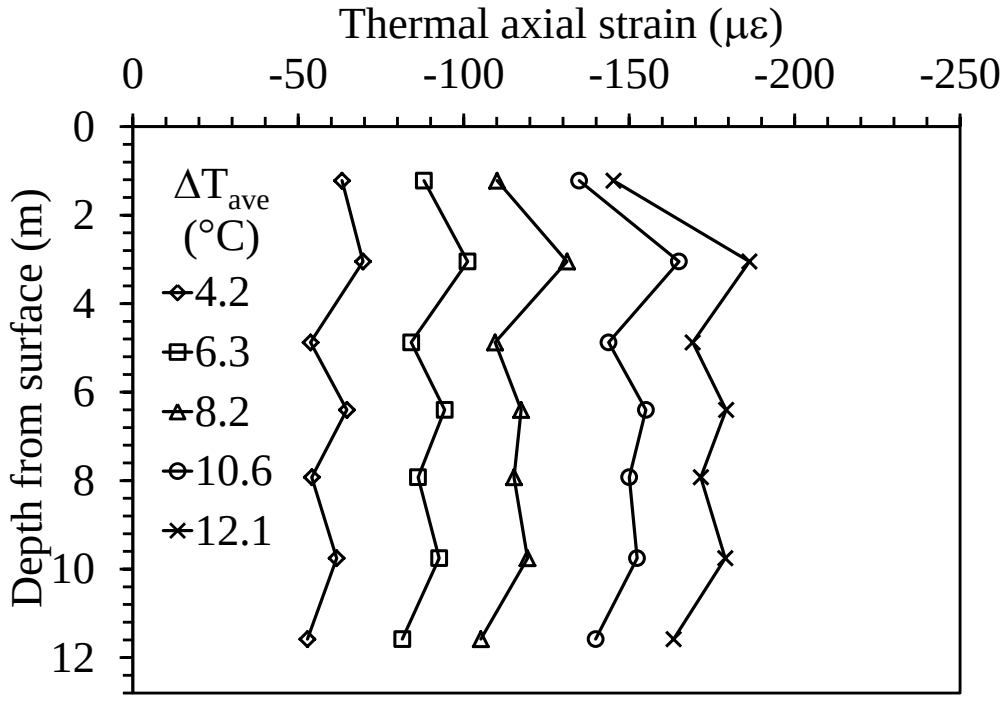

Figure 6.4.2-10 Thermal axial strain profile during heating for the heated (ΔT = 12 °C) stiffness control test on the end-bearing foundation in Nevada sand.

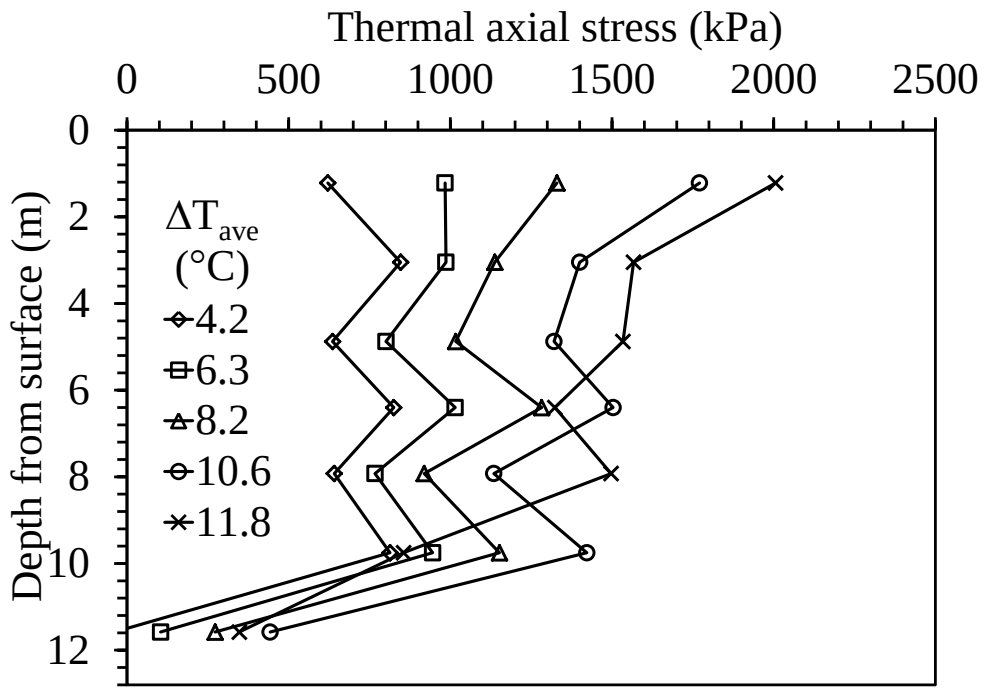

Figure 6.4.2-11 Prototype thermal stress profile for the heated (ΔT = 12 °C) stiffness control test on the end-bearing foundation in Nevada sand.

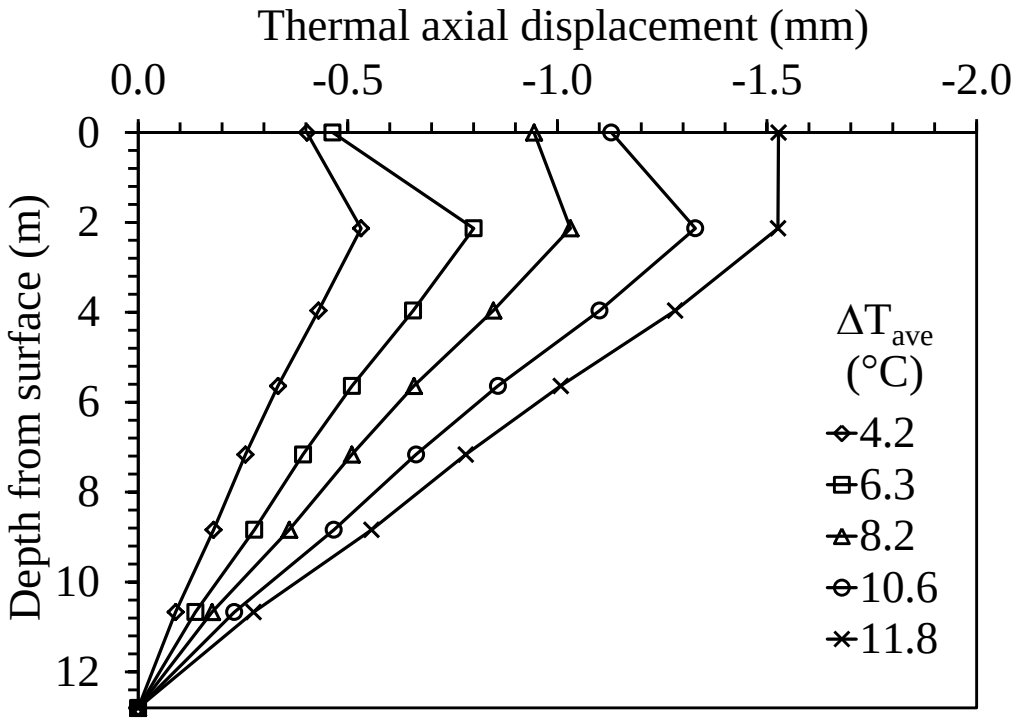

Figure 6.4.2-12 Thermal axial displacement profiles for the heated (ΔT = 12 °C) stiffness control test on the end-bearing foundation in Nevada sand.

6.4.3 Results from Test L-NS-SCL

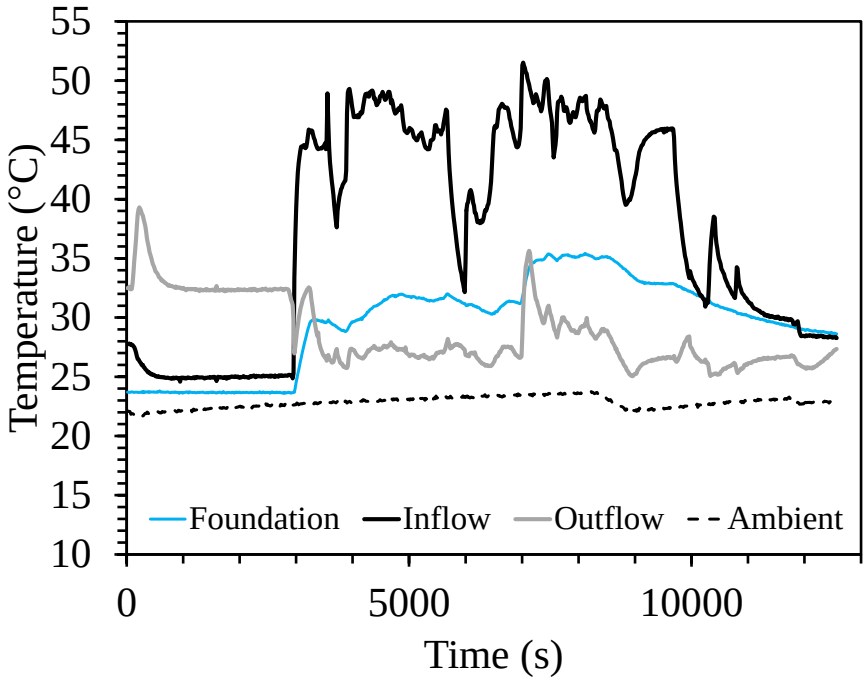

Figure 6.4.3-1 Temperatures during testing for the staged heated load test on the end-bearing foundation in Nevada sand.

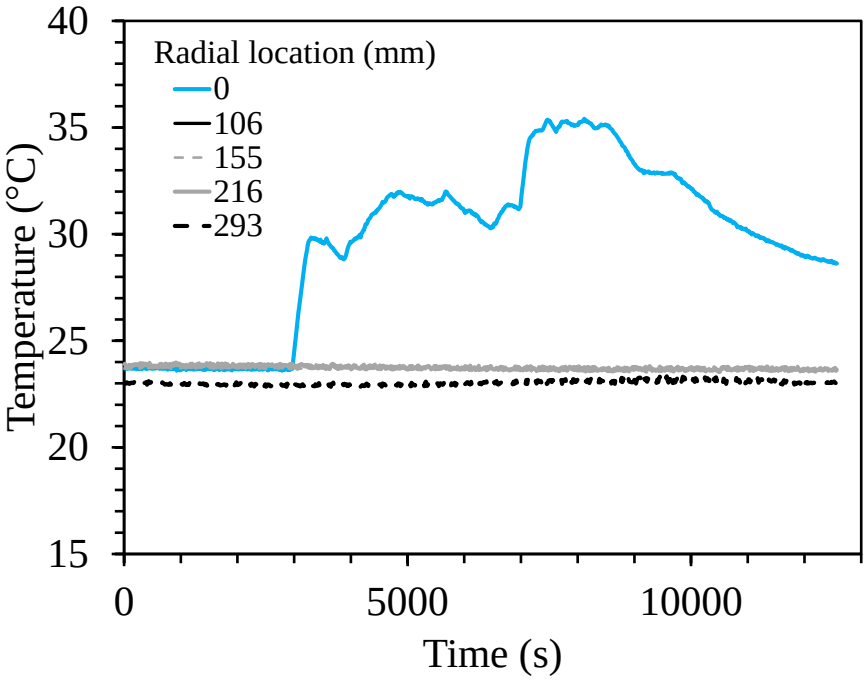

Figure 6.4.3-2 Average temperatures of foundation and four thermal probes for the staged heated load test on the end-bearing foundation in Nevada sand.

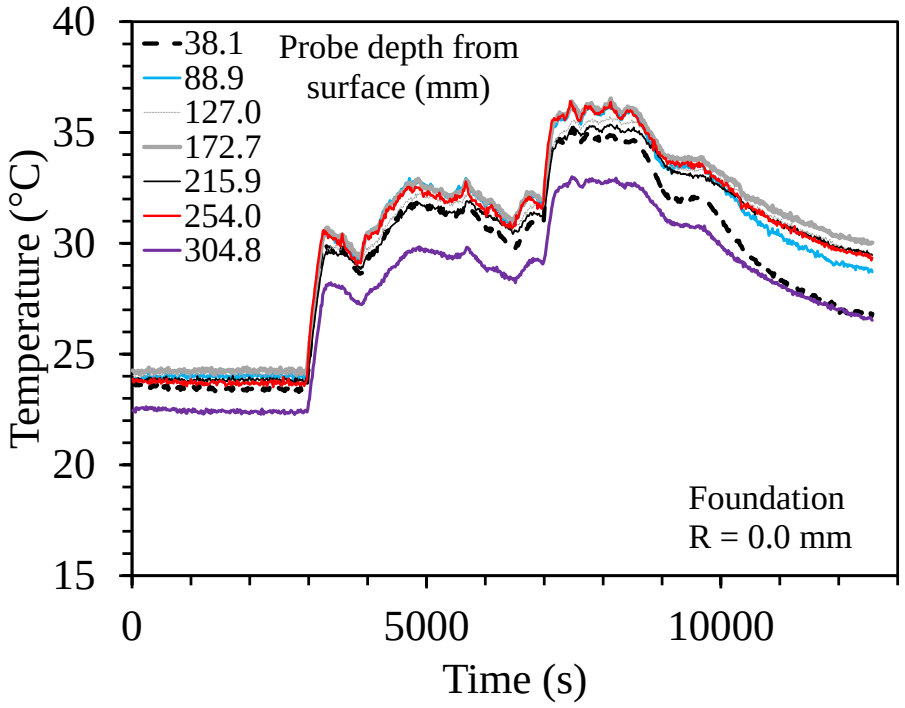

Figure 6.4.3-3 Foundation temperatures for the staged heated load test on the end-bearing foundation in Nevada sand.

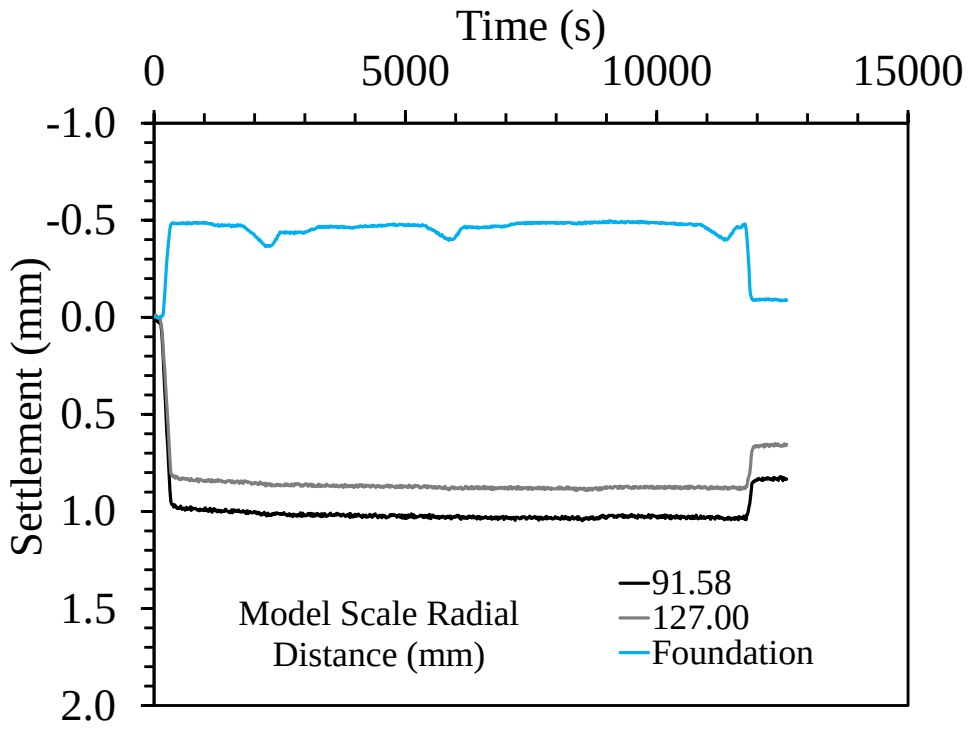

Figure 6.4.3-4 Model scale settlements with spin up for the staged heated load test on the end-bearing foundation in Nevada sand.

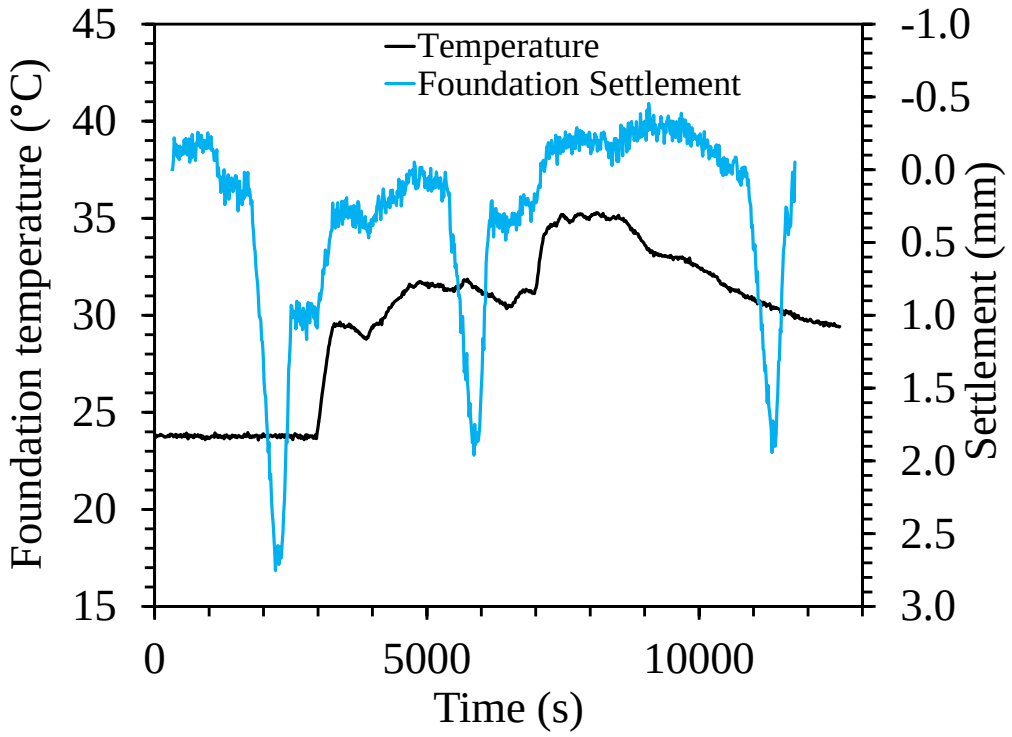

Figure 6.4.3-5 Foundation temperature and overall foundation settlement for the staged heated load test on the end-bearing foundation in Nevada sand.

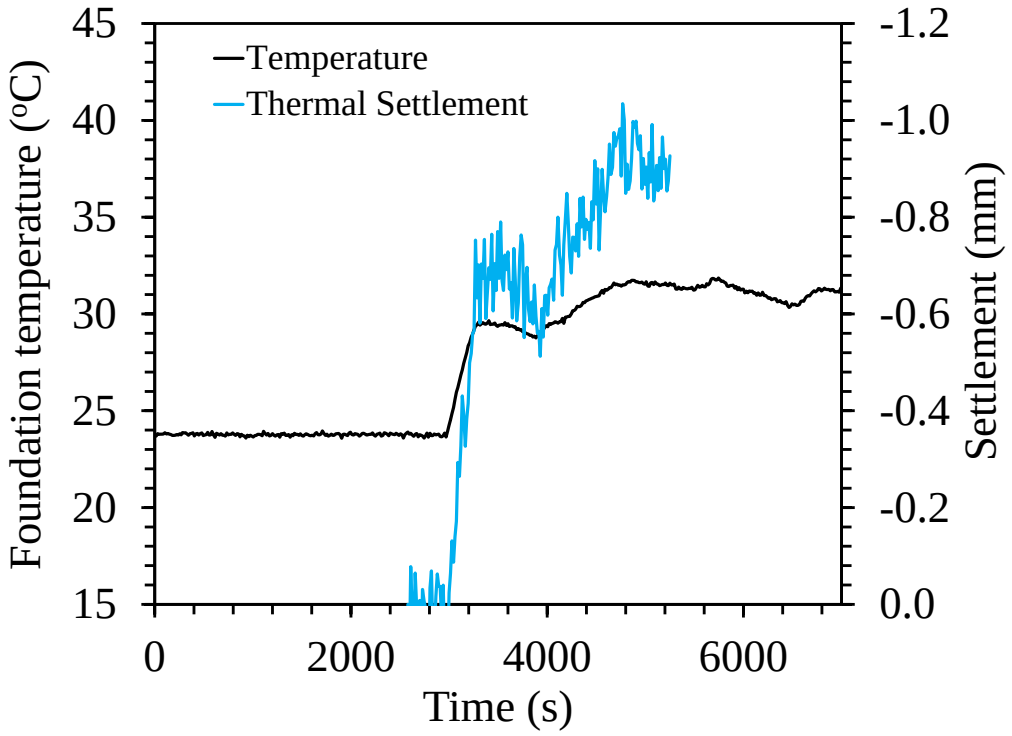

Figure 6.4.3-6 Thermal foundation settlement and respective temperature increase during the first heating cycle of the staged heated load test on the end-bearing foundation in Nevada sand.

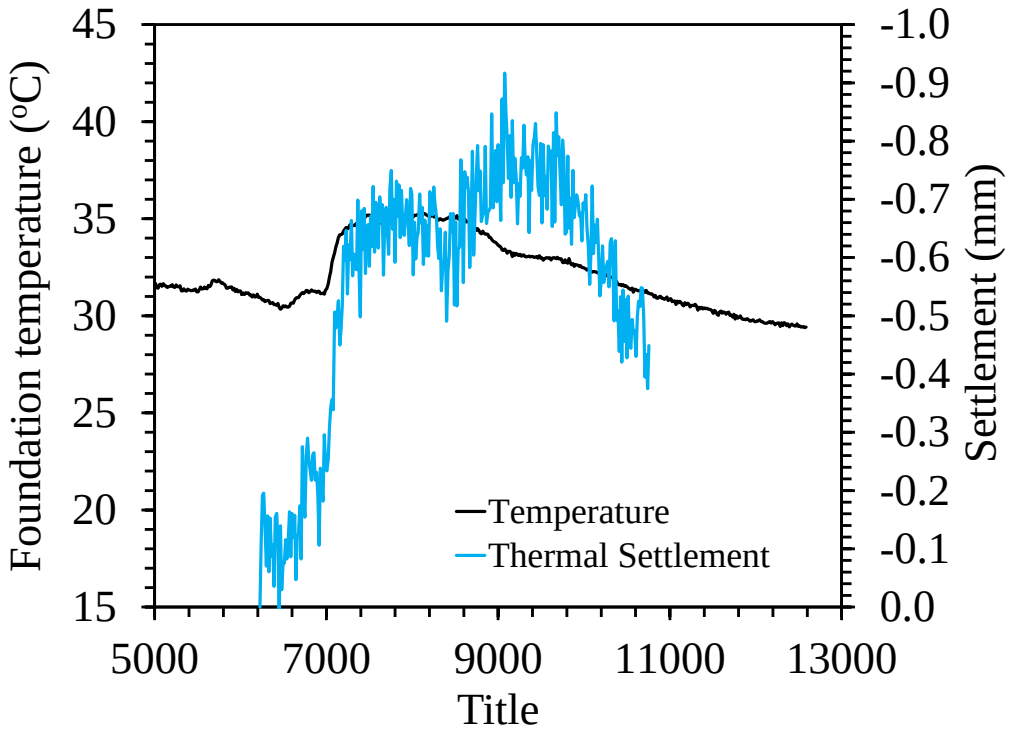

Figure 6.4.3-7 Thermal foundation settlement and respective temperature increase during second heating cycle for the staged heated load test on the end-bearing foundation in Nevada sand.

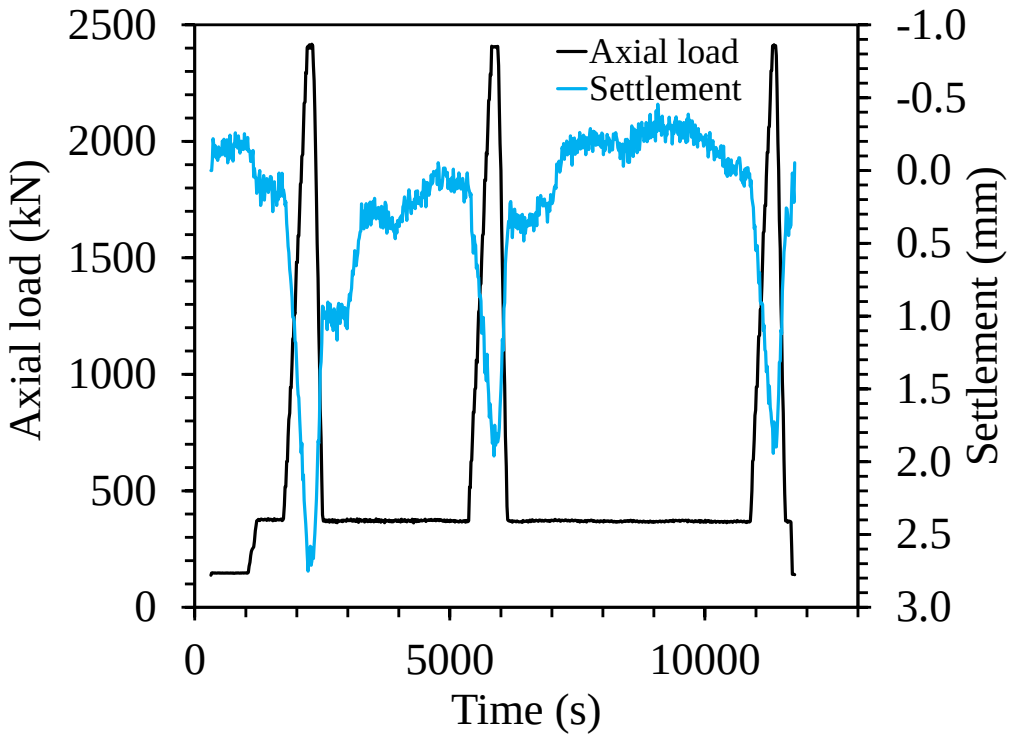

Figure 6.4.3-8 Prototype foundation settlements and axial load for the staged heated load test on the end-bearing foundation in Nevada sand.

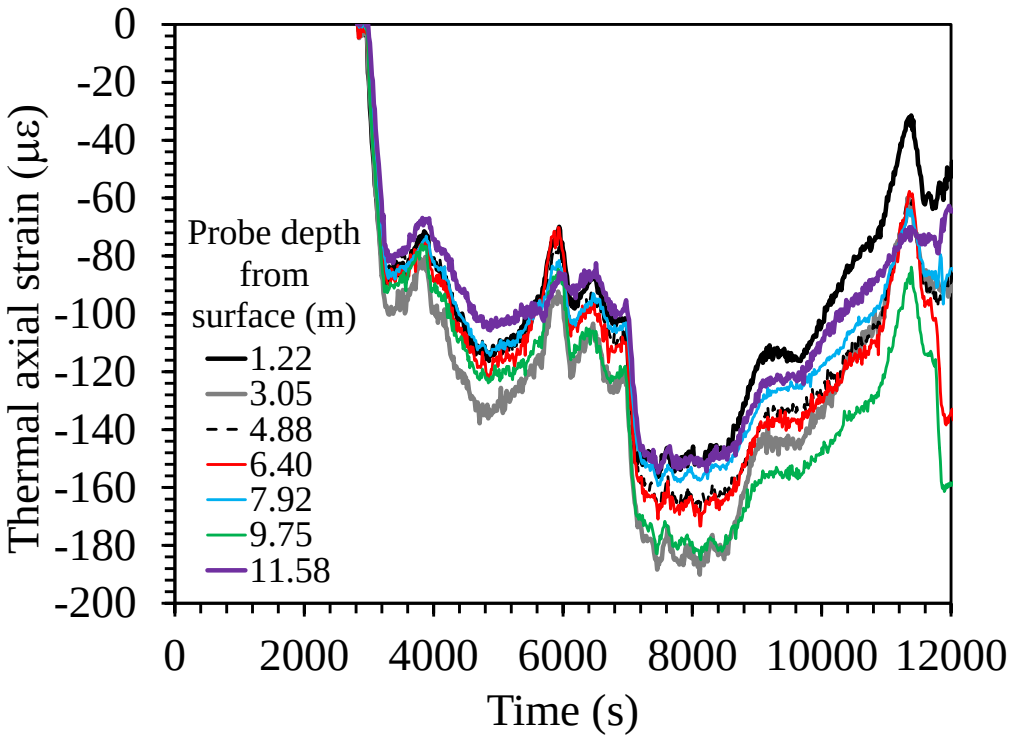

Figure 6.4.3-9 Thermal axial strain time series for the staged heated load test on the end-bearing foundation in Nevada sand.

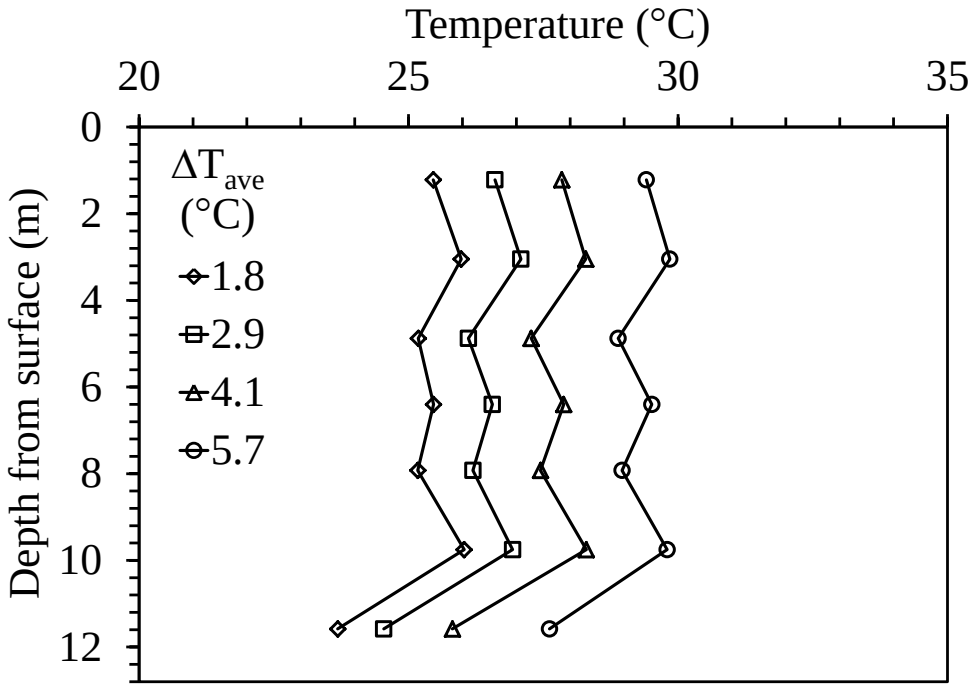

Figure 6.4.3-10 Temperature profile with depth for the staged heated load test on the end-bearing foundation in Nevada sand.

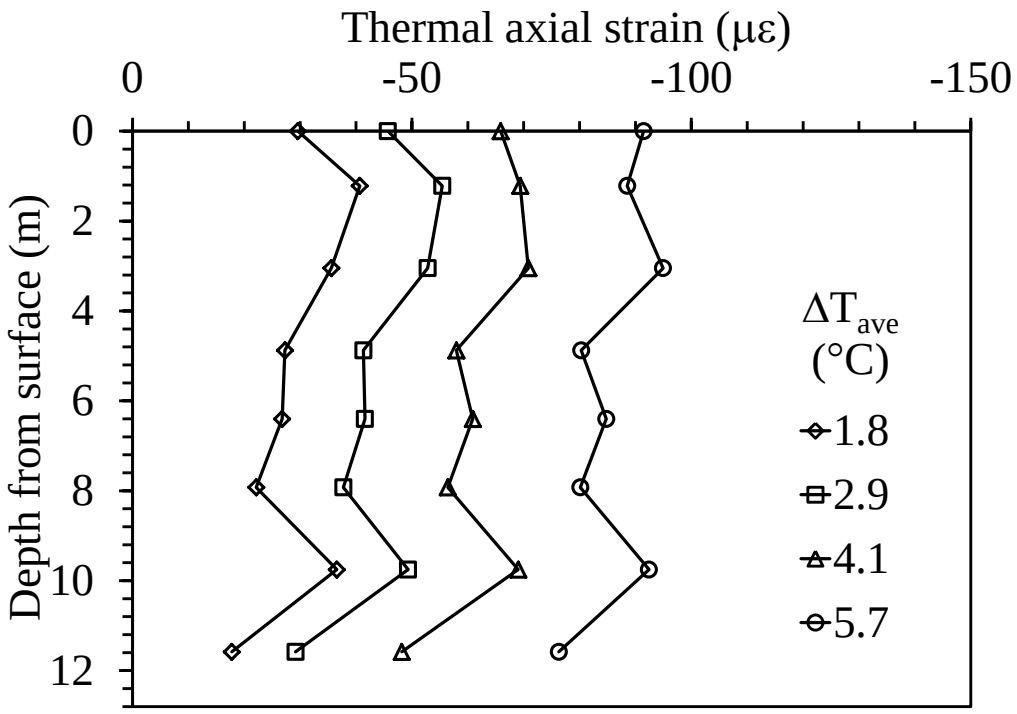

Figure 6.4.3-11 Prototype thermal axial strain for the staged heated load test on the end-bearing foundation in Nevada sand.

6.4.4 Results from Test L-NS-SCL

Table 6-6 Summary of L-NC-SCL test program.

Heat Cycle	Soil	Load Temperature	ΔT	Const. Heat Duration	Total Heat Time	Initial Load	Final Load
		(°C)	(°C)	(min)	(min)	(kN)	(kN)
1	Nevada	35.64	12.64	48.5	111	365	2440
2	Nevada	39.8	16.8	17.25	97	365	2440
3	Nevada	33.2	-6.6	-	70	365	2440

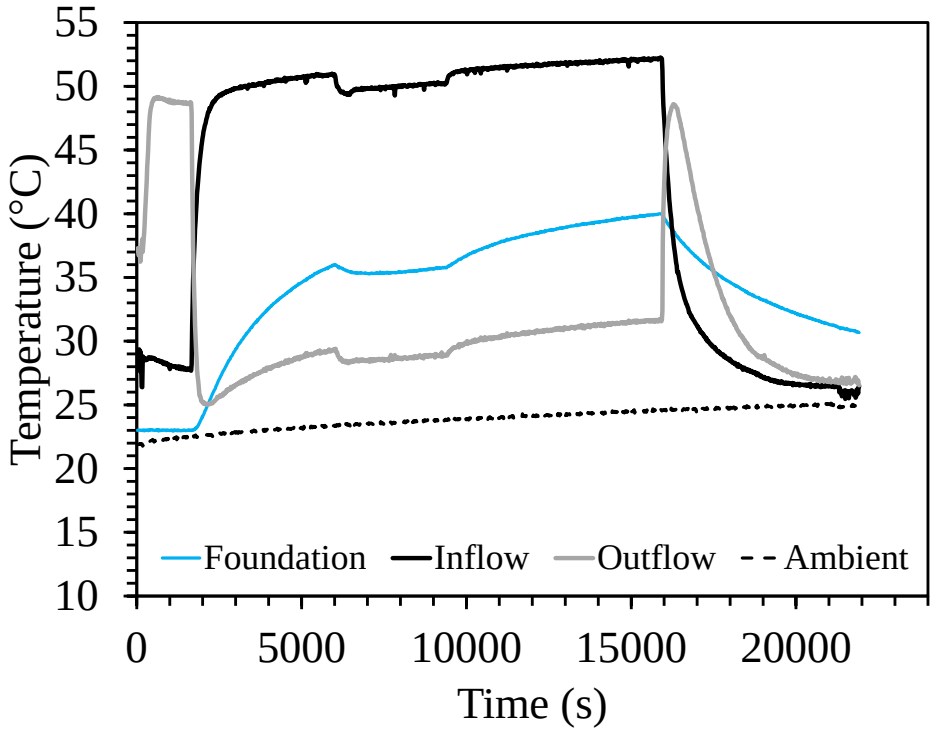

Figure 6.4.4-1 Temperatures during testing for the staged heated and cooled load test on the end-bearing foundation in Nevada sand.

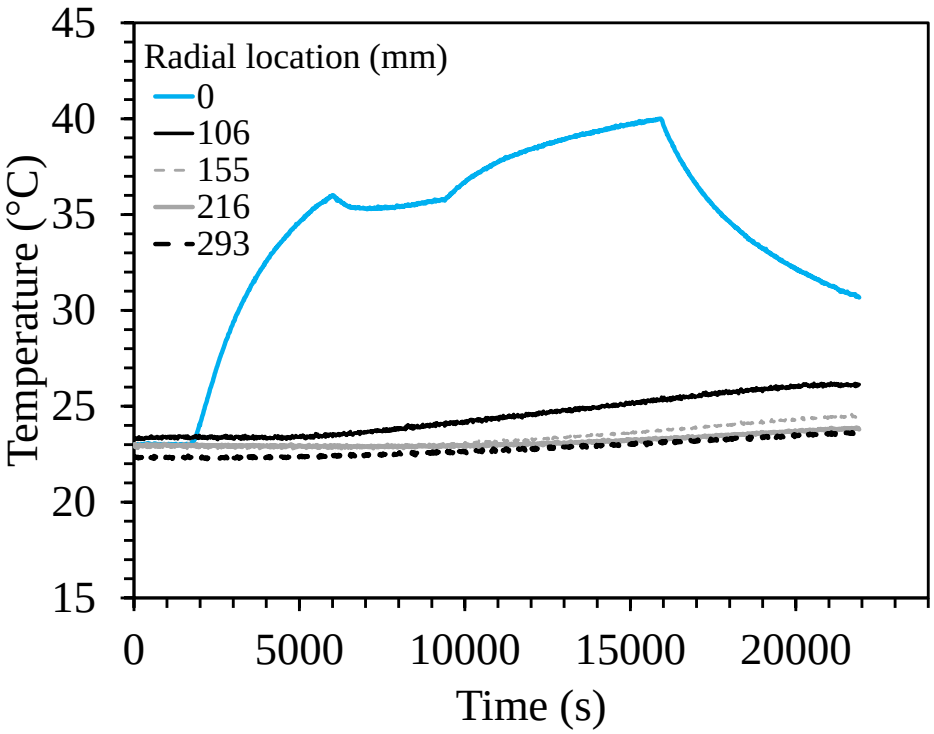

Figure 6.4.4-2 Average temperatures of the foundation and four thermal probes for the staged heated and cooled load test on the end-bearing foundation in Nevada sand.

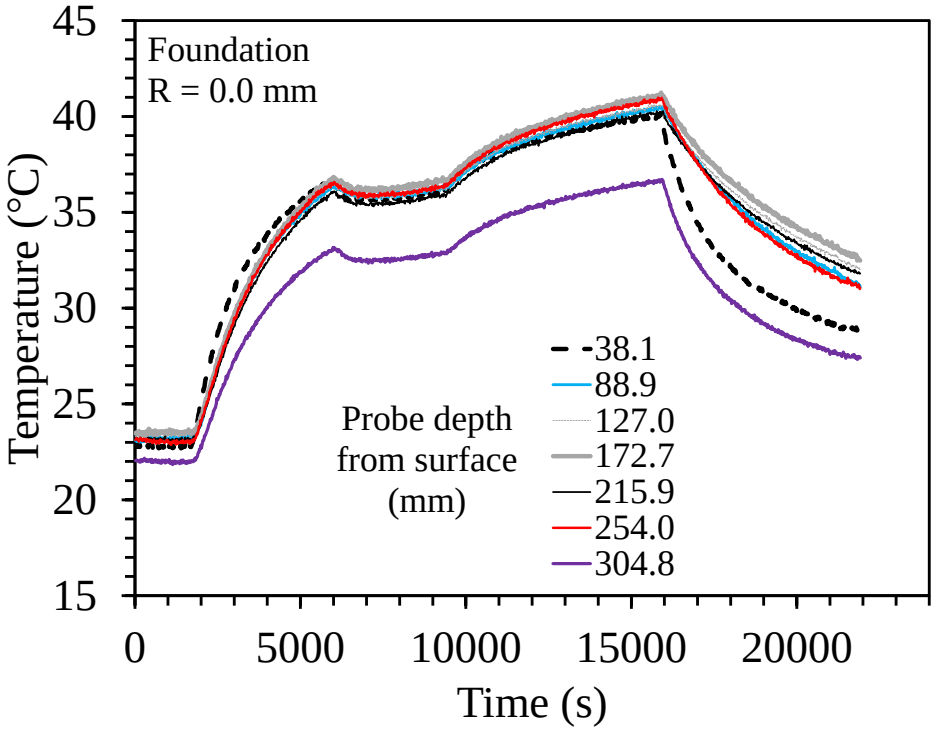

Figure 6.4.4-3 Foundation temperatures for the staged heated and cooled load test on the end-bearing foundation in Nevada sand.

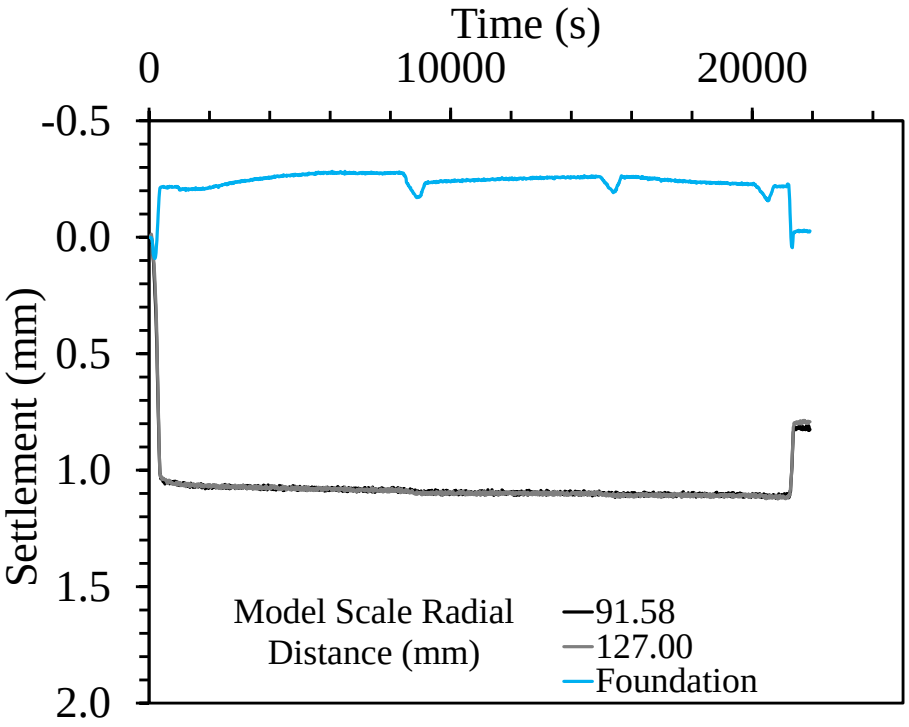

Figure 6.4.4-4 Model scale settlements with spin up for the staged heated and cooled load test on the end-bearing foundation in Nevada sand.

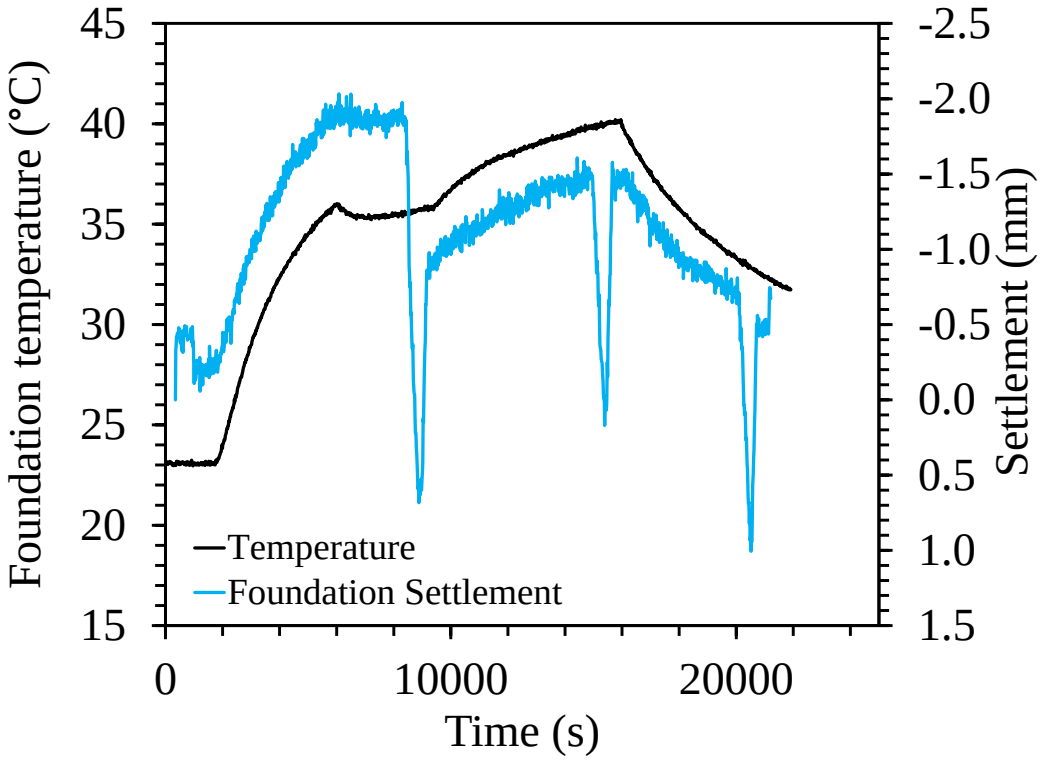

Figure 6.4.4-5 Foundation temperature and overall foundation settlement for the staged heated and cooled load test on the end-bearing foundation in Nevada sand.

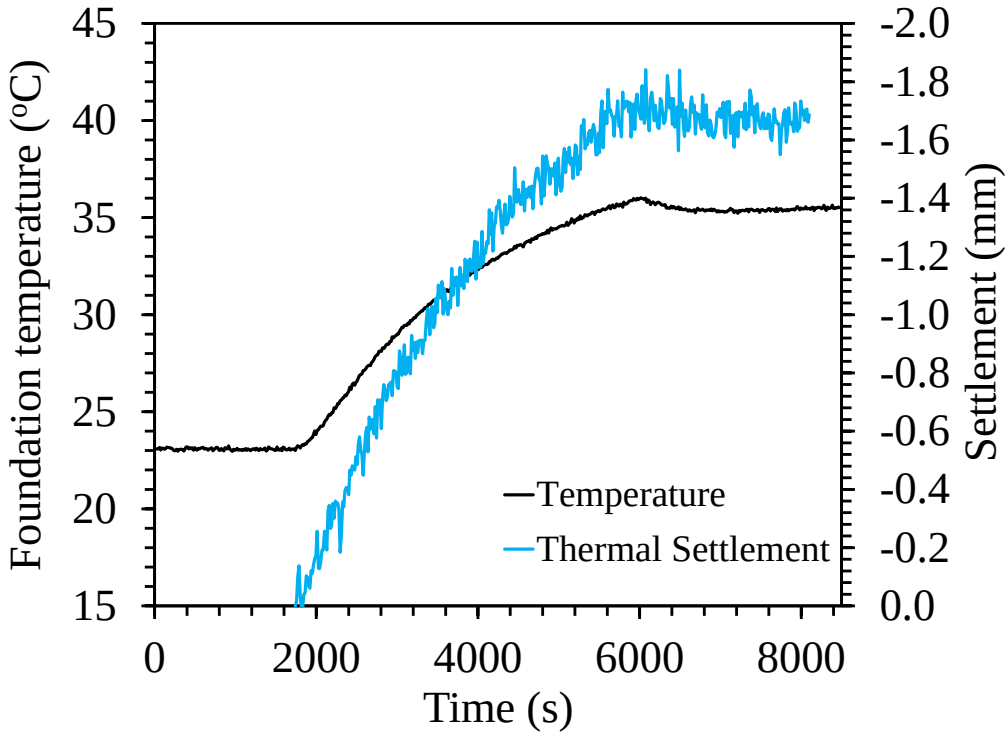

Figure 6.4.4-6 First heating cycle to 35 °C and respective foundation expansion for the staged heated and cooled load test on the end-bearing foundation in Nevada sand.

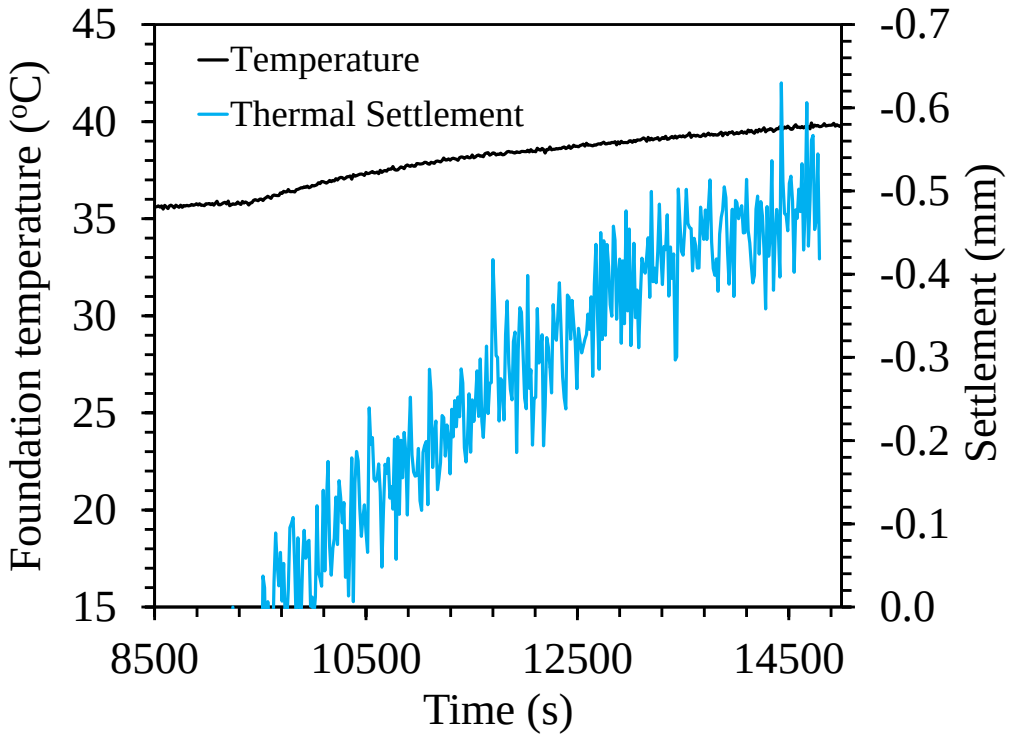

Figure 6.4.4-7 Second heating cycle to 40 °C and respective foundation expansion for the staged heated and cooled load test on the end-bearing foundation in Nevada sand.

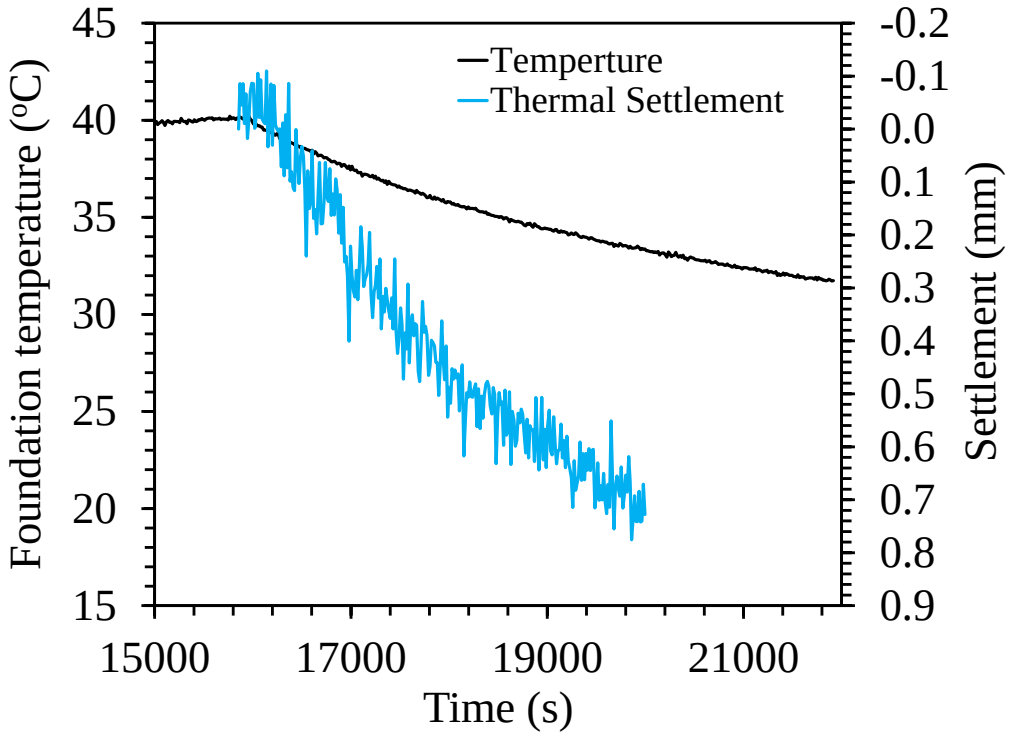

Figure 6.4.4-8 Third heating cycle from 40 °C to 33 °C and foundation contraction for the staged heated and cooled load test on the end-bearing foundation in Nevada sand.

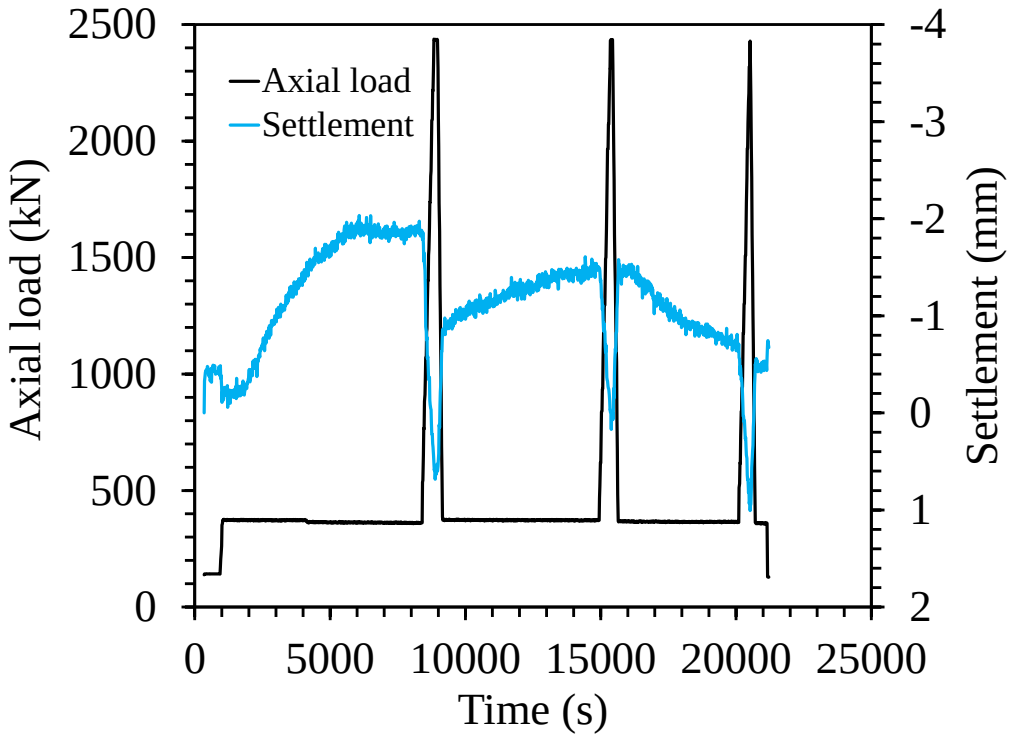

Figure 6.4.4-9 Prototype foundation settlements with axial load for the staged heated and cooled load test on the end-bearing foundation in Nevada sand.

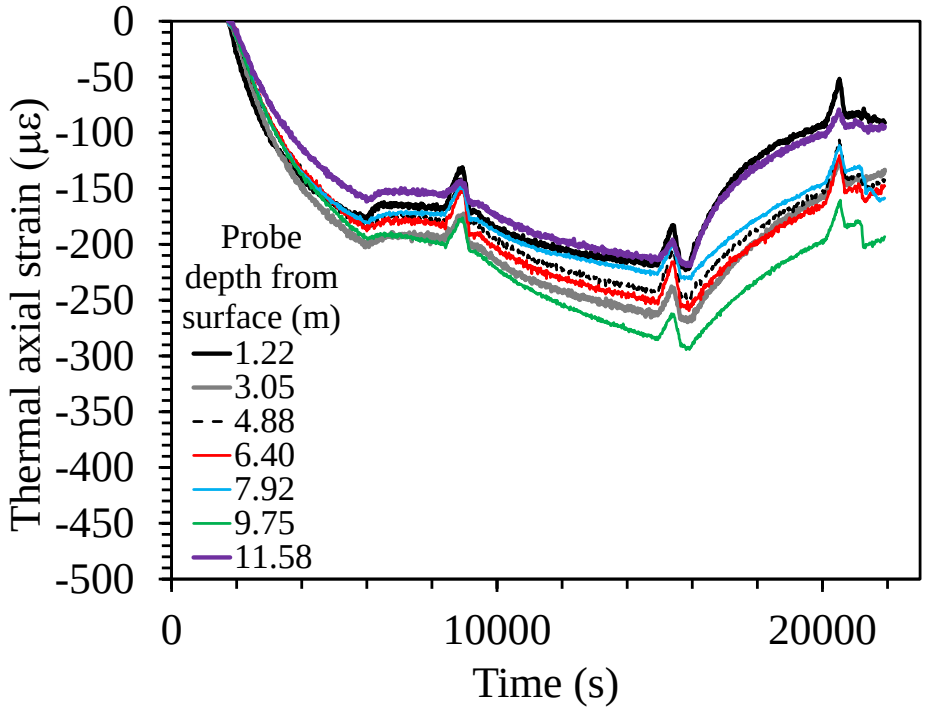

Figure 6.4.4-10 Thermal axial strain time series for the staged heated and cooled load test on the end-bearing foundation in Nevada sand.

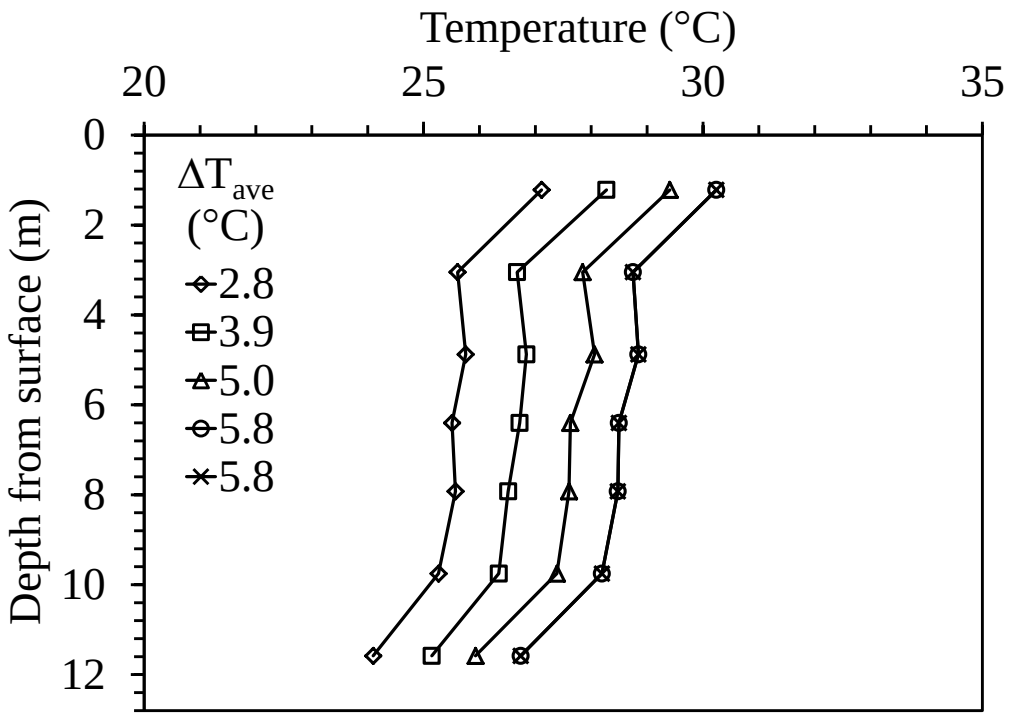

Figure 6.4.4-11 Temperature profile with depth for the staged heated and cooled load test on the end-bearing foundation in Nevada sand.

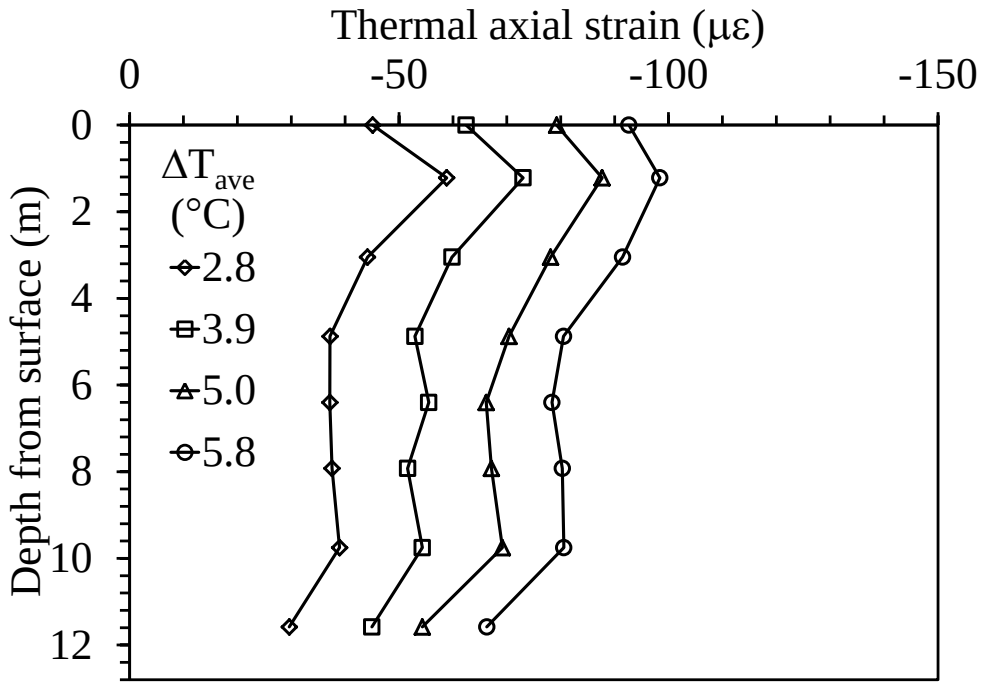

Figure 6.4.4-12 Prototype thermal axial strain for the staged heated and cooled load test on the end-bearing foundation in Nevada sand.

6.4.5 Results from Test L-BS-SCL

Table 6-7 Summary of L-BS-SCL test program

Heat Cycle	Soil	Temperature at Final Loading Stage	ΔT	Const. Heat Duration	Total Heat Time	Initial Load	Final Load
		(°C)	(°C)	(min)	(min)	(kN)	(kN)
1	Bonny	21.2	-0.1			365	2440
2	Bonny	30.3	8.9	44	57	365	2440
3	Bonny	34.7	13.3	58	68	365	2440
4	Bonny	35.9	14.6	33	56	365	2440
5	Bonny	27.1	-8.8	76	76	365	2440

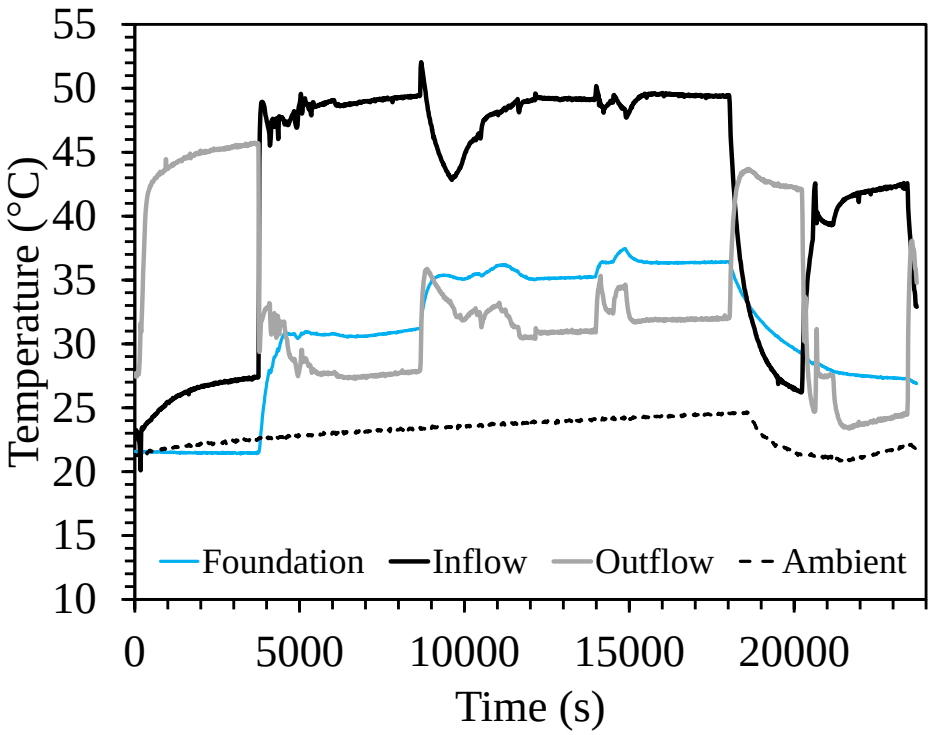

Figure 6.4.5-1 Temperatures during testing for the staged heated and cooled load test on the end-bearing foundation in Bonny silt.

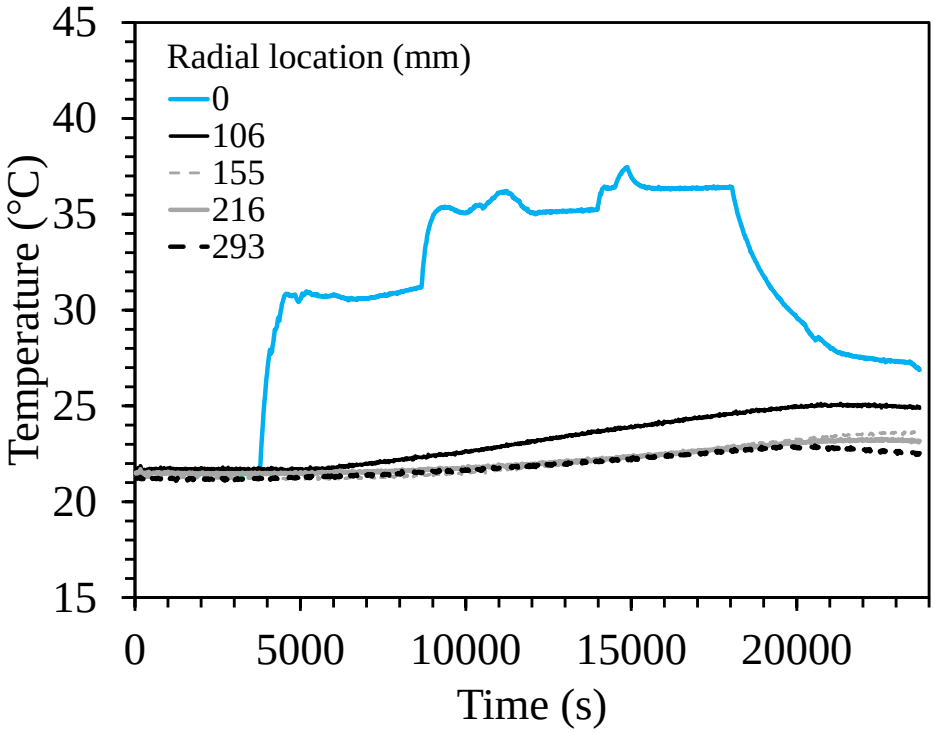

Figure 6.4.5-2 Average temperatures of foundation and four thermal probes for the staged heated and cooled load test on the end-bearing foundation in Bonny silt.

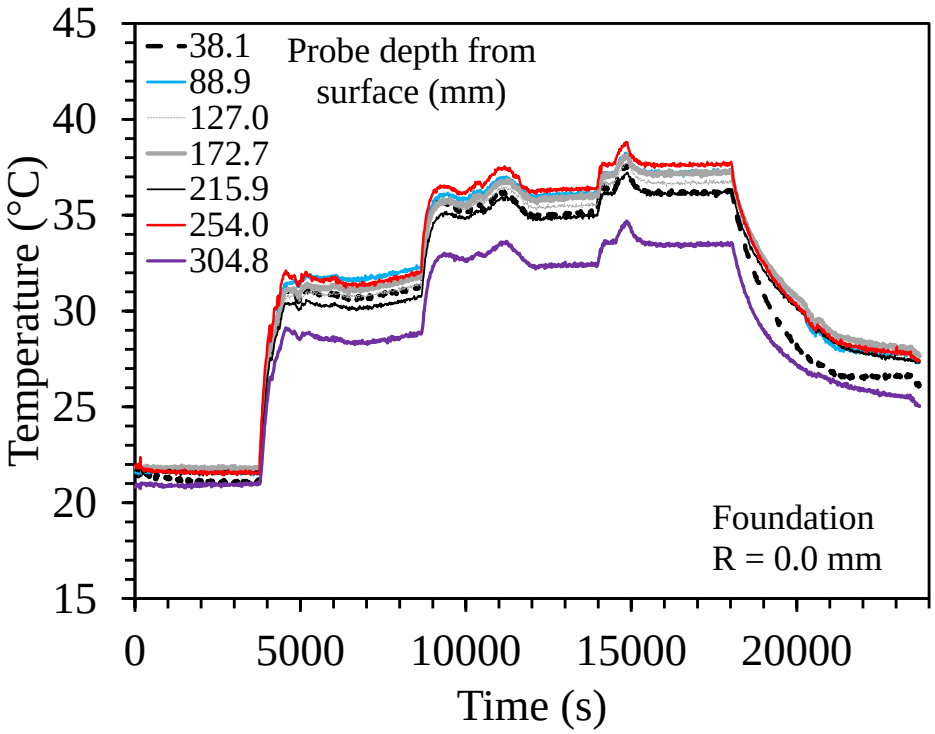

Figure 6.4.5-3 Foundation temperatures for the staged heated and cooled load test on the end-bearing foundation in Bonny silt.

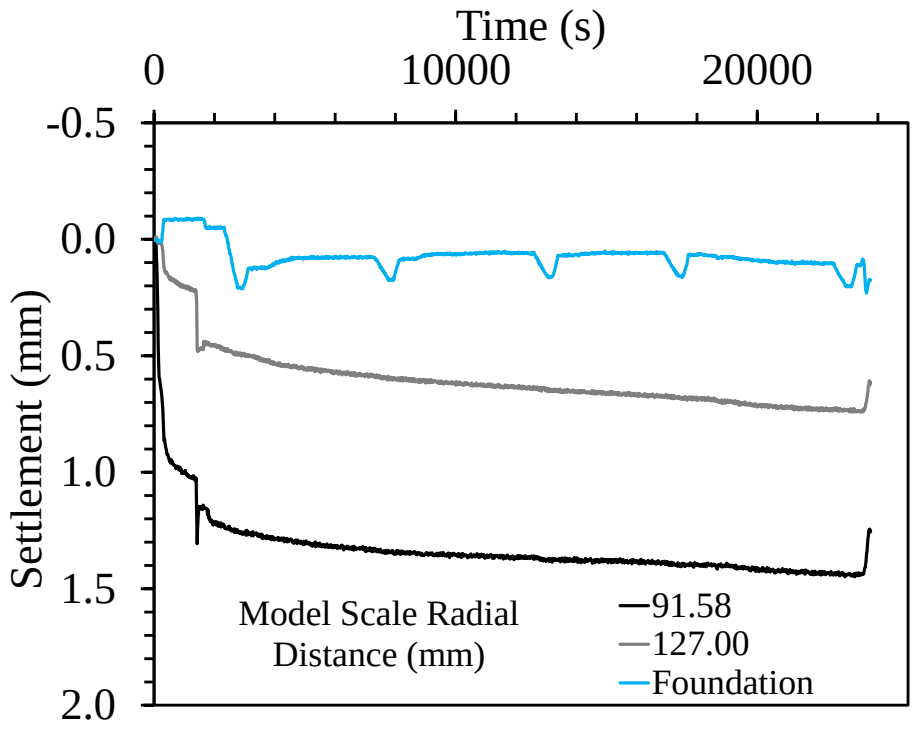

Figure 6.4.5-4 Model scale settlements with spin up for the staged heated and cooled load test on the end-bearing foundation in Bonny silt.

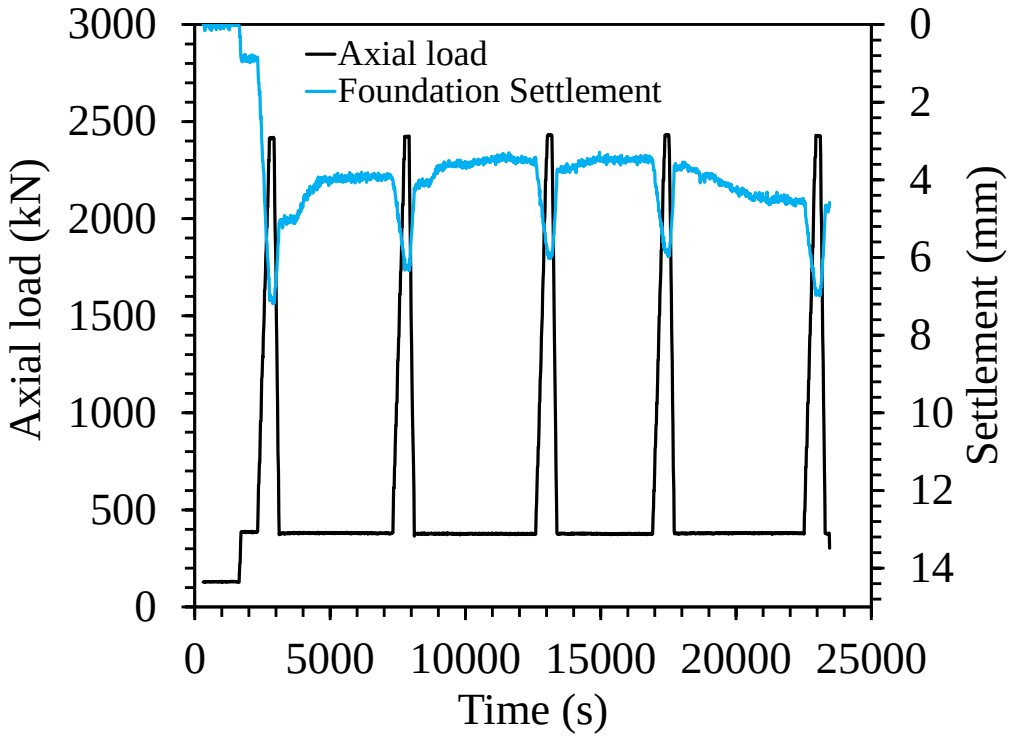

Figure 6.4.5-5 Prototype foundation settlement and axial load for the staged heated and cooled load test on the end-bearing foundation in Bonny silt.

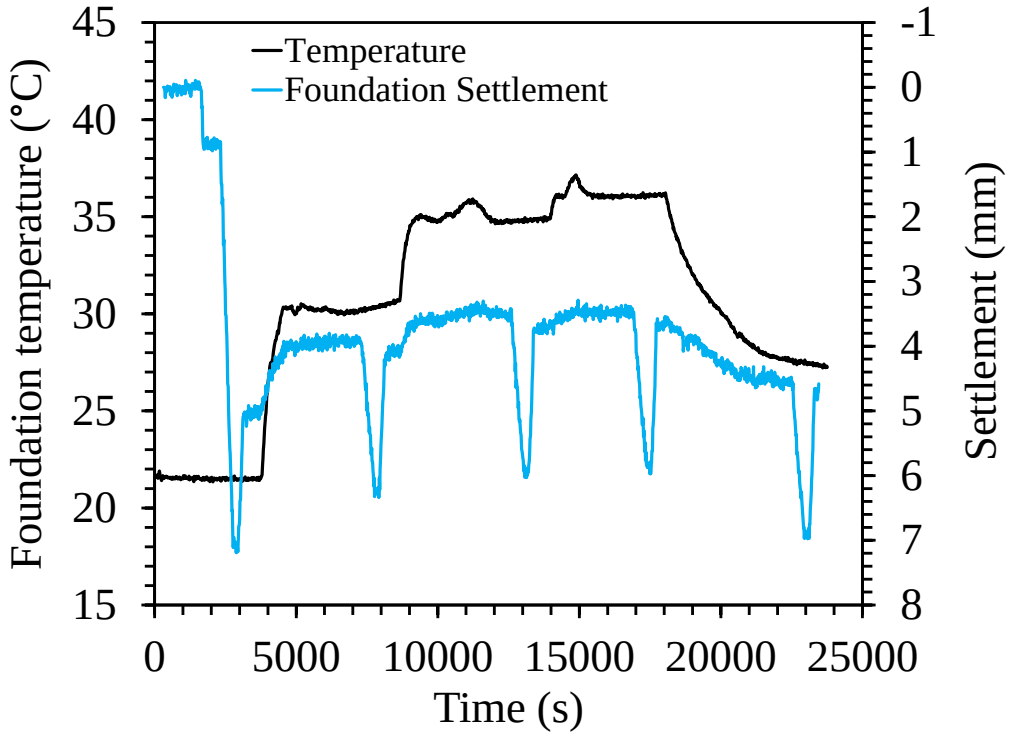

Figure 6.4.5-6 Foundation temperature and overall foundation settlement for the staged heated and cooled load test on the end-bearing foundation in Bonny silt.

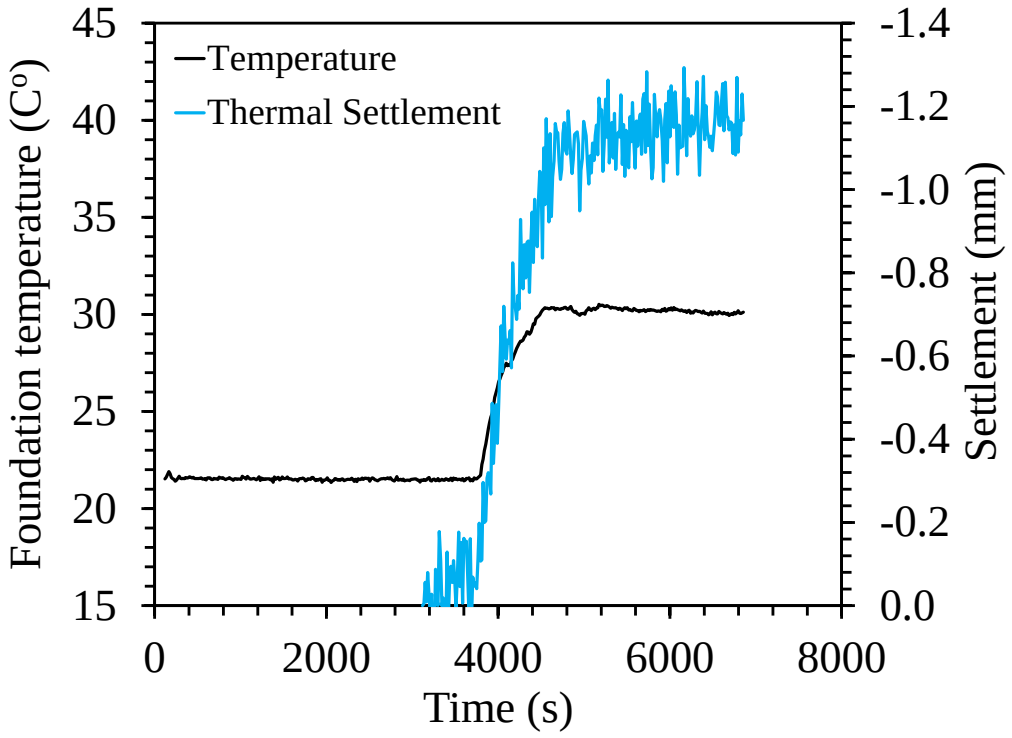

Figure 6.4.5-7 First heat cycle foundation thermal settlement and temperature for the staged heated and cooled load test on the end-bearing foundation in Bonny silt.

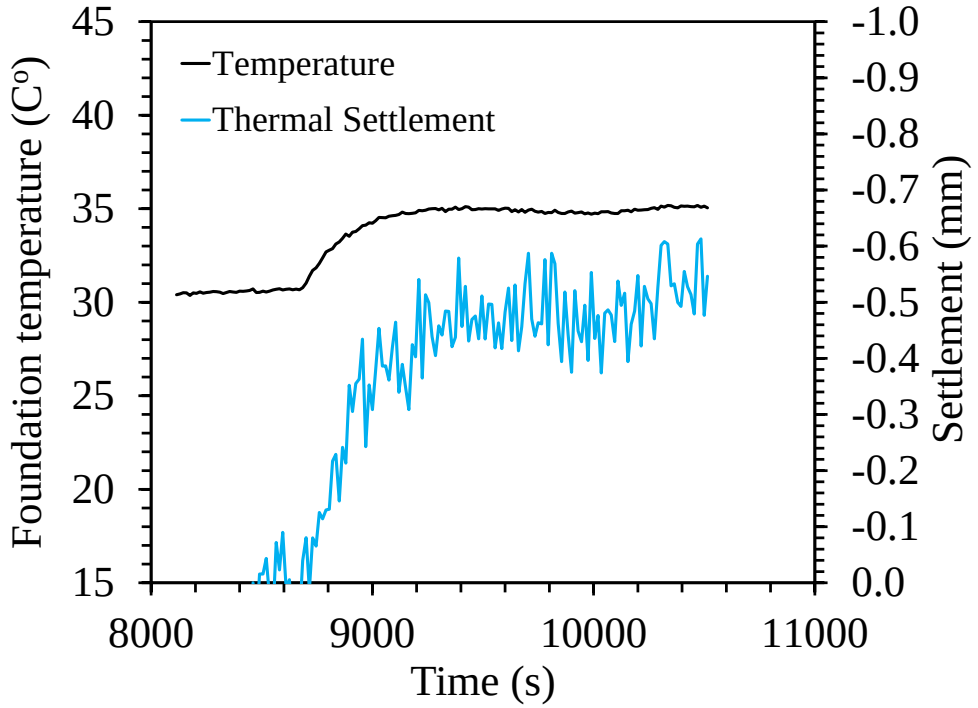

Figure 6.4.5-8 Second heat cycle foundation thermal settlement and temperature for the staged heated and cooled load test on the end-bearing foundation in Bonny silt.

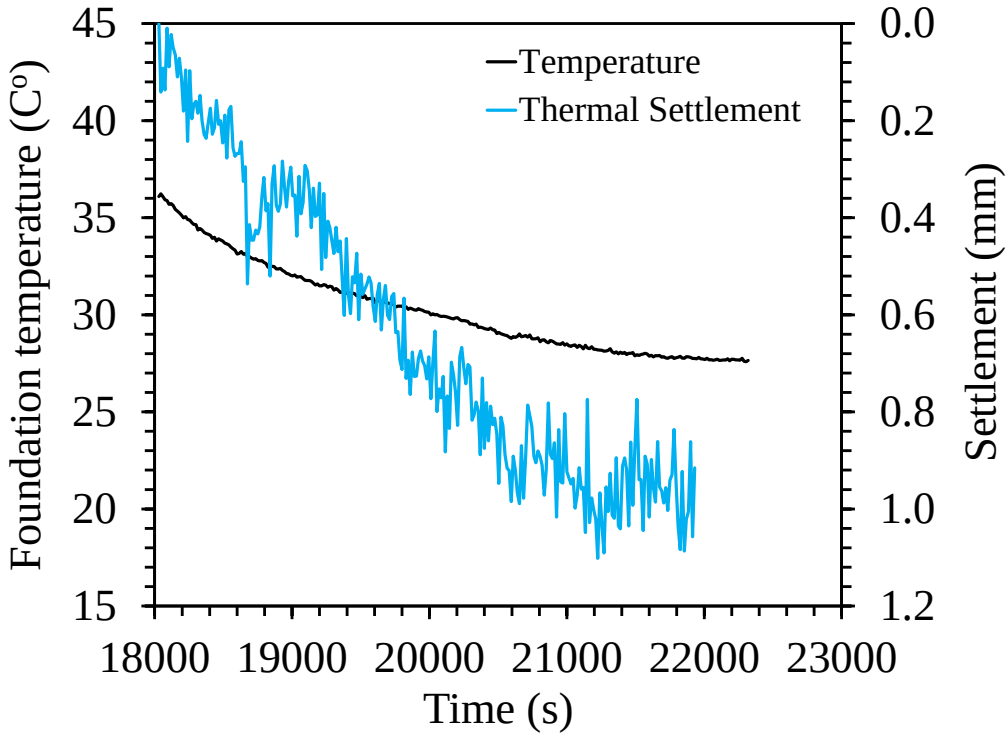

Figure 6.4.5-9 Third temperature cycle foundation settlement and temperature for the staged heated and cooled load test on the end-bearing foundation in Bonny silt.

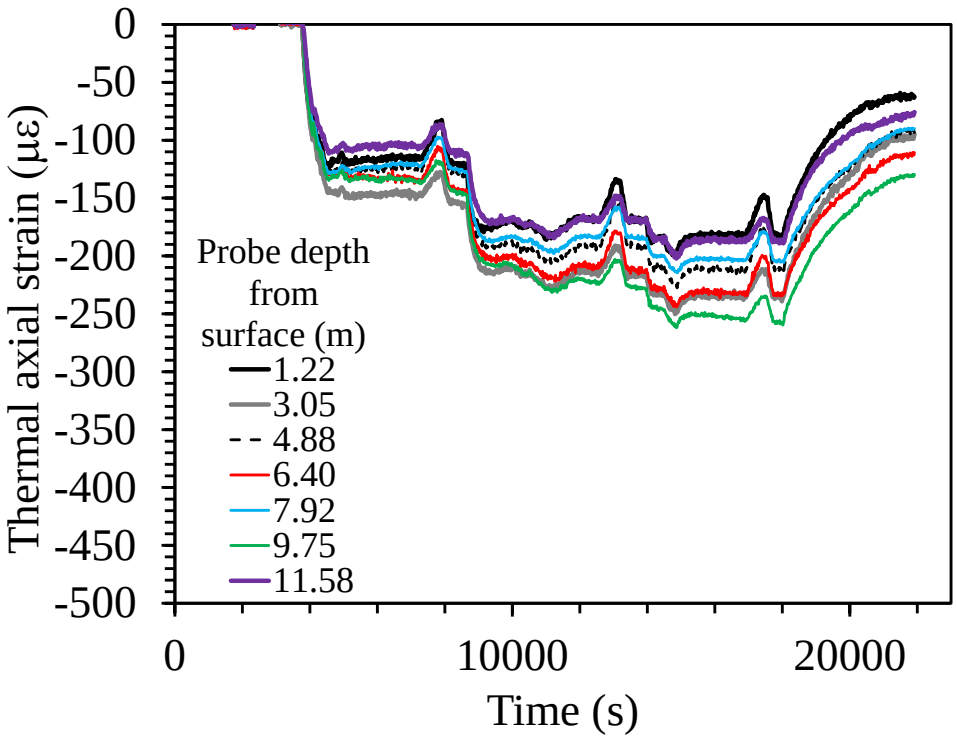

Figure 6.4.5-10 Axial strain time series for the staged heated and cooled load test on the end-bearing foundation in Bonny silt.

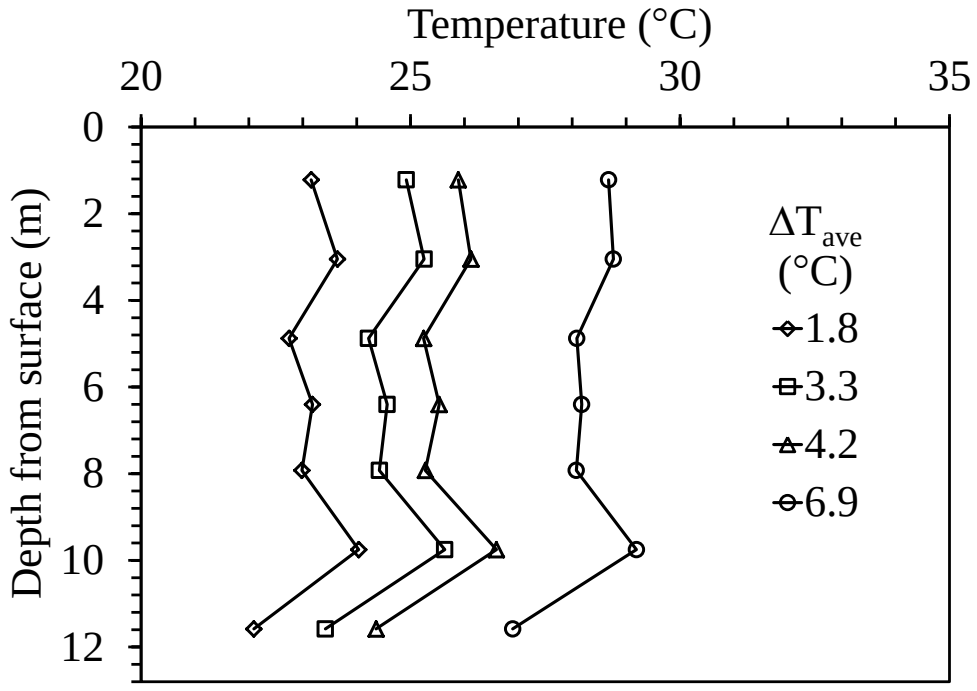

Figure 6.4.5-11 Temperature profile with depth for the staged heated and cooled load test on the end-bearing foundation in Bonny silt.

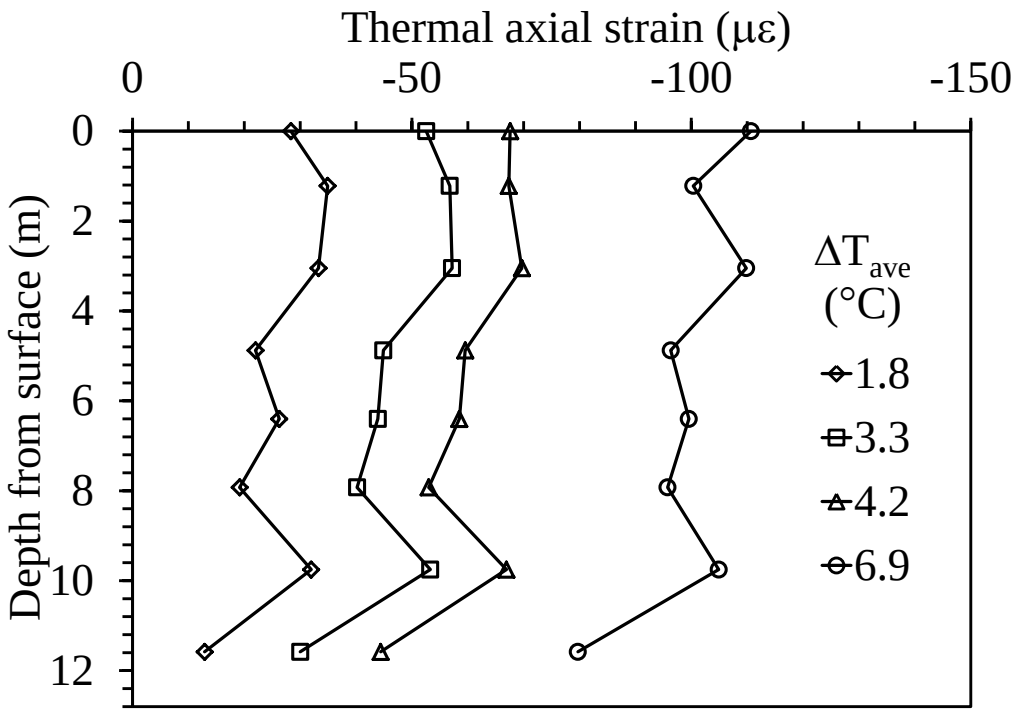

Figure 6.4.5-12 Thermal axial strain profile with depth for the staged heated and cooled load test on the end-bearing foundation in Bonny silt.

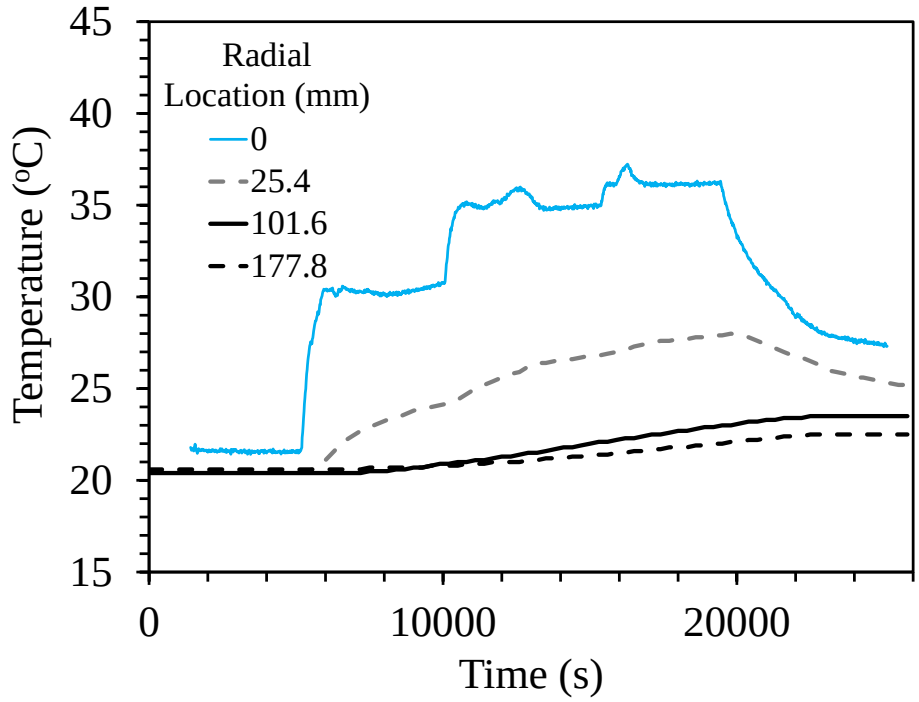

Figure 6.4.5-13 Temperature readings from dielectric sensors at radial locations for the staged heated and cooled load test on the end-bearing foundation in Bonny silt.

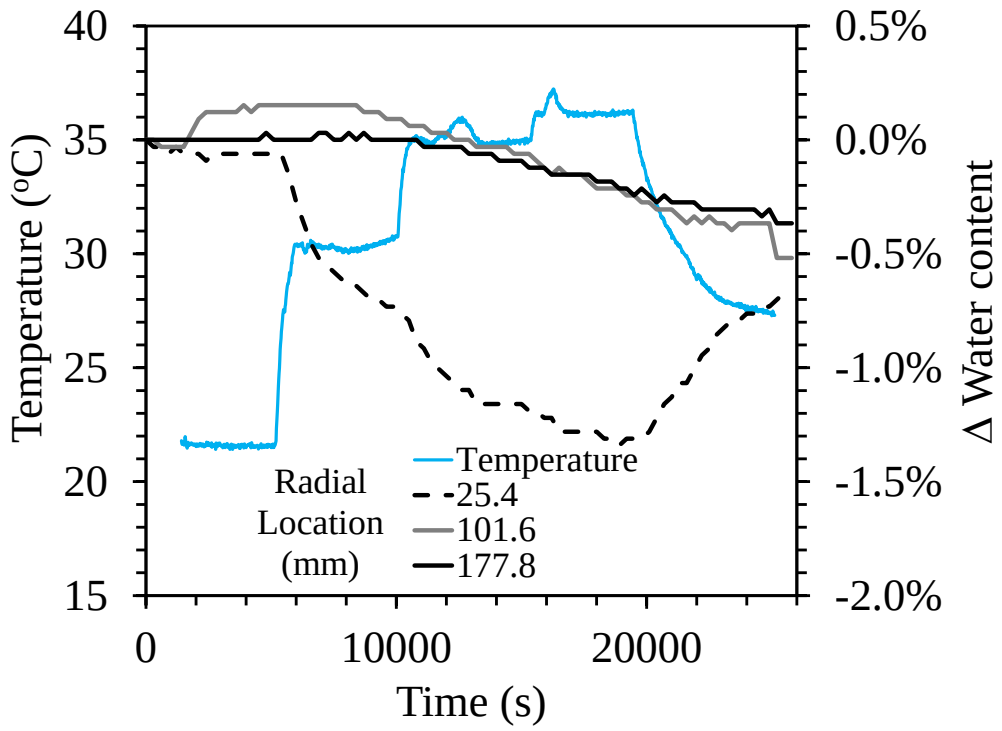

Figure 6.4.5-14 Change in water content at radial locations along with foundation temperature for the staged heated and cooled load test on the end-bearing foundation in Bonny silt.

CHAPTER 7 Analysis

7.1 Impact of Soil Type on the Behavior of Semi-Floating Foundations

This section presents a comparison of the results from different tests performed on semi-floating foundations in both Nevada sand and Bonny silt. Results are presented in terms of the thermal axial strain and thermal axial displacement at equilibrium under the applied temperature, as well as in terms of the load-settlement curve measured after reaching thermal equilibrium.

7.1.1 Thermal Axial Strain at Equilibrium Temperatures

The thermal axial strains after reaching equilibrium temperature conditions in the different tests are shown in Figure 7.1.1-1. In both soils, the thermal axial strain was relatively constant with depth. The strain at the top of the foundation is that related to free-expansion conditions. The foundations in Bonny silt show a slightly more non-linear response.

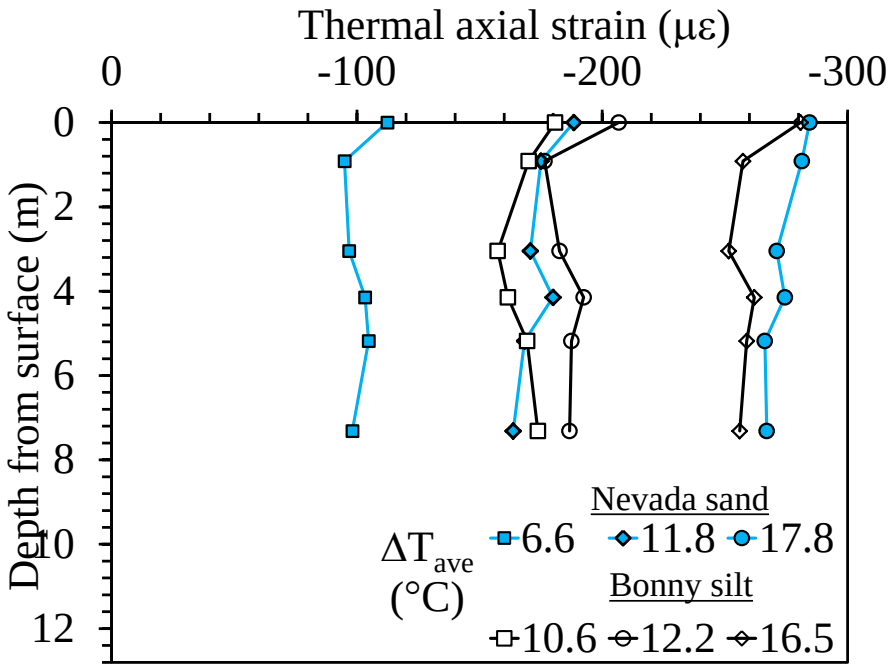

Figure 7.1.1-1 Thermal axial equilibrium strain profiles with depth at different temperatures for the semi-floating foundation in Nevada sand and Bonny silt.

7.1.2 Thermal Axial Displacements

Thermal axial displacement profiles for the semi-floating foundation in Nevada sand and Bonny silt are shown in Figure 7.1.2-1. The profiles correspond to the equilibrium displacement profile from each of the monotonically heated tests. The Nevada sand profiles are shown in blue and the Bonny silt profiles are shown in black. These thermal axial displacements are derived from the head displacement and axial strains during heating. The semi-floating foundation in Nevada sand is observed to expand about its center, which means that it can expand both upwards and downwards into the underlying soil. Similar results are seen in Bonny silt, although the null point is higher in the foundation than with the Nevada sand. This higher null point for the Bonny silt may be due to increases in friction in the soil. Greater thermal axial displacements in both directions are observed with increasing temperature.

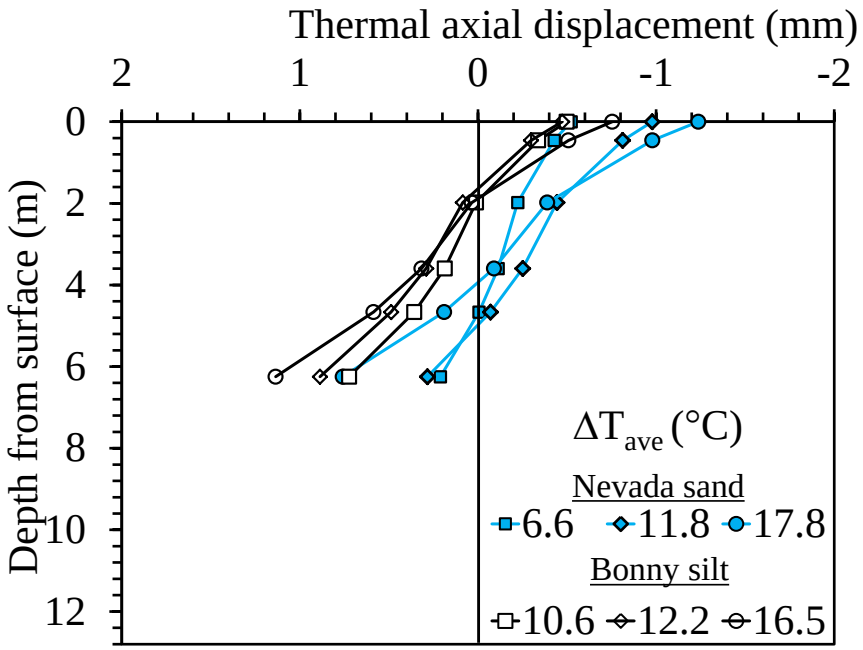

Figure 7.1.2-1 Thermal axial displacements showing the equilibrium profile for the semi-floating foundation in Nevada sand and Bonny silt.

7.1.3 Load Settlement Curves

A comparison of the prototype load-settlement curves for the semi-floating foundation in dry Nevada sand heated to different temperatures is shown in Figure 7.1.3-1. A slight increase in ultimate capacity is observed with increasing temperature, especially from the ambient tests, but the effect is not significant. Load settlement curves for the four tests performed in Nevada sand are presented. Comparison of these four curves indicates that there is no effect of temperature on the mechanical response of the soil. This is different than the results presented by McCartney and Rosenberg (2011), which indicated and increase in ultimate capacity with increase in temperature. The reason for the discrepancy may be that the sand and foundation expanded by a similar amount during heating, which didn't lead to a change in the normal stress against the foundation during heating. This would not lead to a change in the side shear resistance with temperature.

A comparison of the prototype load-settlement curves for the semi-floating foundation in Bonny silt heated to different temperatures is shown in Figure 7.1.3-2. Temperature clearly has an impact on the ultimate capacity of the semi-floating foundation in Bonny silt, which is similar to the results presented by McCartney and Rosenberg (2011). It is possible that the increased capacity is due to differential radial expansion of the foundation and surrounding soil, to the increased soil-structure interaction due to thermally induced water flow in the unsaturated soil away from the foundation, or to thermal consolidation of the soil surrounding the foundation. The comparison of the Nevada sand and Bonny silt suggests that soil type can play a major role in the capacity of an energy foundation.

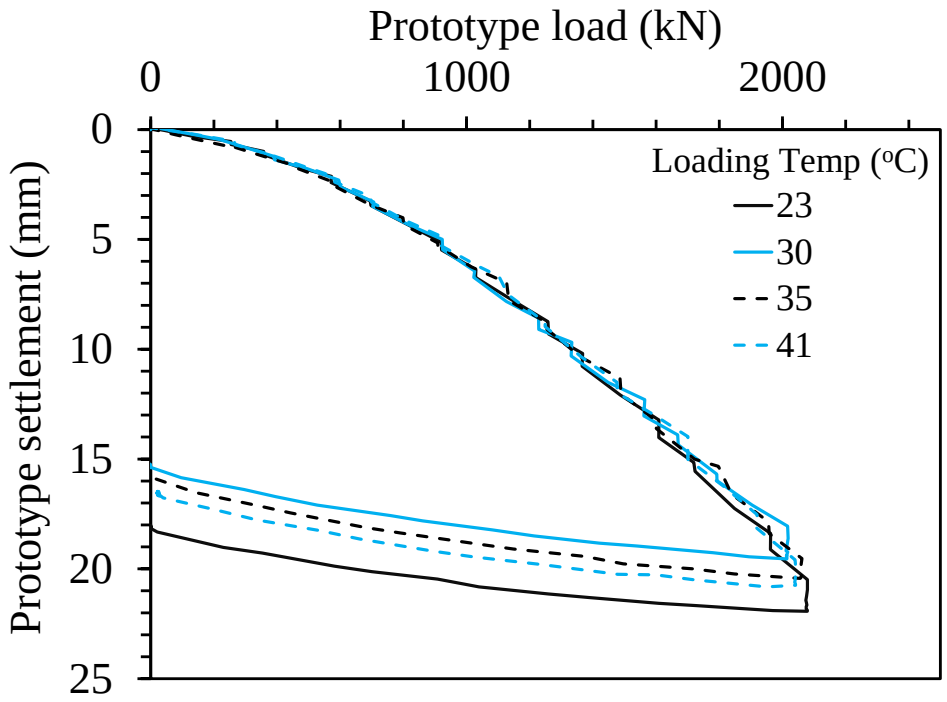

Figure 7.1.3-1 Prototype load settlement curves for the semi-floating foundation in Nevada sand at different equilibrium temperatures.

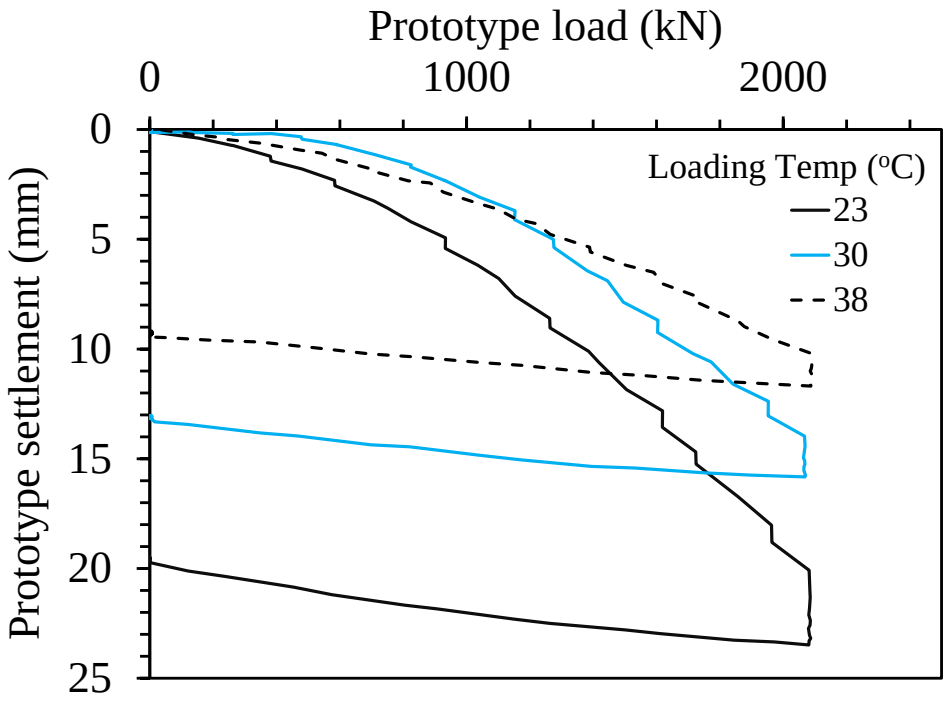

Figure 7.1.3-2 Prototype load settlement curves for the semi-floating foundation at different equilibrium temperatures in Bonny silt.

7.2 Thermal Axial Head Movement

Soil type is expected to play a major role in pile-soil interaction as observed from the results presented in Section 7.1.2, and that can also be shown with a plot of displacement and temperature. It can be seen in Figure 7.2.1-1 that the soil type plays a role in the thermal expansion of a foundation. Bonny silt provides a stiffer restraint to expansion than the dry Nevada sand for a particular change in temperature. This particular comparison involves two of the end-bearing foundation tests, so their toe displacement is zero, and all displacements can be seen at the foundation head.

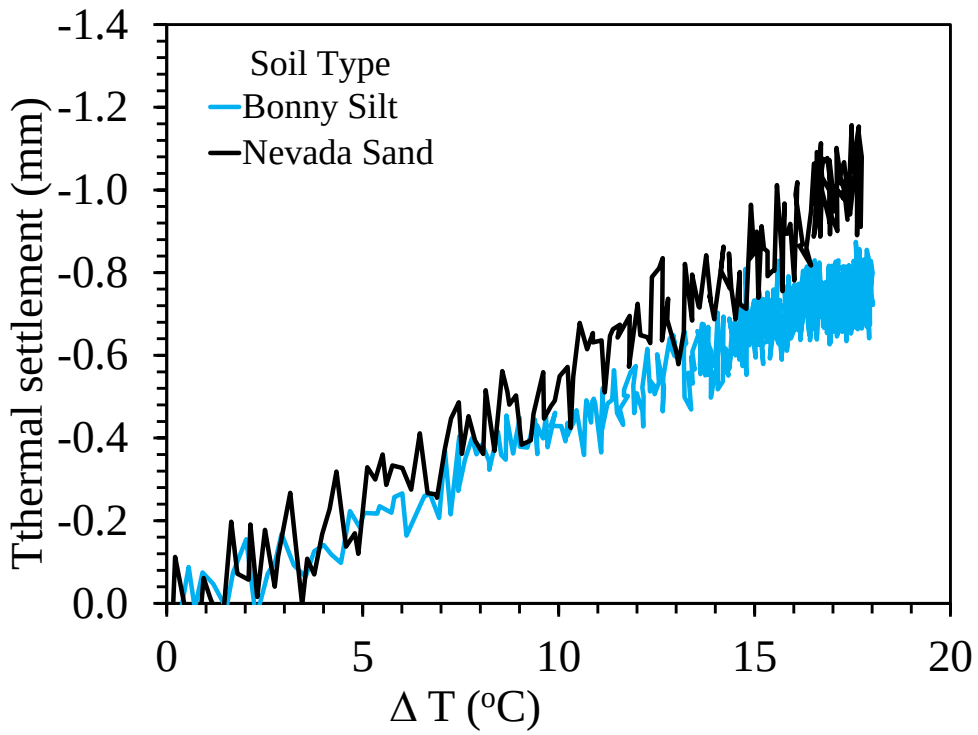

Figure 7.2.1-1 Comparison of thermal head movement for a semi-floating foundation in Nevada sand and Bonny silt with change in temperature.

7.3 Impact of End-Restraint Boundary Conditions at the Foundation Toe

The end-restraint boundary conditions at the toe of the foundation play a major role in the thermo-mechanical response of a foundation. A stiff bottom boundary is expected to result in a

greater magnitude of thermal axial stress at the toe of the foundation. Thermal axial strain profiles for the end bearing foundation are shown in Figure 7.3.1-1. It can be noticed that the thermal axial strain is lower than at the top. This follows the trend shown in the full scale data tests. The semi-floating foundation strain profile is shown in Figure 7.3.1-2. The thermal axial stress profiles are shown in Figure 7.3.1-3 and 7.3.1-4 for the end-bearing and semi-floating foundation respectively. The profile shapes are similar for the semi-floating and end-bearing foundation, although a larger thermal axial stress is observed at the base of the end-bearing foundation. This observation is consistent with field test results (Laloui et al. 2006; Bourne-Webb et al. 2009; McCartney and Murphy 2012).

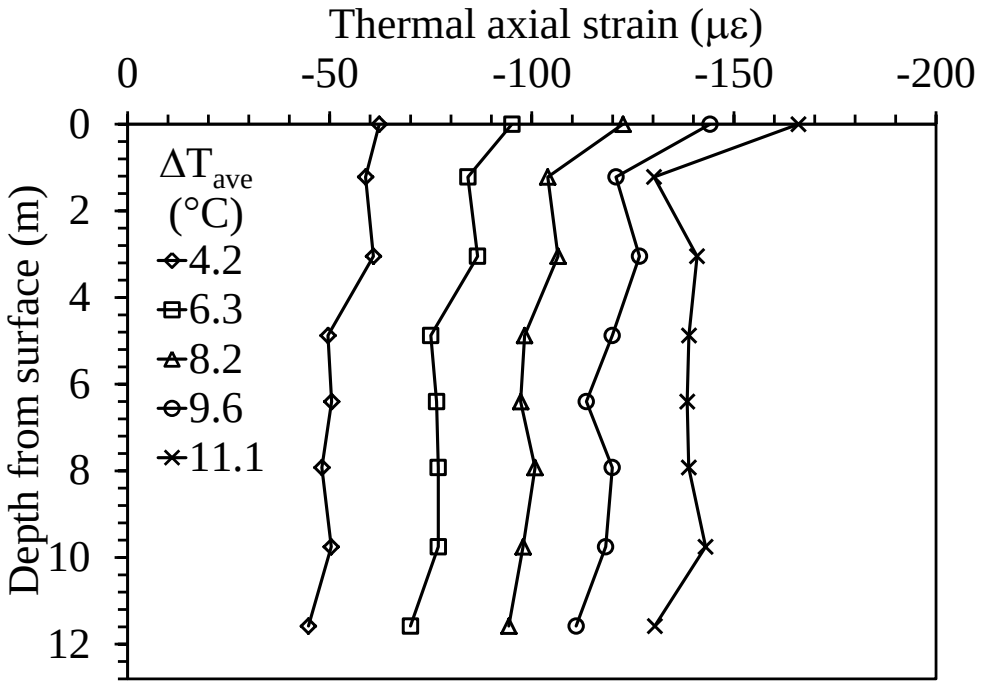

Figure 7.3.1-1 Thermal axial strain profiles for the end bearing foundation in Nevada sand.

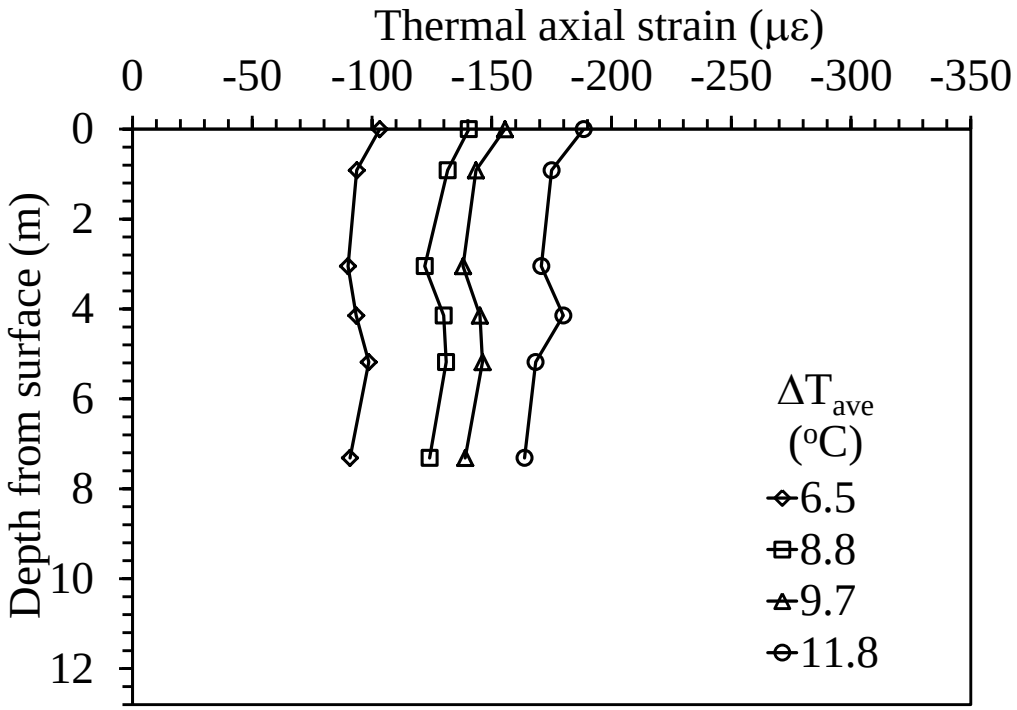

Figure 7.3.1-2 Thermal axial strain profiles for the semi-floating foundation in Nevada sand.

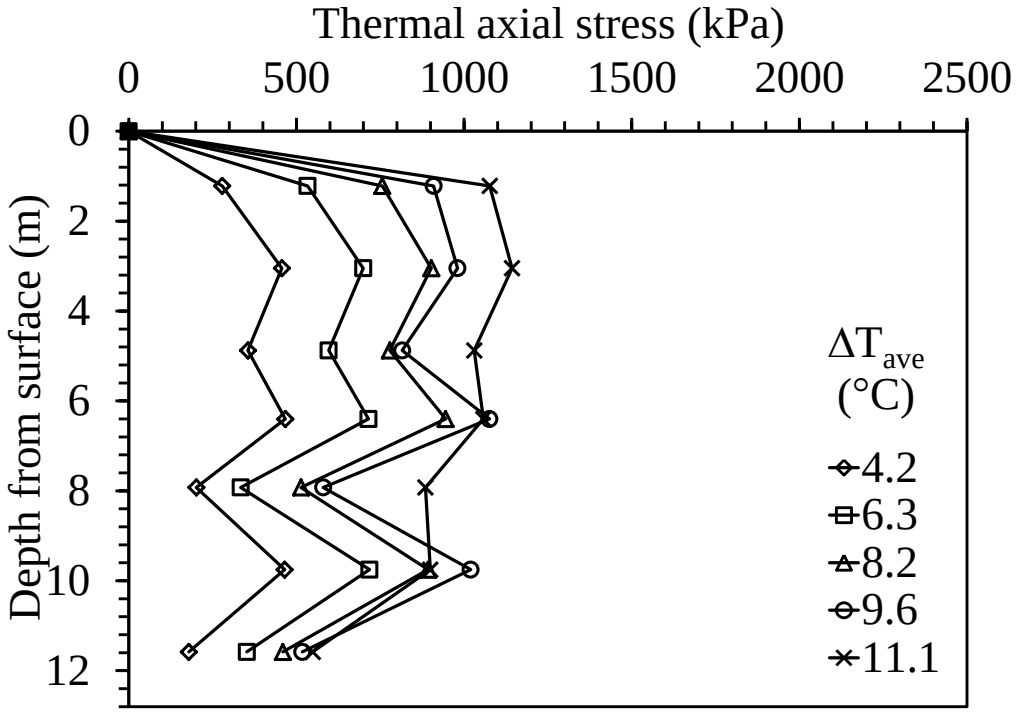

Figure 7.3.1-3 Thermal axial stress profiles for the end-bearing foundation in Nevada sand.

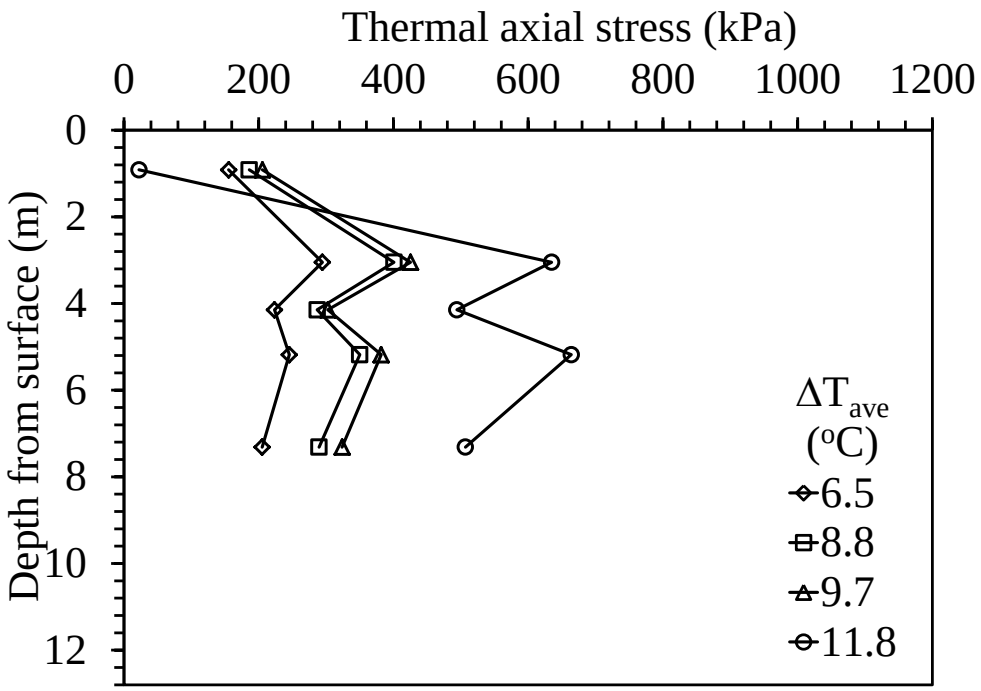

Figure 7.3.1-4 Thermal axial stress profiles in the semi-floating foundation in Nevada sand.

Load settlement curves are presented for the two Nevada sand tests and one Bonny silt test on end-baring foundations. The load-settlement curves from two tests on the end-bearing foundations in Nevada sand are shown in Figures 7.3.1-5 and 7.3.1-6, while that from the end-bearing foundation in Bonny silt is shown in Figure 7.3.1-7. After application of different temperatures to the foundation, the load-settlement curve has similar stiffness. This may indicate the temperature does not have a significant impact on the mobilized side shear for this foundation type. The first load in each test was slightly steeper and this is attributed to the seeding of the foundation in the soil layer.

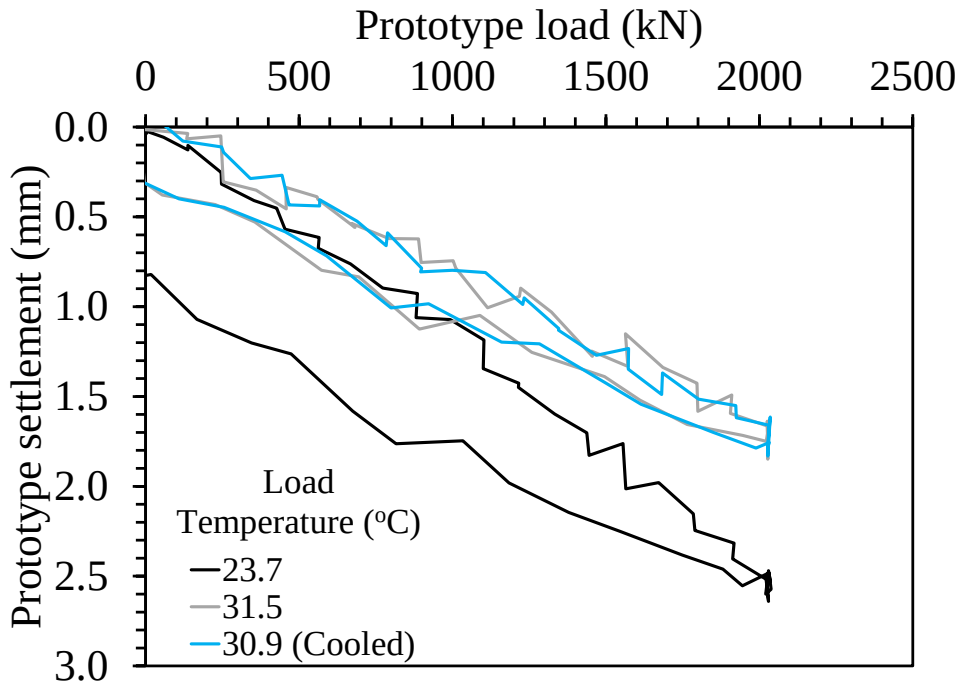

Figure 7.3.1-5 Load-settlement curves for mechanical loading at different temperatures for the end-bearing foundation in Nevada sand.

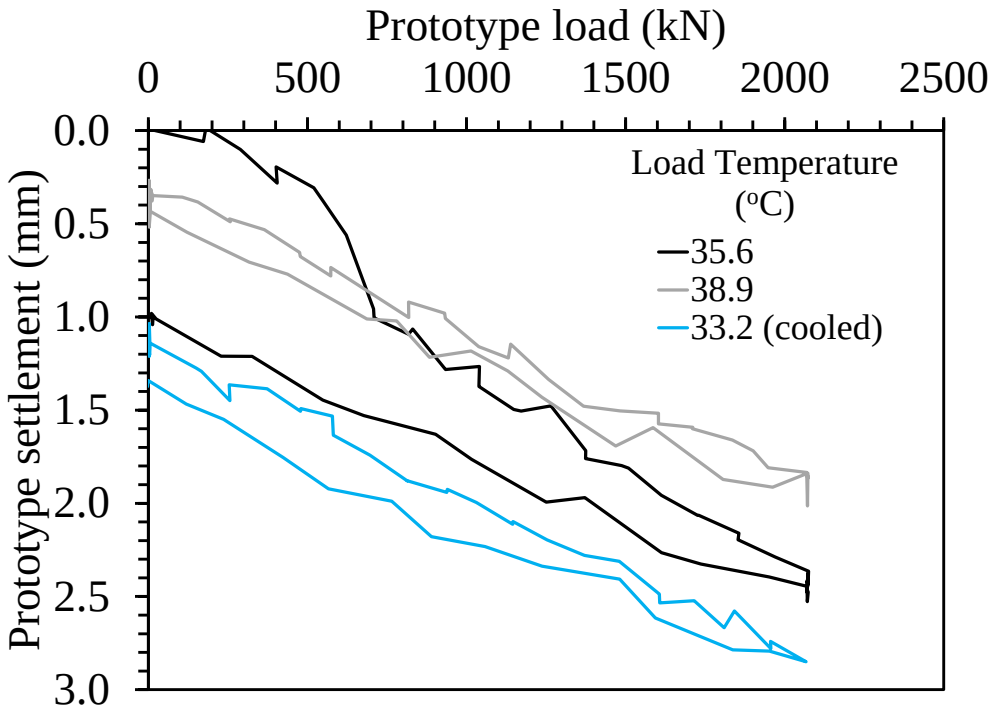

Figure 7.3.1-6 Load-settlement curves for mechanical loading at three different temperatures for the end-bearing foundation in Nevada sand.

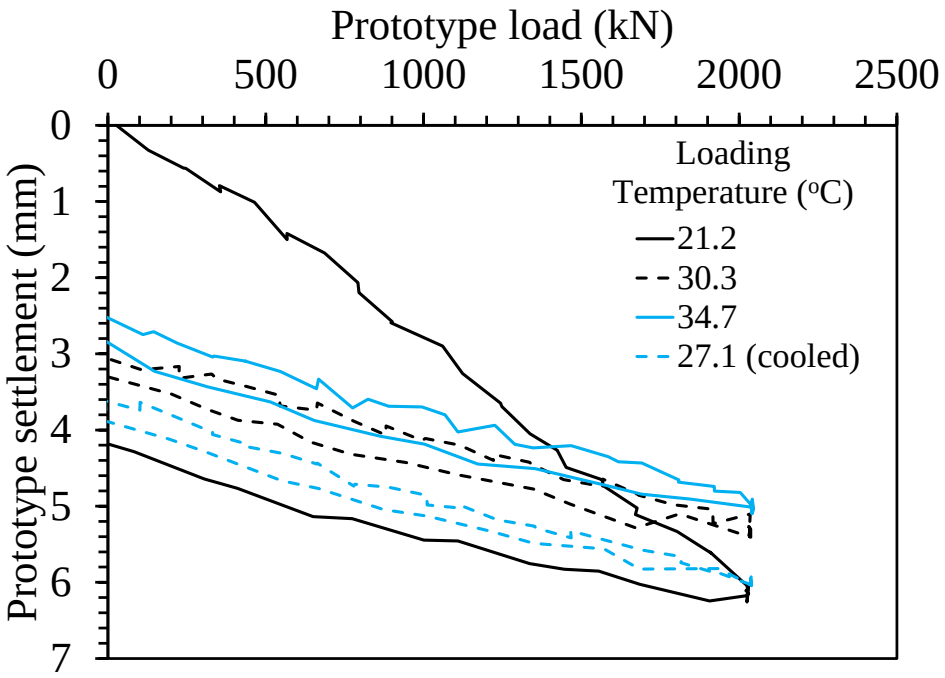

Figure 7.3.1-7 Load-settlement curves for mechanical loading at four different temperatures for the end-bearing foundation in Bonny silt.

7.4 Impact of End-Restraint Boundary Condition at the Foundation Head

The impact of head boundary conditions were investigated with two tests for the end-bearing foundation in Nevada sand, one with load control and the other with stiffness control. The synthesis of the test is shown in this section comparing the two tests. The thermal settlement and associated axial load is shown in Figure 7.4.1-1. This shows the increase in axial load for stiffness control while the load control axial load stays constant throughout the test. This increase in load has an effect on the total thermal expansion of the pile. This difference may be small, but a more rigid stiffness element may cause even more drastic differences in thermal expansion. The thermal settlement is also shown with the temperature of the foundation in Figure 7.4.1-2. The foundations were heated at slightly different rates due to variations in the valve control system but the final result is the same.

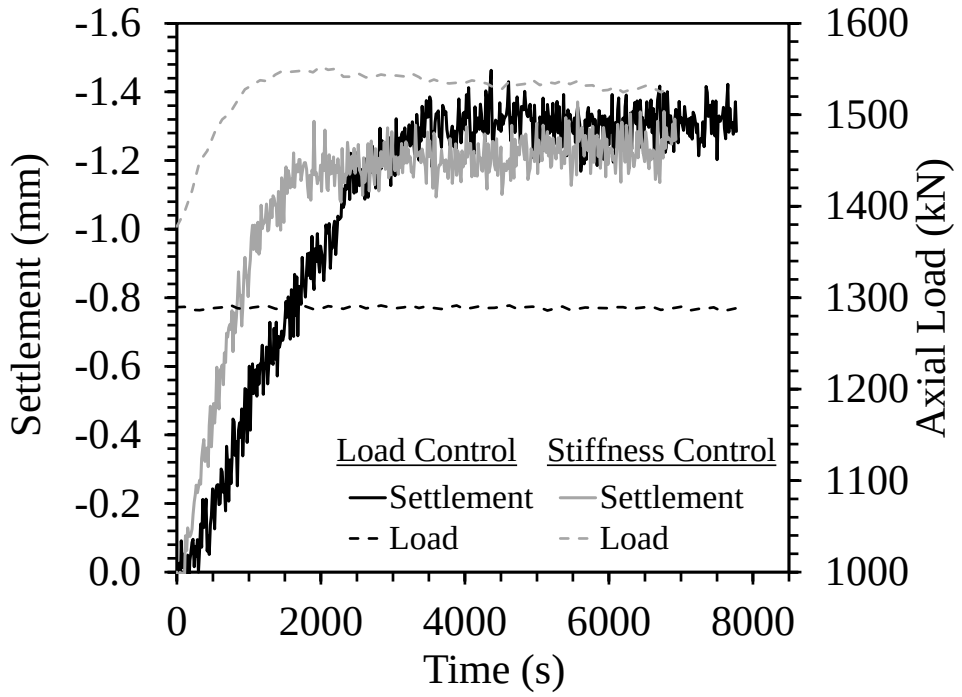

Figure 7.4.1-1 Comparison of foundation thermal axial displacement for tests performed in both load and stiffness control.

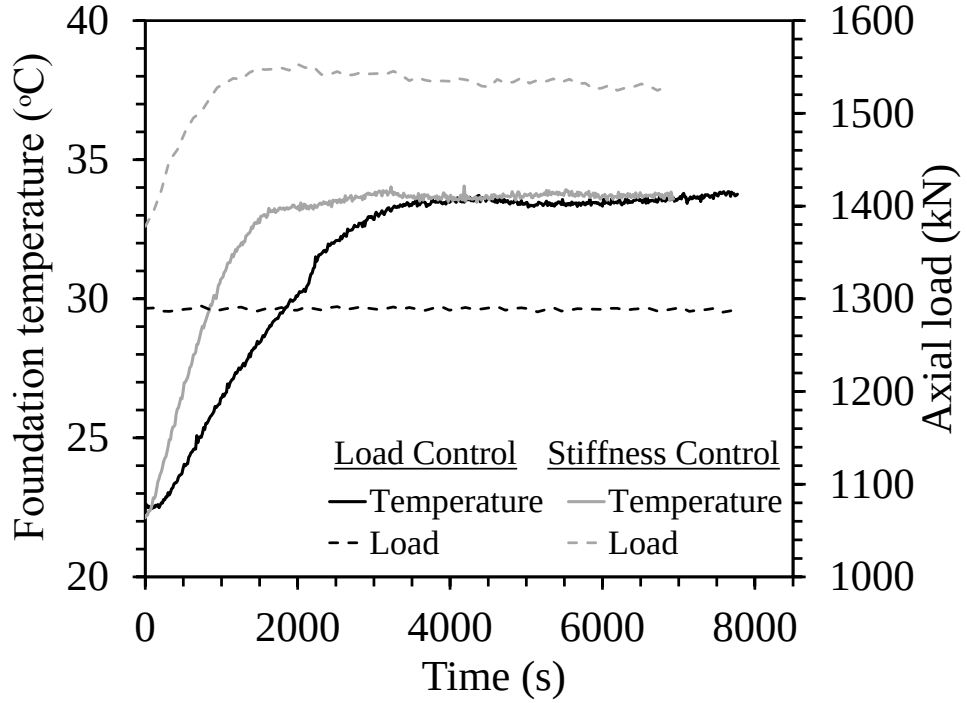

Figure 7.4.1-2 Comparison of temperature and foundation thermal displacement for load and stiffness control.

The displacement and change in temperature are shown in Figure 7.4.1-3 where it can be seen that the stiffness control setup allows less displacement throughout the process of heating due to the increase in load during the test. The foundation in stiffness-control conditions had lower thermal axial strains near the ground surface and greater thermal axial stresses. the thermal axial stresses in the end-bearing foundation are shown in Figure 7.4.1-4 for both head restraint boundary conditions. The thermal stresses were greater in the foundation during the stiffness-control test, especially near the top of the foundation. The thermal stresses at the bottom of the foundation were expected to be the greatest, but the actual change in temperature at this depth was lower than in the rest of the foundation, contributing to the lower thermal axial stress values.

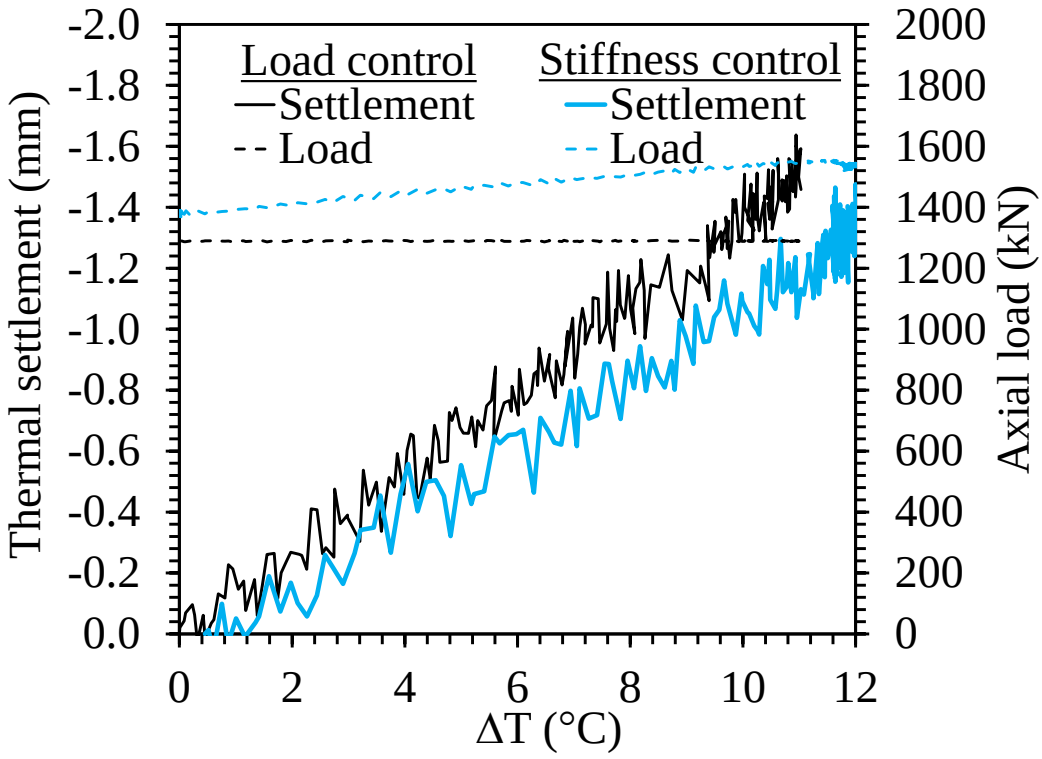

Figure 7.4.1-3 Foundation thermal expansion as a function of the change in temperature for tests with load and stiffness control.

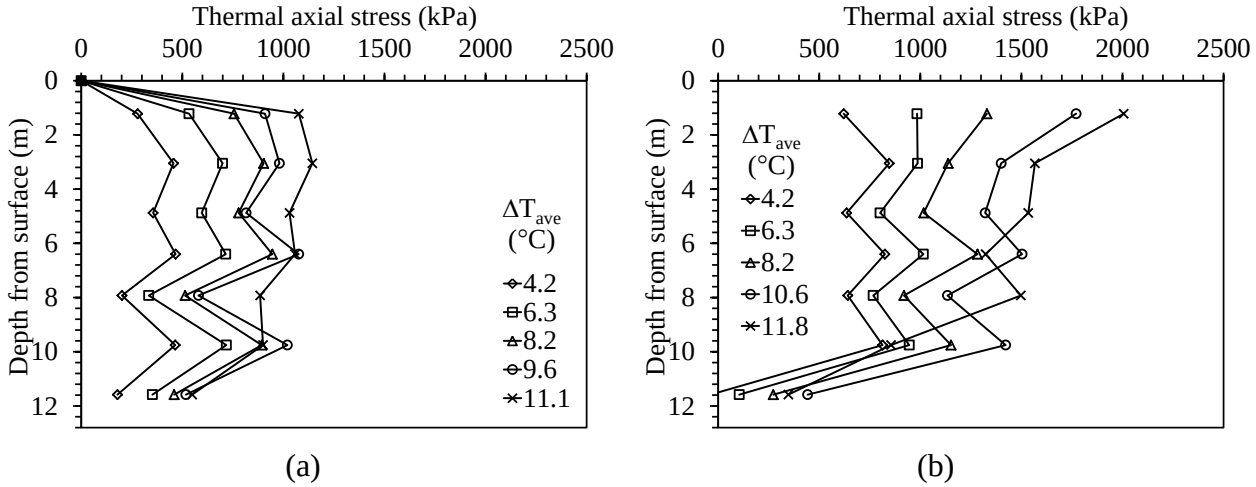

Figure 7.4.1-4 Thermal axial stresses: (a) Load-control test; (b) Stiffness-control test

7.5 Impact of Temperature Cycles

The impact of temperature cycles on the semi-floating foundation was tested in Bonny silt (S-BS-CL-Cyclic). The displacement profile of the foundation show a ratcheting effect of strain hardening as the foundation was continuously heated and cooled. Specifically, the foundations thermal axial strains showed a slight increasing strain with each consecutive cycle. The results from the test in this study confirm the results found by Stewart (2013). These trends are slight but as shown in Figure 7.5.1-1 with increasing cycle numbers. The results indicate that some strain softening could be occurring after each cycle.

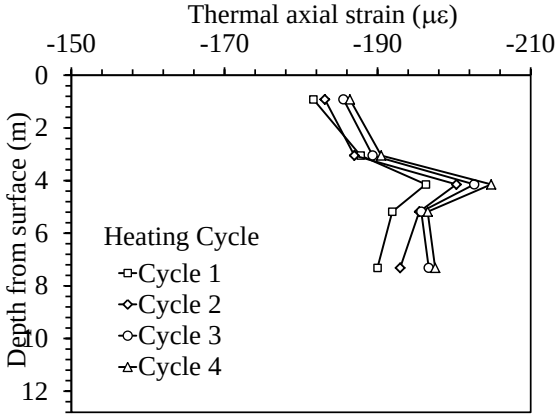

Figure 7.5.1-1 Thermal axial strains observed at the maximum temperature during cycles of heating for the semi-floating foundation in Bonny silt.

CHAPTER 8 Conclusions

This study involved a centrifuge modeling study on the impacts of different variables on the thermo-mechanical response of energy foundations with semi-floating and end-bearing boundary end-restraint boundary conditions in dry sand and unsaturated silt. The major conclusions that can be drawn from this study include:

1. A new method to correct the thermo-mechanical response of embedded strain gages was developed in this study, with corrections for mechanical response, thermal response, and steel-concrete thermal interaction.
2. The soil type (cohesionless vs. cohesive) plays a major role in the thermo-mechanical response of an energy foundation during heating by providing a stiff or weak stiffness response and thus restraining thermal expansion. Specifically, little change in the load-settlement curve of semi-floating foundations in dry sand that had been heated to different temperatures. However, an increase in the ultimate capacity was observed for the semi-floating foundation in unsaturated silt, potentially due to thermally induced water flow, thermal consolidation of the soil, and the initially greater radial stresses on the foundation induced by compaction.
3. The end-restraint boundary condition at the toe of an energy foundation affects the magnitude of thermal axial strain and stress profiles, leading to greater thermal axial stresses at the base of end-bearing energy foundations than at the base of semi-floating energy foundations. Stiffness control conditions (i.e., non-zero head restraint) were found to lead to less upward foundation movement and higher axial stresses than load control conditions (i.e., zero head restraint). The foundation in stiffness-control conditions had lower thermal axial strains near the ground surface and greater thermal axial stresses.

4. The load-settlement stiffness of an end bearing foundation in dry sand remains the same after application of different temperatures, confirming that the temperature doesn't affect the side shear resistance in this material.
5. Cyclic loading was found to affect the semi-floating foundation in Bonny silt by inducing a slight strain softening response with each successive thermal cycle. Less upward expansion was observed on successive heating of the foundation to the same foundation.

The soil type is observed to restrain thermal expansion as well as carry significant implications in load failure criteria. The differences observed in this study for the same foundations in different soil types can be used in future studies to quantify the role of soil type on thermo-mechanical soil-structure interaction in energy foundations. The results also reflect that care must be taken to understand the underlying soil stratigraphy for energy foundations in the field. The tests with different end-restraint boundary conditions on the end-bearing foundation provided insightful results into how a change in head condition can lead to pile response, which is something that is very difficult to quantify in field tests.

REFERENCES

Amatya, B.L., Soga, K., Bourne-Webb, P.J., Amis, T., Laloui, L. (2012). "Thermo-mechanical behaviour of energy piles." Géotechnique 62(6), 503–519.

Bourne-Webb, P., Amatya, B., Soga, K., Amis, T., Davidson, C., Payne, P. (2009). "Energy pile test at Lambeth College, London: Geotechnical and thermodynamic aspects of pile response to heat cycles." Géotechnique. 59(3), 237-248.

Brandl, H. (1998). "Energy piles and diaphragm walls for heat transfer from and into the ground." BAP III, Ghent, Belgium. October 19-21. Balkema, Rotterdam. 37–60.

Brandl, H. (2006). "Energy foundations and other thermo-active ground structures." Géotechnique. 56(2), 81-122.

Ennigkeit, A. & Katzenbach, R. (2001). "The double use of piles as foundation and heat exchanging elements." *Proc. 15th ICSMGE*. Istanbul, Turkey. 893-896.

Knellwolf, C., Peron, H., Laloui, L. (2011). "Geotechnical analysis of heat exchanger piles." *J. of Geotech. and Geoenv. Engineering*. ASCE. 137(12), 890-902.

Ko, H.-Y. (1988). "Summary of the state-of-the-art in centrifuge model testing." *Centrifuges in Soil Mechanics*. Craig, James, Scofield, eds. Balkema, 1988, 11-28.

Krishnaiah, S. Singh, D.N. (2004). "Centrifuge modelling of heat migration in soils," *Int. J. of Physical Modelling in Geotechnics*. 4(3), 39-47.

Laloui, L., Nuth, M. Vulliet, L. (2006). "Experimental and numerical investigations of the behaviour of a heat exchanger pile." *IJNAMG*. 30(8), 763–781.

McCartney, J.S. Rosenberg, J.E. (2011). "Impact of heat exchange on side shear in thermo-active foundations." *GeoFrontiers 2011*. March 13-16th, 2011. ASCE. 10 pg.

Murphy, K.D., McCartney, J.S. (2012). "Strain distributions in full-scale energy foundations." *DFI Journal*. vol. 6, no. 2, 2012, 28-36.

Plaseied, N. (2011). *Load-Transfer Analysis of Energy Foundations*. M.S. Thesis. Univ. of Colorado Boulder. 90 pg.

Popescu, R. and Prevost, J.H. (1993). "Centrifuge validation of a numerical model for dynamic soil liquefaction." Soil Dynamics and Earthquake Engineering. 12, 73-90.

Savvidou, C. (1988). "Centrifuge modelling of heat transfer in soil." *Centrifuge 8*8, Corté, ed., Balkema. 583-591.

Stewart, M. (2012). *Centrifuge Modeling of Strain Distributions in Energy Foundations*. MS Thesis. Univ. of Colorado Boulder. 110 pg.

Stewart, M.A. and McCartney, J.S. (2013). "Centrifuge modeling of energy foundations under cyclic heating and cooling." ASCE Journal of Geotechnical and Geoenvironmental Engineering. In 2nd review.